Surface-Assisted Chemistry at Interfaces between Metals and Organic Thin Films

D i s s e r t a t i o n

zur Erlangung des
Doktorgrades der Naturwissenschaften
(Dr. rer. nat.)

dem Fachbereich Chemie
der Philipps-Universität Marburg

vorgelegt von

Min Chen
Master of Engineering

aus Bengbu, China

Marburg an der Lahn
2016

Der praktische Teil der vorliegenden Arbeit wurde unter Leitung von Herrn Prof. Dr. J. Michael Gottfried in der Zeit von September 2010 bis März 2012 im Department Chemie und Pharmazie der Friedrich-Alexander-Universität Erlangen-Nürnberg und in der Zeit von April 2012 bis Februar 2016 am Fachbereich Chemie der Philipps-Universität Marburg angefertigt.

Vom Fachbereich Chemie der Philipps-Universität Marburg (Hochschulkennziffer: 1180) als Dissertation am 15.02.2016 angenommen.

Tag der Disputation:	24.03.2016
Erstgutachter:	Prof. Dr. Michael Gottfried
Zweitgutachter:	Prof. Dr. Gerhard Hilt

Selbständigkeitserklärung

gemäß § 10, Absatz 1 der Promotionsordnung der Mathematisch-Naturwissenschaftlichen Fachbereiche und des Medizinischen Fachbereichs für seine mathematisch-naturwissenschaftlichen Fächer der Philipps-Universität Marburg vom 15.07.2009.

Ich erkläre, dass eine Promotion noch an keiner anderen Hochschule als der Philipps-Universität Marburg, Fachbereich Chemie, von mir versucht wurde und versichere, dass ich meine vorgelegte Dissertation

Surface-Assisted Chemistry at Interfaces between Metals and Organic Thin Films

selbst und ohne fremde Hilfe verfasst, nicht andere als die in ihr angegebenen Quellen oder Hilfsmittel benutzt, alle vollständig oder sinngemäß übernommenen Zitate als solche gekennzeichnet sowie die Dissertation in der vorliegenden oder einer ähnlichen Form noch bei keiner anderen in- oder ausländischen Hochschule anlässlich eines Promotionsgesuches oder zu anderen Prüfungszwecken eingereicht habe.

Marburg, den 25.02.2016

Min Chen

Abstract

Interfaces between metals and organic thin films are of paramount importance for organic electronic devices. By photoemission spectroscopy (XPS), scanning tunneling microscopy/spectroscopy (STM/STS), temperature programmed desorption/reaction (TPD/TPR) and density functional theory calculations (DFT), chemical reactions and diffusion processes during the formation of interfaces/interphases, and their electronic structures are investigated.

The presented thesis focuses on two distinct substance classes, arranged by the reacting functional groups of the involved organic phases. Various reaction systems including organic-on-metal and metal-on-organic interfaces are visited.

In the first major topic, the surface coordination chemistry of thin films formed by porphyrinoid molecules with coinage metals – the latter either as crystalline substrate surface or dosed onto the films as atoms – is characterized. Molecular film thicknesses extend from incomplete layers, *i.e.*, submonolayer coverages, to a few ten nanometers, *i.e.*, multilayers. Metalation of 2*H*-tetraphenylporphyrin (2HTPP) at submonolayer coverages and 2*H*-phthalocyanine (2HPc) for up to multilayer coverages is found to be possible at elevated temperatures even from an atomically flat copper substrate. TPD/TPR studies reveal that the presence of an exchange mechanism could be responsible for the observed substrate based multilayer metalation.

Besides the interfacial chemical bond, *i.e.*, between the surface and the metal complex, secondary effects – such as charge transfer and weak band bending – are characterized in detail for cobalt phthalocyanine adsorbed on Cu(111). Individual molecules in porphyrin or phthalocyanine thin films are able to oxidize cobalt atoms into formal Co(II) species. By modification of the reaction center from porphin to corrole, *i.e.*, essentially by the replacement of an iminic by a pyrrolic nitrogen in the macrocycle, the formation of Co(III) complexes is rendered possible.

Moreover, multilayer metalation of 2HTPP molecules with deposited cobalt atoms is investigated in detail by both laboratory X-ray source (XPS) and synchrotron-based hard X-rays (HAXPES). Since the latter is a nondestructive method for bulk composition probing, chemical and physical properties can be investigated. This technique is also applied to obtain a depth profile of a layered battery cathode – initially comprising lithium-nickel-manganese-oxide and lithium-titanium-oxide – after

ex situ electrochemical cycling.

The second major topic is dedicated to the behavior of purposively designed terminal oligophenylene dibromides on the flat hexagonal single crystal surfaces of copper and silver.

Submonolayer amounts of oligophenylene dibromides deposited at cryogenic temperatures on the copper substrate show bromine detachment upon moderate temperature increase along with an intermediate formation of metal-organic oligomers. Upon further annealing, the metal is eliminated and entirely organic covalent structures are formed on the surface in analogy to the Ullmann coupling.

The here presented surface reaction allows *in situ* synthesis of giant hexagonal macrocycles consisting of thirty phenylene units. Macrocycles with altered numbers of members are also accessible with reduced yield. Since these square, pentagonal and heptagonal shapes are not fully compatible with the hexagonal motive of the oligophenylene monomers, they exhibit strained geometries leading to modified electronic structures. These huge molecules are further used as organic quantum corrals to achieve and analyze the induced surface state confinements.

Similar precursor compounds are deposited on a silver substrate in order to increase the mobility of the organic molecules as well as to suppress the formation of covalent bonds with the metal. This enables the generation of equilibrium based, self-assembling structures. Utilizing building blocks with three-fold symmetry, defect-free molecular fractal-like patterns – resembling Sierpiński triangles – are obtained.

Revealing the chemical and physical processes at the interfaces important for device performance is the intent of this thesis. By fine tuning various intrinsic and external conditions, structural and chemical control of two-dimensional supramolecular phases is achieved.

Surface-assisted chemistry – here *in situ* metalation of porphyrinoid molecules, synthesis of giant honeycombene macrocycles, and two-dimensional molecular self-assembled networks – as well as the properties, *e.g.*, adsorbate-substrate interaction, of formed, and in some cases buried, interfaces/interphases between metals and organic thin films are comprehensively studied with a wide range of complementary ultrahigh vacuum based surface science techniques. The results and conclusions of the therefrom emerged publications are summarized in this work.

Kurzzusammenfassung

Grenzflächen zwischen Metallen und organischen Dünnschichten sind von herausragender Wichtigkeit für organoelektronische Bauteile. Mittels Photoelektronenspektroskopie (XPS), Rastertunnelmikroskopie bzw. -spektroskopie (STM/STS), Temperatur-programmierter Desorptions- bzw. Reaktionsspektroskopie (TPD/TPR) und Dichtefunktionaltheorie (DFT) werden chemische Reaktions- und Diffusionsprozesse während der Bildung von Grenzflächen/Grenzphasen, sowie deren elektronische Strukturen untersucht.

Die inhaltlichen Schwerpunkte dieser Dissertation liegen auf zwei verschiedenen Substanzklassen und sind nach den reagierenden funktionellen Gruppen der involvierten organischen Phasen geordnet. Eine Vielzahl an Reaktionssystemen, unter anderem Organik-auf-Metall- und Metall-auf-Organik-Grenzflächen, werden dabei betrachtet.

Der erste Hauptaspekt befasst sich mit der Charakterisierung der Oberflächen-Koordinationschemie von Dünnschichten aus porphyrinoiden Molekülen mit Münzmetallen – letztere entweder als kristalline Substratoberfläche oder in atomarer Form auf die Dünnschichten dosiert. Die Stärken der molekularen Dünnschichten reichen von unvollständigen Lagen, d.h. Submonolagen, bis zu einigen zehn Nanometern, d.h. Multilagen. Als wesentliches Ergebnis lässt sich festhalten, dass bei erhöhten Temperaturen die Metallierung von 2H-Tetraphenylporphyrin (2HTPP) Submonolagen und von 2H-Phthalocyanin (2HPc) Multilagen mit Kupfer sogar von atomar flachen Oberflächen möglich ist. Untersuchungen mittels TPD/TPR ergeben, dass die Gegenwart eines Austauschmechanismuses für die beobachtete Metallierung von Multilagen verantwortlich sein könnte.

Zusätzlich zu der chemischen Bindung an der Grenzfläche zwischen Cobaltphtalocyanin und Cu(111) werden sekundäre Effekte – wie z.B. Ladungsverschiebung (*charge transfer*) und schwache Bandverbiegung (*weak band bending*) – detailliert charakterisiert. Einzelne Moleküle in Dünnschichten aus Porphyrinen oder Phthalocyaninen können Cobaltatome zu formal zweiwertigen Co(II) Spezies oxidieren. Durch Modifikation des reaktiven Zentrums der organischen Komponente, die im Wesentlichen aus dem (formalen) Ersatz eines iminischen durch einen pyrrolischen Stickstoff im Makrocyclus besteht, und Porphin in Corrol wandelt, wird die Bildung von Co(III) Komplexen ermöglicht.

Weiterhin wird die Metallierungsreaktion von 2HTPPP mit deponierten Cobaltatomen, sowohl mit einer Laborröntgenquelle (XPS) als auch mit einer synchrotronbasierten Quelle für harte Röntgenstrahlung (HAXPES), im Detail untersucht. Da die letztgenannte Methode zerstörungsfrei arbeitet, ist es möglich, die chemischen und physikalischen Eigenschaften im Volumen der Probe zu bestimmen. Dieses Verfahren wird hier auch angewandt, um ein Tiefenprofil einer mehrschichtigen Akkumulatorkathode – ursprünglich bestehend aus Lithium-Nickel-Magnesium-Oxid und Lithium-Titan-Oxid – nach *ex situ* durchgeführten Lade- und Entladezyklen zu erstellen.

Der zweite Hauptaspekt widmet sich dem Verhalten von gezielt entwickelten endständigen Oligophenylendibromiden auf flachen, hexagonalen Einkristalloberflächen aus Kupfer und Silber.

Submonolagen aus Oligophenylendibromiden, die bei kryogenen Temperaturen auf dem Kupfersubstrat abgeschieden wurden, zeigen bei einer moderaten Temperaturerhöhung eine gleichzeitige Abspaltung einer Bromspezies und die Bildung eines intermediären metallorganischen Oligomers. Bei weiterem Erhitzen wird, in Analogie zur Ullmann-Kupplung, das Metall eliminiert und kovalente, rein organische Strukturen werden auf der Einkristalloberfläche gebildet.

Die hier präsentierte Oberflächenreaktion erlaubt die *in situ* Synthese von hexagonalen Makrozyklen, die aus dreißig Phenyleneinheiten bestehen. Ringsysteme mit anderen Größen sind, wenn auch mit reduzierter Ausbeute, erhältlich. Da diese quadratischen, penta-, und heptagonalen Gebilde nicht vollständig mit dem hexagonalen Motiv der Oligophenylenmonomere verträglich sind, weisen sie gespannte Geometrien auf, die zu einer veränderten elektronischen Struktur führen. Weiterhin werden diese Riesenmoleküle als rein organische Quantengehege (*quantum corrals*) genutzt, um die durch sie induzierten und begrenzten elektronischen Oberflächenzustände zu untersuchen.

Ähnliche Vorläuferverbindungen werden auf ein Silbersubstrat abgeschieden, um die Mobilität der organischen Moleküle zu erhöhen und um gleichzeitig die Bildung von kovalenten Bindungen mit dem Metall zu unterdrücken. Dies ermöglicht die Erzeugung von gleichgewichtsbasierten, selbstorganisierten Strukturen. Durch die Verwendung von Bausteinen mit dreizähliger Symmetrie können defektfreie, molekulare fraktalartige Muster erhalten werden, die an Sierpiński Dreiecke erinnern.

Die Intention dieser Doktorarbeit ist es, die chemischen und physikalischen Prozesse an Grenzflächen, die für die Leistungsfähigkeit von Bauteilen wichtig sind, aufzudecken. Durch sorgsames Einstellen von immanenten und externen Parametern konnte chemische und strukturelle Kontrolle über zweidimensionale supramolekulare Phasen erhalten werden.

Aspekte der oberflächenunterstützten Chemie – hier die *in situ* Metallierung von

porphyrinoiden Molekülen, die Synthese von riesigen, wabenartigen Makrozyklen (*honeycombenes*) und zweidimensionalen molekularen selbstorganisierten Netzwerken – sowie die Eigenschaften, z.B. Adsorbat/Substrat-Wechselwirkungen, von gebildeten, und in machen Fällen verborgenen, Grenzflächen bzw. Grenzphasen zwischen Metallen und organischen Dünnschichten werden mit einer Vielzahl von sich gegenseitig ergänzenden, ultrahochvakuumbasierten Techniken der Oberflächenwissenschaften umfangreich untersucht. Die Ergebnisse und Folgerungen, die sich im Rahmen der daraus entstandenen Publikationen ergeben haben, sind in dieser Arbeit zusammengefasst.

Contents

Abbreviations

Symbols

(hkl)	Crystal plane
$(hkil)$	Crystal plane (hexagonal)
$[hkl]$	Crystal axis
$\ldots\vert_x$	Evaluated at x
$\vert\ldots\vert$	Absolute value
d	Total differential
δ	Difference
	Range
∞	Infinity
$\int$	Integral
$\sum$	Sum
$'$	Alternative
$\cdot$	(Dot-)Product
$\propto$	Proportional
$\approx$	Approximately
$\equiv$	Identical

Constants[1]

π	Pi	3.14159265358979
Ag L_α	X-ray line	2984.3 eV
Al K_α	X-ray line	1486.7 eV
e	Euler's number	2.71828182845905
	Elementary charge	1.60217663·10−19 C
h	Planck constant	$6.62607 \cdot 10^{-34}$ J·s
		$4.13567 \cdot 10^{-15}$ eV·s
$\hbar$	Reduced Planck constant	$1.05457 \cdot 10^{-34}$ J·s
		$6.58212 \cdot 10^{-16}$ eV·s
Mg K_α	X-ray line	1253.6 eV
R	Gas constant	8.3144621 $^{J}/_{K \cdot mol}$

1 Including units and the used accuracy.

Functions

δ	Delta function
cos	Cosine
exp	Exponential function
f	Fermi-Dirac function
inf	Infimum
lim	Limit
ln	Natural logarithm
log	Common logarithm

Variables[2]

β	Heating rate	$^{K}/_{s}$	
Δ	Dipole barrier		
ε	Orbital energy	eV	
θ	Coverage	d.l.	ML
ϑ	Emission angle	$^{\circ}$	
λ	Inelastic mean free path	m	
ν	Pre-exponential frequency factor	$^{1}/_{s}$	
	Photon frequency	$^{1}/_{s}$	
ϱ	Density of states	$^{1}/_{J \cdot m^3}$	
σ	Photoionization cross section	m^2	
ϕ	Angular efficiency factor		
Φ	Work function	eV	
	Injection barrier	eV	
Ψ	Wave function		
A	Area	m^2	
d	Thickness	m	
E	Energy	J	eV
EA	Electron affinity	eV	
F	Flux	$^{1}/_{m^2 \cdot s}$	
I	Intensity	a.u.	$^{1}/_{s}$
	Current	A	
IE	Ionization energy	eV	
J	Total angular momentum		
K	Calibration factor		

2 Given together with the context dependent units. "d.l.", *i.e.*, dimensionless, is omitted were possible.

$\mathbf{M}$	Tunneling matrix	
n	Atomic density	$1/m^3$
	Desorption order	
	Molecular generation	
R	Rate	$1/s$
	Ratio	
t	Time	s
T	Temperature	K
	Analyzer transmission function	
V	Potential	V
x	Position	m
y	Photoelectric ground state efficiency factor	
	Position	m
z	Position	m

Indices

$_0$	Basis	$_M$	Metal
$_\mu$	Summation index	$_{max}$	Maximal
$_\nu$	Summation index	$_{min}$	Minimal
$_B$	Binding	$_p$	Pristine
	Bias	$_P$	Pristine layer
$_{bi}$	Built-in	$_r$	Reacted layer
$_c$	Cover layer	$_s$	Substrate
$_{des}$	Desorption	$_{sa}$	Sample
$_e$	Electron	$_{sp}$	Spectrometer
$_F$	Fermi	$_t$	Tip
$_h$	Hole	$_{vac}$	Vacuum
$_{kin}$	Kinetic		

Methods

DFT	Density functional theory
ESCA	Electron spectroscopy for chemical analysis
HAXPES	Hard X-ray photoemission spectroscopy
IPES	Inverse photoemission spectroscopy
LEED	Low energy electron diffraction
NEXAFS	Near edge X-ray absorption fine structure
PES	Photoemission spectroscopy
ToF-SIMS	Time-of-flight secondary ion mass spectrometry
STM	Scanning tunneling microscopy
STS	Scanning tunneling spectroscopy
TPD	Temperature programmed desorption
TPR	Temperature programmed reaction
UP	Ultraviolet photoemission
UPS	Ultraviolet photoemission spectroscopy
XAFS	X-ray absorption spectroscopy measurements
XP	X-ray photoemission
XPS	X-ray photoemission spectroscopy

Materials

2HPc	21*H*,23*H*-Phthalocyanine
	2*H*-Phthalocyanine
	Phthalocyanine
2HTTBPP	Tetrakis(3,5-di-*tert*-butylphenyl)-21*H*,23*H*-porphyrin
2HTPP	5,10,15,20-Tetraphenyl-21*H*,23*H*-porphin
	2*H*-Tetraphenylporphyrin
	Tetraphenylporphyrin
2HTPyP	5,10,15,20-Tetra(4-pyridyl)-21*H*,23*H*-porphin
	2*H*-Tetrapyridylporphyrin
	Tetrapyridylporphyrin
3HHEDMC	2,3,8,12,17,18-Hexaethyl-7,13-dimethyl-21*H*,23*H*,24*H*-corrole
	3*H*-Hexaethyldimethylcorrole
	Hexaethyldimethylcorrole
Ag	Silver
Al	Aluminum
Al_2O_3	Aluminum oxide
Ar	Argon

Au	Gold
Br	Bromine
C	Carbon
Cl	Chlorine
CO	Carbon monoxide
Co	Cobalt
CoHEDMC	Cobalt(III) 2,3,8,12,17,18-hexaethyl-7,13-dimethyl-corrole
	Cobalt-hexaethyldimethylcorrole
CoPc	Cobalt(II) phthalocyanine
CoTPP	Cobalt(II) 5,10,15,20-tetraphenyl-porphin
	Cobalt-tetraphenylporphyrin
Cu	Copper
CuPc	Copper(II) phthalocyanine
CuTPP	Copper(II) 5,10,15,20-tetraphenyl porphin
	Copper-tetraphenylporphyrin
CuTPyP	Copper(II) 5,10,15,20-tetrapyridyl porphin
	Copper-tetrapyridylporphyrin
DB*m*TP	4,4″-Dibromo-*meta*-terphenyl
DB*m*QaP	4,4‴-Dibromo-*meta*-quaterphenyl
DB*m*″QiP	4,4⁗-Dibromo-*meta*″-quinquephenyl
DB*p*TP	4,4″-dibromo-*para*-terphenyl
F	Fluorine
Fe	Iron
FeTPP	Iron(II) 5,10,15,20-tetraphenyl porphin
	Iron-tetraphenylporphyrin
H	Hydrogen
He	Helium
Li	Lithium
LNMO	Lithium nickel manganese oxide
LTO	Lithium titanium oxide
Mn	Manganese
N	Nitrogen
−NH−	Pyrrolic nitrogen
−N=	Iminic nitrogen
−N*M*−	Metalated nitrogen *M*=Co, Cu
N_P	Pyridylic nitrogen
Ni	Nickel

NiPc	Nickel(II) phthalocyanine
O	Oxygen
P	Phosphorous
Pd	Palladium
ph	Phenylene unit
TBB	1,3,5-Tris(4-bromophenyl)benzene
Ti	Titanium

Instruments

HDL	Helium discharge lamp
LEED	Low energy electron diffraction
QCM	Quartz crystal microbalance
QMS	Quadrupole mass spectrometer

Miscellaneous

CF	ConFlat™
CW	Clockwise
CCW	Counterclockwise
e.g.	*exempli gratia*
et al.	*et alii*
FWHM	Full width at half maximum
HOMO	Highest occupied molecular orbital
i.e.	*id est*
IMFP	Inelastic mean free path
K	K shell
L	L shell
LDOS	Local density of states
LUMO	Lowest unoccupied molecular orbital
OLED	Organic light emitting diode
OTFT	Organic thin film transistor
OPV	Organic photovoltaic
SOMO	Singly occupied molecular orbital
ST	Sirpińsky triangle
UHV	Ultra-high vacuum
UV	Ultraviolet
VB	Valence band
VL	Vacuum level

Non SI-Units

%	Percent
Å	Ångström
a.u.	Arbitrary units
d.l.	Dimensionless
h	Hours
mbar	Millibar
min	Minute
ML	Substrate referenced monolayers
ML_M	Adsorbate referenced monolayers
ML_S	Substrate referenced monolayers

1 Introduction

Nowadays, well-characterized single crystal surfaces under ultra-high vacuum conditions routinely serve as model systems for studying elementary processes on surfaces in the field of surface science. Due to the reduced coordination of surface atoms and the broken periodicity in the surface normal direction, study and characterization of physical and chemical reactions on solid surface is very intriguing. Variations of the solids' terminations, *e.g.*, by deposition of molecules, lead to altered properties of both partners. Extension of the top layer leads to metal-organic or organic-metal interfaces which are wide spread in human's everyday life, for example in electronic devices.

The interface can be formed by vapor deposition of metals onto primed organic layers (metal-organic interface) or by vapor deposition of organic molecules onto solid metal surfaces (organic-metal interface). The focus of this thesis lies on characterization under ultra-high vacuum conditions of buried metal-organic interfaces as well as on buried organic-metal interfaces. Due to the methodical challenges, buried interfaces are a largely unexplored field and are often idealized as sharp transitions from one material to another. Conditions under which diffusion processes and reactions lead to the formation of an *interphase*, *i.e.*, a diffuse transition zone between the substrate and the pure deposited layer, are also explored in this work.

1.1 Surface Coordination Chemistry with Porphyrinoid Macrocycles

Porphyrins, phthalocyanines and related macrocycles play an important role in biological and biochemical processes, and also in medical treatment nowadays. For example, iron porphyrins embedded in heme-proteins are responsible for oxygen transport and magnesium porphyrins in chlorophyll are indispensable for the photosynthetic process in plants.[1] Most of the photosensitizers used in photodynamic cancer therapy are based on tetrapyrrole structures, including phthalocyanines. Their strong absorption for deep-red light which is able to pervade tissue and the resulting localized generation of toxic oxygen species lead to an effective therapy of cancer.[2]

In the context of surface chemistry, porphyrinoid macrocycles are intensively studied.[3,4] This substance class includes porphyrins, phthalocyanines, corroles, *etc.* as well as their substituted analogues and metalated derivatives. Their remarkable thermal stability, sublimability, specific ligand-functionality, planar macrocycle structures, and their capability to interact with a surface and an additional ligand at the same time make them ideal model substances for investigating a wide range of scientific questions. Due to their enormous variability in peripheral substituents, it is possible to tune geometric and electronic properties of the derived molecules. As an additional benefit, the targeted molecules can often be directly synthesized with moderate efforts.

One aspect of the mentioned geometrical modification is the possibility to adjust the distance, *i.e.*, bond length, between the central metal atom of a metallotetrapyrrole to a substrate surface by different *inert* spacer substituents on the periphery of the molecule. As a consequence of this adjustment, the resulting changes regarding chemical properties of the oxidized central metal atom are dominated by the distance to the substrate. Hence, this substance class provides excellent model systems for studying the interaction between metal ions and surface at well-defined distances.[5]

Due to their tailorable properties, those adsorbed metal complexes are promising candidates for heterogeneous catalysts,[6] gas sensors,[7] or molecular electronics.[8] The family of tetrapyrrole molecules is associated with a rich coordination chemistry.[9–12] A vast number of researches have proven that the metalation of porphyrins and phthalocyanines can be achieved not only by wet chemistry, but also by direct synthesis under ultrahigh vacuum conditions from the corresponding free bases. This coordination reaction of the macrocycle performs especially well with transition metals, *e.g.*, iron,[13] cobalt,[14] nickel,[15] copper,[16] zinc[17–19] and others.[4,20,21] Common to these processes is the oxidation of the metal atom into the corresponding cation and the reduction of the pyrrolic hydrogen to molecular hydrogen.[19] This *in situ* synthesis approach is

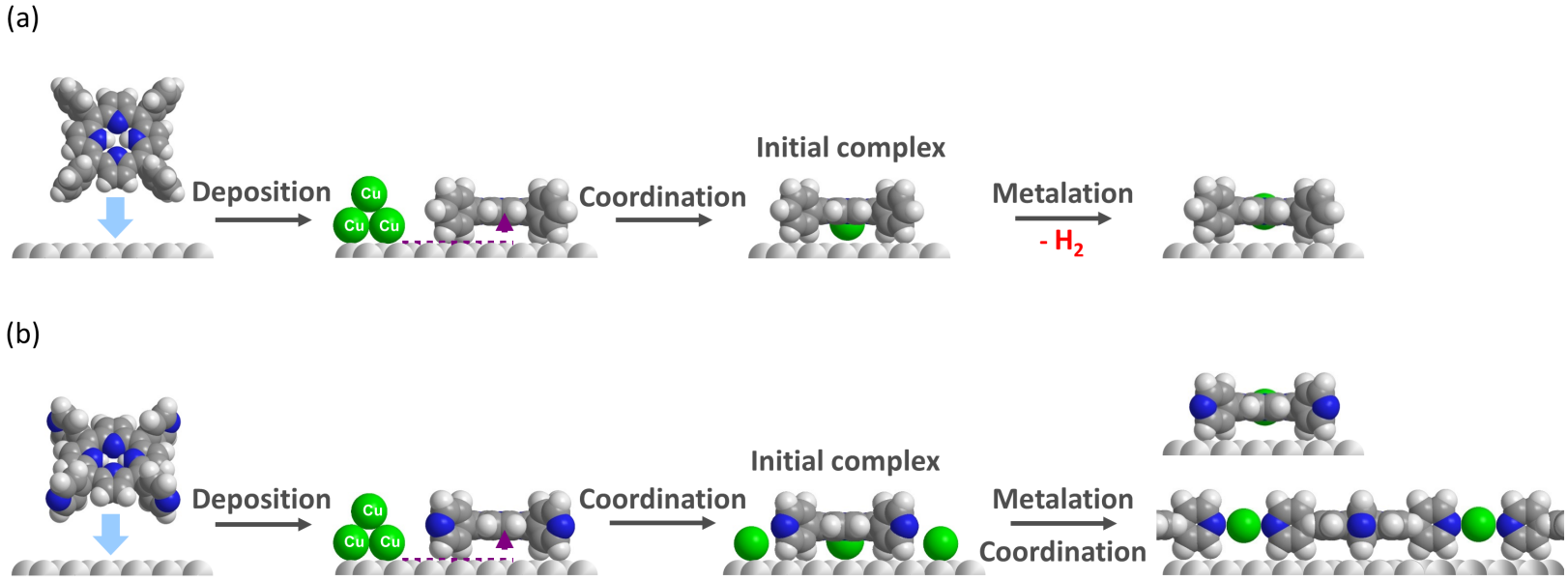

Figure 1.1: *Examples of Surface Coordination Chemistry.*

(a) Illustration for reaction of a unifunctional porphyrin: Tetraphenylporphyrin (2HTPP) reacts with co-deposited metal atoms (M) and forms the metalated complex M(II)TPP on a single crystal surface.

(b) Illustration for reaction of a bifunctional porphyrin: Tetrapyridylporphyrin (2HTPyP) undergoes the same reaction as described in (a). In addition, the peripheric, pyridylic nitrogen atoms are able to coordinate to further metal atoms to form a two-dimensional metal-organic network which contains the metal in two oxidation states – M(II) species inside the macrocycle and M(0) species as linkers.

even suitable for oxygen sensitive compounds like Fe(II)-tetraphenylporphyrin, which is not stable under ambient conditions.[13]

While the metalation of the core of free-base porphyrinoid molecules is widely studied in surface science,[4] the opportunity to introduce a secondary functionality in the periphery of the molecules is rarely seized in this context. The additional coordination sites allow for formation of network structures by hydrogen bonding using phenyl bromide[22] or by bridging metal atoms, *e.g.*, gold, using pyridyl[23] substituents. The presented work also uses the latter substance on a Au(111) substrate but introduces copper atoms as additional reactant acting as linker between the pyridylic nitrogen atoms of the organic molecules in addition to the metallation reaction.

Since the porphyrinoid molecules can be modified in various ways, the motivation to modify the macrocycle as well is obvious. Formal removal of one out of the four methin bridges in porphin leads to corrole. This stem compound also exhibits an aromatic macrocycle. As a new feature, it carries three pyrrole moieties which are able to react with an available metal atom. On the one hand, the metal should react as in the known situation for porphyrines and on the other hand being able to be oxidized further into a M(III) state. The latter corresponds to a reduction of all three pyrrolic hydrogen atoms. A promising candidate as reactive metal is cobalt since it forms stable Co(II) and Co(III) ions. Its usage is further motivated by the experience obtained from investigations on other porphyrinoid macrocycles.[24–26]

In general, the reactive metal atoms are deposited by physical vapor deposition onto the previously prepared organic mono- and multilayers.[1] This procedure is motivated by the assumption that individual atoms are expected to exhibit an increased reactivity compared to atoms attached to other (substrate) atoms. In this thesis, the reverse approach is studied as well. In this case, the deposited molecules react with pre-deposited metal atoms on a substrate or even with atoms originating from the single crystals surface.

Most of these here presented metalation reactions were realized on single crystal surfaces. As a consequence, the products represent well-defined organic-metal interfaces and can be used for further examination of adsorbate-substrate interactions by various techniques. In order to achieve even more defined systems, the preparation aims at a final situation in which the coverage does not exceed one layer of the organic molecule on single crystal surfaces of noble metals. Additionally, most surface characterizing methods are optimized for clean substrates and monomolecular adsorbate layers.

1 In this context, a monolayer refers to a dense, flat layer of the organic molecule on a variable substrate with the unit "ML_M" differing from the classical, but here inconvenient, definition as adsorbed molecules per substrate atom with the unit "ML_S".

However, many configurations in applications – for example organic electronic devices, such as organic light emitting diodes (OLED), organic thin film transistors (OTFT) and organic photovoltaic cells (OPV) – use thick organic layers with thicknesses of several nanometers or even micrometers on metallic substrates with low work functions.[27–31] These deeply *buried* metal-organic interfaces elude investigation with the aforementioned methods. Since the performance of these devices depends on the properties of the intrinsic metal-organic interface,[32] deeper knowledge about the chemical, electronic, and geometric structure is obviously desirable. Especially the presence of a sharp transition from the substrate to the adsorbate layer, *i.e.*, an interface, is questionable and deserves further investigation.

In this thesis, the application side of these layered systems is approximated by organic layers with thicknesses of a few monolayers. On the one hand, this situation allows for the formation of transition zones between the substrate and the pristine adsorbate, *i.e.*, *interphases*. On the other hand, the prepared structures are thin enough to be studied by photoemission spectroscopy. However, the usage of hard X-ray photons with variable photon energy – typically between 2 keV and 10 keV – is required in order to increase the probing depth. Hence, this approach requires the availability of monochromatized synchrotron radiation. The interaction of electrons with matter generally decreases with increasing kinetic energy, at least above 100 eV.[33] The reduced interaction manifests itself in a larger distance an electron can travel before it gets scattered, *i.e.*, a larger inelastic mean free path (IMFP). Since the probing depth is generally assumed to be three times the IMFP, this depth becomes a function of excitation photon energy. As a consequence, the vertical composition profile of a specimen can be probed by variation of the photon energy.

Since the previous method requires a synchrotron, the method of choice in a laboratory is based on the variation of the electron collecting angle. However, this is not possible due to the strong damping by the top layers for the resulting photoelectrons and thus vanishing signal intensity from the interface. Another common method to investigate the vertical composition of a sample is based on ion sputtering and analysis of the volatile compounds or the freshly exposed area. The application of this technique is also not possible in this case since it is destructive and might affect the chemistry of the interphase.

1.2 Depth Profiles of Rechargeable High Potential Cathodes

Lithium-ion battery is one of the most popular types of rechargeable batteries. With advantages of high energy density, small memory effect, large stored volume, and slow self-discharge,[34,35] nowadays lithium-ion batteries are widely used in consumer electronics, such as mobile phones, laptops, digital cameras, *etc.* Considering its high energy density, usage of this battery type becomes interesting for transport related technical applications, *e.g.*, electric vehicles and aerospace applications.

For further development and improvement of lithium-ion batteries, intense investigations focused on characterization of electrode and electrolyte materials have attracted more and more attention. The nondestructive properties of hard X-ray photoemission spectroscopy rendered acquisition of an unperturbed depth profile of a high-potential cathode made from lithium nickel manganese oxide coated (LNMO) with lithium titanium oxide (LTO) used in lithium-ion batteries possible. LNMO crystallizes in spinel structure which favors fast three-dimensional lithium ions transport within the framework.[36] This material has shown promising properties to extend the energy density of lithium-ion batteries by increasing the redox potential. However, it suffers from complex surface reactions during cycling. This leads to passivation layers on the electrode's surface and thus limits the chemical stability. As a consequence, the life of the whole device is compromised.[37,38]

In order to protect the cathode from reaction with the electrolyte, a buffer layer, *e.g.*, LTO, is used in technical applications. This interlayer is known to provide low ionic and electronic conductivity. However, a recent study reveals unexpected low impedance for thin film LNMO cathodes covered with LTO layer.[39] Along these findings, deep understanding of the electrode composition, especially the possible interaction between electrode cathode and the buffer layer after many times of cycling, is necessary and might help to improve the overall performance of lithium-ion batteries.

As mentioned in Section 1.1 the tunable photon energy of a synchrotron beam line allows nondestructive depth profiling of coated electrodes with a maximum information depths of a few ten nanometers.

1.3 Surface-Assisted Ullmann Coupling Reaction

The Ullmann coupling reaction was first described in 1901 by the German scientist Fritz Ullmann, as a method for synthesis of substituted biphenyls from bromobenzenes utilizing metallic copper.[40] The reaction was extended for coupling of aryl halides under the participation of copper. In contrast to general solution-based organic synthesis, understanding of these specific heterogenic organic reactions in detail was quite limited.

On the one hand, participation of a solid reactant impedes the common approach to catch reaction intermediates in order to deduce the reaction mechanism from these compounds. On the other hand, the presence of the metal motivates to perform the determination of the fundamental principles of Ullmann coupling under very well-controlled conditions. In the so-called *surface science approach*, the educts, *i.e.*, aryl halides, are adsorbed on a well-defined copper single crystal surface. Their reaction products as a function of temperature are studied by typical surface science methods such as photoemission spectroscopy as well as scanning tunneling microscopy and spectroscopy.

Model studies are reported in literature using small aromatic halides on noble metal surfaces, *e.g.*, fluorobenzene and chlorobenzene on Pd(111),[41] bromobenzene on Cu(111),[42] and iodobenzene on Cu(111)[43] as well as on Au(111).[44] As a general conclusion, those haloarenes can undergo a carbon-halogen bond scission on metal surfaces, followed by carbon-carbon bond formation.[45] More recently, larger aromatic halides, *i.e.*, terminal polyphenyl halides, and their polymerization into chains or super large macromolecules have been investigated.[46–49] These studies are mainly based on scanning tunneling microscopy (STM) with insight on an atomic level even for transient species. Especially the highly interesting organometallic intermediates are observable. These compounds consist of organic units connected by C-Cu-C[46,50,51] or C-Ag-C[47,52] bridges. However, these pictorial results provide only limited information about the reactions and the chemical nature of intermediates.

In addition to imaging techniques and in order to gain deeper insight into the electronic structure, X-ray and ultraviolet photoemission spectroscopy measurements were performed for several model systems in this work. These experiments are mainly based on straight, angled, and branched terminal oligophenylene bromides on primitive hexagonal copper and silver single crystal surfaces. The Ullmann coupling reaction on a defined substrate opens a new reaction pathway to synthesize regular molecular or polymeric covalent nanostructures.

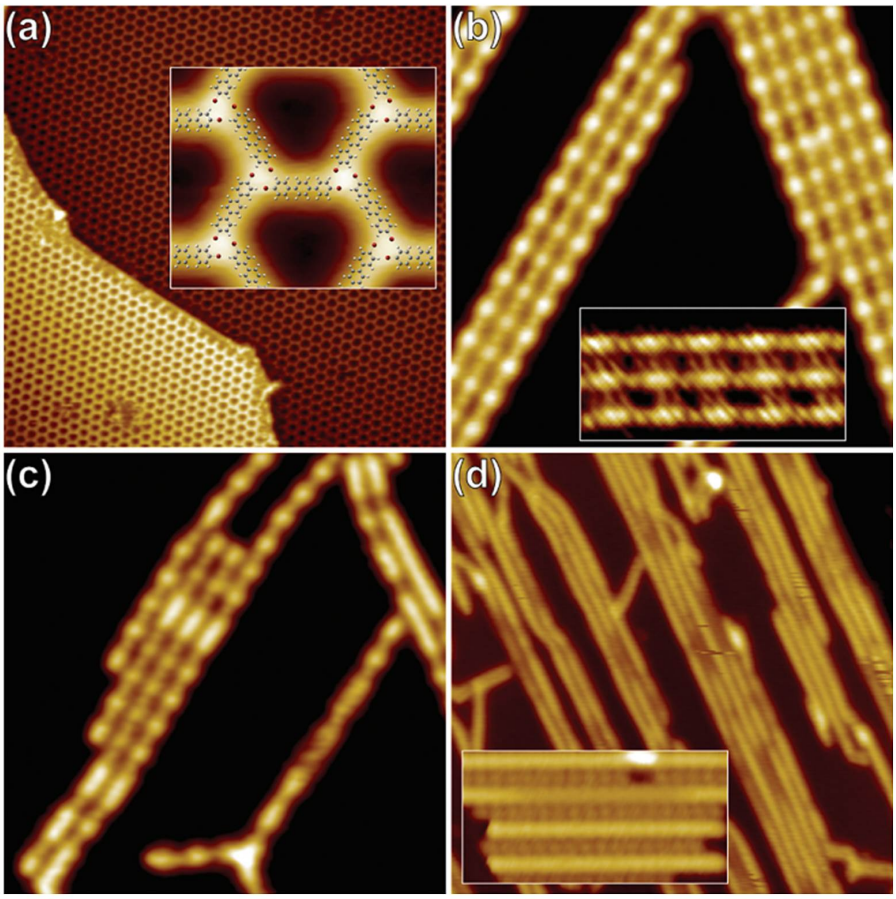

Figure 1.2: *STM Study of Surface-Assisted Ullmann Coupling Reaction* of Br – $(ph)_3$ – Br to Poly(*para*-phenylene) on Cu(111) *via* an organometallic intermediate. Graphs taken from Wang and coworkers.[46] Insets show a magnified sector.

(a) STM image of sample prepared with substrate kept at 77 K. The inset superimposes molecular structure models. Bromine atoms are shown in red. Tunneling parameters: $U = 1.0\,\mathrm{V}$, $I = 0.2\,\mathrm{nA}$ ($6\,\mathrm{nm} \times 5\,\mathrm{nm}$).

(b) STM image of the sample annealed to 300 K. The molecules undergo debromination and carbon fragments are linked by copper atoms forming organometallic intermediates aligned in ribbons. Tunneling parameters: $U = 1.0\,\mathrm{V}$, $I = 0.3\,\mathrm{nA}$ ($20\,\mathrm{nm} \times 20\,\mathrm{nm}$).

(c) STM image of the sample annealed to 393 K. The intermediate partially reacted to poly(*para*-phenylene) under release of copper. Tunneling parameters: $U = 1.0\,\mathrm{V}$, $I = 0.2\,\mathrm{nA}$ ($20\,\mathrm{nm} \times 20\,\mathrm{nm}$).

(d) STM image of the sample annealed to 473 K. The reaction is completed and the polymer chains sinter together into bands and are separated by rows of bromine atoms. Tunneling parameters: $U = 1.0\,\mathrm{V}$, $I = 0.5\,\mathrm{nA}$ ($40\,\mathrm{nm} \times 40\,\mathrm{nm}$).

1.4 Molecular Self-Assembly Assisted by Metal Surfaces

The surface-assisted synthesis of supramolecular nanostructures provides a promising bottom-up approach towards functionalized surfaces. They potentially can provide tailored properties in applications such as catalysis, electronic devices, sensor systems, gas storage and so on. Tuning of the functionality implies specific control over symmetries, dimensions, functional organic ligands, and bonding motifs on a molecular scale. Considering microscopic or larger areas with huge numbers of molecules on the surface, it is self-evident that an autonomous process is necessary to form theses surface structures.

By meticulous design and selection of building blocks with specific characteristics it is possible to create reaction conditions in which supramolecular *self-assembled* structures are formed. One mandatory requirement on the reaction environment is reversibility during arrangement of the molecules into a network. This step provides the possibility to remove misplaced building blocks from the network and to *heal* defects in the long range pattern by reattaching them in a correct position. Certainly, this mechanism also requires mobility of the participating reactants on the surface.[53].

An example is reported for the cobalt-carbonitrile coordination motive forming honeycomb networks on Ag(111) surfaces.[54,55] Another example for this reversible situation is the formation of organometallic intermediates in the Ullmann coupling reaction described in Section 1.1. The surface science approach allows for tuning of the reaction conditions by choice of substrate, linker molecule or metal, and the larger building blocks, *i.e.*, *struts*. In this work, the choice of building blocks is inspired by the aforementioned Ullmann coupling reaction, *i.e.*, copper and phenyl bromides, while the reaction conditions are adjusted by substrate metal and temperature.

Considering the criterion for reversibility, one has to consider the individual strengths of the involved attractive and repulsive interactions. The latter, under the assumption of a *matching* geometry of the interacting partners, is typically dominated by temperature effects, thus easy to control and hence the preferred variable in experiments. The situation for attractive forces is more diverse due to the simple fact that several interaction types need to be considered. Table 1.1 lists some of the basic molecule-molecule interactions. In general, van-der-Waals interactions are too weak and not selective enough to form stable networks while covalent bonds are often too strong to establish a reversible reaction. Especially hydrogen bonds and metal-ligand-like interactions are suitable to establish supramolecular entities in variable dimensions since they are of medium strength, directed, and selective.[56] Extending two-dimensional networks

Table 1.1: *Intermolecular Interaction Types* are listed with typical interaction energies, bonding lengths, and their individual properties. Values are taken from References [53,56–59]. Covalent bond strengths are added for comparison.

Interaction Type	Energy Range	Distance	Character
van der Waals [a]	0.02 eV – 0.1 eV	< 100 pm	Non-selective
Hydrogen Bonding [b]	0.05 eV – 0.5 eV	15 pm – 35 pm	Selective, directed
Covalent [c]	0.36 eV – 3.6 eV	Short	Irreversible
Dipole-Dipole	0.1 eV – 0.5 eV	20 pm – 30 pm	Directed
Metal-Ligand Interactions	0.5 eV – 2.0 eV	15 pm – 25 pm	Selective
Electrostatic	0.05 eV – 3.0 eV	< 50 nm	Non-selective

a In case of small molecules, *e.g.*, methane, or atoms, *e.g.*, xenon. Large molecules can bind stronger.
b In most cases. The $FH\cdots F^-$ bond is a rare exception (1.65 eV).[60]
c Considering single bonds. Higher bond orders can be stronger.

into the third dimension using the latter kind of connection leads to the concept of *metal-organic frameworks.*[61]

It is important to note that – in addition to the listed direct intermolecular interactions – the substrate-mediated interactions can also play an important role in network formation and even dominate the resultant structures. For instance, anthraquinone molecules self-assemble on a Cu(111) surface into a large two-dimensional honeycomb network. However, solely hydrogen bond coordination cannot explain the corresponding structure. Later, it was found to be related to the confinements of substrate electrons in the assembled pores.[62,63] This result also emphasizes the influence of the substrate structure and the requirement of well-ordered surfaces .

Another important aspect to be considered is the molecular coverage. Obviously, the formation of an ordered network is disturbed in case an excessive amount of substance is deposited. However, variable – but less than stoichiometric – amounts can lead to formation of different patterns rather than to a corresponding incomplete covering of the available surface. An example for this behavior is reported for the self-assembly of a perylene derivative on Cu(111), which gives three distinctly different molecular assembly patterns in dependence on the coverage.[64]

The images in the presented project exhibit, besides the scientific results, a certain esthetic component. The formed structures resemble Sierpiński triangles known from fractal geometry.

1.5 Surface State Confinement in Organic Quantum Corrals

As mentioned in Section 1.4, the surface state of substrate could mediate self-assembly of molecules into a regular porous network. Since the formed pattern influences the electronic structure, this interplay can be used to establish an altered electronic structure on the surface. Hence, those molecular pores at surfaces can serve elucidating fundamental physics of adsorbates in confinement.

Surface state oscillations on (111) surfaces of coinage metals have been imaged and studied now for more than two decades.[65–67] It is revealed that surface states can be confined in corrals which were built up by either adsorbed atoms[68–71] or molecules on surfaces.[54,72,73]

One aspect of this thesis focuses on the influence of self-assembled structures on the electronic structure of a Ag(111) surface. The regular adsorbate pattern consists either of oligophenylene bromide molecules or of polypropylene macrocycles obtained *via* surface Ullmann reaction from the previous case, see Section 1.3.

The macrocycles act as quantum corrals and lead to the confinement of surface state electrons inside the central cavity. Furthermore, these highly robust supramolecular networks may serve as templates for the incorporation or trapping of guest molecules. Typically, energy dispersion as a function of the electron wave vector of confined electron states is measured by angle-resolved photoemission spectroscopy for occupied states or inverse photoemission spectroscopy for unoccupied states.

The development of scanning tunneling microscopy and scanning tunneling spectroscopy (STS) offered complementary techniques to investigate electronic structures with atomic resolution. These versatile methods found various applications in research areas dedicated to carbon nanotubes,[74,75] metal oxides,[76] and electronic excitations at the metal surfaces.[77] While STM is able to give topographic information about the specimen, STS provides spectroscopic insight to the molecular orbitals at a certain position of the probed molecule. A combination of the two techniques leads to the so-called $\mathrm{d}I/\mathrm{d}V$ *mapping* which is able to provide coarse spectroscopic information with high lateral resolution. These methods based on tunneling electrons also provide new opportunities for direct imaging of electron confinements in surface-confined supramolecular networks.[54,78,79]

Characterization of the particular properties of surface state confinement in those large single-molecule quantum corrals for the first time is also presented in this work utilizing STM/STS to gain real space visualization of the local density of states of surface state electrons. Surface states which are confined in large organic corrals in this

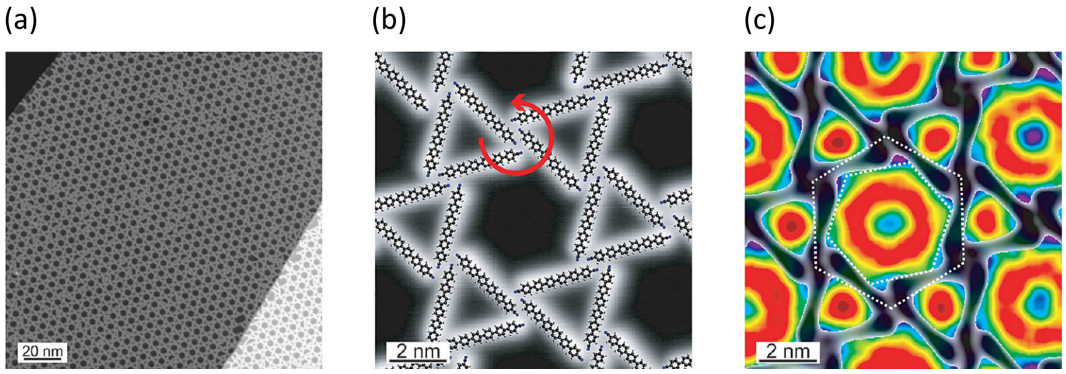

Figure 1.3: *STM Study of a Chiral Kagomé Network* formed by $\mathrm{CN}-(ph)_6-\mathrm{CN}$ on a Ag(111) surface. Graphs reprint from Klappenberger and coworkers.[73]

(a) Topographical image of large-area domains in a chiral kagomé network formed by self-assembly of $0.4\,\mathrm{ML_M}$ $\mathrm{CN}-(ph)_6-\mathrm{CN}$ on Ag(111) surface. Tunneling parameters: $U = 1.25\,\mathrm{V}$, $I = 0.14\,\mathrm{nA}$.

(b) High-resolution image of the kagomé structure with superimposed ball-and-stick models of the molecules. Tunneling parameters: $U = -0.5\,\mathrm{V}$, $I = 0.1\,\mathrm{nA}$. Basically two different types of pores are presented, hexagons and triangles. The red arrow shows the chirality originating from the nodes in which the molecules are counterclockwise rearranged.

(c) The dichotomous confinement of surface states within quasi-hexagonal and triangular-terminated areas. The two white dotted hexagons highlight the rotation of the electronic mode inside the quasi-hexagon with respect to the kagomé lattice caused by the chirality of the network.

project are typically of the Shockley type. The $\mathrm{d}I/\mathrm{d}V$ maps received for the investigated patterned surfaces are compared to simple quantum mechanical approximations. One widely known example is the *particle-in-a-box* model using simple geometries for an infinite potential well providing to approximate the dimensions of the molecular corrals.[80]

Combination of the theoretical description with the STM results allows for decision whether there is a substantial penetration of the wave functions into the confining potential or not.

1.6 Electrical Properties of Interfaces between Metals and Organics

For electronic devices, such as organic light emitting diodes (OLEDs), organic thin film transistors (OTFTs) and organic photovoltaic devices (OPV), the energy level alignments of the highest occupied molecular orbital (HOMO) or the lowest unoccupied molecular orbital (LUMO) at the interface with respect to the metal Fermi level, is one of the key factors for the devices' performance. It determines the so-called energy barriers for electron injection at the cathode as well as the hole injection at the anode. They influence the efficiency of charge injection and finally dictate the device efficiency. Hence, the energy level alignment at the interface is one of the fundamental issues concerning organic electronic devices. It involves a number of physical and chemical processes. Among these processes, an interface dipole is almost always present at the heterojunctions of such structures.

1.6.1 Origins of Interfacial Dipoles

In the early theories of metal-organic interfaces, a simple alignment, *i.e.*, identical potential, of the previously individual vacuum levels of the metal of the organic layer is established, similar to the situation in a Schottky-contact. Later, it was proven that such a simple situation is not representative for most metal-organic heterojunctions.[81]

A more elaborate model includes the presence of an interface dipole layer between the metallic and the organic unperturbed phases. Instead of a constant potential, this theory assumes a linear transition between the individual vacuum potentials. It was first suggested by Seki *et al.*, mainly supported by ultraviolet and X-ray photoemission spectroscopy as well as by Kelvin probe techniques.[81–87] This interfacial dipole also occurs at contacts between two different inorganic semiconductors[27,88] and can originate from at least seven possible mechanisms,[27] as illustrated in Figure 1.4.

The case illustrated in Figure 1.4 (a) is the most common, simplest situation for a metal surface in vacuum. The dipole originates from the evanescent part, *i.e.*, the exponential *tail* extending in the vacuum, of the Bloch-states. Since there is finite probability for the electron to be found outside the surface, the vacuum can be attributed with a negative charge. Normalization involves a lowered electron density in the bulk material and thus a positive charge. Since the properties of the evanescent wave depend *via* the Bloch states on the crystal structure perpendicular to the surface, the resulting dipole differs for different crystal faces. As a consequence, crystals exhibit variations in their work function depending on the considered crystal faces.[90]

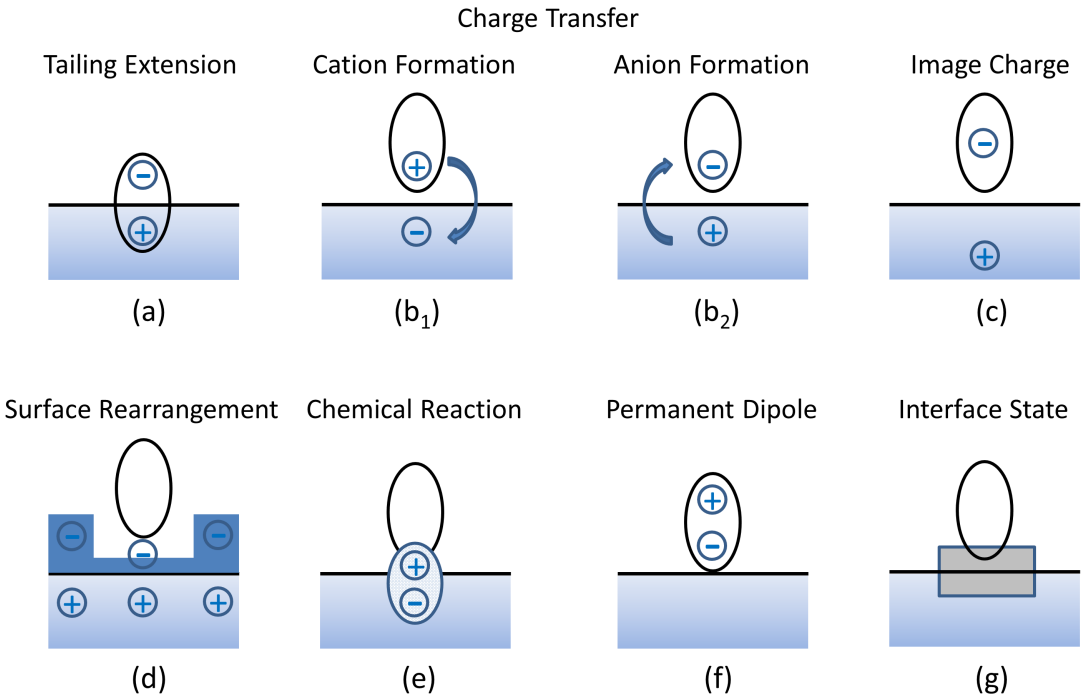

Figure 1.4: *Possible Mechanisms for the Formation of Interfacial Dipole Layers.* Details are given in the text. Cited from References [27,89].

(a) Electron orbital tailing into the vacuum.

(b) Charge transfer across the interface.

(c) Image charge formation.

(d) Rearrangement of the electron cloud on metal surfaces.

(e) Chemical reaction between adsorbate and substrate.

(f) Interfacial dipole caused by the permanent dipole of an adsorbed functional molecule.

(g) Interface state.

The second contribution is electron transfer between adsorbate and substrate, with the positive and negative charges separated across the interface as shown in Figures 1.4 (b_1) and (b_2). The transfer direction depends on the relative Fermi respectively HOMO levels of these two materials. Examples are known for cation formation[86] as well as for anion formation.[91]

Another factor, *i.e.*, an image force, may explain cases of ionic species adsorbed on metals. The charge close to the surface affects the population of the electrons in the metal. This manifests itself as an image charge generated in the metal, as shown in Figure 1.4 (c), and thus forms a dipole.

In addition, vacuum level shifts, which indicate dipole layer formation, were also observed for atomic[92] or molecular insulators[93] on metals. Insulators exhibit a

wide HOMO-LUMO gap rendering electron transfer not probable. However, an alternative explanation for these cases with nonreactive adsorptives is possible. Here, the rearrangement of the electron cloud on the metal surface is not induced by a charge but results from Pauli-repulsion of the electron in the adsorbate and substrate, as illustrated in Figure 1.4 (d). This is also known as cushion effect.[94] The *cushion* of electronic charge at the metal surface is impressed by the molecule, *i.e.*, the tailing part of electronic cloud is pushed back, resulting in a pronounced charge decrease in the surface below the adsorbed molecule.

In some cases, chemical reaction between the organic layer and metal substrate, *i.e.*, chemisorption, cannot be ruled out, *e.g.*, for small strong binding molecules like CO on nickel.[95] Chemisorption, *i.e.*, adsorption including a change in electronic structure, is in principle another kind of charge transfer, and serves as another source for the surface dipole layer. However, this concept is limited to cases preserving the molecular structure of the adsorbate. A counterexample is dissociative adsorption, *e.g.*, the adsorption of hydrogen on platinum,[96] which leads to the formation of new species which can be interpreted by themselves.

An additional possibility is the existence of a dipole within the adsorbate itself[97]. Orientation of the dipole moment parallel to the surface normal can lead to a large interfacial dipole at the interface as shown in Figure 1.4 (f).

The last factor in this collection arises from interfacial states as displayed in Figure 1.4 (g). These states are formed by penetration of metal electron wave function into the semiconductor layer, analogue to the evanescent wave in the first item. Such interface states are well known for inorganic semiconductor-metal junction where gap states are induced.[98]

Those factors discussed above do not always happen separately. In real interfaces, combinations of the mentioned cases play a role in the energy level alignment.

Due to the formation of interface dipoles, the vacuum level alignment does not occur in most organic-metal interface.[27,30,81,83–87,91,93,99–101]

Details about the energy level alignment with interfacial dipoles will be discussed in the next section.

1.6.2 Energy Level Alignment at the Metal-Organic Interface

As mentioned above, the electrical contact between the functional organic layer and the metal electrode plays a critical role to make the involved electronic devices practical and efficient. However, a scientific understanding of the interface mechanisms has not matched up with the large progress in industrial material design and manufacturing

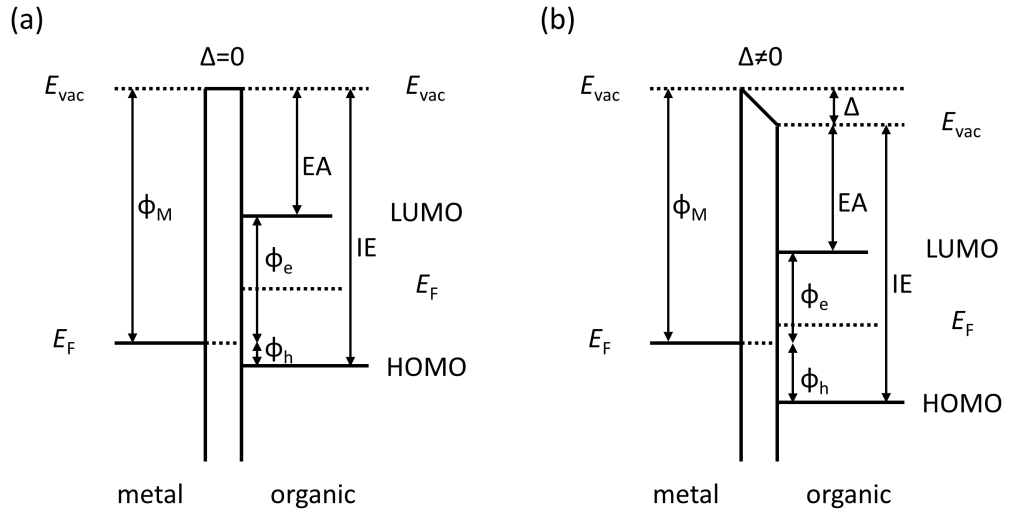

Figure 1.5: *Schematic Representation of a Metal-Organic Interface without Band Bending.* ϕ_e denotes to the electron injection barrier, calculated by the difference between the work function of the metal ϕ_M and the electron affinity (EA) of the organic film. ϕ_h denotes to the hole injection barrier, which can be calculated by the difference between ionization energy (IE) of the organic material in the solid phase and the metal work function ϕ_M. The individual electronic levels are unaffected by the contact and are taken from the pure materials. Graphs adapted from References [30,83,100].

(a) The Schottky-Mott limit is shown exhibiting identical vacuum levels.

(b) Abandonment of the vacuum level alignment and introduction of a dipole barrier Δ interpolating the individual vacuum levels.

yet.

At the beginning of the period of intensive work on organic electronic devices, the mechanism at metal-organic interfaces has often been discussed on the basis of vacuum level alignment theories, *e.g.*, the Schottky-Mott limit. The initial naive assumption was that the surface of organic films, which consists of closed-shell molecular entities, would not interact significantly with the metal surface. In this scheme, a common potential was established by simple alignment of the vacuum levels of the organic molecules and electrode metal as shown in Figure 1.5 (a).

In general, work functions of metals and organic layers reside in different ranges. When two members, one from each material class, get into contact, the interface is not in electrical equilibrium as displayed in Figure 1.5. As a result, a redistribution of mobile charge carriers takes part, *i.e.*, the electrons will flow from one side to the other side until the Fermi levels are aligned.[27] Assuming the Fermi level of the organic layer to be higher than that of the metal (as shown in Figure 1.5), alignment of the Fermi levels on both sides requires some electrons to move from the organic layer to

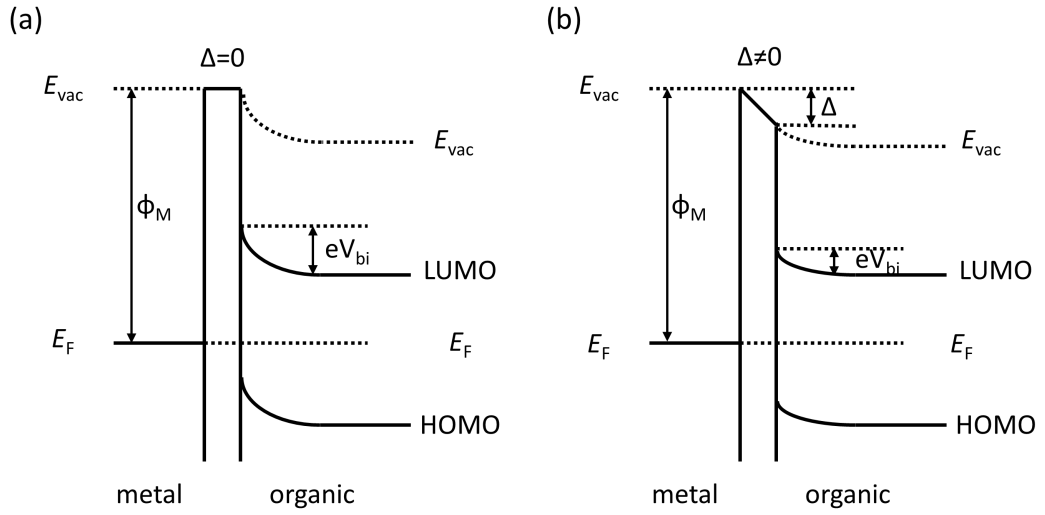

Figure 1.6: *Schematic Representation of a Metal-Organic Interface with Band Bending.* The energy levels from Figure 1.5 are bent by the charge redistribution in the organic layer to achieve the electrical equilibrium with Fermi level alignment in both cases. ϕ_M denotes to the work function of the metal ϕ_M, eV_{bi} denotes to the built-in potential. Graphs adapted from References [30,83,100].

(a) The Schottky-Mott limit with identical vacuum levels is assumed.

(b) Individual vacuum levels and the presence of an interface dipole barrier Δ are presumed.

the metal. This leads to the formation of a built-in potential V_{bi} in the organic layer.

While the traditional models assume a vacuum level alignment, the here discussed Schottky-Mott rule, shown in Figure 1.6 (a), uses a bending of the energy levels in the interface layer to achieve a match of the individual Fermi levels. This situation is similar to the theory regarding semiconductor-metal interfaces. According to the work by Seki *et al.*energy levels of organics in organic-metal interface are fixed to the vacuum level of the metal with an energy shift of Δ as shown in Figure 1.6 (b).

2 Experimental Methods

In this chapter the most fundamental aspects of experimental techniques that have been utilized in this thesis will be briefly introduced. At first, photoemission spectroscopies including X-ray photoemission spectroscopy (XPS), hard X-ray photoemission spectroscopy (HAXPES), and ultraviolet photoemission spectroscopy (UPS) will be discussed together with the details of their quantitative analysis. Subsequently, temperature programmed desorption (TPD) and temperature programmed reaction (TPR) will be introduced. In the next chapter, scanning tunneling microscopy (STM) and scanning tunneling spectroscopy (STS) will be briefly reviewed. In the last section of this chapter, different experimental setups employed in this thesis will be described along with the respective relevant techniques they provide.

2.1 Photoemission Spectroscopy

Photoemission spectroscopy, also called photoelectron spectroscopy, is based on the photoelectric effect, which relies on the creation of photoelectrons from solids, liquids or gases *via* interaction between photons and the sample's electrons. It is usually characterized by a three-step process. First, the incoming photon is absorbed by an electron. Second, this electron gets excited and travels to the sample surface. This process generates core-hole in the struck atoms, *i.e.*, a highly excited photo-ion, which can undergo further decay, such as X-ray fluorescence or Auger processes. Third, the electron is ejected into the vacuum and the kinetic energy of this emitted electron is measured by an electron analyzer. Since the total energy must be conserved in this process, the kinetic energy of the emitted photoelectrons can be finally written as

$$E_{\mathrm{kin}} = \mathrm{h}\nu - E_{\mathrm{B}} - \phi_{\mathrm{sp}} \tag{2.1}$$

where $\mathrm{h}\nu$ is the photon energy, ϕ_{sp} the work function of the spectrometer, and E_{B} binding energy of the initial state of electrons, with respect to the Fermi level. Depending on the photon energy, photoelectrons can originate from the valence band in solids or upper molecular orbitals, as well as from core levels of closed atomic shells.[101]

After photoelectrons are created by the photoelectric effect and while they travel through the solid, the majority of those electrons will interact with the matter and lead to secondary electrons, shake-up satellites, vibrational excitations, and so on. As a result, the intensity of primary electrons I_0 reaching the analyzer is damped as a function of distance d in the solid. Analogue to the Beer-Lambert law, the intensity attenuation can then be expressed as

$$I = I_0 \exp\left(-\frac{d}{\lambda\left(E_{\mathrm{kin}}\right)}\right) . \tag{2.2}$$

The concept of inelastic mean free path (IMFP) is consequently introduced here, defined as the average distance λ_{IMFP} an electron beam with a certain kinetic energy E_{kin} can travel before its intensity decays to $1/\mathrm{e}$ of the initial value. It can roughly be described by a universal curve, shown in Figure 2.3, as a function of the kinetic energies of the emitted electrons. For instance, with Al K_α radiation the IMFP of C 1s electrons ($\approx 1200\,\mathrm{eV}$) is between 1 nm and 3 nm, which indicates an average escape depth corresponding to only the topmost atomic layers of the sample.

Because of this damping process, the information depth is limited. Implying a

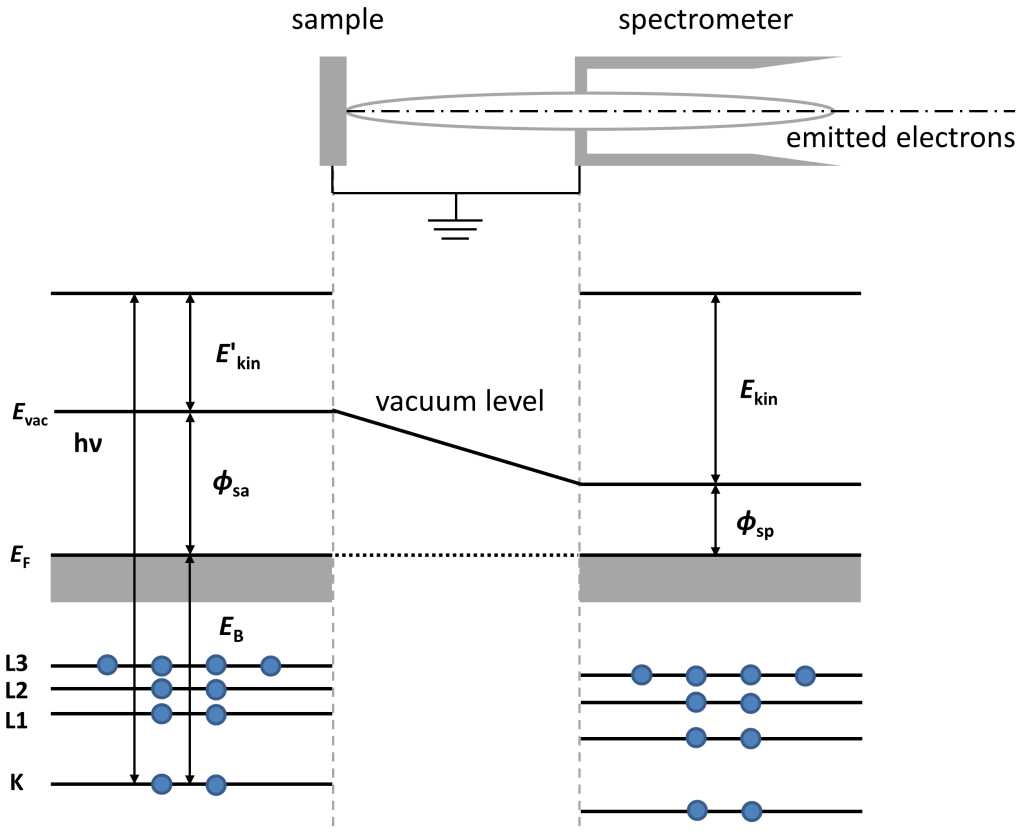

Figure 2.1: *Energy Scheme for Photoemission Spectroscopy.* The electronic energy levels, work functions, and vacuum levels of the sample and spectrometer are opposed to each other. Details are discussed in the text.

threshold value of 5 % of electrons contributing from *deeper* layers one can calculate a corresponding probe depth of $3 \cdot \lambda_{\mathrm{IMFP}}$ which can be studied by photoemission spectroscopy. In summary, the technique of photoemission spectroscopy obtains information that is mostly originating from the thin surface layer with a thickness of several nanometers. It is also a powerful tool for quantitative surface analysis as will be shown in Section 2.1.4.

As shown in Figure 2.1, the spectrometer and the sample are electrically connected to align the Fermi levels from both sides. Since the spectrometer and the sample have different work function, a contact potential of $\phi_{\mathrm{sp}} - \phi_{\mathrm{sa}}$ exists between the connected sample surface and the spectrometer. The binding energy of emitted electrons from sample surface is given by:

$$E_{\mathrm{B}} = \mathrm{h}\nu - E'_{\mathrm{kin}} - \phi_{\mathrm{sa}} \tag{2.3}$$

where ϕ_{sa} is the work function of the sample, E'_{kin} is the kinetic energy of photoelectrons right at sample surface, while E_{kin} is the kinetic energy measured by the spectrometer.

From the basic energetic properties described in Figure 2.1 follows

$$E'_{\mathrm{kin}} + \phi_{\mathrm{sa}} = E_{\mathrm{kin}} + \phi_{\mathrm{sp}} \ . \tag{2.4}$$

After calibrating the work function of the spectrometer, the binding energy of the sample relative to the Fermi level can be measured by

$$E_{\mathrm{B}} = \mathrm{h}\nu - E_{\mathrm{kin}} - \phi_{\mathrm{sp}} \tag{2.5}$$

without knowledge of the sample's work function.

2.1.1 X-ray Photoemission Spectroscopy

X-ray photoemission spectroscopy was developed by Kai Siegbahn in 1957[102] and is extensively used to study the energy levels of atomic core electrons. Generally there are two different classifications of X-ray sources employed for XPS study, one is normal laboratory X-ray source with magnesium, aluminum, or silver anode – due to technical details also sometimes called anticathodes – providing Mg K_α (1253.6 eV), Al K_α (1486.7 eV), and Ag L_α (2984.3 eV) radiation. The other is based on synchrotron radiation with much higher photon fluxes and tunable photon energies usually ranging from terahertz radiation to hard X-rays.

The common notation of diagrams containing XP spectra displays electron intensity *versus* binding energy. The latter is given relative to the Fermi level of the measured sample. Since each element has its own unique set of binding energies, photoemission spectroscopy can be used to identify the elemental composition of a sample. Applications of minor correction allows to identify even the elemental concentrations of the sample.

In principle, photoemission spectroscopy can detect all elements, but in practice the intensities for hydrogen and helium are too low for practical applications. All other elements with higher atomic number (from lithium on) are accessible.[103]

Rather than merely elemental information, the technique of XPS can also provide chemical information like oxidation states, which is well known as electron spectroscopy for chemical analysis (ESCA) coined by Siegbahn's research group.[104–106] The origin of this technique can be dated back to the beginning of the last century.[107,108] When the chemical surrounding of probed system is changed, *e.g.*, the electronegativity of adjacent atoms or the adsorption site of molecules on surfaces, a corresponding binding energy shift will be introduced and be visible in the photoemission spectrum. XPS is one of the most sensitive and accurate techniques for surface science studies.

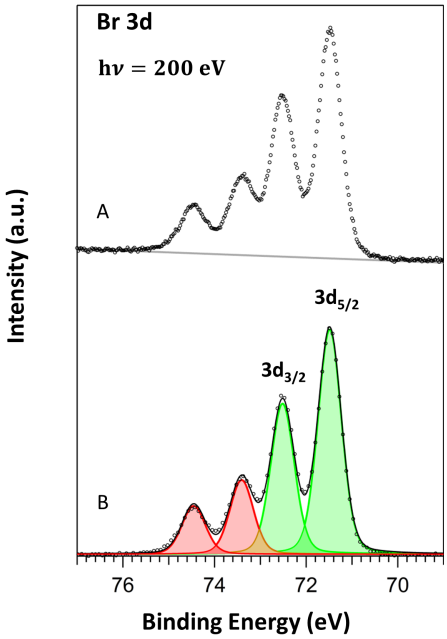

Figure 2.2: *Exemplary Br 3d XP Spectrum of Multilayers of DBm″QiP on a Ag(111) Substrate.* The same XP spectrum (circles) for multilayers of 4,4′′′′-dibromo-*meta*″-quinquephenyl (DB*m*″QiP) molecules adsorbed on Ag(111) at room temperature recorded using synchrotron excitation energy of hν = 200 eV is displayed for two data treatment steps. (A) shows the raw spectrum of the Br 3d core level together with the assumed background (gray line), while (B) represents the situation after its removal. In addition, (B) superimposes the contribution of the two species (red, green) and the resulting peak areas (shaded).

A typical measured photoemission spectrum comprises intensity from two processes. The unperturbed photoelectrons, including their satellites from distinct processes, provide chemical information while inelastically scattered photoelectrons form a continuous background, as shown in Figure 2.2 (A). The spectra display the Br 3d region of partially reacted 4,4′′′′-dibromo-*meta*″-quinquephenyl on a Ag(111) substrate at ambient temperature.

The first step in the data treatment consists of a removal of the inelastic part. The removed background, gray line in Figure 2.2 (A), is approximated by a combination of linear and "Shirley-type" contributions.

The next steps involve the successive decomposition of the recorded spectrum into its individual components. Typically pseudo-Voigt functions, approximating the convolution of a Gaussian and a Lorentzian function by a weighted sum, are used to model the experimental data.[109] The process mainly aims at determination of the center energies, peak widths, weighing factors, and the areas associated with each individual species in the sample. The latter, in combination with element specific

correction factors, allows for a quantitative analysis.

Figure 2.2 (B) presents the results of the fitting process. Two species can be distinguished and comparison with the pristine educt (not shown) allows for the assignment of unreacted (red) and reacted (green) species with different binding energies and total areas. Due to spin-orbit splitting, both assigned features comprise substructures with an explicit intensity ratio arising from the degeneracy of atomic states.

The center energies of the resulting doublets are primarily a function of the effective charge of the atomic nucleus, *i.e.*, the atomic number reduced by screening effects by the remaining electrons. Smaller variations of the binding energy are caused by the chemical environment, *e.g.*, the oxidation state, and bound atoms. Their impact is summarized as *initial state effects*. Secondary relaxation processes, *e.g.*, a reaction of the electronic structure to the creation of the core-hole in the probed molecule, are referred to as *final state effects*.

While the fitting routine uses all measured data points, the number of data points is reduced by a small integer factor to reduce scatter and improve readability.

2.1.2 Hard X-ray Photoemission Spectroscopy

Along the quick development of organic electronic devices, more and more interests have been attracted to investigations of chemical processes at buried metal-organic interfaces under ultra-high vacuum conditions. With the technique of photoemission spectroscopy, depth profiling of surface layers is normally achieved by mainly two means in the past decades: Either the information depth is varied by the electron collecting angle, or the top layers are removed successively by ion sputtering. However, there are individual drawbacks. The first method is limited to very small profiling depths and the second method causes damage to the sample intrinsically. In the third approach, the IMFP of the photoelectron, and thus the information depth, is altered by variation of the excitation energy. In order to achieve noticeable changes, the range of the used radiation needs to be extended to hard X-rays. Hence, depth profiling using HAXPES requires the use of synchrotron hard X-ray beam lines, where photon energy are available between approximately 1 keV and more than 10 keV.

In Figure 2.3, the attenuation lengths of electrons with different kinetic energies are shown, where a variety of experimental data is summarized.[33,110] At early time, attenuation lengths were regarded identical to the IMFPs in solids. Both terms are used synonymously and given values refer to IMFPs in this work. Later it was realized that the value can differ due to elastic scattering in the solid and led to usage of

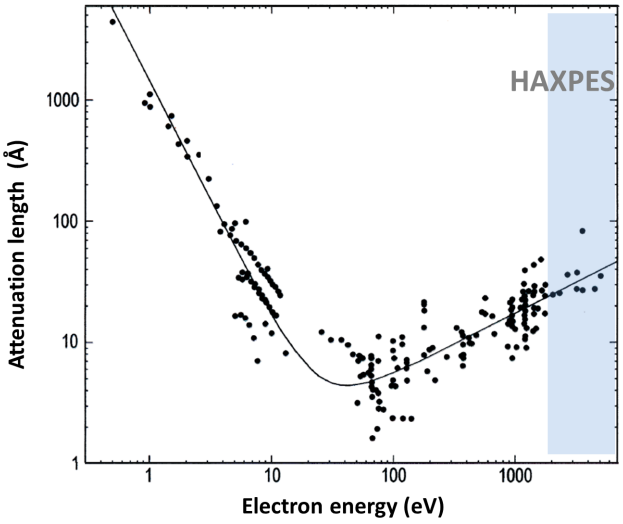

Figure 2.3: *Attenuation Lengths of Electrons in Solids.* Attenuation lengths of electrons in solids as a function of corresponding electron kinetic energies, adapted from References [33,110]

effective attenuation lengths.[110,111] As can be seen in the so-called *universal curve* in Figure 2.3, the attenuation length of photoelectrons exhibits a pronounced minimum for a kinetic energy about 100 eV. As a consequence, the information depth increases with the kinetic energy of the emitted electrons above this limit. Electrons emitted from the deeper layers which were previously not able to escape the sample can now reach the detector. Starting from the excitation energy dependent intensities one can draw conclusions about the vertical composition of the specimen.

With this idea one cannot only profile the surface layers, but also inspect the interface between two different materials without causing extra sample damage. A direct application for HAXPES is schematically displayed in Figure 2.4. Furthermore, by using the advantage of tunable synchrotron radiation, the detection depth of HAXPES can be tuned and consequently the chemical, electronic, and compositional depth profile of the probed sample can be obtained. Arising from the benefit of larger escape depths for electrons with higher kinetic energies, HAXPES has become a new promising nondestructive technique to study the bulk of materials or buried interfaces. Further advantage lies in the increased accessibility of deep core levels which cannot be probed with conventional laboratory X-ray sources. This allows for selection of atomic levels which provide increased photoelectron yields and can avoid overlap with features from other species.

Figure 2.5 shows an example of an excitation energy varied HAXPES measurement investigating the Al 1s region. An organic layer with a thickness of several nanometers

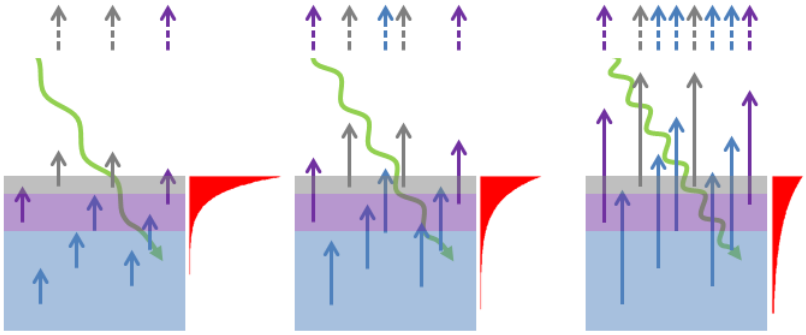

Figure 2.4: *Illustration of Escape Depth for Photoelectrons with Different Kinetic Energies.* Visualization of the increasing probing depth with increasing (left to right) photon (green) energy, *i.e.*, shorter wavelength, and thus larger kinetic energy. The photoelectron escape probability from different layers (gray, purple, blue) is indicated by arrows. The length of the arrows correlates with the IMFP. The contribution, normalized to total area, as a function of vertical position is given as the width in red. This scheme assumes a constant photoelectron production rate (number of arrows) and hence is not taking photon fluxes and cross sections into account which typically lead to a global decrease of signal intensity with increasing photon energy.

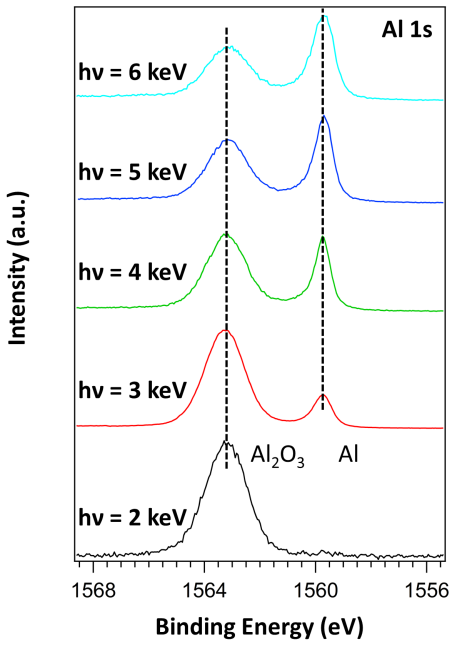

Figure 2.5: *Al 1s HAXPES Spectra of Oxidized Aluminum Foil* covered with a thin layer of 2HTPP. At low photon energy hν only the Al 1s peak corresponding to the oxide layer is visible. As the excitation energy increases this feature exhibits reduced intensity while the peak corresponding to the metallic bulk aluminum first appears and then increases. This demonstrates the increase in probing depths. A broadening of the peaks due to reduced resolution at high energies is also visible.

is deposited on a naturally oxidized aluminum substrate. As indicated from bottom to top in the graph, the sample has been probed with photon energies ranging from 2 keV to 6 keV. For better comparison, all spectra were normalized to the same intensity. At "low" photon energy (black line), only the peak corresponding to the aluminum in the oxide layer is visible. An increase of the excitation energy renders the underlying metallic phase observable. Upon further decrease of the wavelength the relative contribution of the metallic species increases, *i.e.*, more of the bulk is probed.

In this thesis HAXPES is applied to study the multilayer metalation of cobalt atoms with 2*H*-tetraphenylporphyrin (2HTPP) films, the diffusion behavior of metal atoms, *e.g.*, cobalt, in organic films, *e.g.*, 2HTPP, and the corresponding metal-organic interfaces and interphases, see Section 3.3.

2.1.3 Ultraviolet Photoemission Spectroscopy

Ultraviolet photoemission spectroscopy is a method related to XPS since it uses the same principle. However, different excitation sources are employed. Typically helium discharge lamps (HDL), which can – depending solely on the operation conditions – offer two excitation energies,[1] or synchrotron radiation with low photon energies ($h\nu < 100\,eV$) are employed. Due to the narrow line widths, UPS exhibits excellent energy resolution of the binding energy and allows to probe the details-rich valence structure of samples. Especially HDLs exhibit quasi-monochromatic character of the excitation lines.[112] The high photon fluxes, in combination with the large photoelectron production efficiency, *i.e.*, cross sections, in this spectral region make these photon sources superior to X-ray providing instruments. The apparent drawback of insufficient energy to excite core levels is more than compensated by these properties. In addition, the high fluxes enable improved statistics or faster measurements, respectively.

The shape and structure of photoelectron spectra strongly depend on exciting photon energy. It is possible to suppress s-band or d-band, respectively, by tuning the wavelength of the used light, while p-bands are less affected.[113] In combination with quantum chemical calculation, this allows for a precise assignment of the observed features in the recorded spectra. In general, UPS can provide more precise information about the density of occupied valence states than XPS which, in principle, could also be used for band structure studies. Due to its advantages, UPS has been extensively used in recent years for studying organic semiconductor surfaces and interfaces.

In this thesis UPS was mainly utilized for characterization of metal-organic systems. Its application covered the measurement of work function changes introduced by

1 $He\,I_\alpha$ with $h\nu = 21.2\,eV$ and $He\,II_\alpha$ with $h\nu = 40.8\,eV$.

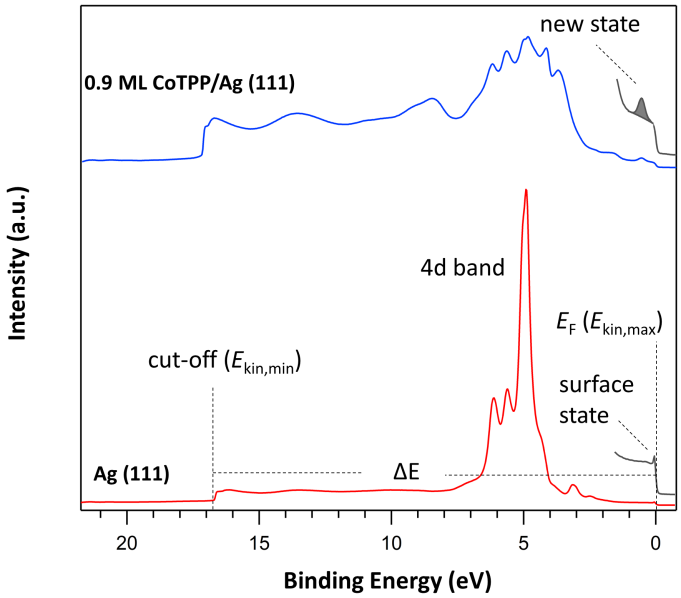

Figure 2.6: *Display of Exemplary UPS Spectra.* He I_α UP spectra ($h\nu = 21.2\,eV$) of a clean Ag(111) surface (red) and covered with approximately one monolayer of CoTPP. Magnification of the low binding energy areas (gray) show the Fermi edge E_F in detail. In case of the clean surface, the surface state is visible while the CoTPP-covered surface exhibits a new state. The useable range of the spectrum is indicated by ΔE. All spectra were taken in normal emission with a sample bias of $-5\,V$ with respect to the spectrometer.

adsorption, monitoring of the adsorbate/substrate interaction in the valence region, and inspection whether Shockley-type substrate surface states are affected by the adsorbed layers.

In the following, the routine of work function measurements and valence band investigations *via* UPS are explained along an example of data obtained from an almost complete monolayer of cobalt-tetraphenylporphyrin (CoTPP) adsorbed on Ag(111) as shown in Figure 2.6.

The red trace in Figure 2.6 shows the UP spectrum of a clean Ag(111) surface. Electrons with the highest energy in the solid, which is identical to the smallest binding energy, are emitted from the Fermi edge labeled E_F. Consequently, these electrons have the largest kinetic energy $E_{kin,max}$ in the spectrum. The other end of the spectrum is marked by the cut-off, *i.e.*, a sudden drop of the intensity to zero, of the spectrum, *i.e.*, it describes electrons with minimum kinetic energy $E_{kin,min}$ which is necessary to reach the detector. As a result, the useable range ΔE is confined by these two energies

$$\Delta E = E_{kin,max} - E_{kin,min} \ . \tag{2.6}$$

Usage of Equation (2.1) and Equation (2.4) gives

$$E'_{\mathrm{kin,max}} = \mathrm{h}\nu - \phi_{\mathrm{sp}} \tag{2.7}$$

and

$$E'_{\mathrm{kin,min}} + \phi_{\mathrm{sp}} = E_{\mathrm{kin,min}} + \phi_{\mathrm{sa}} \tag{2.8}$$

Figure 2.1 reveals that the infimum energy required to reach the detector is given by

$$\inf\left(E_{\mathrm{kin,min}}\right) = 0 \tag{2.9}$$

and the energy range ΔE is thus given by

$$\Delta E = E_{\mathrm{kin,max}} - E_{\mathrm{kin,min}} = \mathrm{h}\nu - \phi_{\mathrm{sp}} - \left(E'_{\mathrm{kin,min}} + \phi_{\mathrm{sa}} - \phi_{\mathrm{sp}}\right) = \mathrm{h}\nu - \phi_{\mathrm{sa}} \tag{2.10}$$

which can be simplified to

$$\phi_{\mathrm{sa}} = \mathrm{h}\nu - \Delta E \ . \tag{2.11}$$

Thus, by measuring the distance from the secondary electron cut-off to the Fermi edge, one can quantify the work function of investigated system. With this idea, the work function of Ag(111) was calculated to be 4.67 eV, which is very close to the reported values.[114,115]

UPS is a powerful tool to inspect the subtle interaction between adsorbate and substrate manifested in the valence band. As displayed in Figure 2.6, for the clean Ag(111) crystal the UP spectrum is dominated by the 4 d band with a surface state very close to the Fermi edge E_{F}. This surface state intrinsically originates from the two-dimensional electrons on surface, confined on one side by the vacuum barrier and on the other side by a band gap in the bulk states.

Deposition of almost one monolayer of CoTPP onto the Ag(111) surface results in the blue trace in Figure 2.6. The surface state is quenched and the 4 d band is suppressed. An additional electronic state appears at around 0.6 eV which is induced by the adsorbate-substrate interaction. This feature is attributed to the interaction of half-occupied Co $3d_{z^2}$ orbitals and sp occupied states of the silver surface.

The shift of the cut-off allows calculation of the adsorbate-induced work function changes. By analysis of UPS measurements of a clean Ag(111) surface and the surface covered with roughly one monolayer of CoTPP molecules, the energy diagram

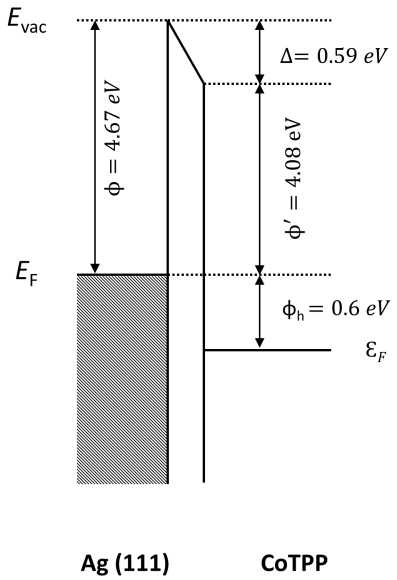

Figure 2.7: *Energy Diagram of the CoTPP/Ag(111) Interface.* The drawing of this energy diagram is based on He I_α UP spectra ($h\nu = 21.2$ eV) in Figure 2.6. The work function of the clean Ag(111) surface ϕ decreases after deposition of almost one monolayer of CoTPP to ϕ'. The formed dipole layer induces a shift of Δ on the vacuum level corresponding to the CoTPP/Ag(111) interface. An additionally observed state, representing the hole injection barrier ϕ_h from the metal to the organic layer, is formed by the interaction of the former SOMO[a] of the molecule and the sp band from the substrate.

a Singly Occupied Molecular Orbital.

of the CoTPP/Ag(111) interface can be drawn as shown in Figure 2.7. It reveals that the work function of the system is decreased by 0.59 eV compared to pristine Ag(111) surface. The UV spectra presented here suggest an electronic interaction between the cobalt center and the silver surface. This result agrees well with the findings of a photoelectron study reported by Lukasczyk *et al.*.[5] The adsorbate-substrate interaction results in a transfer of electron density from the surface to the ion, manifesting itself as an additional spectroscopic feature located at 0.6 eV below the Fermi level.

The energy ε_F of the new highest occupied state relative to the Fermi energy is of importance, since it is identical to the height of the hole injection barrier of the organic-metal interface. Comparison of the peak position (2.3 eV) corresponding to the singly occupied molecular orbital (SOMO) without surface influence, *i.e.*, for multilayers,[5] reveals that the barrier height is reduced due to the interaction-induced state. This behavior is typically desired in applied devices since it might increase their electrical performance.

It should be pointed out that, compared to conventional laboratory X-ray sources, the much higher fluxes of UV source might cause beam damage to the specimen during data acquisition and special precautions have to be taken in order to avoid misinterpretation of the recorded spectra.

2.1.4 Layer Thickness and Reaction Depth Determination by Photoemission Spectroscopy

As mentioned before, photoemission spectroscopy is appropriate for quantitative analysis. Here, this topic will be elaborated in more detail. Based on the photoelectron generation rate, the dampening due to the Beer-Lambert law, and the transmission function of the analyzer T, the peak intensity as a function of given atomic shell emitted from a homogeneous material is given in differential form by

$$\mathrm{d}I = n\sigma y\phi FA \cdot T \cdot \exp\left(-\frac{z}{\lambda \cos\vartheta}\right) \mathrm{d}z \ . \tag{2.12}$$

In this equation n is the density of the given atom, *i.e.*, the number of atoms per unit volume, σ is the photoionization cross section for a given atom within a given shell and given photon excitation energy, y is photoelectric ground state efficiency factor, ϕ is the angular efficiency factor, F is the average flux of X-rays on sample, A is the area irradiated by X-ray and viewed by the analyzer, λ is the IMFP of electrons with a certain kinetic energy in a given attenuation material, and z is the distance through the material that photoelectrons must travel.[116–119] Since in this thesis mainly organic layers are studied which are adsorbed on the (111) surfaces of single crystals, in the following section the discussion will focus on this model.

For quantitative work with XPS or ESCA the saturated signal for a clean substrate is often necessary and can be calculated by

$$\begin{aligned} I_{\mathrm{s},\infty} &= \int_0^\infty n_\mathrm{s}\sigma_\mathrm{s} y\phi FAT_\mathrm{s} \exp\left(-\frac{z}{\lambda_{\mathrm{s},E_\mathrm{s}} \cos\vartheta}\right) \mathrm{d}z \\ &= n_\mathrm{s}\sigma_\mathrm{s} y\phi FAT_\mathrm{s}\lambda_{\mathrm{s},E_\mathrm{s}} \cos\vartheta \end{aligned} \tag{2.13}$$

assuming infinitive substrate thickness. Here, the index $_\mathrm{s}$ refers to substrate related quantities. E refers to the kinetic energy of photoelectrons of the observed orbital. When the substrate is covered by an organic layer with the thickness of d, as shown in Figure 2.8 (a), the signal from the substrate, in this work typically Cu 2p, Ag 3d,

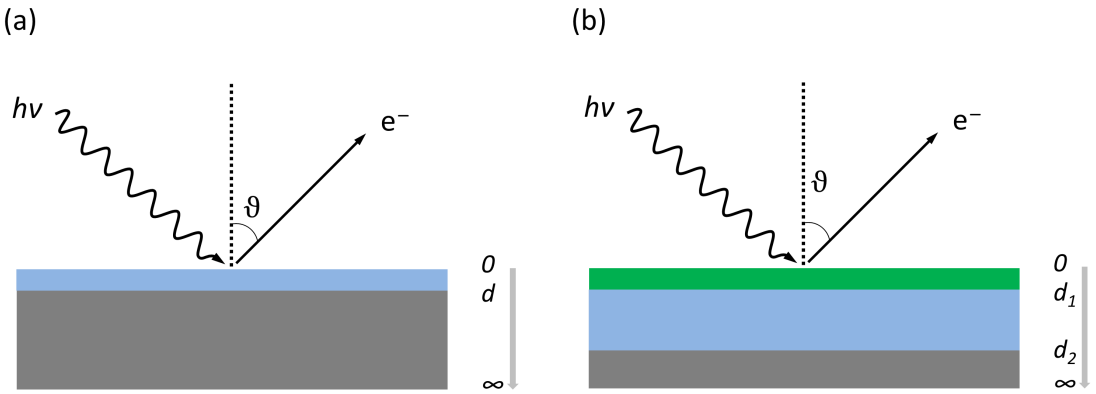

Figure 2.8: *Schematic Arrangements for XPS Sample Configurations.* Photoelectrons are emitted at the angle of ϑ relative to the surface normal.

(a) The sample is a clean single crystal substrate covered with an organic layer with the thickness of d.

(b) The sample is also a clean single crystal substrate but covered with two kinds of organic layers on top with the total thickness of d_2, *i.e.*, the reacted layer of d_1, the unreacted layer of $(d_2 - d_1)$.

and Au 4f, can be expressed by

$$\begin{aligned} I_{\mathrm{s},d} &= \int_d^\infty n_\mathrm{s}\sigma_\mathrm{s} y\phi F A T_\mathrm{s} \exp\left(-\frac{z-d}{\lambda_{\mathrm{s},E_\mathrm{s}}\cos\vartheta}\right)\cdot\exp\left(-\frac{d}{\lambda_{\mathrm{c},E_\mathrm{s}}\cos\vartheta}\right)\mathrm{d}z \\ &= n_\mathrm{s}\sigma_\mathrm{s} y\phi F A T_\mathrm{s}\lambda_{\mathrm{s},E_\mathrm{s}}\cos\vartheta\cdot\exp\left(-\frac{d}{\lambda_{\mathrm{c},E_\mathrm{s}}\cos\vartheta}\right) \\ &= I_{\mathrm{s},\infty}\exp\left(-\frac{d}{\lambda_{\mathrm{c},E_\mathrm{s}}\cos\vartheta}\right)\ . \end{aligned} \tag{2.14}$$

Similarly, one can calculate the saturated signal from an infinitely thick cover layer by

$$\begin{aligned} I_{\mathrm{c},\infty} &= \int_0^\infty n_\mathrm{c}\sigma_\mathrm{c} y\phi F A T_\mathrm{c}\exp\left(-\frac{z}{\lambda_{\mathrm{c},E_\mathrm{c}}\cos\vartheta}\right)\mathrm{d}z \\ &= n_\mathrm{c}\sigma_\mathrm{c} y\phi F A T_\mathrm{c}\lambda_{\mathrm{c},E_\mathrm{c}}\cos\vartheta\ . \end{aligned} \tag{2.15}$$

Here the index $_\mathrm{c}$ denotes the adsorbate. In case of a finite thickness d of the, *e.g.*, organic, adsorbate layer, the expression for intensity computes to

$$I_{\mathrm{c},d} = \int_0^d n_\mathrm{c}\sigma_\mathrm{c} y\phi F A T_\mathrm{c}\exp\left(-\frac{z}{\lambda_{\mathrm{c},E_\mathrm{c}}\cos\vartheta}\right)\mathrm{d}z$$

$$= n_{\mathrm{c}}\sigma_{\mathrm{c}} y \phi F A T_{\mathrm{c}} \lambda_{\mathrm{c},E_{\mathrm{c}}} \cos\vartheta \left(1 - \exp\left(-\frac{d}{\lambda_{\mathrm{c},E_{\mathrm{c}}} \cos\vartheta}\right)\right)$$
$$= I_{\mathrm{c},\infty} \left(1 - \exp\left(-\frac{d}{\lambda_{\mathrm{c},E_{\mathrm{c}}} \cos\vartheta}\right)\right) . \tag{2.16}$$

Since the geometry of the measurement arrangement usually remains unchanged when two regions – in this case of the substrate and of the adsorbate layer – on the same sample are measured, the corresponding parameters are identical. This reduction of parameters renders a determination of the layer thickness from the individual intensities possible. Combination of Equation (2.14) with Equation (2.16) yields

$$\frac{I_{\mathrm{c},d}}{I_{\mathrm{s},d}} = \frac{I_{\mathrm{c},\infty}\left(1 - \exp\left(-\frac{d}{\lambda_{\mathrm{c},E_{\mathrm{c}}} \cos\vartheta}\right)\right)}{I_{\mathrm{s},\infty} \exp\left(-\frac{d}{\lambda_{\mathrm{c},E_{\mathrm{s}}} \cos\vartheta}\right)}$$
$$= \frac{n_{\mathrm{c}}\sigma_{\mathrm{c}} T_{\mathrm{c}} \lambda_{\mathrm{c},E_{\mathrm{c}}} \left(1 - \exp\left(-\frac{d}{\lambda_{\mathrm{c},E_{\mathrm{c}}} \cos\vartheta}\right)\right)}{n_{\mathrm{s}}\sigma_{\mathrm{s}} T_{\mathrm{s}} \lambda_{\mathrm{s},E_{\mathrm{s}}} \exp\left(-\frac{d}{\lambda_{\mathrm{c},E_{\mathrm{s}}} \cos\vartheta}\right)} . \tag{2.17}$$

Collection of constants in the *calibration factor*

$$\mathrm{K} = \frac{n_{\mathrm{c}}\sigma_{\mathrm{c}} T_{\mathrm{c}} \lambda_{\mathrm{c},E_{\mathrm{c}}}}{n_{\mathrm{s}}\sigma_{\mathrm{s}} T_{\mathrm{s}} \lambda_{\mathrm{s},E_{\mathrm{s}}}} \tag{2.18}$$

simplifies the expression to

$$\frac{I_{\mathrm{c},d}}{I_{\mathrm{s},d}} = \mathrm{K} \cdot \frac{1 - \exp\left(-\frac{d}{\lambda_{\mathrm{c},E_{\mathrm{c}}} \cos\vartheta}\right)}{\exp\left(-\frac{d}{\lambda_{\mathrm{c},E_{\mathrm{s}}} \cos\vartheta}\right)} . \tag{2.19}$$

Usually, the atomic density n can be easily calculated from crystallographic data, cross section σ can be found in databases,[120,121] the transmission function T can be measured for the specific spectrometer, IMFPs λ can be found in literature or databases.[122–134] Numerical solving of this transcendental equation leads to the layer thickness d. Thickness calculations are an important method in this thesis, since they are used to calculate the reaction depths of metalation reactions of organic multilayers, *e.g.*, cobalt atoms dosed on 2*H*-tetraphenylporphyrin.

As shown in Figure 2.8 (b), the thickness of the reacted layer is d_1, while the thickness of the pristine layer is given by $(d_2 - d_1)$. Assuming a sharp interface

between these layers, the intensity of reacted layer can be calculated by

$$\begin{aligned} I_\mathrm{r} &= \int_0^{d_1} n_\mathrm{r}\sigma_\mathrm{r} y\phi FA \cdot T_\mathrm{r} \cdot \exp\left(-\frac{z}{\lambda_\mathrm{r}\cos\vartheta}\right)\mathrm{d}z \\ &= n_\mathrm{r}\sigma_\mathrm{r} y\phi FA \cdot T_\mathrm{r} \cdot \lambda_\mathrm{r}\cos\vartheta\left(1-\exp\left(-\frac{d_1}{\lambda_\mathrm{r}\cos\vartheta}\right)\right) . \end{aligned} \tag{2.20}$$

Here the subscript $_\mathrm{r}$ refers to parameters related to the reacted layer. The intensity for the pristine layer beneath is given by

$$\begin{aligned} I_\mathrm{p} &= \int_{d_1}^{d_2} n_\mathrm{p}\sigma_\mathrm{p} y\phi FA \cdot T_\mathrm{p} \cdot \exp\left(-\frac{z-d_1}{\lambda_\mathrm{p}\cos\vartheta}\right)\cdot\exp\left(-\frac{d_1}{\lambda_\mathrm{r}\cos\vartheta}\right)\mathrm{d}z \\ &= n_\mathrm{p}\sigma_\mathrm{p} y\phi FA \cdot T_\mathrm{p} \cdot \lambda_\mathrm{p}\cos\vartheta\exp\left(-\frac{d_1}{\lambda_\mathrm{r}\cos\vartheta}\right)\left(1-\exp\left(\frac{d_1-d_2}{\lambda_\mathrm{p}\cos\vartheta}\right)\right) \end{aligned} \tag{2.21}$$

with the subscript $_\mathrm{p}$ referring to parameters considering the pristine layer. If data acquisition is performed under identical conditions, the ratio of intensities of photoelectrons coming from the same atomic shell of both layers is represented by

$$R = \frac{I_\mathrm{r}}{I_\mathrm{p}} = \frac{n_\mathrm{r}\cdot T_\mathrm{r}\cdot\lambda_\mathrm{r}}{n_\mathrm{p}\cdot T_\mathrm{p}\cdot\lambda_\mathrm{p}}\cdot\frac{1-\exp\left(-\frac{d_1}{\lambda_\mathrm{r}\cos\vartheta}\right)}{\exp\left(-\frac{d_1}{\lambda_\mathrm{r}\cos\vartheta}\right)\left(1-\exp\left(\frac{d_1-d_2}{\lambda_\mathrm{p}\cos\vartheta}\right)\right)} . \tag{2.22}$$

In the following, an example is given by data processing of the Co/2HTPP system, where the ratio R is given by the intensity ratio of the N 1s signal from reacted layer, *i.e.*, CoTPP, and pristine layer, *i.e.*, 2HTPP. According to the individual crystal structures, the atomic density of nitrogen atoms in 2HTPP and CoTPP vary by less than 1 % and can be considered the same.[135,136] Since the kinetic energies of N 1s photoelectrons from either 2HTPP or CoTPP layer differ only by approximately 2 eV, only tiny differences will be introduced in the transmission function, regardless of species and they can also be assumed to be identical. With the additional assumption that the IMFPs λ for N 1s electrons in these two components are similar, the ratio can be simplified to

$$R = \frac{I_\mathrm{r}}{I_\mathrm{p}} \approx \frac{1-\exp\left(-\frac{d_1}{\lambda\cos\vartheta}\right)}{\exp\left(-\frac{d_1}{\lambda\cos\vartheta}\right)-\exp\left(-\frac{d_2}{\lambda\cos\vartheta}\right)} \tag{2.23}$$

and under the assumption that the photoelectrons are collected in normal emission direction, *i.e.*, $\vartheta = 0$

$$R = \frac{I_\mathrm{r}}{I_\mathrm{p}} \approx \frac{1 - \exp\left(-\frac{d_1}{\lambda}\right)}{\exp\left(-\frac{d_1}{\lambda}\right) - \exp\left(-\frac{d_2}{\lambda}\right)} \,. \tag{2.24}$$

By solving this equation, the thickness of reaction layer d_1 can be deduced.

In general, a more simple equation is used for the thickness calculation of a reacted cover-layer. However, it requires the very important premise of an infinitely thick pristine layer.[122,137,138] Considering the limit of Equation (2.23) for d_2 approaching infinity, one obtains

$$R = \frac{I_\mathrm{r}}{I_\mathrm{p}} = \lim_{d_2 \to \infty} \frac{1 - \exp\left(-\frac{d_1}{\lambda \cos\vartheta}\right)}{\exp\left(-\frac{d_1}{\lambda \cos\vartheta}\right) - \exp\left(-\frac{d_2}{\lambda \cos\vartheta}\right)} \approx \frac{1 - \exp\left(-\frac{d_1}{\lambda \cos\vartheta}\right)}{\exp\left(-\frac{d_1}{\lambda \cos\vartheta}\right)} \tag{2.25}$$

and by rearrangement

$$d_1 = \lambda \cos\vartheta \ln\left[\left(\frac{I_\mathrm{r}}{I_\mathrm{p}}\right) + 1\right] \tag{2.26}$$

It is worthwhile to point out that the organic layers on the samples studied in this thesis are not thick enough to be considered as bulk-like, *i.e.*, appear as infinitely thick. Hence, the idea of a saturated thickness intensity as used in Equation (2.26) is not suitable in this work[137,138] as it would overestimate the reaction thicknesses.

2.2 Temperature Programmed Desorption

Another intensively applied technique in surface science – temperature programmed desorption (TPD) or in some cases temperature programmed reaction (TPR) – is introduced here. It is complementary to the photoelectron based techniques described before. In a TPD measurement, the sample is pre-covered with a certain amount of adsorbate and then heated with a defined constant heating rate under ultrahigh vacuum conditions. During this process, the amount of desorbed molecules will be measured by mass spectrometers or, in the simplest cases, by pressure reading devices. In the first case, several masses can be simultaneously recorded. The intensity of each mass as a function of time, and, due to the constant heating rate, also of temperature is recorded. For quantitative interpretation of TPD data, frequently the Polanyi-Wigner equation is involved:[139]

$$R_{\mathrm{des}} = -\frac{\mathrm{d}\theta}{\mathrm{d}t} = -\frac{\partial\theta}{\partial T}\frac{\partial T}{\partial t} = \nu_n \theta^n \exp\left(-\frac{E_{\mathrm{des}}}{\mathrm{R}T}\right) . \tag{2.27}$$

R_{des} represents the corresponding desorption rate, θ the sample coverage, t the time, T temperature, n desorption order, ν_n the pre-exponential frequency factor, R the gas constant, and E_{des} the activation energy for desorption. For a constant heating rate β

$$\frac{\mathrm{d}T}{\mathrm{d}t} = \beta \tag{2.28}$$

the corresponding Polanyi-Wigner equation is given by

$$-\frac{\mathrm{d}\theta}{\mathrm{d}T} = \frac{\nu_n}{\beta}\theta^n \exp\left(-\frac{E_{\mathrm{des}}}{\mathrm{R}T}\right) . \tag{2.29}$$

At highest desorption rate, the corresponding desorption temperature T_{max} can be written as,

$$\frac{\mathrm{d}}{\mathrm{d}T}\left(-\frac{\mathrm{d}\theta}{\mathrm{d}T}\right) = \frac{\mathrm{d}}{\mathrm{d}T}\left(\frac{\nu_n}{\beta}\theta^n \exp\left(-\frac{E_{\mathrm{des}}}{\mathrm{R}T}\right)\right)\Bigg|_{T=T_{\mathrm{max}}} = 0 \tag{2.30}$$

Combining the last two equations, one yields

$$\frac{E_{\mathrm{des}}}{\mathrm{R}T_{\mathrm{max}}^2} = \frac{\nu_n}{\beta} n\theta^{n-1} \exp\left(-\frac{E_{\mathrm{des}}}{\mathrm{R}T_{\mathrm{max}}}\right) . \tag{2.31}$$

Logarithmic transformation leads to

$$\ln\left(\frac{T_{\mathrm{max}}^2}{\beta}\right) = \frac{E_{\mathrm{des}}}{\mathrm{R}T_{\mathrm{max}}} + \ln\left(\frac{E_{\mathrm{des}}}{\nu_n \mathrm{R}n}\right) + (1-n)\ln\theta \tag{2.32}$$

as a relation of temperature of maximal desorption to the frequency factor and the desorption activation energy. For details on the derivation of the formula, please refer to Reference [140]. By a series of TPD measurements with varying heating rate β, the plot of $\ln\left({}^{T_{\max}^2}/_{\beta}\right)$ versus ${}^{1}/_{T_{\max}}$ can be drawn and the slope and intercept in the plot provide the desorption activation energy and the frequency factor, respectively.

In case of first order desorption, a more convenient equation was proposed by Redhead in 1962:[141]

$$E_{\mathrm{des}} = \mathrm{R}T_{\max}\left[\ln\left(\frac{\nu_1 T_{\max}}{\beta}\right) - \ln\left(\frac{E_{\mathrm{des}}}{\mathrm{R}T_{\max}}\right)\right] \tag{2.33}$$

and can be approximated by

$$\approx \mathrm{R}T_{\max}\left[\ln\left(\frac{\nu_1 T_{\max}}{\beta}\right) - 3.64\right] . \tag{2.34}$$

In this approximation, the frequency factor ν_1 is similar to vibrations in a solid and amounts to $10^{13}\,\mathrm{s}^{-1}$. With this Redhead equation, the desorption energy E_{des} can be obtained directly by the temperature $T_{\max}$ at which the maximum desorption rate is observed in the TPD measurement.

In the following we will discuss situations with different desorption orders n:

(i) Zero-Order Desorption ($n = 0$)

$$-\frac{\mathrm{d}\theta}{\mathrm{d}T} = \frac{\nu_0}{\beta}\exp\left(-\frac{E_{\mathrm{des}}}{\mathrm{R}T}\right) \tag{2.35}$$

implies that the desorption rate does not depend on coverage and increases exponentially with temperature T. As a consequence, the temperature of peak desorption rate, *i.e.*, $T_{\max}$, will increase with initial coverage. Zero-order desorption can typically be observed in multilayer desorption, or in case of strong attractive interactions between adsorbates.

(ii) First-Order Desorption ($n = 1$)

$$\frac{E_{\mathrm{des}}}{\mathrm{R}T_{\max}^2} = \frac{\nu_1}{\beta}\exp\left(-\frac{E_{\mathrm{des}}}{\mathrm{R}T_{\max}}\right) \tag{2.36}$$

is typical for non-dissociative molecular and atomic adsorption. In case of a fixed heating rate, the temperature at maximal desorption rate $T_{\max}$ is constant and independent of the initial coverage. This is a fingerprint property of first-order desorption.

(iii) Second-Order Desorption ($n = 2$)

$$\frac{E_{\mathrm{des}}}{\mathrm{R}T_{\mathrm{max}}^2} = 2\frac{\nu_2}{\beta}\theta \exp\left(-\frac{E_{\mathrm{des}}}{\mathrm{R}T_{\mathrm{max}}}\right) \tag{2.37}$$

is usually observed for recombination desorption, *e.g.*, desorption of molecular hydrogen atomically adsorbed on tungsten.[142] With increasing initial coverage the T_{max} will shift to lower values. This character can be used to distinguish from the first order desorption.

(iv) Fractional Desorption Orders
are also possible and appear in cases where two-dimensional islands evaporate from their rim or upon recombination of dissociatively adsorbed species.

In the presented work, the TPD technique is utilized to investigate the desorption behavior of porphyrins. The focus here lies on the reaction of the adsorbate with the substrate and whether layer exchange occurs in the multi-layered adsorbates. Details are given in Publication [P1].

2.3 Scanning Tunneling Microscopy and Spectroscopy

The above mentioned techniques exhibit integrating behavior, *i.e.*, the obtained information is averaged over "large" areas. In order to receive lateral information on a molecular or even an atomic level, different methods have to be employed. As STM is feasible to explore specific sites on surfaces, it has also been used for the work presented in this thesis.

STM instruments are able to image surface geometries on an atomic level and often also the electronic structure of surface systems. Since its development in 1981 by Gerd Binnig and Heinrich Rohrer,[143] STM has attracted enormous attention, being widely utilized in scientific research. Especially the solution of intricate surface science problems – like surface reconstructions, geometric, and electronic properties of adsorbates – were only possible with obtained real space images.[21]

The technique of STM is based on quantum mechanics since electrons are tunneling between tip and sample. It is typically operated in either constant height or constant current mode. In the dominantly used constant current mode,[144–146] the tip is scanned over a certain area (x, y) on the surface, while a feedback-loop keeps the tunneling current I constant by adjusting the corresponding gap distance z. Thus, a height profile of scanned area $z(x, y)$ can be calculated from the amount of adjustment.

The tunneling current I can be expressed as[147]

$$I \propto V_{\mathrm{B}} \rho_{\mathrm{s}}(0, E_{\mathrm{F}}) \exp\left(-2\frac{\sqrt{2m\phi}}{\hbar} z\right) \tag{2.38}$$

where V_B is the bias potential applied to the sample, ρ_s is the local density states of sample, ϕ is the average work function of sample and tip, and z is the distance between sample and tip. With a typical value of 5 eV of average work function, a distance change in vertical position z of one angstrom will result in a change of the tunnel current I, which is typically in the sub-nanoampere range, of about one order of magnitude. Since this technique depends on the local work function of the sample, an STM image is actually a convoluted image of the morphology and electronic structure.

In first order perturbation theory, by employing Bardeen's transfer Hamiltonian formalism the tunneling current I can be more accurately described from the overlap of the tails of the wave functions Ψ_μ and Ψ_ν in the region of the tunneling barrier.[148–150]

$$I = \frac{2\pi \mathrm{e}}{\hbar} \sum_{\mu,\nu} f(E_\mu)\left[1 - f(E_\nu + V_{\mathrm{B}})\right] \left|\mathbf{M}_{\mu,\nu}\right|^2 \delta(E_\mu - E_\nu) \tag{2.39}$$

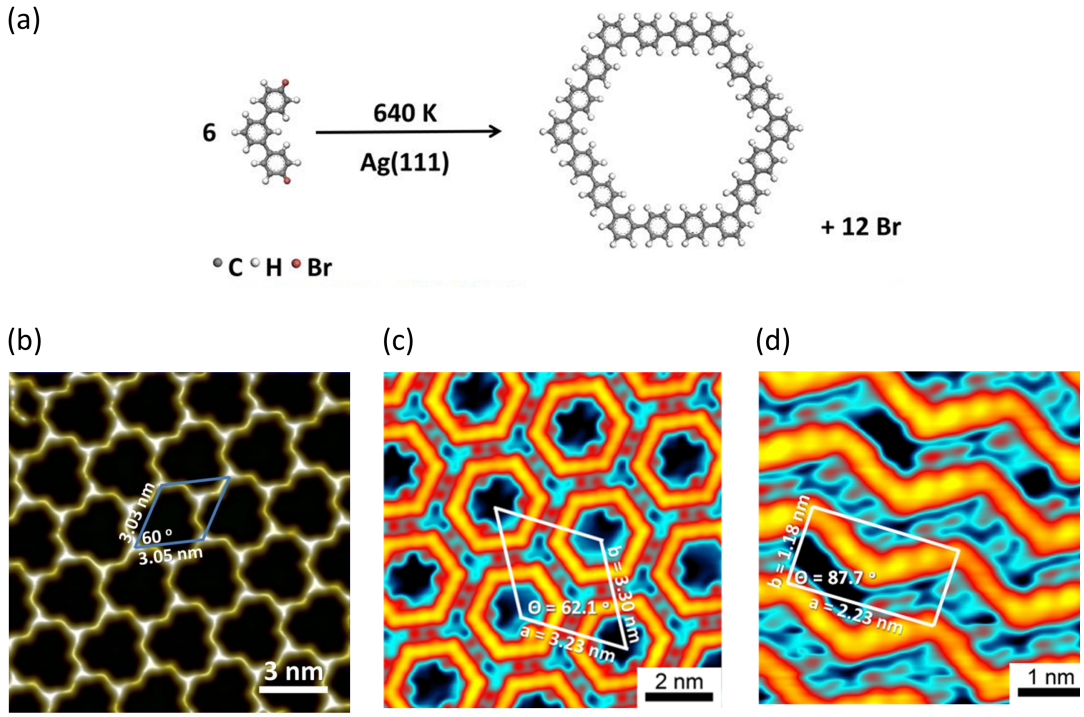

Figure 2.9: *STM Study of the Adsorption and Annealing of DB*m*TP on Ag(111).* Red dots between chains or [18]-honeycombene macrocycles are considered to be detached bromine atoms chemisorbed on the surface.

(a) Schematic drawing for the formation of the [18]-honeycombene from DB*m*TP using a modified Ullmann reaction.

(b) STM image of two-dimensional network formed by DB*m*TP molecules on Ag(111), tunneling parameters: $U = 0.01\,\mathrm{V}$, $I = 0.2\,\mathrm{nA}$.

(c) STM image of an island of [18]-honeycombene, imaged at 4.4 K, tunneling parameters: $U = 0.01\,\mathrm{V}$, $I = 0.02\,\mathrm{nA}$.

(d) STM image of an island of zig-zag polyphenylene chains.

In Equation (2.39), V_B is the bias potential applied to the sample, $\mathbf{M}_{\mu,\nu}$ is the tunneling matrix element between states Ψ_μ of the tip and Ψ_ν of the sample, with eigenenergies of E_μ and E_ν, respectively. The delta function implies that during tunneling electrons do not lose energy, and the Fermi-Dirac function $f(E)$ takes into account that tunneling happens, for instance, from a filled tip state into the empty sample state.[144]

This work uses STM images to observe and characterize the structures formed by molecular self-assembly, as presented in Section 1.4. An STM measurement is shown in Figure 2.9 as an example. As can be seen in Figure 2.9 (b), the vapor deposited 4,4″-dibromo-*meta*-terphenyl molecules arrange in a well-ordered two-dimensional pattern on the sample's surface. Annealing leads to the formation of either islands of the cyclooctadecaphenylene macrocycles, *i.e.*, [18]-honeycombene, or to one-dimensional

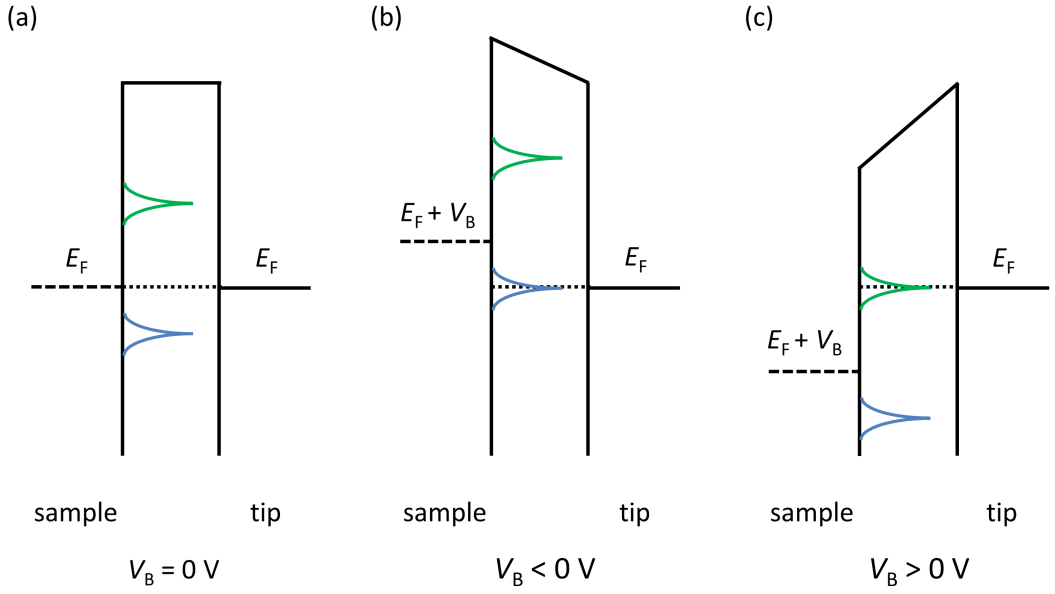

Figure 2.10: *Illustration of the Principle of Scanning Tunneling Spectroscopy.* Density of states that contribute to the tunneling current is affected by the constant Fermi level of the tip E_F and states in the sample. Their energy levels are shifted to $E_F + eV_B$ *via* a bias potential V_B modifying the available tunneling pathways. Negative biases affect the accessible occupied states (blue), while positive potentials give access to unoccupied states (green). The spectroscopic information is derived from the thus variable contribution of individual energy levels to the tunneling current. Figures are adapted from Reference [153].

(a) To simplify discussion, work function of the tip and sample is assumed the same.

(b) By applying negative bias voltage, the occupied states are detected.

(c) By applying positive bias voltage, the unoccupied states are detected.

zigzag-shaped polymer chains *via* the modified, *i.e.*, carried out on silver, Ullmann reaction.[40,151,152] The bromine atoms on the surface, formed as a byproduct, are still detectable by STM with high resolution and indicated by red dots in the STM images.

Since the measured tunneling current I is related to the local electronic structure, its usage to obtain spectroscopic information is obvious. Due to the high accuracy of lateral tip position, it is possible to collect this information from single molecules or even individual sub-molecular entities in the specimen. This technique for spatially resolved spectroscopy, named scanning tunneling spectroscopy, was soon developed after the invention of STM.[154,155]

Based on the Tersoff and Hamann model,[148,149] the tunneling conductance can be approximately derived as

$$\left.\frac{\mathrm{d}I}{\mathrm{d}V}\right|_{V_B} \propto \rho_{sa}\left(E_F + eV_B\right)\rho_t\left(E_F\right) \tag{2.40}$$

where ρ_{sa} and ρ_t are the density of states of sample and tip, respectively. The so called dI/dV signal can be interpreted as a measure of the overlap of local density of states (LDOS) of the sample and the tip under the assumption that ρ_t is constant over the interesting energy range, as illustrated in Figure 2.10.

Experimentally, the dI/dV signal can be obtained by application of a small modulation to the bias voltage and recording the current oscillation with a lock-in amplifier.[21] Measurement of the dI/dV signal with an active feedback-loop allowed image states and surface states to be resolved.[156,157] Furthermore, by recording the lock-in signal while measuring the topography, the spatial extent of a specific spectroscopic feature can be investigated. This methodology is called dI/dV *mapping*.

Since the transmission function depends on the tip and its position to the probed position, movement of the tip can cause artifacts in the spectroscopic maps. Thus, it is recommended to obtain spectroscopic information with a fixed tip position. First, the position of the tip is defined in constant-current mode and subsequently, the dI/dV signal is recorded for different voltages.[21,67,158,159] The fixed tip position avoids a spatially varying background which would strongly influence the spectral features[160]

To avoid the possible artifacts introduced by the tip, especially for the samples with nanoporous molecular networks in Publication [P11], a proper distance of the tip to the sample was stabilized and hereafter the dI/dV map was recorded with in constant height, *i.e.*, open feedback loop, mode.

However, it should be pointed out that the occupied or unoccupied density states obtained from STS are not identical to the results gained either by conventional UPS (occupied states) or inverse photoemission spectroscopy (IPES, unoccupied states).[112] In STS only the states that protrude into vacuum and constructively overlap with tip wave functions can be probed. While information about the filled and unfilled states provided by UPS and IPES measurements respectively is integrated over several surface layers, STS is a more surface sensitive technique, which crucially depends on the extension of relevant states.[144]

2.4 Experimental Setup

This section presents a description of the different ultra-high vacuum (UHV) setups with the individual available techniques. In order to obtain comprehensive information of the investigated systems, experiments presented in this thesis have been carried out with complementary techniques requiring different UHV systems.

Some of the shown work has been done in cooperation with other laboratories, *e.g.*, at Peking University in Beijing, China. Other parts have been conducted at major research facilities, *i.e.*, at BESSY II. In addition, the relocation of the research group from Erlangen to Marburg involved different laboratory equipment.

All UHV systems that have been utilized in this thesis generally provide a vacuum in the range of 10^{-9} mbar or 10^{-10} mbar which enables for almost contamination-free conditions during the experiments. Prior to the vapor deposition process, all organic substances have been thoroughly degassed in vacuum.

2.4.1 PES/TPD Setup in Erlangen – "Scienta"

XPS, UPS and TPD/TPR data discussed in this thesis have been collected on a Scienta UHV system (shown in Figure 2.11) located at the Friedrich-Alexander-Universität Erlangen-Nürnberg. It has been modified to meet the requirements of specific experiments over the past years. This UHV system exhibits a base pressure of typically $2 \cdot 10^{-10}$ mbar, consists of two main compartments, namely a preparation chamber and an analysis chamber. The XPS measurements were carried out with a Scienta ESCA-200 spectrometer equipped with an X-ray monochromator, an Al K_α X-ray source (1486.6 eV), a differentially pumped helium discharge source (21.2 eV and 40.8 eV), and a hemispherical energy analyzer (SES-200). The overall energy resolution amounts to 0.3 eV. The corresponding reported XPS binding energies in this thesis are referenced to the Fermi edge of a clean Cu(111) surface ($E_F \equiv 0$).

In order to enhance the signal from the topmost layers compared to the contribution from the bulk of the crystal, in some experiments photoelectrons were collected at an angle of 70° relative to the surface normal. UPS has been usually carried out with the photoelectrons collected along the surface normal. The overall energy resolution for UPS was < 0.1 eV. In addition to the photoemission setup, this system is equipped with low energy electron diffraction optics (LEED, ErLEED-1000 A), two ion guns for sample cleaning and ion-scattering experiments, a mass spectrometer and several evaporators.

For TPD/TPR, a Pfeiffer HiQuad QMA 400 quadrupole mass spectrometer (QMS) has been used. During TPD/TPR data acquisition, three channels for 2*H*-phthalo-

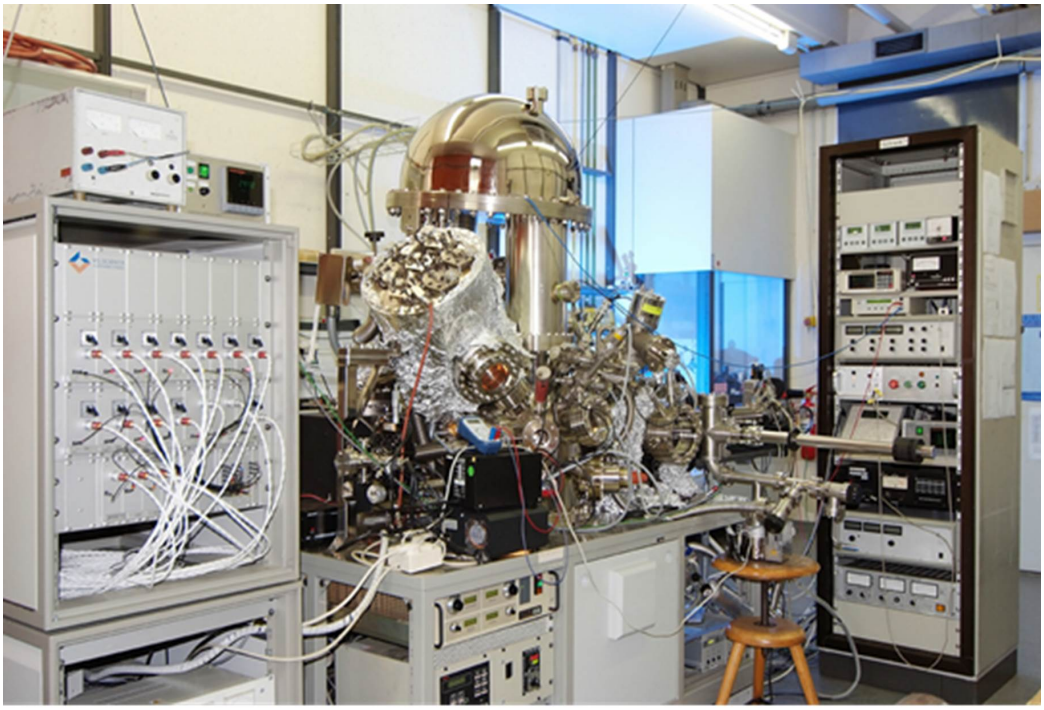

Figure 2.11: *PES System from Scienta in Erlangen.* Center: Scienta ESCA-200 spectrometer with a hemispherical energy analyzer (SES-200); right: preparation chamber with mass spectrometer, LEED optics and evaporators; left: X-ray monochromator. Photo taken from Reference [161].

cyanine (2HPc, m/z = 515), nickel phthalocyanine (NiPc, m/z = 571), and copper phthalocyanine (CuPc, m/z = 576) were monitored quasi-simultaneously by computer-controlled multiplexing of the mass spectrometer. Crosstalk between different mass channels, *e.g.*, due to the related isotope patterns, has been strictly checked and successfully avoided.

The work related to the Publications [P1], [P2], [P3], [P4], [P5], and [P7] has mainly been achieved on this UHV system.

The molecules have been evaporated from a home-built Knudsen cell evaporator. The evaporation and substrate temperatures as well as used crucible materials and vendors for each substance are summarized in Table 2.1. For Publications [P1], [P2], [P3], [P4], and [P7], a copper single crystal (purity > 99.999 %) with a thickness of 2 mm, diameter of 10 mm, and polished (111) surface, aligned to < 0.1° with respect to the nominal orientation, has been used as substrate. For Publication [P5], a gold single crystal with similar specifications has been utilized. In order to achieve precise temperature measurement and control, a type K thermocouple was mounted directly to the rim of crystal. The crystal was attached to a manipulator that allows for cooling and heating in the range from 95 K to 900 K.

Table 2.1: *Evaporation Conditions for the Work in Erlangen.* The evaporation parameters, purities, and suppliers for the substances used in Erlangen are summarized here. All adsorbates have been evaporated from quartz crucibles.

Substance	Crucible Temperature	Sample Temperature	Purity	Supplier
2HPc [a]	640 K	Ambient	98 %	Sigma-Aldrich
CoPc [b]	680 K	Ambient	97 %	Sigma-Aldrich
NiPc [c]	640 K	Ambient	97 %	Sigma-Aldrich
CuPc [d]	640 K	Ambient	99 %	Sigma-Aldrich
2HTPP [e]	640 K	160 K	99 %	Sigma-Aldrich
2HTPyP [f]	650 K	Ambient	97 %	Sigma-Aldrich
DB*p*TP [g]	450 K	170 K	> 97 %	Sigma-Aldrich
TBB [h]	450 K	170 K	> 97 %	Sigma-Aldrich

a 2*H*-Phthalocyanine.
b Cobalt phthalocyanine.
c Nickel phthalocyanine.
d Copper phthalocyanine.
e 2*H*-Tetraphenylporphyrin.
f 2*H*-Tetrapyridylporphyrin.
g 4,4″-Dibromo-*para*-terphenyl.
h 1,3,5-Tris(4-bromophenyl)benzene.

2.4.2 PES Setup in Marburg – "Specs"

Further parts of XPS and UPS experiments with conventional laboratory X-ray and UV sources have been carried out at the University of Marburg. The here presented UHV apparatus comprises three chambers, as shown in Figure 2.12. One is used as load lock and preparation chamber, while the other two compartments house the XPS and STM equipment, respectively. A flow cryostat to cool down the sample with liquid nitrogen is available in both analysis chambers. The base pressure in these compartments is below $2 \cdot 10^{-10}$ mbar.

PES measurements are performed with a commercial photoelectron spectrometer (SPECS Phoibos 150, MCD-9 detector). X-rays are provided by twin anode setup enabling the use of two photon energies. Both X-ray lines, Al K_α ($h\nu$ = 1486.6 eV) and Ag L_α ($h\nu$ = 2984.3 eV), are enhanced by a FOCUS 500 monochromator. In addition, the X-ray source is mounted on an extra manipulator, allowing precise positioning of the source. An ultimate excitation energy resolution of 0.25 eV can be reached, for instance for Al K_α. In addition, the PES chamber is equipped with a gas discharge lamp for UPS measurement and a three-grid LEED optics (SPECS ErLEED-1000A).

The STM is situated in a distinct chamber separated by a gate valve from the XPS

Figure 2.12: *PES System from Specs in Marburg.* Right: XPS chamber with Phoibos 150 hemispherical electron analyzer; left: STM chamber; front: load lock; behind: monochromator FOCUS 500.

chamber. The UP spectra presented in this thesis, taken with this setup, were excited with He I_α radiation ($h\nu$ = 21.2 eV) and a sample bias of −5 eV. The reported XPS and UPS binding energies are referenced to the Fermi edge of the clean Ag surface ($E_F \equiv 0$). The photoelectrons have been collected in normal emission, *i.e.*, at an angle of 0° to the surface normal.

The experiments included in Publications [P8] and [P10] have been carried out on this UHV system.

Organic thin films have been prepared by physical vapor deposition from a home-built Knudsen cell evaporator. The individual evaporation conditions are summarized in Table 2.2. Measurements involving 2*H*-tetraphenylporphyrin multilayers use cleaned aluminum foil substrates while 2,3,8,12,17,18-hexaethyl-7,13-dimethyl-corrole is vapor-deposited onto a Ag(111) surface with crucible hold at 430 K. Individual deposition parameters are given in Table 2.2. The Ag(111) substrate has been cleaned by repeated cycles of Ar^+ ion bombardment with a kinetic energy of 500 eV and annealing up to 800 K. An Omicron electron beam evaporator (FOCUS EFM 4) is used for the deposition of cobalt atoms. The rod shaped evaporant with a diameter of 2 mm and a

Table 2.2: *Evaporation Conditions for the Work in Marburg.* The evaporation parameters, purities, and suppliers for the substances used in Marburg and at HIKE end-station are summarized here. All adsorbates have been evaporated from stainless steel crucibles.

Substance	Crucible Temperature	Sample Temperature	Purity	Supplier
DB*m*TP [a]	360 K	80 K	—	AG Hilt
DB*m*″QiP [b]	380 K	80 K	—	AG Hilt
2HTPP [c]	540 K	Ambient	99 %	Sigma-Aldrich
3HHEDMC [d]	430 K	160 K	—	AG Bröring

a 4,4″-Dibromo-*meta*-terphenyl.
b 4,4‴″-Dibromo-*meta*″-quinquephenyl.
c 2*H*-Tetraphenylporphyrin.
d 3*H*-Hexaethyldimethylcorrole.

purity of 99.99 % has been purchased from Mateck. The deposition rates have been monitored with a quartz crystal microbalance (QCM).

2.4.3 HAXPES Setup at BESSY in Berlin – "HIKE"

Some of the photoemission spectroscopy studies in this thesis have been performed via synchrotron radiation at the third generation storage ring BESSY II with the ring energy of 1.7 GeV at the *Helmholtz-Zentrum*[2] in Berlin. Compared to conventional laboratory excitation sources, synchrotron radiation has its own specific advantages of which the higher photon fluxes and the continuously tunable photon energy are of highest importance in this work. Especially the use of variable high photon energies is crucial. It correspond to larger kinetic energies of the photoelectrons and thus IMFPs. This feature allows for an increased – and adjustable – information depth.

The HAXPES measurements presented in this thesis have been carried out at the "HIKE" end-station, shown in Figure 2.13. It is located at the beamline "KMC-1" which is equipped with a crystal monochromator. It provides a photon flux ranging from 10^{11} photons per second to 10^{12} photons per second in a focus size of 0.3 mm × 0.4 mm. The selectable energy covers a range from soft (1.7 keV) to hard X-rays (12 keV). The monochromator comprises three crystal pairs which are optimized for different energy ranges and can be exchanged *in situ* within few minutes.[162,163] Before each measurement with the pre-chosen photon energy, beamline and monochromator have been optimized for high flux and high resolution.

2 *Berliner Elektronenspeicherring-Gesellschaft für Synchrotronstrahlung m.b.H.*

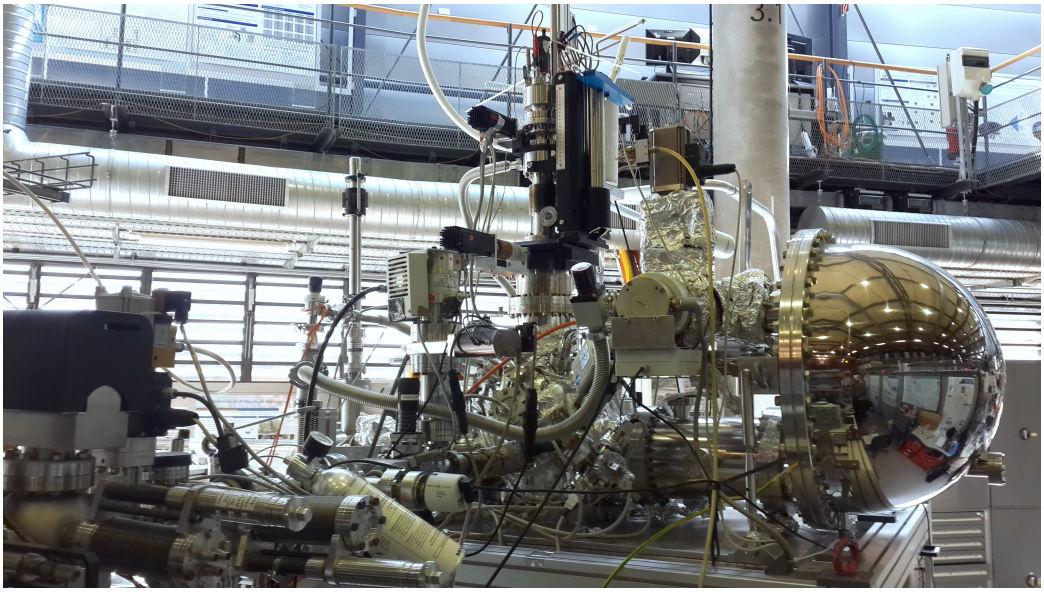

Figure 2.13: *The PES HIKE End-Station at BESSY II, Berlin.* Right: analysis chamber with Scienta R4000 hemispherical electron analyzer; left: the preparation chamber and fast load-lock.

This HIKE end-station is designed for multiple purposes involving high photon energies. It is suitable for near-edge X-ray absorption fine structure (NEXAFS) measurements, absorption and fluorescence spectroscopy, and HAXPES experiments. It comprises an analysis chamber, a preparation chamber, and a fast load-lock system. A VG Scienta-manipulator modified to accept Omicron type specimen holders for sample adjustment and a Scienta R4000 hemispherical electron analyzer are located in the analysis chamber. The Scienta R4000 is a high-resolution analyzer with a 200 mm radius and can be used in the provided configuration for electron kinetic energies up to 10 keV. The analyzer is installed perpendicular to the incident beam. Since the photoelectrons have been collected in normal emission direction, this geometry implies grazing incidence for the photons.

With the Omicron type sample holder, it is possible to mount samples with dimensions ranging from 2 mm × 2 mm to 10 mm × 10 mm with a maximum thickness of 3 mm. The reported binding energies can be calibrated to the Au 4 f peak of a clean gold flag mounted on the manipulator. The preparation chamber can accommodate versatile sample preparation devices on several ports with different sizes and is equipped with a QCM. Up to six samples can be stored in the fast load-lock.[162]

The studies presented in Publication [P9] have been carried out using this UHV system. 2HTPP multilayers have been prepared by vapor deposition from a home-built Knudsen cell onto clean, naturally oxidized aluminum foil. The deposition parameters

are identical to the ones described in Table 2.2. An Omicron electron beam evaporator (FOCUS EFM 4) is used for the deposition of cobalt atoms. The rod shaped evaporant with a diameter of 2 mm and a purity of 99.99 % has been purchased from Mateck. The deposition rates have been monitored by QCM.

In case of the *layered sample*, 12 nm 2HTPP have been deposited onto the substrate before additional 1.8 nm cobalt have been dosed onto the specimen. The *homogeneous sample* has been prepared by simultaneous deposition of both reactants. In order to ensure a high metallation rate, a single stoichiometric excess of cobalt has been applied. All steps have been carried out at moderate rates while the sample remained at ambient temperature.

2.4.4 PES Setup at BESSY in Berlin – "SurICat"

A part of the photoemission spectroscopy data has been obtained at another synchrotron end-station called SurICat (surface investigation and catalysis), shown in Figure 2.14. It was located at the beamline PM4 at BESSY and is equipped with a plane grating monochromator providing photon energies ranging from 20 eV to 2000 eV. The bending magnet provides a photon flux ranging from 10^9 photons per second to 10^{10} photons per second, depending on wavelength. The whole set up comprises four compartments, *i.e.*, a main preparation chamber (sample sputtering and annealing), analysis chamber, organic preparation chamber (deposition of organics, load lock), and non-organic preparation chamber, which are separated by gate valves.

The main instrument in this setup is a Scienta SES-100 electron energy analyzer for photoemission spectroscopy. The tunable photon energy and the possibility to measure the sample's photo current allows for X-ray absorption spectroscopy measurements (XAFS). A VG Helistat manipulator mounted on this chamber allows for sample temperatures ranging from 80 K to 800 K. Specimens are mounted on Omicron sample holders with a maximum size of 10 mm × 10 mm with a thickness up to 3 mm.

A Ag(111) single crystal purchased from Mateck has been prepared by cycles of argon ion sputtering and subsequent annealing. The surface purity has been verified by photoemission spectroscopy. Subsequently, DBm''QiP molecules have been evaporated from a home-built Knudsen cell evaporator according to Table 2.2 onto the sample.

This setup is especially suitable to characterize the delicate oligophenylene dibromides which are used in the Ullmann reactions, see Section 1.3, and the self-assembled structures, see Sections 1.4 and 1.5. The use of tunable synchrotron radiation allows to adjust the kinetic energy of the photoelectrons to about 100 eV in order to reach maximal surface sensitivity, *i.e.*, a minimum IMFP, see Figure 2.3. The rather low

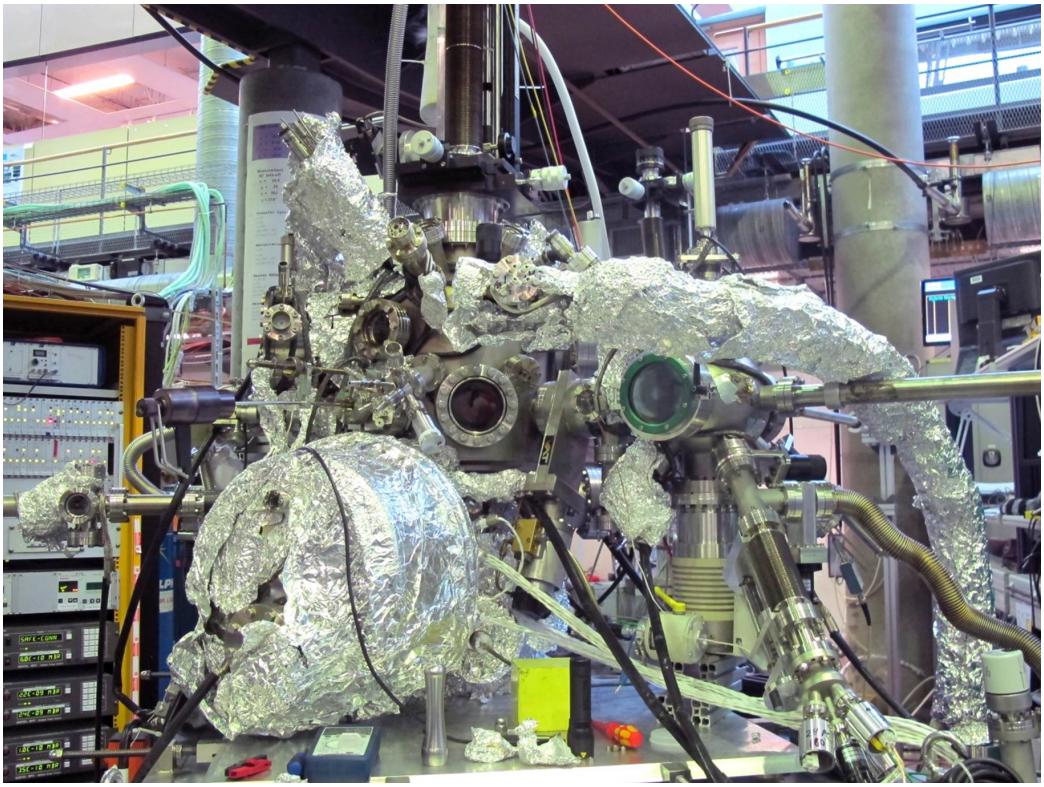

Figure 2.14: *The PES SurICat End-Station at BESSY II, Berlin.* Right: organic preparation chamber Igel which also serves as a fast load lock; left up: the main preparation chamber with a VG Helistat manipulator; left bottom: the analysis chamber with SES-100 hemispherical electron energy analyzer.

photon flux and the large focus size on this beamline avoids extensive beam damage on the sensitive organic adsorbates.

2.4.5 STM Setup at Peking University in China – "Unisoku"

Part of the STM studies presented in this thesis was performed with a Unisoku low-temperature STM (USM-1200S controlled by an RHK SPM 100 R9) through cooperation with Peking University, shown in Figure 2.15. This UHV system has two sections, *i.e.*, a preparation chamber and an observation chamber with a base pressure of $2 \cdot 10^{-10}$ mbar. The preparation chamber is equipped with standard sample preparation facilities (sputtering, annealing, and evaporation). This system also allows tip cleaning under UHV conditions. STM measurements with high resolution at cryogenic temperatures of 78 K or 4.4 K can be performed by cooling with liquid nitrogen or liquid helium, respectively. For monitoring of the sample's temperature, two pairs of thermocouple are attached to the cryostat and the sample, respectively. During measurement, the tip is grounded and a bias voltage is applied to the sample.

Figure 2.15: *The STM Unisoku UHV System at Peking University, China.* Right: preparation chamber; left: the analysis chamber with low-temperature STM and two *in situ* evaporators for organic compounds.

STS measurements used a standard lock-in amplifier (Stanford Research System, SR830) with a typical modulation of 20 mV.

The STM/STS experiments in Publication [P11] have been mainly performed on this chamber. The Ag(111) single crystal was prepared by cycles of argon ion sputtering and annealing (773 K). The terminal oligophenylene dibromide precursors were sublimated onto the sample kept at ambient temperature. The individual evaporation conditions are summarized in Table 2.3. Subsequently, the sample was annealed at 640 K for 10 min to trigger the substrate-mediated Ullmann coupling. The as-prepared sample

Table 2.3: *Evaporation Conditions for the Work in Beijing.* The evaporation parameters, purities, and suppliers for the substances used in Beijing and at SurICat end-station are summarized here. Adsorbates have been evaporated from tantalum boats in Beijing and from stainless steel crucibles in Berlin.

Substance	Crucible Temperature	Sample Temperature	Purity	Supplier
DB*m*TP [a]	333 K	Ambient	—	AG Hilt
DB*m*QaP [b]	363 K	Ambient	—	AG Hilt
DB*m″*QiP [c]	585 K	Ambient	—	AG Hilt

a 4,4″-Dibromo-*meta*-terphenyl.
b 4,4‴-Dibromo-*meta*-quaterphenyl.
c 4,4⁗-Dibromo-*meta″*-quinquephenyl.

was instantaneously transferred into the observation chamber to perform STM/STS measurements at 78 K or 4.4 K with an electrochemically etched tungsten tip. STM images were all acquired in constant-current mode, while $\mathrm{d}I/\mathrm{d}V$ mappings were performed in constant-height mode to avoid signal artifacts. All images in this project have been processed with the software "WSxM".[164]

2.4.6 Crucible Design

Most of the molecules studied in this thesis has been evaporated from Knudsen cell type evaporators. The here presented deposition source has been originally designed for this thesis but has not been realized yet.

As shown in Figure 2.16, a quartz crucible with an inner diameter of 2.6 mm, outer diameter of 3.8 mm, and a length of 10 mm is inserted in a copper liner which is wrapped with a clamped vacuum compatible coaxial heating element (Thermocoax) ensuring a homogeneous temperature. A shutter mounted on a rotational feedthrough above the crucible's opening provides defined deposition times. Connections to power the heating element and for temperature measurement are located on a combination feedthrough. The whole setup fits on a CF 40 flange which is a standard port size on most vacuum systems for deposition purposes. The working distance can be adjusted by usage of supporting threaded rods with variable length.

Since the focus of this evaporator lies on gentle and uniform heating of delicate organic substances, the common approach – an electrically heated, arbitrary shaped tungsten coil wrapped around a non-conductive crucible – is not suitable since the copper liner would simply short the heating wire. The simple solution to this issue typically involves the use of ceramic adhesives to establish electrical isolation. Since

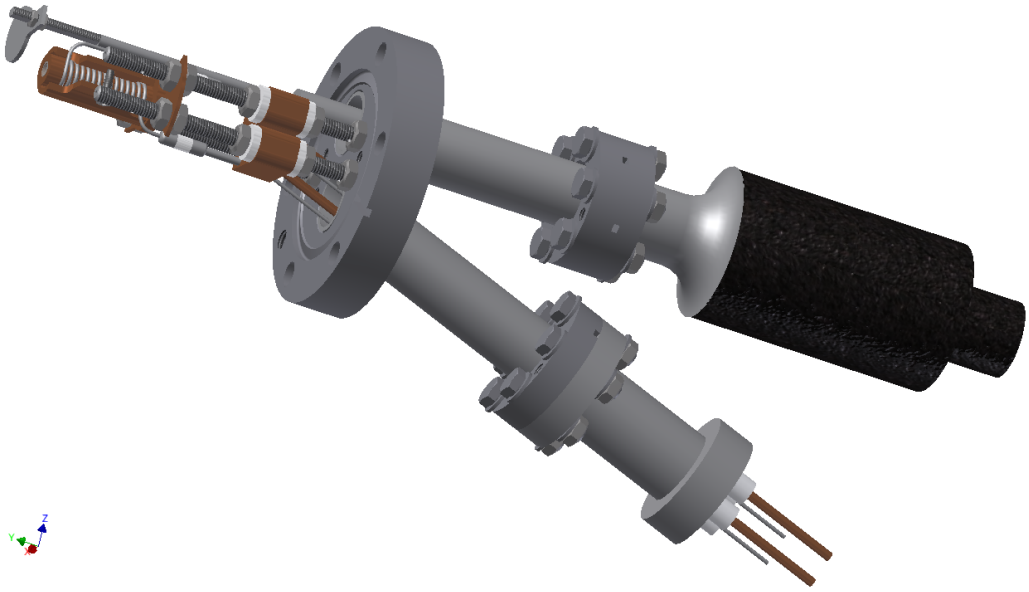

Figure 2.16: *Design of Home-Built Evaporator for Delicate Evaporants* using Autodesk Inventor Professional. The crucible is heated by a coaxial heating wire. For improved temperature control, the crucible is placed in a copper reception equipped with a thermocouple. A current/temperature combination feedthrough established electrical connection to the air side. For precises deposition timing, a shutter at the outlet of the crucible is mounted on a rotational feedthrough.

this arrangement is known for its contamination potential, a coaxial heating element is used.

Part numbers and the design drawings are given in Appendix A.

3 Results and Discussion

The findings presented in this thesis can be divided into four sections. Each section deals with a specific aspect of the chemical reactions and physical properties. Three of them have the fundamental investigation of metal-organic interfaces as a common motive, while the fourth one aims at the study of an applied system. The following sections give a brief summary of the investigated projects reported in the publications cited in Appendix B.

Section 3.1 collects the findings related to coordination chemistry of the studied porphyrinoids, *i.e.*, 2*H*-phthalocyanine (2HPc), 2*H*-tetraphenylporphyrin (2HTPP), 2*H*-tetrapyridylporphyrin (2HTPyP), 2*H*-tetrakis(3,5-di-*tert*-butylphenyl)porphyrin (2HTTBPP), and 2,3,8,12,17,18-hexaethyl-7,13-dimethyl-corrole (3HHEDMC), deposited on coinage metal single crystals. The chemical and electronic properties of interfaces between thin layers of tetrapyrrole molecules and several substrate obtained is discussed in this part.

Section 3.3 focuses on the metalation of thicker films, *i.e.*, multilayers, of 2*H*-tetraphenylporphyrin with cobalt atoms deposited *on top* of the organic layer. The investigations using X-ray photoemission spectroscopy (XPS), ultraviolet photoemission spectroscopy (UPS), and temperature programmed desorption/reaction (TPD/TPR), benefit from the synergies from conventional, *i.e.*, laboratory, and synchrotron X-ray sources. The laboratory experiments aim at coverage dependent effects while the synchrotron study focuses on the chemical depths profile of the formed interface. This comprehensive research serves as a model study for the buried metal-organic interfaces or interphases, which play an important role in the performance of electronic devices.

Section 3.4 gathers the results from a hard X-ray photoemission spectroscopy (HAXPES) study of a *used* electrode for lithium-ion batteries. The vertical chemical composition of this layered thin-film lithium ion storage cathode has been obtained by variation of the excitation energy using synchrotron radiation.

In Section 3.5 several surface-assisted (modified) Ullmann reactions are investigated by a combination of photoelectron spectroscopies and scanning tunneling microscopy (STM) as well as scanning tunneling spectroscopy (STS). This leads to a detailed view on electronic and geometric properties of the reactions. The reaction of dibromo-*para*-terphenyl (DB*p*TP) and tris(4-bromophenyl)benzene (TBB) is studied on Cu(111)

as proof of concept measurement. In addition, the *in situ* surface-assisted organic synthesis of honeycombene molecules from dibromo-*meta*-terphenyl (DB*m*TP) and dibromo-*meta*-quinquephenyl (DB*m*″QiP) is investigated on Ag(111). Furthermore, self-assembling of molecular fractals on a Ag(111) surface comprising the precursors DB*m*TP and dibromo-*meta*-quaterphenyl (DB*m*QaP) is examined.

It should be pointed out that coverages θ are typically given in monolayers (ML), defined as the number of adsorbed molecules or atoms divided by the number of substrate atoms. This definition is obviously straight-forward if the adsorption of small molecules, which bind to a few surface atoms, is regarded. The advantage of coverages referenced to the substrate lies in the fact that given values for different compounds on the same surface can be easily compared. However, this definition becomes unhandy when large molecules, such as porphyrines, adsorb flat lying on a surface and cover more than thirty surface atoms at once. In order to keep the used terms simple, the written term *monolayer* refers to a close-packed adlayer of molecules, that is, the maximum number of molecules or atoms with direct contact to the substrate surface, and carries the unit "$\mathrm{ML_M}$". For better distinction, the coverages with respect to substrate atoms are denoted by $\mathrm{ML_S} \equiv \mathrm{ML}$. As an example, one close-packed adlayer of 2HTPyP molecules on a Au(111) surface corresponds to coverages of $\theta = 0.035\,\mathrm{ML_S} = 1\,\mathrm{ML_M}$.[16] This definition is also very convenient if covered areas on a surface are to be compared in case molecules of different sizes are adsorbed on substrates with similar surface geometries. As a drawback, the number of molecules in a monolayer differs for different molecules on the surface which might lead to, on a first glance, mismatching values of reaction partners. However, both definitions are not based on absolute amounts but use a reference. This has to be kept in mind in each case.

Data points are given by small open circles. The corresponding fitted envelope of multi-component spectra is given by a black line and not listed explicitly. All other assignments are given in the corresponding caption of the figure. All ultraviolet photoemission spectra and X-ray photoemission spectra of multilayers ($\theta \geq 2\,\mathrm{ML_M}$) are recorded with normal emission, *i.e.*, 0° relative to the surface normal. Unless otherwise stated, X-ray photoemission spectra of adsorbates with coverages of less than two monolayers ($\theta < 2\,\mathrm{ML_M}$) are acquired with photoelectrons detected under an angle of 70° relative to the surface normal, in order to achieve a higher surface sensitivity.

3.1 Coordination Chemistry of Porphyrinoids on Single Crystal Surfaces

Tetrapyrroles and their derivatives are wide-spread in nature and of considerable technological importance as candidates for the construction of functional devices. The investigation of direct metalation of adsorbed metal-free porphyrin and phthalocyanine molecules with *pre-* or *post*-deposited metal atoms has become an actively explored field in the surface science community. As shown previously,[4,20,165] free-base porphyrins readily form ordered monolayers on single-crystalline substrates and represent redox-active ligand precursors, which can oxidize and coordinate adsorbed metal atoms. For instance, the reactions of 2HPc (Figure 3.1), 2HTPP (Figure 3.2), 2HTPyP (Figure 3.3), and 2HTTBPP (Figure 3.4) with iron,[13,166–168] cobalt,[14] nickel,[15] copper,[16] zinc,[17–19] and cerium.[169,170]

In this part, the focus lies on the reactivity of various tetrapyrrole derivatives at submonolayer coverages towards adsorbed copper atoms and metalation by copper substrate atoms[1]. As a first model system, the reaction of 2HTPP and 2HTPyP, respectively, is studied with copper atoms deposited on a Au(111) surface. Metalation of 2HPc molecules with substrate atoms from Cu(111) substrate is also investigated and discussed here as the second model system.

1 Metaphorically speaking, the crystal is feeding the reaction and is partially consumed in this process.

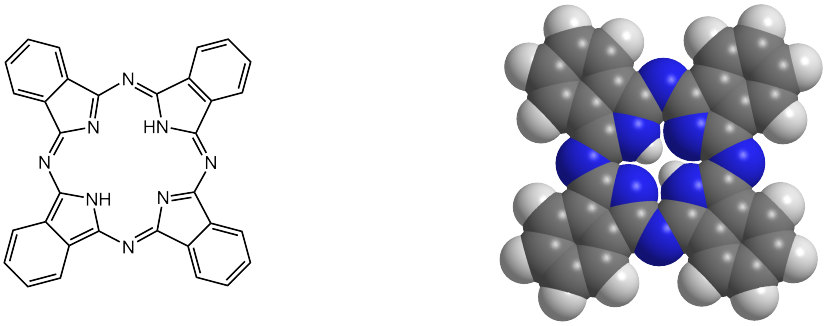

Figure 3.1: 2H-*Phthalocyanine (2HPc).* The central four nitrogen atoms (blue) are able to react with provided metal atoms. Due to steric hindrance, the remaining four nitrogen atoms in the bridging position remain inert. As a consequence of the absence of spacer groups, the whole phthalocyanine macrocycle is in contact with the substrate for coverages of up to one monolayer

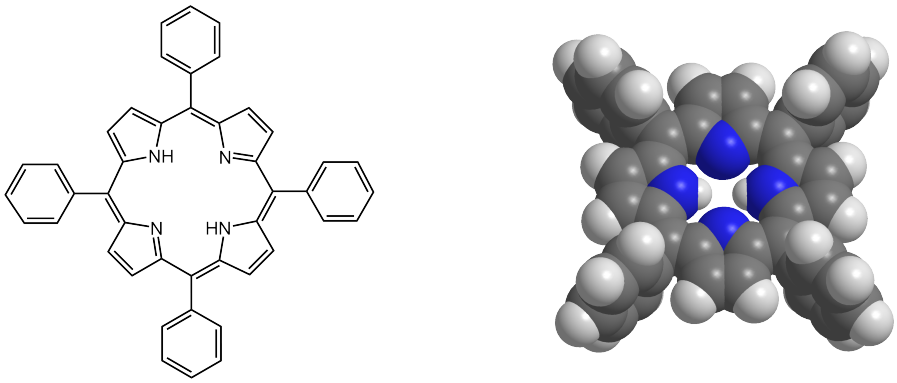

Figure 3.2: 2H-*Tetraphenylporphyrin (2HTPP).* The four nitrogen atoms are able to coordinate provided metal atoms, *e.g.*, iron, cobalt, nickel and copper. Oxidation of the metal and reduction of the pyrrolic hydrogen leads to M(II)TPP complexes and the release of molecular hydrogen. This substance serves as the reference material to all porphyrinoid substances investigated in this thesis. The phenyl substituents on the macrocycle provide a certain distance to the underlying metal substrates.

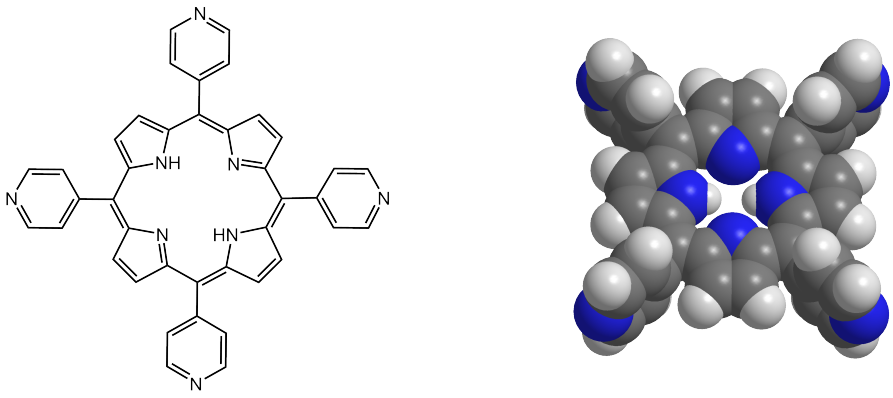

Figure 3.3: 2H-*Tetrapyridylporphyrin (2HTPyP)*. In addition to the redox reaction between the central four nitrogen atoms and dosed metal atoms, the other four nitrogen atoms in the peripheral pyridyl groups can coordinate neutral Cu(0) atoms, and form two-dimensional metal-organic networks.

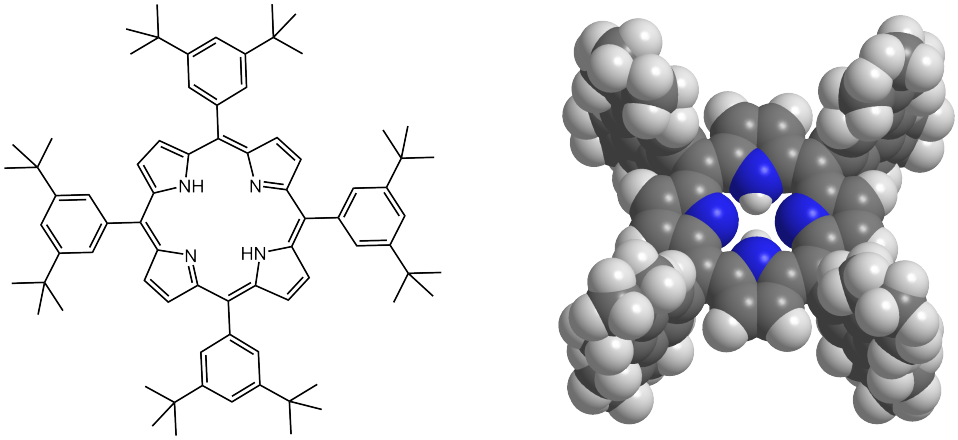

Figure 3.4: 2H-*Tetrakis(3,5-Di*-tert-*Butylphenyl)Porphyrin (2HTTBPP)*. The bulky di-*tert*-butylphenyl spacer substituents increase the distance between adsorbate and substrate compared to other porphyrinoid molecules presented here. This geometrical shaping results in reduced orbital overlap with the substrate's wave functions, and thus in a decreased adsorbate-substrate interaction, compared to 2HPc and 2HTPP.

3.1.1 Metalation of Tetrapyrroles on Au(111)

The metalation of tetrapyrrole molecules, including 2HTPP and 2HTPyP, on Au(111) surfaces by coordination with vapor deposited copper atoms is summarized here. The individual influences of uni- and bi-functional ligands towards the coordinated copper atoms are discussed. Moreover, metalation reactions of 2HTPyP molecules with different deposition sequences are also discussed in detail.

Metalation of 2HTPP on Au(111) with Copper Atoms

The organic layer on the sample is prepared by thermal desorption of metal-free 2HTPP multilayers at 570 K on Au(111). This procedure leaves one well-ordered monolayer of 2HTPP on the substrate.[13] The two peaks in the N 1s spectrum represent two different species, *i.e.*, pyrrolic (−NH−, 399.8 eV) and iminic (−N=, 397.8 eV) nitrogen, with a relative peak distance of 2.0 eV. After deposition of copper atoms onto this sample, the distance is reduced to 1.5 eV while the iminic nitrogen species exhibits a larger peak shift than the pyrrolic nitrogen species.

This can be explained by the formation of an initial complex between copper and 2HTPP at room temperature. In this complex, the intact 2HTPP molecules coordinate to neutral copper, *i.e.*, Cu(0) atoms, with the metal atom sitting atop the molecular plane. Density functional theory (DFT) calculations suggest that the iminic nitrogen atoms form shorter bonds to center metal atom than the pyrrolic nitrogen atoms.[19] The copper atom is mostly coordinated by the iminic nitrogen atoms. This agrees well with the binding energy shifts observed for the N 1s peaks.

Annealing of the sample at 420 K leads to substantial changes in the spectrum. A new peak appears at 398.1 eV in the N 1s region at expense of the two other species. This proves reaction of both nitrogen species in the 2HTPP molecules. The simultaneous rise of a small signal in the Cu $2p_{3/2}$ spectra indicates a reaction for the copper atoms a well. Since the species exhibits a higher binding energy of 934.3 eV compared to the neutral species (932.2 eV), as shown on right panel of Figure 3.5, an oxidation of the copper atom in the complex is suggested. Comparison with the results from the cobalt/2HTPP system[14] suggests the formation of the copper(II)-tetraphenylporphyrin (CuTPP) complex. Further annealing the sample to even higher temperature (470 K), more and more 2HTPP molecules are metalated to CuTPP. Complete metalation of 2HTPP with copper atoms was found to occur at 520 K.

It is worth to mention that upon sample annealing from room temperature to 520 K, the Cu(0)-related peak at 932.2 eV decreases due to diffusion of copper atoms into the bulk phase of the gold substrate.

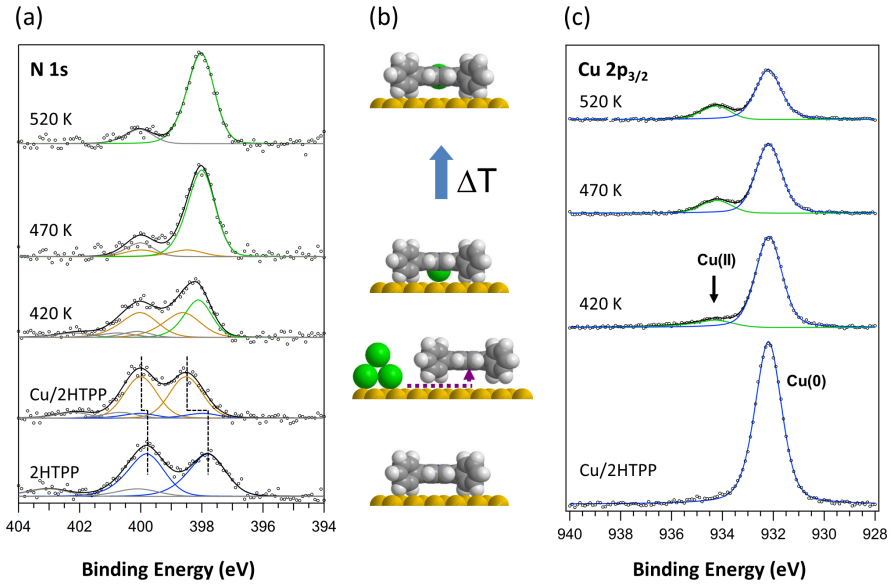

Figure 3.5: *Metalation of 2HTPP with Copper Atoms on Au(111).*
0.037 ML_S = 1 ML_M 2HTPP on Au(111) is investigated at 300 K before (bottom) and after deposition of 0.32 ML_S copper at 300 K as well as after subsequent annealing to the indicated temperatures.

(a) The two nitrogen species of the free base in the N 1s XP spectra shift their binding energy due to formation of an initial complex and become equivalent upon heating in the product complex.
Line Colors: blue – unreacted iminic and pyrrolic nitrogen; brown – iminic and pyrrolic nitrogen of the initial complex; green – metalated nitrogen; gray – satellites.

(b) 2HTPP (gray and white spheres) is deposited on Au(111) (bottom). Deposited copper atoms (green) diffuse to reaction centers. Initial complexes with copper atoms sitting on one side of 2HTPP are formed. Annealing leads to reaction of copper atoms with 2HTPP and formation of CuTPP (top).

(c) The Cu $2p_{3/2}$ XP spectra of the system after deposition of copper contains two features. The peak at 932.2 eV is attributed to Cu(0) while the peak at 934.7 eV is attributed to Cu(II) originated from direct metalation of 2HTPP to CuTPP by copper atoms. The decrease of Cu(0) signal is due to diffusion of copper atoms into the gold bulk.
Line Colors: blue – metallic copper; green – reacted copper.

The four nitrogen atoms in the porphyrin macrocycle coordinate the copper atom and form CuTPP while the remaining molecule is not affected by the metalation reaction. Hence, the 2HTPP molecule shows a *unifunctional* behavior towards copper atoms, *i.e.*, it exhibits only one reactive moiety.

Metalation of Predeposited 2HTPyP on Au(111) with Copper

The temperature induced metalation process of 2HTPyP molecules on Au(111) by copper atoms deposited on the organic layer has been examined by XPS and STM, see Publication [P5]. The individual experimental steps are shown together with the corresponding photoemission spectra for copper and nitrogen in Figure 3.6.

After deposition of a tenfold excess of copper atoms onto a submonolayer ($< 1\,\mathrm{ML_M}$) amount of 2HTPyP at room temperature, the formation of an initial complex Cu(0)-2HTPyP has been observed. Its presence can be deduced from the signal shown by the brown peaks in the N 1s spectra in Figure 3.6 (a). Further, it also has been identified by STM measurements, see Publication [P5].

In this initial complex, the intact 2HTPyP molecules coordinate with neutral copper atoms. The main interaction occurs *via* the iminic nitrogen atoms (−N=). The metal atom sits on one side of the porphyrin plane while the two hydrogen atoms bonded to the pyrrolic nitrogen atoms (−NH−) are pushed to the opposite side.[19,171]

DFT gas-phase calculations provided additional insight into the oxidation state of the copper atom in this initial complex. The population analysis retrieves a charge of the copper atom of +0.5 e. Similar complexes between a porphyrin and a neutral metal atom have been previously reported for the metalation of 2HTPP with zinc and the reaction of 2HTPP molecules with a Cu(111) surface.[19,171]

Upon the deposition of copper atoms it is revealed by STM that islands with rhombic shape emerge. Comparison with the pure organic layer shows that the copper atoms are necessary for the formation of the islands. XPS studies allow for an assignment of the chemical nature of species in these islands. The two-dimensional metal-organic coordination network with rather large voids is stabilized by coordination of the pyridylic nitrogen atoms to "free" copper atoms on the surface. This binding motive, *i.e.*, coordination of copper with pyridine derivatives, has been observed before.[172,173]

After deposition of $0.19\,\mathrm{ML_S}$ copper onto the sample, all 2HTPyP-related peaks undergo a rigid shift of 0.6 eV towards higher binding energy compared to the pure 2HTPyP monolayer on Au(111). This shift could originate from two contributions. On the one hand, the work function could be decreased by copper atoms on Au(111).[174] On the other hand, the positive charge of the coordinated copper atoms might lead to a weakening of the interfacial dipole and thus to a reduced work function. A coaction of both effects is also possible.

Subsequent annealing of the sample to 450 K for two minutes leads to reaction of the copper atoms bound in the initial complex. Similar to the reaction of 2HTPP, the coordinated copper atom is oxidized, hydrogen is released, and the metalated

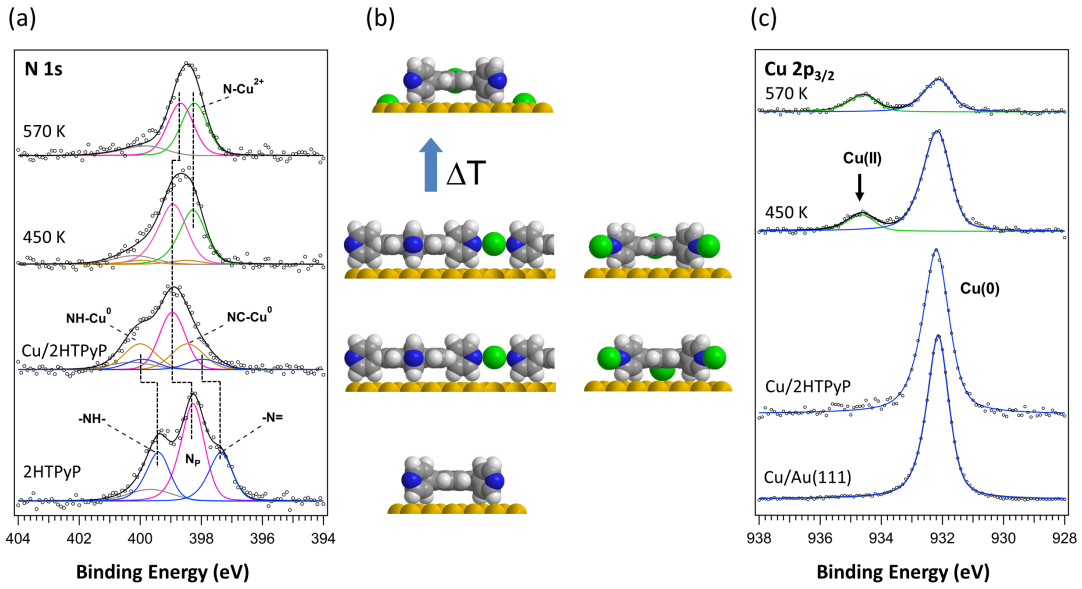

Figure 3.6: *Copper Metalates Predeposited 2HTPyP on Au(111).*
$0.018\,\mathrm{ML_S} \approx 0.5\,\mathrm{ML_M}$ 2HTPyP on Au(111) has been investigated before (bottom) and after deposition of $0.19\,\mathrm{ML_S}$ copper at 300 K and subsequent heating to the indicated temperatures.

(a) The two nitrogen species of the macrocycle (−N= and −NH−) in the N 1s XP spectra shift their binding energy due to formation of an initial complex while the pyridyl groups (N_P) experience a shift due to coordination of copper atoms. The species of the macrocycle become equivalent in the product complex. The reduction of the total intensity from bottom to top is caused by partial desorption at the elevated temperatures and signal damping by copper atoms.
Line Colors: blue – unreacted iminic and pyrrolic nitrogen in the macrocycle; magenta – pyridylic nitrogen in the side groups; gray – satellites; brown – iminic and pyrrolic nitrogen of the initial complex; green – metalated nitrogen.

(b) 2HTPyP (gray and white spheres) is deposited on Au(111) (bottom). Deposited copper atoms (green, tenfold excess) coordinate to two iminic nitrogen atoms of the 2HTPyP macrocycle, forming the initial complex and link two pyridyl groups of neighboring 2HTPyP molecule forming linear bridges. For better visibility, model structures are displayed from different points of view. Annealing to moderate temperatures leads to reaction of copper atoms with 2HTPyP and formation of CuTPyP. The py-Cu-py bridges maintain at this temperature. Upon further annealing, copper atoms are released from the py-Cu-py motives and diffuse into the Au(111) substrate.

(c) The peak at 932.2 eV in the Cu $2p_{3/2}$ XP spectra is attributed to Cu(0) while the peak at 934.7 eV is assigned to Cu(II) in CuTPyP. The decrease of the Cu(0) signal is due to diffusion of copper into the gold bulk.
Line Colors: blue – metallic copper; green – reacted copper.

compound copper(II)-tetrapyridylporphyrin (CuTPyP) is produced. Its formation is corroborated by the new spectral feature in the N 1s spectrum in Figure 3.6 at 398.3 eV (−NCu−, green) and the Cu^{2+}-related Cu $2p_{3/2}$ peak at 934.7 eV. In the metalated porphyrin, a charge of +0.9 e is attributed to the coordinated copper atoms by population analysis of DFT calculations. This increased *oxidation state* of copper in CuTPyP compared to the initial complex agrees well with the higher binding energy shift observed in the Cu $2p_{3/2}$ spectra. According to quantitative analysis of XPS data, only 14 % of the initial complex remain with this preparation sequence. Prolonged annealing leads to a complete reaction.

The changes of the photoemission spectra are dominated by the reaction in the molecular center region. Population analysis in corresponding DFT calculations provides a charge for the bridging copper atom of +0.4 e. Since this value is only slightly smaller than the charge for the copper atom in the initial complex (+0.5 e), it is difficult to distinguish these two species by their corresponding Cu $2p_{3/2}$ spectroscopic fingerprints. However, STM measurements provide complementary information about the arrangement of the CuTPyP molecules on the surface. It turns out that the network islands persist and the Cu(0) in the py–Cu–py bridge stays intact.

In order to investigate the temperature-dependent structural changes of the two-dimensional coordination network, the sample is further annealed to 570 K. STM topographs reveal that the open network collapses and a close-packed arrangement becomes visible. This implies a release of copper atoms from the bridging positions. A possible explanation for this observation arises from the fact that copper alloys into gold surfaces at elevated temperatures.[175] This leads to a reduced concentration of copper on the surface and thus to a deficiency for metal-organic coordination.

The reduced total intensity of the Cu $2p_{3/2}$ signal shown in Figure 3.6 and the emission angle dependent measurement of the Cu $2p_{3/2}$ signal presented in the supporting information of Publication [P5] prove that alloy formation is indeed the case here.

The N 1s spectrum taken after annealing to 570 K shows only contributions from CuTPyP, which indicates all 2HTPyP molecules on Au(111) are metalated. The pyridyl-related peak is shifted to lower binding energy by 0.2 eV relative to peak positions at 300 K and 450 K. This change can be easily interpreted by the fact that the peripheral nitrogen atoms lose their coordination with copper atoms and thus regain electron density from the coordination bond.

Compared to the unifunctional behavior, *i.e.*, complex formation, of 2HTPP molecules on Au(111), 2HTPyP molecules show a bifunctional behavior, *i.e.*, complex formation and bridging, towards co-adsorbed copper atoms. The four nitrogen atoms of the 2HTPyP macrocycle oxidatively coordinate to copper atoms and form the

complex CuTPyP. In contrast, the four nitrogen atoms in the peripheral pyridyl groups coordinate to neutral atoms with one copper atom linking two pyridyl groups of neighboring molecules. The formation of four linear py-Cu-py bridges per building block leads to a two-dimensional metal-organic coordination network.

Most importantly, this network comprises copper in two different oxidation states in different local environments and thus can be considered as *mixed valent*. This is in contrast to most metal-organic networks or frameworks which typically use one kind of metal ion to connect the struts. By choice of the annealing temperature, different chemical and structural properties of the network can be achieved or, in case of individual annealing steps, induced.

Metalation of 2HTPyP with Predeposited Copper Atoms on Au(111)

It is well known that isolated atoms, like in the previously described experiment, exhibit an increased reactivity compared to atoms adsorbed on surfaces or embedded in clusters.[17] This enhancement might lead to the formation of the previously discussed coordination compounds. However, it is questionable whether the individual copper atoms react directly with the organic molecules or are initially adsorbed on the gold substrate and diffuse to the reaction centers. In order to decide if the latter mechanism is possible, a sample has been prepared using a *reverse* deposition sequence. First, 0.19 ML_S copper are vapor deposited onto a Au(111) surface and subsequently 0.5 ML_M = 0.019 ML_S 2HTPyP are deposited on top.

This preparation method gives very similar results compared to the aforementioned study with the original deposition sequence as shown in Figure 3.6.

The N 1s spectrum recorded at 300 K (bottom) contains five peaks plus a shake-up satellite. The peak assignment is included in Figure 3.7 (a). The amount of the initial complex species (brown curve) is significantly lower compared to the case of first deposited porphyrin (Figure 3.6). This observation can be explained by the fact that deposited copper forms clusters on Au(111).[175] In the previous case, the diffusing copper atoms can find reaction centers before they are gathered in the clusters while in this case they are already trapped.

With sample annealing to higher temperatures, *i.e.*, 470 K and 570 K, the respective spectra are very similar to the first case. About 76 % of the central nitrogen atoms are metalated with copper at 470 K in Figure 3.7, compared to 86 % at 450 K in Figure 3.6. Comparing the individual Cu $2p_{3/2}$ spectra the overall intensity decreases. This suggests that copper atoms are thermally released from the py-Cu-py bridges as well as copper clusters and diffuse into the bulk of the Au(111) substrate.

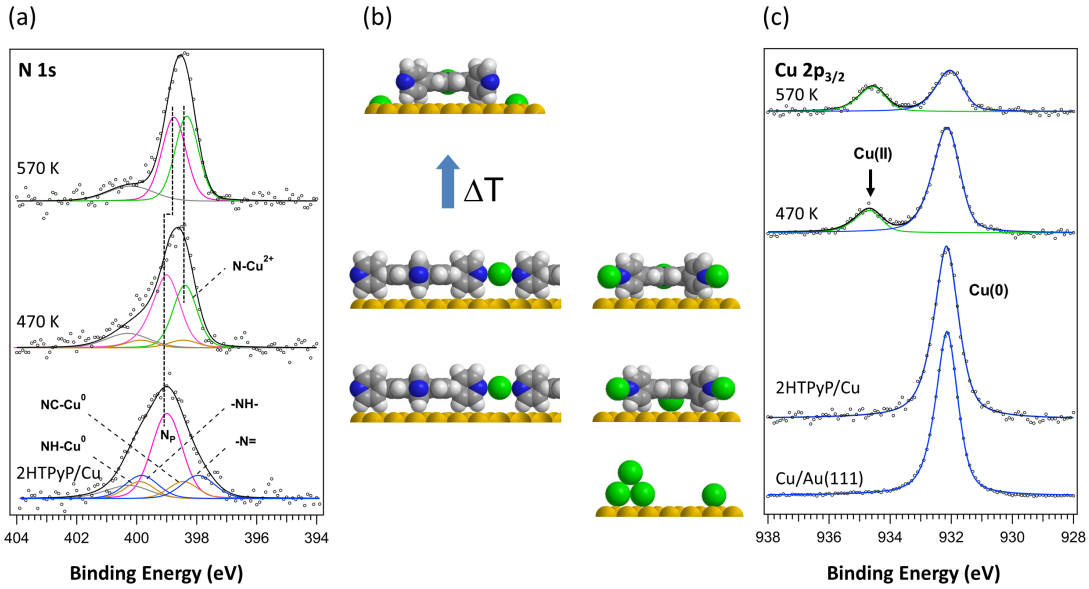

Figure 3.7: *2HTPyP Complexes Predeposited Copper on Au(111).*
$0.019\,\mathrm{ML_S} \approx 0.5\,\mathrm{ML_M}$ 2HTPyP are evaporated onto Au(111) with pre-deposited $0.19\,\mathrm{ML_S}$ copper at 300 K and investigated directly after preparation and after subsequent heating to the indicated temperatures.

(a) The two nitrogen species of the macrocycle (−N= and −NH−) in the N 1s XP spectra shift their binding energy due to formation of an initial complex while the pyridyl groups (N_P) experience a shift due to coordination of copper atoms. The species of the macrocycle become equivalent in the product complex. The reduction of the total intensity from bottom to top is caused by partial desorption at the elevated temperatures.
Line Colors: blue – unreacted iminic and pyrrolic nitrogen in the macrocycle; magenta – pyridylic nitrogen in the side groups; brown – iminic and pyrrolic nitrogen of the initial complex; green – metalated nitrogen; gray – satellites.

(b) Copper atoms (green spheres) are deposited onto the Au(111) surface first (bottom). Subsequently, 2HTPyP (gray and white spheres) is deposited on top. At ambient temperature, copper is coordinated by iminic nitrogen of the 2HTPyP macrocycle, forming the initial complexes as well as linear bridges linking two pyridyl groups of neighboring molecules. Annealing leads to formation of CuTPyP without affection of the py-Cu-py bridges. At higher temperatures, copper atoms are released from the links and diffuse into the substrate. The model structures are displayed from two different points of view.

(c) Cu $2p_{3/2}$ XP spectra of the copper on Au(111) before (bottom) and after vapor deposition of 2HTPyP at 300 K (second from bottom) as well as after annealing the sample are shown. The peak at 932.2 eV is attributed to Cu(0) while the peak at 934.7 eV corresponds to Cu(II) in CuTPyP. The decrease of Cu(0) signal is due to diffusion of copper into the gold bulk.
Line Colors: blue – metallic copper; green – reacted copper.

STM investigations on the sample with reversed preparation reveal that 2HTPyP also exhibits bifunctional behavior and coordinates copper with the pyridyl substituents as well as with the central nitrogen atoms. This leads to the same metal-organic coordination network as in the previous case. Again, the network structure can persist at an elevated temperature of 450 K. Upon further annealing of the sample to 570 K, the coordination network established py-Cu-py bridges disappears and a densely packed CuTPyP monolayer structure is formed. The copper atoms are released from the bridges and diffuse into the Au(111) substrate. This results in the same effect of a reduced binding energy shift for the pyridylic nitrogen peaks in the N 1s spectrum shown in Figure 3.6. The unchanged intensity of the Cu(II) species in the Cu $2p_{3/2}$ spectra indicate that neither metalated molecules are desorbing nor that copper is released out of the central position.

3.1.2 Metalation of Tetrapyrroles with Substrate Atoms from Cu(111)

As demonstrated in Section 3.1.1, adsorbed 2HTPyP molecules are able to react with pre-deposited copper atoms on Au(111) surfaces and form CuTPyP. This implies that adsorbed tetrapyrrole molecules can "pick up" extra metal atoms from surfaces.[13,16,17] This result and the strong interaction of iminic nitrogen atoms with the copper substrates[171,176,177] raise the question whether the atomically flat substrate might serve as a metal source by itself. In fact, this metalation reaction has been observed for 2HTPP as well as 2HPc and is presented in this section.

Metalation of 2HTPP with Substrate Atoms from Cu(111)

Inspired by previous studies concerning the multilayer metalation of 2HTPP on Cu(111),[178] metalation of 2*H*-porphyrin and 2*H*-diphenylporphyrin on Cu(110),[179] and metalation of protoporphyrin IX on Cu(110) as well as Cu(100),[180] the temperature-dependent chemical reaction and structural changes of 2HTPP on Cu(111) have been investigated by means of XPS, UPS, and STM in this thesis.

The evolution of the nitrogen containing species of 0.4 ML_M 2HTPP deposited on Cu(111) has been monitored by XPS, STM, and UPS. The N 1s spectra in Figure 3.8 (a) indicate that a fraction of 2HTPP molecules has undergone the metalation to CuTPP with the substrate at an annealing temperature of 400 K and that the metalation is complete at 450 K. Due to the enormous intensity of the Cu $2p_{3/2}$ signal from the bulk phase, the Cu(II)-related signal from CuTPP is concealed and thus cannot be discussed as in the last sections.

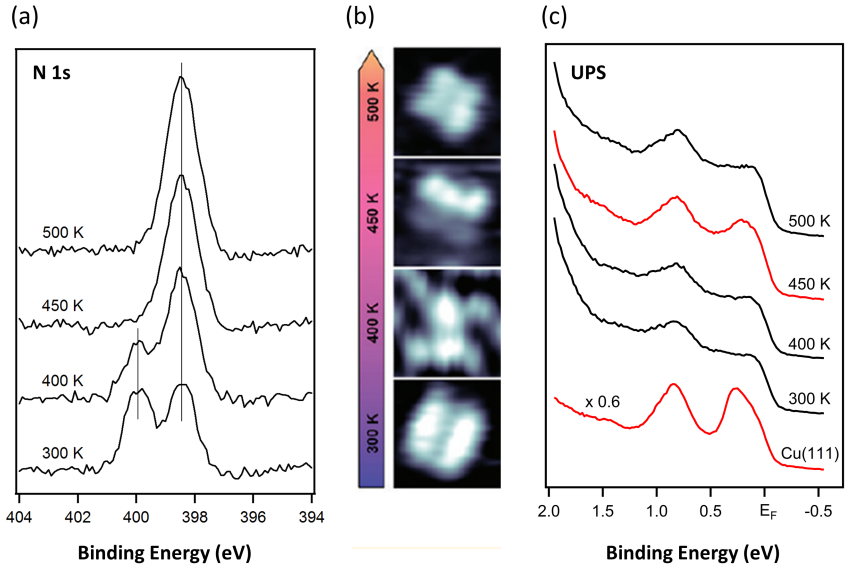

Figure 3.8: *Metalation of 2HTPP with Substrate Atoms from Cu(111).* Results obtained from complementary techniques are opposed for $0.014\,\mathrm{ML_S} \approx 0.4\,\mathrm{ML_M}$ 2HTPP on Cu(111). The photoemission data has always been recorded at ambient temperature directly after deposition and after annealing to the indicated temperatures for two minutes, respectively. Graphs are adapted from Reference [181].

(a) The two individual nitrogen species in the N 1s spectra of the free base become equivalent due to reaction with the substrate in the product complex.

(b) STM images of single molecules after deposition and after sample annealing for two minutes each at the indicated temperatures. At 400 K, the formed CuTPP exhibits a larger distance to the surface than 2HTPP. After heating to 450 K, CuTPP presents a tilted configuration relative to the substrate with one molecule side brought closer to surface. The whole molecule appears parallel to the surface with a reduced height subsequent to annealing at 500 K.

(c) UV spectra (He I_α – 21.2 eV) of a clean Cu(111) surface and this system are shown. The peak located at 0.3 eV is attributed to the Cu(111) Shockley surface state. It gets suppressed due to adsorption of the organic layer, recovers due to a reduced effective coverage,[181] and is quenched again by the carbonaceous residue on the surface. The peak at 0.9 eV corresponds to a phantom peak of the Cu 3d band arising from additional He I_β radiation (23.1 eV).

Among the sample annealing treatment, a subtle effect was discovered by thorough STM studies. At room temperature, 2HTPP appears as individual molecules adsorbed parallel to the surface on Cu(111). This arrangement results from a strong localized adsorbate-substrate interaction between the iminic nitrogen atoms and surface copper atoms.[171] Due to the local geometry, the phenyl substituents on the macrocycle are unable to align parallel to the surface and appear as two lobes in the STM images.

Upon annealing to 450 K for two minutes, all 2HTPP molecules react to CuTPP. Due to the high mobility of the now metalated molecules, imaging is only possible at low temperature. In these images, the complexes appear with brighter and darker sides which indicates tilted molecular planes.

According to the reported dehydrogenation of porphyrins on Cu(110) at 420 K,[179] this can be interpreted as a partial dehydrogenation. Removal of hydrogen – in the *ortho* position in the phenyl substituents or from the pyrrolic subunits in the macrocycle – results in a reduced steric hindrance between these groups.[182] As a consequence, two neighboring phenyl rings exhibit smaller dihedral angles and get closer to the substrate. The side with reduced apparent height appears darker in STM image.

Further annealing to 500 K leads to a situation in which the CuTPP molecule exhibits a rather symmetric appearance again in the STM images. In addition, the molecular plane is aligned parallel to the substrate's surface again. However, the distance to the surface is reduced after annealing. These finding can be explained by a successive dehydrogenation process of the molecule. At a certain extent, all phenyl rings are able to align almost parallel to substrate and the whole molecule gets closer to the substrate.

This behavior can also be verified by ultraviolet photoelectron spectroscopy, as shown in Figure 3.8 (c). The Cu(111) surface exhibits a pronounced Shockley surface state centered at 0.3 eV which is largely suppressed by adsorption of 2HTPP on the sample. It partially recovers after annealing to 450 K due to the decrease of effective coverage on the substrate. This effect is related to the observed tilting of the molecules. Upon further annealing to 500 K, the surface state is suppressed again. This correlates very well with the consequences of flat-lying molecules as seen in the STM study.

Upon annealing, copper atoms from a (111) surface can incorporate into 2HTPP macrocycles under the formation of CuTPP. Structural changes of the molecules are observed by STM studies and originate from successive dehydrogenation reactions of CuTPP. This decomposition could be verified further by UPS studies.

Metalation of 2HPc with Substrate Atoms from Cu(111)

Analogue to the metalation of 2HTPP on Cu(111) at submonolayer coverages discussed in the previous section, the metalation of 2HPc is studied at similar conditions. 2HPc is deposited on a Cu(111) surface cooled to 160 K. Here, the coverages start at submonolayers and extend to multilayers comprising a few molecular layers. The deposited 2HPc reacts with copper from the surface to copper(II) phthalocyanine

(CuPc) according to the equation

$$2\mathrm{HPc} + \mathrm{Cu} \quad \longrightarrow \quad \mathrm{CuPc} + \mathrm{H_2}(g) \ . \tag{3.1}$$

In case of submonolayer coverages of 2HPc, the reaction starts already below 240 K and is almost completed at ambient temperature (not shown, see Publication [P1]). For 2HPc multilayers ($4\,\mathrm{ML_M}$) the metalation process is complete at an elevated temperature of 500 K, as shown in Figure 3.9 (a). After annealing to 500 K, the observed reduction of N 1s intensity, compared to original intensity at 300 K, is attributed to thermally activated growth of three-dimensional islands. This situation resembles structures growing in Stranski-Krastanow-mode and has also been observed for other organic multilayers.[183–186]

The observation of this multilayer metalation of 2HPc[187] raises the question how the molecules above the contact layer gain access to copper atoms and get metalated. There are two mechanisms imaginable. On the one hand, copper atoms might diffuse into the organic phase and react there. On the other hand, an exchange process could replace metalated molecules from the interface with pristine molecules from the organic phase and establish a situation similar to the submonolayer metalation.

To decide this question, a series of particularly designed experiments comprising different layer arrangements have been performed using TPD/TPR. The layer sequences and the corresponding results for multilayer metalation are illustrated in Figure 3.9 and discussed in detail here.

In a first simple case, as shown in Figure 3.10 (a), 2HPc multilayers are deposited on Cu(111) at low temperature. Upon increased temperature, a reaction of the organic molecules with the copper substrate is expected and at even higher temperature desorption of CuPc should occur according to the previous experiments. Depending on the heating rate, the reaction might not be complete and unreacted 2HPc could desorb as well. The experimental results are in total agreement with the theory in this case.

In order to prevent direct interaction of the 2HPc layer with the substrate a monolayer of inert nickel(II) phthalocyanine (NiPc) is inserted between the 2HPc layer and the copper substrate as shown in Figure 3.10 (b). Since NiPc in direct contact to a Cu(111) surface is unable to desorb, it should not be observed in the TPD spectrum which should comprise 2HPc and CuPc. The latter would originate from reaction of copper atom which diffused through the NiPc layer and reacted with 2HPc.

In contrast to this hypothesis, the TPD spectrum of $2\,\mathrm{ML_M}$ 2HPc deposited onto $0.8\,\mathrm{ML_M}$ NiPc on Cu(111) shows not only CuPc as the majority species and a small

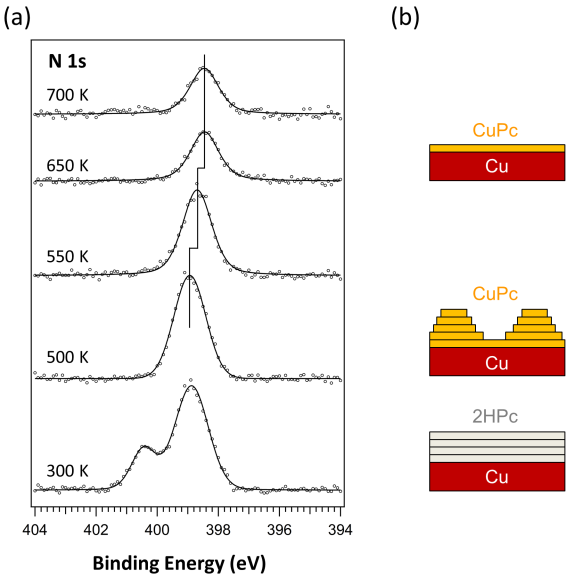

Figure 3.9: *Metalation of 2HPc with Substrate Atoms from Cu(111).* All XP spectra have been taken at room temperature after annealing the sample to the indicated temperatures for two minutes. The solid vertical line indicates the shifted peak position resulting from increased core hole screening at reduced coverages. All spectra have been obtained with normal emission geometry. Graphs are adapted from Reference [187]. Details concerning TPD data are given in Publication [P1].

(a) The N 1s XP spectrum of 4 ML_M 2HPc vapor deposited onto Cu(111) at 300 K is opposed to the ones taken after annealing to the indicated temperatures. At 500 K the metalation reaction is completed. Only one molecular adlayer remains at 650 K.

(b) 4 ML_M 2HPc at 300 K are fully converted to CuPc at 500 K under the transformation from a smooth two-dimensional film into three-dimensional islands with lower XPS intensity. Upon annealing to 650 K, multilayer desorption occurs leaving one monolayer of CuPc on the surface.

contribution of 2HPc, but also desorption of NiPc. The latter can be explained by the exchange of molecules between the monolayer and the higher layers. An additional experiment involves an excessive deposition of 1.8 ML_M NiPc on the copper surface to ensure a complete covering of the substrate and to prevent any direct contact between 2HPc and the copper surface. The sample is completed by 1 ML_M 2HPc deposited on top of NiPc. In this case, desorption of all three species is expected. Again, TPD shows that CuPc desorbs as the majority species, accompanied by NiPc and 2HPc. This result shows unambiguously that, even though both reactants are separated by a closed NiPc layer in the beginning, the 2HPc molecules can still react with the Cu(111) surface.These findings reveal the exchange of molecules between the interface layer, which is directly in contact to the metal surface, and the higher layers consisting

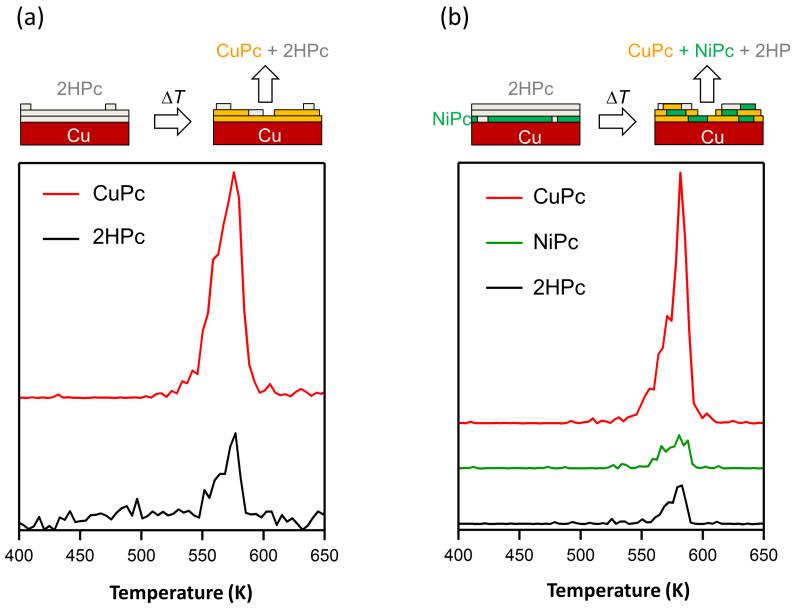

Figure 3.10: *Exemplary TPD/TPR Spectra of the Metalation of 2HPc with Substrate Atoms from Cu(111).* The desorption rate as a function of sample temperature of two exemplary samples with different layer arrangements have been recorded using a heating rate of 5 K/s. The intensities of the individual masses have been measured quasi-simultaneously. Desorption occurs only above the reaction temperature of 500 K. Samples have been studied immediately after preparation. Graphs adapted from Reference [187]. A detailed discussion of the TPD data is given in Publication [P1].

Line Colors: black – 2HPc, m/z = 515; red – CuPc, m/z = 576; green – NiPc, m/z = 571.

(a) The prepared sample carries 2.2 ML_M 2HPc on the Cu(111) crystal. The major species is CuPc. The small amount of unreacted 2HPc desorbing at the same time indicates a fast propagation of the metalated species into the top layers.

(b) The sample comprises 0.8 ML_M NiPc on the Cu(111) surface capped by 2 ML_M 2HPc. The NiPc layer is stable and does not desorb or react up to 700 K (see supporting information in Publication [P1]). Besides the major species CuPc, desorption of NiPc and 2HPc has also been observed. This implies a fast exchange of molecules between the first adlayer and the remaining organic phase.

of 2HPc, NiPc, or CuPc molecules. This process allows 2HPc molecules from the top layers to come in contact with the copper substrate and form CuPc. Repetition of this scheme can result in a complete metalation of the organic adsorbate.

Even though it cannot be completely excluded that additionally copper atoms diffuse from the substrate up into the organic layers and react there, this variant seems quite unlikely. A direct metal exchange of NiPc with the substrate can be ruled out, since TPD spectra of NiPc multilayers on Cu(111) show no contribution of

CuPc. Desorption spectra of CuPc covering a layer of NiPc however exhibits similar intensities of both species. This observation strongly favors a molecule exchange mechanism.

These findings have important implications for metal-organic interfaces in organic electronic devices. Organic monolayers have been proposed as contact primers for adjusting the energy level alignment at the interface in a way that the electron (hole) injection barrier is lowered. If such a contact primer layer is replaced with molecules from the organic semiconductor layers through this exchange process, drastic changes of injection barriers could occur at the metal-organic interface and affect its performance.

3.1.3 Interaction of Tetrapyrroles with Substrates

As discussed above, the metalation of 2HTPP by Cu(111) requires elevated temperatures while 2HPc is metalated below room temperature. In order to interpret this, the interaction between tetrapyrroles and the substrate has been studied in detail. Either an exchange of the substrate (Figure 3.11) or a variation of the distance between molecule and substrate (Figure 3.12) is employed to tune the interaction.

The spectra of unperturbed molecules in the multilayers, *i.e.*, on top of a *thick* layer, are independent on the choice of substrate. The peak separation between pyrrolic nitrogen (−NH−) and iminic nitrogen (−N=) is 2.1 eV. A similar value is measured for the adsorption directly on the substrate in case of Au(111) and Ag(111). Due to the weak adsorbate-substrate interaction,[176,188,189] this peak separation changes only slightly to 2.0 eV for molecules in these monolayers. In contrast, 2HTPP adsorbed on Cu(111) exhibits a reduced peak separation of 1.5 eV. This effect arises mainly from the substantial shift to higher binding energy of the iminic nitrogen-related peak by 0.65 eV.

It is reasonable to propose that 2HTPP molecules form strong localized bonds to the copper substrate by the lone pairs of the iminic nitrogen atoms. This bonding situation here is very similar to the case discussed in Section 3.1.1, *i.e.*, the iminic nitrogen atoms preferably interact with the copper surface and form the initial complex. This manifests itself in similar binding energies.

In case of 2HTPP multilayers, the full width at half maximum (FWHM) of the N 1s signal is 1.0 eV, while on Ag(111) and Au(111) the FWHM increases to 1.5 eV, which is attributed to inhomogeneity broadening. 2HTPP molecules can form long range well-ordered structures on Ag(111) and Au(111). In these structures, the locations of individual molecules are rather determined by intermolecular interaction than by interaction with the substrate. Hence, the nitrogen atoms locate at a variety of

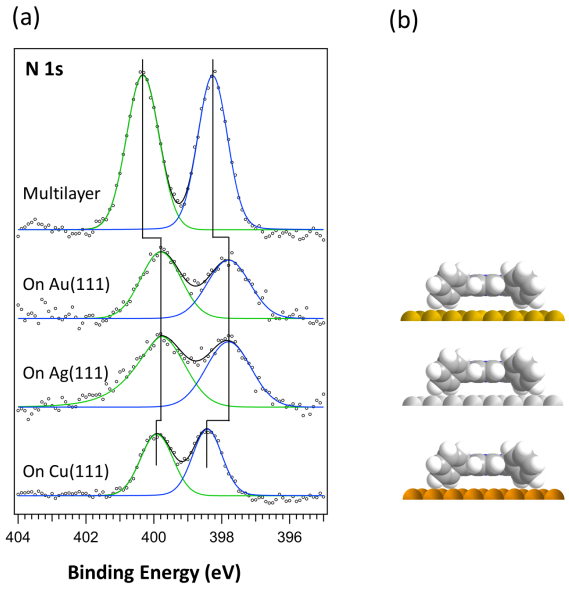

Figure 3.11: *Adsorbate-Substrate Interaction: Substrate Variation.* 2HTPP with varying coverages on coinage metals is studied by XPS.

(a) N 1s XP spectra of 2HTPP multilayers (top, intensity of the signal multiplied by 0.5), 2HTPP monolayers on Au(111) and Ag(111), and 2HTPP on Cu(111) at a coverage of $0.022\,\mathrm{ML_S} = 0.6\,\mathrm{ML_M}$ (bottom). Gold and silver exhibit no interaction with 2HTPP since the peak distance is constant. On copper the distance is reduced indicating an interaction of the iminic nitrogen with the substrate. Graphs adapted from Publication [P3]. [171]
Line Colors: green – pyrrolic nitrogen (−NH−); blue – iminic nitrogen(−N=).

(b) Illustration of the same adsorbate placed on different substrates.

different adsorption sites. [176,188,189] As a consequence, the photo-ion experiences a modulated screening from the substrate.

The FWHM on Cu(111) is reduced to 1.0 eV which is the same as in the multilayer case. The strong adsorbate-substrate interaction between 2HTPP and Cu(111) leads to fixed adsorption sites with respect to the substrate. This eliminates the variable substrates' influence and eliminates the inhomogeneity broadening. Further studies prove that this strong N−Cu interaction between the iminic nitrogen and Cu(111) surface can even force an in-plane tilting of the peripheral phenyl groups. This induces a decreased distance of the porphyrin plane to the surface and thus influences the interaction between adsorbate and substrate even further. [176,190]

In order to investigate the adsorbate-substrate interaction by tuning the distance between adsorbate and substrate, porphyrinoids with different spacer groups are investigated on the same substrate.

Submonolayer coverages of three substituted tetrapyrrole molecules, *i.e.*, 2HPc,

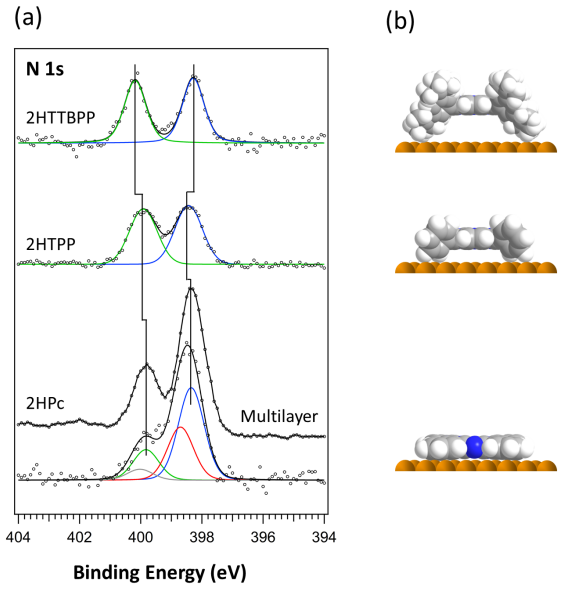

Figure 3.12: *Adsorbate-Substrate Interaction: Adsorbate Variation.*
Different submonolayer coverages of porphyrinoids with varying spacer groups are deposited on Cu(111) and studied by XPS.

(a) N 1s XP spectra of 0.5 ML_M 2HPc, 0.6 ML_M 2HTPP, and 0.9 ML_M 2HTTBPP deposited on Cu(111) are recorded at 300 K. The 0.5 ML 2HPc spectrum (bottom) already indicates a partial metalation. The corresponding multilayer (> 20 ML_M) spectrum (reduced intensity, shifted by −0.6 eV) is added for comparison of the peak shape. 2HTPP exhibits a similar inter-peak distance and thus a comparable interaction with the substrate. Since this distance is increased for 2HTTBPP, the molecule interacts less with the substrate due to a larger displacement from the surface. The fit for 2HPc neglects the small binding energy difference of 0.4 eV [191,192] between the iminic nitrogen atoms in the peripheral meso-positions and the center and combines them into one single peak.
Line Colors: green – pyrrolic nitrogen (−NH−); blue – iminic nitrogen(−N=); red – metalated nitrogen (−NCu−).

(b) Illustration of different adsorbates placed on the same substrate pointing out the different distance from the molecular plane to the surface.

2HTPP, and 2HTTBPP, have been adsorbed on Cu(111) at room temperature. For each substance N 1s XP spectra have been recorded and are shown in Figure 3.12. The figure includes illustrations of their individual geometry on a copper surface to emphasize on the varying distance between the molecular plane and the substrate. It should be noted that the apparent distances do not represent the real distances for each molecule adsorbed on Cu(111). This is especially true for 2HTPP and 2HTTBPP whose distances depend highly on the deformation of the side groups. However, it is reasonable to assume that 2HTTBPP provides a larger spacing than 2HTPP and

2HPc.

2HTTBPP, which has the largest side groups among these three molecules, exhibits two well resolved N 1s peaks at submonolayer coverages. The peak spacing of 2.0 eV marked by vertical lines in Figure 3.12 is the same as for 2HTPP adsorbed on the inert substrates Ag(111) and Au(111).

2HTPP, which carries phenyl substituents, shares the same molecular core as 2HTTBPP and thus intrinsic reactivity. As the phenyl groups are smaller than the 3,5-di-*tert*-butylphenyl-groups which are much larger but also *softer*, *i.e.*, deformable, and can rotate, the distance between adsorbate and substrate is reduced for 2HTPP. As expected, the submonolayer (0.6 ML) spectrum of 2HTPP on Cu(111) shows a similar N 1s spectrum as the corresponding to 2HTTBPP. As the major difference, the peak spacing shrinks to 1.5 eV, which is due to the interaction of iminic nitrogen with the substrate's copper atoms as discussed above.

Since 2HPc has only hydrogen as substituents, it is planar and hence has the smallest distance to the Cu(111) substrate in the discussed cases. Since it comprises additional iminic nitrogen atoms in the macrocycle, the natural intensity ratio of the peaks is altered in the N 1s XP spectrum. Close inspection of the spectra reveals a reduced pyrrolic to iminic nitrogen peak intensity ratio compared to the theoretical value of $1:3$ which is observed in multilayer spectra. This finding indicates that a partial metalation reaction of 2HPc with substrate copper atoms already occurs at room temperature. This result is in agreement with the observations presented in Section 3.1.2.

Furthermore, both pyrrolic and iminic nitrogen peaks experience a binding energy shift of −0.1 eV for 2HPc compared to 2HTPP. This indicates an enhanced electron hole screening effect by the substrate and implies a stronger interaction of 2HPc with the copper substrate than 2HTPP.

3.1.4 Electronic Properties of the Cobalt-Phthalocyanine/ Cu(111) Interface

In studies of cobalt(II) phthalocyanines on Au(111),[193] Au(110),[194] Ag(100),[195,196] Ag(111),[26] and MnO,[197] a comprehensive description of the electronic and magnetic properties is reported. There, it is proposed that a charge transfer from the substrate to the adsorbed molecules occurs mainly *via* the Co 3d atomic orbital. Due to the presence of unpaired electrons, multiplet splitting in photoelectron spectra is expected. This renders the investigation of the open-shell system of CoPc adsorbates on single crystal surfaces more interesting but also more challenging.

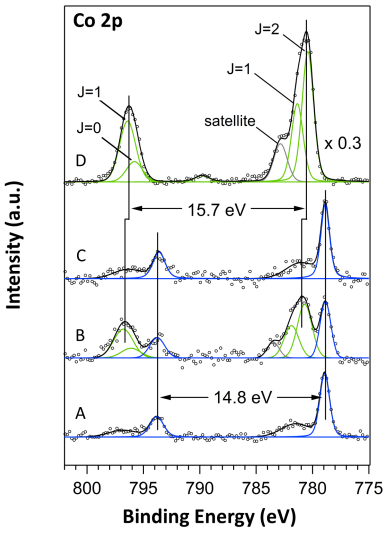

Figure 3.13: *Electronic Properties of the Interface between CoPc and Cu(111): Core Levels.* Co 2p XP spectra for (A) 1 ML_M, (B) 2 ML_M, (C) 2 ML_M annealed to 630 K for two minutes leaving 1 ML_M, and (D) 10 ML_M CoPc on Cu(111) have been recorded at room temperature. The Co 2p signal comprises a multiplet structure arising from photo-hole/orbital angular momentum interaction (green) and a *closed shell* species in contact with the substrate exhibiting a pure doublet (blue). The assignment of the each fitted green sublevel is discussed in detail in the text. The doublet positions and separations for the Co 2p doublets are marked by vertical lines. The intensity of the multilayer spectrum (D) is scaled for better comparison.

In previous studies it has been demonstrated that the interaction between cobalt tetrapyrroles and a Ag(111) substrate can be interpreted in terms of a charge transfer from the substrate to the central metal in cobalt(II)-porphyrin (CoTPP) or cobalt(II)-phthalocyanine (CoPc).[5,26] Extending this previous work by another substrate, the valence band and core levels of CoPc on Cu(111) instead of silver are investigated. The room temperature sample has been studied by XPS and UPS.

Spectrum (D) in Figure 3.13 explains the complicated Co 2p peak structure observed for multilayers of CoPc on Cu(111). Due to the *J*-*J* coupling of the Co 2p photohole with the unpaired electron in the Co 3d orbital, the typical spin-orbit splitting of p-orbitals, *e.g.*, $2p_{1/2}$ and $2p_{3/2}$, further splits into additional sublevels with degeneracy $2J + 1$. In addition, a satellite structure due to the shake-up process is observed.

These sublevel peaks, indicated by green curves in Figure 3.13, are fitted with intensity ratio of 1:3 and 3:5 for $2p_{1/2}$ and $2p_{3/2}$, respectively. As can be seen, the apparent distance between the two major components, *i.e.*, the spin-orbit split between Co $2p_{1/2}$ and Co $2p_{3/2}$, amounts to 15.7 eV.

The intensity ratio of the multiplets in combination with the symmetry of the

adsorbate[2] leads to the conclusion that the unpaired electron is located in the d_{z^2} orbital.

In contrast, both spectra of one monolayer of CoPc on Cu(111), see Figure 3.13 (A, C), exhibit a much simpler composition. They show only simple spin-orbit splitting and the satellites. The peak width, *i.e.*, FWHM, is reduced compared to the multilayer spectra. The absence of a complex multiplet split structure of Co 2p indicates that the coupling between the Co 2p photohole and the 3d electron is quenched in the first adlayer. Both doublet components (blue curves) shift to lower binding energy and exhibit a reduced energy separation of 14.8 eV. The latter value is typical for a $2p_{1/2}$-$2p_{3/2}$ energy separation for metallic cobalt.

The spectrum corresponding to the intermediate situation of 2 ML_M CoPc on Cu(111), see Figure 3.13 (B), consists of features related to monolayer and multilayer coverages. The doublet from the layer in direct contact to the surface has identical parameters as the monolayer spectrum. However, it is damped by the second layer and thus exhibits a slightly lower intensity. The contribution from the second layer strongly resembles the multilayer multiplet structure although the position is shifted to higher binding energy.

Since the Co 2p core levels start to resemble the multiplet split structure of bulk material from the second layer on, the strong chemical interaction is limited to the first layer, as also corroborated by investigations on the valence band. An extra peak around 0.9 eV is observed in the vicinity of the Fermi edge, see Publication [P7].

After annealing to 630 K, only the monolayer feature persists, see Figure 3.13 (C). Since this effect is also used in this work to prepare ordered monolayers, see Section 3.1.1, secondary effects leading to the observed features can be excluded.

Based on the involved symmetries, the interaction can only take place *via* the sp_z orbitals of the substrate orbitals and the d_{z^2} orbitals of the metal center in the adsorbate or the π-system of the macrocycle. Since the electronic structure is significantly altered at the cobalt atom, an electron transfer between the copper substrate and the cobalt d_{z^2} is most likely.

The valence band spectra, shown in Figure 3.14, provide additional information about the strong interaction between CoPc and the copper substrate. The SOMO (d_{z^2} from cobalt, see above) is located at 1.2 eV in the interaction-free case, *i.e.*, with multilayer coverages. Due to the hybridization with the orbitals from the surface, new hybrid states are generated. Two states are visible in Figure 3.14 (b) for a CoPc

2 Phthalocyanines typically adsorb with the molecular plane parallel to the substrate surface at low coverages. As a consequence, their D_{4h} gas phase symmetry, recognizable in Figure 3.1, is reduced to C_{4v} on the substrate.

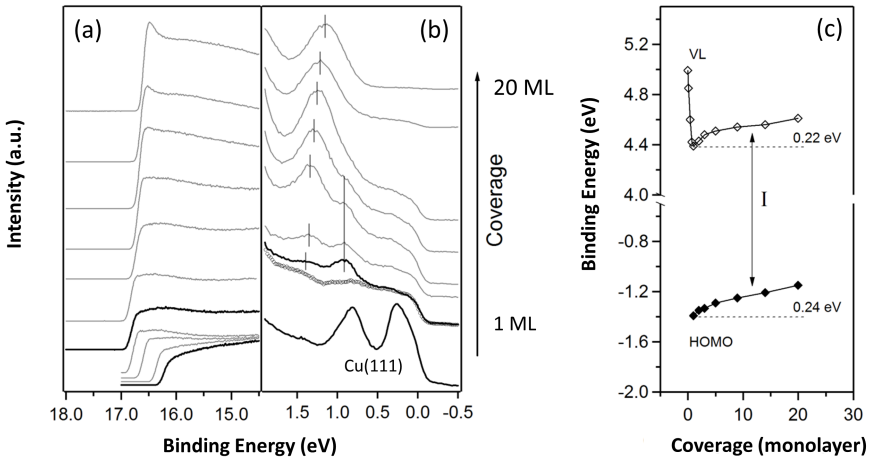

Figure 3.14: *Electronic Properties of the Interface between CoPc and Cu(111): Valence Band.* The evolution of the vacuum level (VL) and HOMO as a function of CoPc coverage on Cu(111) as derived from He I_α UP spectra, see Publication [P7], is shown.

(a) The vacuum level is derived from the secondary electron cut-off shown here.

(b) The position of the HOMO is determined in the presented valence band region close to the Fermi energy E_F.

(c) The ionization potential (IP) exhibits a maximum at submonolayer coverages and becomes constant after the first layer is complete. This indicates a strong electronic interaction of the substrate with the adjacent molecules.

coverage of 1 ML_M with binding energies of 1.4 eV and 0.9 eV, respectively.

Calculations on this system confirm that a new state below the Fermi level is resulting from the strong interaction, *i.e.*, hybridization, of the adsorbed metal complex with the surface *via* the d_{z^2} orbital.[198] Analogue to the results reported for cobalt(II)-octaethylporphyrin on a Ag(111) surface,[199] the shift from the Co 2p signal suggests a charge transfer from the substrate to the adsorbate.

As shown in Figure 3.14 (c), the energy of the vacuum level (VL) experiences a dramatic decrease as the initially clean copper surface becomes gradually covered by CoPc molecules. As the first monolayer is completed, a minimum of the work function of the covered Cu(111) surface is reached. This is a common phenomenon for most of organic adsorptives on metal surfaces.[27,94,200,201] The so-called *cushion* effect is discussed in Section 1.6.1.

Upon further deposition of CoPc the energy of the VL slowly increases again by about 0.2 eV but does not reach its initial value. Simultaneously, the HOMO energy evolves in a similar way as the VL energy, resulting in constant ionization energy (IE) of about 5.8 eV. The binding energies of the C 1s, N 1s, and Co 2p peaks also show

a similar shift within the resolution of the XPS measurement, see Publication [P7]. This is a good indication that band bending might occur in the adsorbed CoPc film. This effect causes a raise of the intrinsic Fermi level of the organic adsorbate near the surface and aligns it with the Fermi level of the copper substrate. Since the energy shift of the HOMO is not reaching a constant value within a few adsorbed monolayers of CoPc, this electronic effect reaches far into the bulk of the organic phase. This observation is somehow in contrast to other adsorbed organic molecules with a low concentration of mobile charge carriers for which the electronic equilibrium is usually achieved within few adlayers.

The presented results from XP and UP spectroscopy on copper samples with different coverages of CoPc provides significant experimental evidence that the electron transfer from the copper substrate to the adsorbate CoPc happens indeed through the $3d_{z^2}$ orbital of the Co(II) ion. This renders the organic on metal system studied in this project unique and interesting.

3.2 Metalation of a Substituted Corrole with Cobalt on Au(111) and Ag(111)

So far, all of the investigated substances contain two reactive species in the central macrocycle, *i.e.*, pyrrolic (−NH−) and iminic (−N=) nitrogen with a stoichiometry of 2 : 2. Since the pyrrolic moieties can be reduced by metal complexation, this substance class favors the formation of a formal +II state of the central metal ion. The influences of the peripheral reactivity, see Sections 3.1.1 and 3.1.2, and of the outer geometry, see Section 3.1.3, have been studied in this thesis. Hence, it is obvious to alter the reactive center in the macrocycle. Since many transition metals form stable di- or tri-cations, *e.g.*, cobalt, the introduction of an additional reducible group in the molecule's core suggests itself.

This situation can be achieved by the usage of corrole instead of porphyrin as stem compound. It can be considered as a porphyrin which has one methin bridge removed under preservation of the aromatic system. As consequences, it contains pyrrolic and iminic nitrogen with a stoichiometric ratio of 3 : 1 and exhibits a slightly smaller void in the center of the molecule.

In nature, its partially saturated analogon, *i.e.*, corrin, plays an important role as active centers in biological processes, *e.g.*, in cobalamin which is also known as vitamin B12. The biochemically rare element cobalt is resting in the center of a highly substituted corrin ring.

This section covers the investigation performed on the metalation of 3HHEDMC (Figure 3.15) with cobalt. The focus here lies on submonolayer coverages of the organic

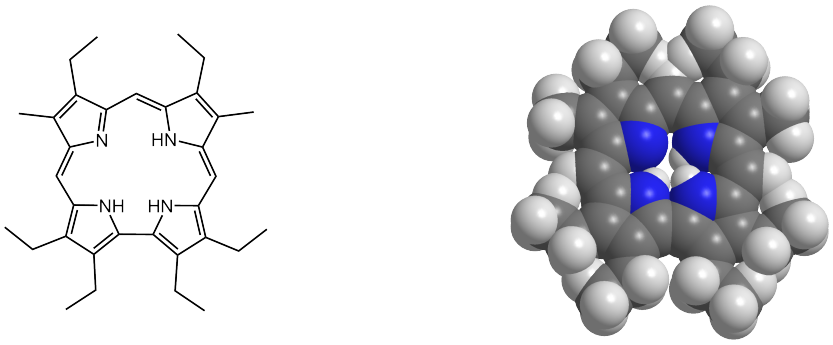

Figure 3.15: 3H-*Hexaethyldimethylcorrole (3HHEDMC).* This substance exhibits a similar yet significantly modified macrocycle as 2HTPP, see Section 3.1. Formal removal of one of the four methin-bridges under preservation of the aromaticity in the macrocycle also leads to replacement of one of the iminic with a pyrrolic nitrogen fragment. This alteration should render the formation of M(III)HEDMC complexes possible.

compound deposited on the inert noble metal surfaces Ag(111) and Au(111). Redox reaction with co-adsorbed cobalt atoms is expected. This would result in the loss of all three pyrrolic hydrogen atoms (−NH−) and metalation of the corrole into a Co(III) complex. Some of the results corresponding to this system are collected in Publication [P8]. Since this is an ongoing project, the presented discussion contains unpublished aspects as well.

3.2.1 Metalation of a Substituted Corrole on Au(111)

The here presented experiments are the first ones comprising 3HHEDMC. Hence, it is advisable to minimize the influence of the substrate and to use a highly inert material. Typically, gold is the first choice in such a case. In addition, gold exhibits no substrate related features in the N 1s region.

Figure 3.16 (a) shows the study of desorption of 1.2 ML_M 3HHEDMC from Au(111). The organic substance has been deposited at ambient temperature on the cleaned gold crystal. The corresponding N 1s spectrum (A) shows two nitrogen species which are assigned to pyrrolic nitrogen (−NH−) and iminic nitrogen (−N=). It should be pointed out that the observed ratio of the peak intensities of 4.6 does not match its theoretical value of 3:1.

Preparation of a monolayer, in a similar way as described in Section 3.1.1, has been attempted. However, upon annealing for one hour to 400 K, a considerable change has been observed on the envelop shape of the N 1s spectrum. This indicates the presence of a new peak, in this specific case between the positions of pyrrolic and iminic nitrogen. In addition, a minor decrease of the total signal intensity by approximately 10 % due to desorption has been observed. After an additional annealing step, this time to 550 K for one hour, the N 1s spectrum is dominated by one single peak indicating an almost complete reaction.

The hydrogen bound to pyrrolic nitrogen atoms can be reduced. Implying a reaction with the substrate, due to the absence of other species, the formation of a Au(III) corrole complex might has been observed, in analogy to the previously discussed metalation reactions. Despite the inertness of gold, a few complexes with square planar geometry, in which gold typically is in the formal oxidation state +III, are known, *e.g.*, chloroauric acid ($HAuCl_4$). Since the hypothetical gold corrole would share both properties and metalation from the bulk phase is possible, see Section 3.1.2, its formation is not completely unreasonable.

As the causes for the observed – so far reproducible – effects remain unclear, further investigations are advised. Special attention should be paid to the purity of the

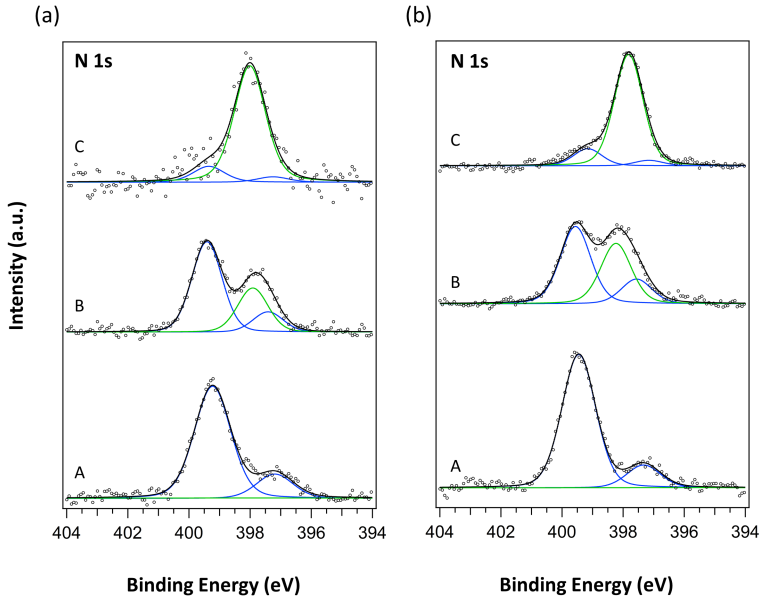

Figure 3.16: *Metalation of 3HHEDMC on Au(111).* Spectra of 3HHEDMC deposited on Au(111) without and with dosed cobalt have been recorded after deposition at ambient temperature and after subsequent annealing. A reaction is observed in both cases.

Line Colors: blue – iminic and pyrrolic nitrogen of 3HHEDMC; green – reacted nitrogen.

(a) N 1s photoelectron spectra of 1.2 ML_M 3HHEDMC on Au(111) are shown directly after deposition (A) on the clean gold surface and after annealing to 400 K (B) as well as 550 K (C) for one hour, respectively.

(b) N 1s photoelectron spectra of 1.6 ML_M 3HHEDMC on Au(111) are shown directly after deposition (A), after e-beam deposition of 0.05 Å cobalt (B), and after additional annealing to 400 K for one hour (C), respectively.

deposited organic layer as well as to contamination from the substrate. Although single crystals exhibit outstanding overall purity, segregation of impurities to the surface during annealing processes might lead to surprising results. This is especially known for new crystals such as the one used in this experiment.

Besides this interesting behavior, the main issue of this investigation addresses the reaction with cobalt. Figure 3.16 (b) shows the spectra of 1.6 ML_M 3HHEDMC on Au(111) and their reaction with 0.05 Å subsequently deposited cobalt. The minor change in peak shape can be attributed to a larger contribution of multilayer species in case of the pristine sample (A). Deposition of cobalt leads to the formation of a new nitrogen species in spectrum (B) which is attributed to the metalated molecule. Upon annealing to 400 K for one hour (C), the spectrum is dominated by a single peak which is ascribed to the cobalt complex. This assignment is supported by the

related Co 2p spectra which are almost identical to the ones taken on silver, see Figure 3.19 (b). The discussion on this feature is given in Section 3.2.2.

The results clearly reveal that 3HHEDMC molecules can be metalated by cobalt, as it has been predicted by the experiments involving the other tetrapyrroles. The apparent reaction of the clean Au(111) substrate with 3HHEDMC is surprising and would be of fundamental interest in gold chemistry. Hence, a verification with extreme attention to impurities is advised. Furthermore, the tracing of precursor states would be of great importance to deduce the detailed reaction steps.

3.2.2 Metalation of a Substituted Corrole on Ag(111) at Ambient Temperature

Submonolayer coverages of 3HHEDMC have been vapor deposited onto a cleaned Ag(111) single crystal at ambient temperature. As can be seen in Figure 3.17 (a), the analysis of the recorded spectra is hindered by the large contribution of a background. This signal originates from the tails of the Ag 3d peaks and their related plasmons. Figure 3.17 (b) shows the same N 1s spectra as in Figure 3.17 (a) but after removal of a scaled and fitted background.

As in the previously presented case involving gold as substrate, see Section 3.2.1, the intensity ratio between pyrrolic (−NH−) and iminic (−N=) nitrogen does not match the stoichiometric ratio of 3:1. In contrast to the previous case, similar signal amplitudes for both species are observed here. This indicates that a reaction with the silver substrate is already occurring at room temperature. Experiments with reduced deposition temperature are addressed in Section 3.2.3.

The reduction of one pyrrolic hydrogen could explain the observed intensity ratio. Due to the lack of other substances, only a reaction with the substrate seems reasonable. This would include the oxidation of silver and the formation of a Ag(I) corrole complex. Since the most common, non-zero, oxidation state of silver is +I, metalation from the substrate is possible. Furthermore, a similar reaction has been observed on the less reactive gold substrate. Due to these indications, a metalation reaction seems possible. Clearly, further input is needed to unambiguously determine the reaction process between 3HHEDMC and the silver substrate.

As can be seen in Figure 3.17, after deposition of 0.05 Å cobalt both nitrogen peaks merge into one single peak. Due to its position between the original peaks and since the change is a consequence of the cobalt deposition, the new species corresponds to the now four equivalent nitrogen atoms (−NCo−) in the metalated molecule cobalt(III)-hexaethyldimethylcorrole (CoHEDMC). The Co 2p spectra discussed in Section 3.2.5

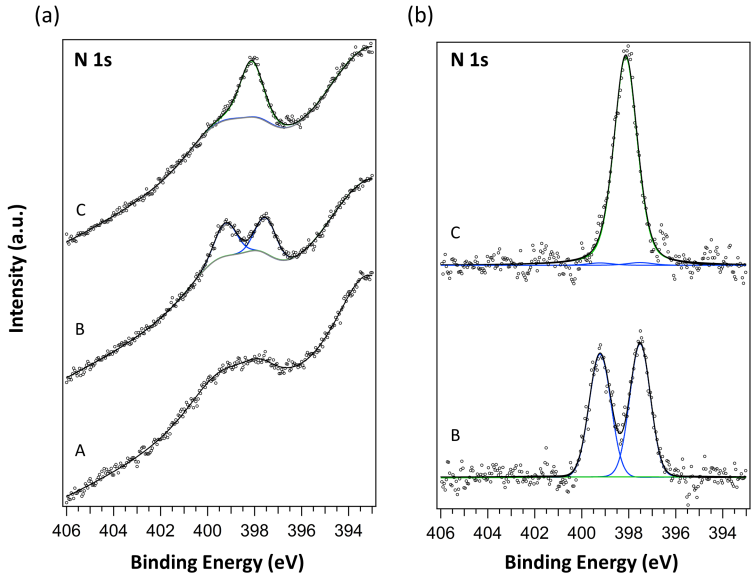

Figure 3.17: *Submonolayer Metalation of 3HHEDMC on Ag(111) at Ambient Temperature.* Spectra of 3HHEDMC deposited on Ag(111) without and with dosed cobalt have been recorded. Spectra (B) show the N 1s spectrum of 0.7 ML_M 3HHEDMC on Ag(111) deposited on the sample at 300 K. Spectra (C) corresponds to the situation after e-beam evaporation of 0.05 Å cobalt onto the sample at ambient temperature.

Line Colors: blue – iminic and pyrrolic nitrogen of 3HHEDMC; green – reacted nitrogen; gray – background.

(a) Spectrum (A) of a clean Ag(111) crystal recorded in the N 1s region is used for background subtraction. The recorded spectra are presented without background correction.

(b) The spectra from (a) are shown with applied background correction.

corroborate this assignment.

Again, the investigation of the possible reaction between 3HHEDMC and silver from the substrate is advised with extreme attention to impurities.

3.2.3 Metalation of a Substituted Corrole on Ag(111) at Low Temperature

Section 3.2.2 documents a pronounced adsorbate/substrate interaction of 3HHEDMC with the Ag(111) surface at ambient temperature, *e.g.*, a possible reaction of silver with the organic molecule under formation of a Ag(I) complex. In order to avoid this possible reaction of the corrole with the substrate, preparation of the organic layer and deposition of cobalt has been carried out at 160 K in this case.

At lowered temperature, the N 1s spectra shown in Figure 3.18 exhibit the expected

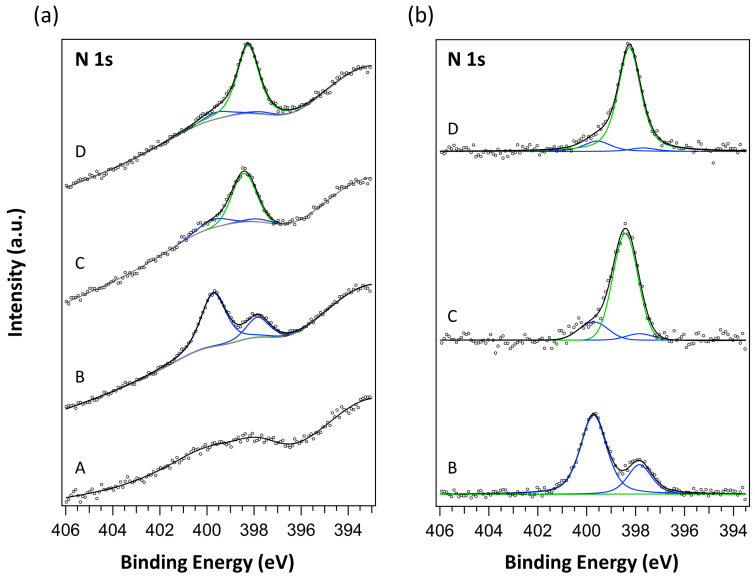

Figure 3.18: *Monolayer Metalation of 3HHEDMC on Ag(111) at Low Temperature.* Spectra of 3HHEDMC deposited on Ag(111) without and with dosed cobalt have been recorded. Spectra (B) show the N 1s spectra of 1 ML_M 3HHEDMC on Ag(111) applied on the sample at 160 K. Spectra (C) correspond to the situation after e-beam evaporation of 0.1 Å cobalt onto the sample at low temperature. Spectra (D) correspond to the same sample at 310 K.

Line Colors: blue – iminic and pyrrolic nitrogen of 3HHEDMC; green – reacted nitrogen; gray – background.

(a) The spectrum (A) of a clean Ag(111) crystal recorded in the N 1s region is used for background subtraction. The recorded spectra are presented without background correction.

(b) The spectra from (a) are shown with applied background correction.

stoichiometric 3:1-ratio of pyrrolic (−NH−, 399.7 eV) to iminic (−N=, 397.8 eV) nitrogen. After deposition of 0.1 Å cobalt, a considerable change is observable in the corresponding N 1s spectrum. A new peak (398.4 eV) arises between the initial features. Its amplitude gain equals the intensity loss of the two initial nitrogen species which keep their natural intensity ratio of 3:1 during this reaction. Therefore, this new species is assigned to the now metal coordinating nitrogen atoms in CoHEDMC (−NCo−).

Heating the sample to ambient temperature causes no pronounced change in the spectrum. This observation implies that the metalation reaction with cobalt is almost complete at 160 K. Since a reaction with silver is not observed at this temperature, the reaction must lead to the CoHEDMC complex.

Sample preparation at low temperature is able to inhibit the reaction of 3HHEDMC with the silver substrate. However, the metalation with cobalt is not suppressed at

160 K. Nevertheless, this experiment allows for an explicit assignment of CoHEDMC as the formed product.

3.2.4 Metalation of 3HHEDMC Multilayers with Cobalt on Ag(111)

In order to obtain substrate independent reference spectra, the metalation of multilayers consisting of 3HHEDMC with cobalt has also been investigated. Spectrum (A) in Figure 3.19 (a) corresponds to 20 ML_M 3HHEDMC deposited on Ag(111) at ambient temperature. The N 1s spectrum exhibits the stoichiometric ratio of 3:1 between pyrrolic (−NH−, 399.8 eV) and iminic (−N=, 397.7 eV) nitrogen. This indicates that physical vapor deposition is able to prepare layers of intact 3HHEDMC molecules.

After deposition of 0.08 Å cobalt, spectrum (B) reveals that a new peak between

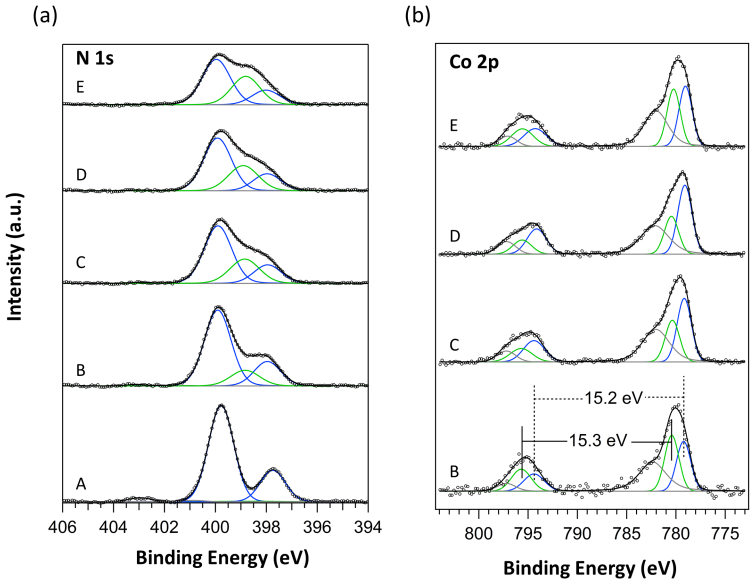

Figure 3.19: *Multilayer Metalation of Corrole on Ag(111).* Spectra of 20 ML_M 3HHEDMC on Ag(111) are shown directly after deposition (A) as well as after cobalt dosages of 0.08 Å (B), 0.28 Å (C), and 0.48 Å (D) onto the multilayer at 300 K. Annealing of the sample to 380 K for 30 minutes yields spectrum (E).

(a) The reaction is shown in the N 1s region. A new species grows at the expense of the initial ones.
Line Colors: blue – iminic and pyrrolic nitrogen of 3HHEDMC; green – reacted nitrogen.

(b) The reaction is shown in the Co 2p region. The oxidized and metallic cobalt increase upon additional dose. Further reaction occurs upon annealing.
Line Colors: blue – metallic cobalt; green – reacted cobalt; gray – satellite.

the two original nitrogen species at 398.8 eV is necessary to explain the measured data. Based on previous studies presented in this chapter, this feature is assigned to the metalated nitrogen species −NCo−.

Stepwise dosage of additional cobalt of up to 0.48 Å onto the organic layers leads to an increasing intensity of metalated nitrogen species. In contrast to the metalation of 3HHEDMC at ambient temperature on Ag(111), see Section 3.2.2, the ratio of the nitrogen species strictly matches its theoretical value for all N 1s spectra of 3HHEDMC in Figure 3.19. This leads to the conclusion that all three pyrrole groups react with the incorporated cobalt.

In order to achieve a higher metalation yield, the sample has finally been annealed to 380 K for 30 minutes. Along the expected contribution of the metalated species to the spectrum, a decrease of total intensity is observed. Since the annealing temperature is similar to the evaporation temperature of 3HHEDMC, see Table 2.2, the desorption of the metalated and pristine corroles explains this effect.

3.2.5 Oxidation State of Cobalt in CoHEDMC

The previous results suggest an oxidation state of +III for the cobalt ion in the CoHEDMC complex. However, a determination of the actual oxidation state requires a more elaborate analysis of the Co 2p core level spectra.

Figure 3.20 comprises the Co 2p spectra of multilayers of 2HTPP (bottom) and 3HHEDMC (top), after each has partially been metalated with cobalt. The spectra have been recorded at ambient temperature and with similar coverages for the organic layers and doses of the metal.

The green peaks represent the multiplet peak structure of oxidized cobalt species. The blue peaks point to residual neutral cobalt, *i.e.*, metallic, which serves as a reference for a doublet without multiplet splitting. The corresponding satellites are colored gray and not discussed in detail.

As discussed in Section 3.1.4, the multiplet splitting of the Co 2p level for the Co(II) species in CoTPP is induced by an unpaired electron spin in the Co 3d subshell. This implies that the CoTPP complex is paramagnetic. This residual spin also leads to an increased spin-orbit split of the Co $2p_{1/2}$ and $2p_{3/2}$ states compared to metallic cobalt.

The spectrum of CoHEDMC comprises the doublet corresponding to the metallic species as well. However, it is quite obvious that other features are distinctly different from the CoTPP spectrum. The multiplet structure of the oxidized species is not present anymore. This absence also infers that the investigated species is diamagnetic. The observed spin-orbit splitting is similar to the one found for metallic cobalt before.

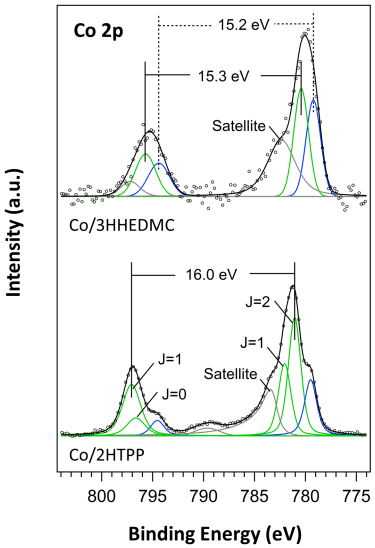

Figure 3.20: *Co 2p XP Spectra for 3HHEDMC and 2HTPP Multilayers Metalated by Cobalt.* 3HHEDMC and 2HTPP multilayers have been deposited and subsequently 0.1 Å cobalt has been added at ambient temperature, respectively. The spectra are normalized with respect to areal intensity for better comparison. The total angular momentum J is given for each peak of reacted cobalt.

(a) The Co 2p XP spectra of 20 ML_M partially metalated 3HHEDMC on Ag(111) exhibit no multiplet splitting.

(b) The Co 2p XP spectra of 10 ML_M partially metalated 2HTPP on and Al_2O_3/Al substrate exhibit a complex multiplet substructure.

Line Colors: blue – metallic cobalt; green – oxidized cobalt; gray – satellites.

Similar binding energy differences are reported for other diamagnetic Co(III) complexes in literature.[202,203]

Since CoHEDMC is diamagnetic, the +II oxidation state is ruled out. Furthermore, the complex must be low spin, which is common for square planar geometries anyway. A participation of the substrate, which led to the diamagnetism of CoPc on Cu(111), see Section 3.1.4, is excluded by the large thickness of the organic layer.

Due to the fact that cobalt prefers the oxidation state +III over the rare +I state and due to the result from Section 3.2.4 that all three pyrrole groups react, the investigated complex must be Co(III)HEDMC. A direct comparison of metallic Co(0), Co(II), and Co(III) spectra are presented with further discussion in Publication [P8].

3.2.6 Valence Band Structure of CoHEDMC and CoTPP

In addition to the exploration of the core level states, a brief overview on the valence band structure of 3HHEDMC submonolayers deposited on Ag(111) metalated by cobalt is presented here. A more detailed discussion is given in Publication [P8].

Several valence regions are shown in Figure 3.21. The spectrum of a clean Ag(111) specimen (A) exhibits the sp-band at low binding energies, the onset of the d-band at higher binding energies as well as the surface state of the Ag(111) surface close to the Fermi level. The latter feature is preserved upon deposition of cobalt as shown in spectrum (B) and quenched upon deposition of 3HHEDMC.

The organic phase causes a new feature around 1.7 eV which is attributed to its HOMO. Deposition of cobalt on the organic layer (D) leads to interaction of the metal's d_{z^2} orbital with the silver substrate's sp band under formation of two new occupied states at 1.3 eV and 0.2 eV, respectively.

These new features are similar to the valence states of iron(II)-tetraphenylporphyrin (FeTPP) on Ag(111) reported in literature.[24,204] Since Fe(II) is isoelectronic to Co(III), close similarity of the valence electronic structure is not surprising. This result also supports the assignment of the oxidation state for cobalt in CoHEDMC, see Section 3.2.5.

CoTPP deposited on Ag(111) gives rise to valence states at 1.7 eV and 0.6 eV, respectively, as shown in Figure 3.21 (E). The similar energy separation of the features in combination with the similar geometry again supports the proposed electronic interaction of the adsorbate with the substrate. Association of the new features with the organic ligand or residual cobalt atoms are excluded, since the UP spectra of the pure materials lack of peaks at the corresponding binding energies.

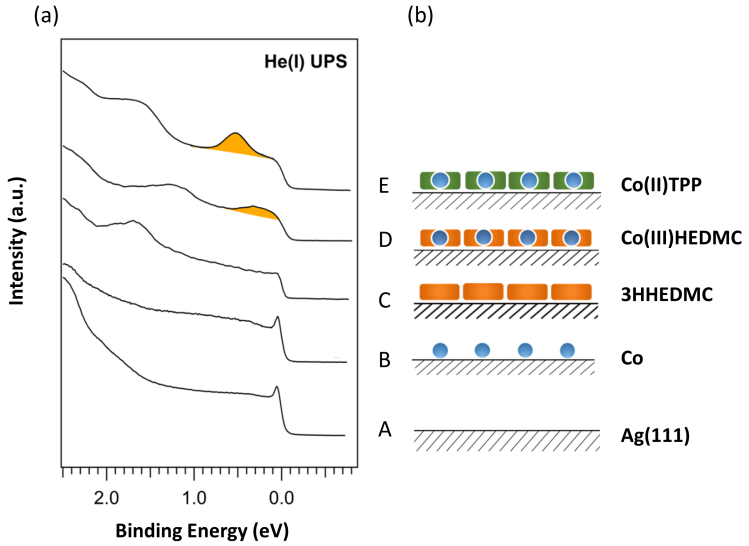

Figure 3.21: *UPS Study for Metalation of 3HHEDMC by Cobalt on Ag(111).* (A) corresponds to the clean Ag(111) surface, (B) to 0.065 ML_S cobalt on Ag(111), (C) to a 3HHEDMC monolayer, (D) to CoHEDMC *in situ* prepared by metalation of a 3HHEDMC monolayer with 0.065 ML_S cobalt, and (E) to a CoTPP monolayer prepared by direct vapor deposition of CoTPP onto the Ag(111) surface.

(a) UP spectra (He I_α– 21.2 eV) of the described situations. The additional signals attributed to the interaction between cobalt in the complex and the silver substrate are marked by orange shading. The narrow peak close to E_F in the spectra (A) and (B) corresponds to the Ag(111) surface state, which is suppressed by adsorbates in cases (C), (D) and (E).

(b) Illustrations of corresponding situations in (a) with different adsorbates, *i.e.*, cobalt atoms (blue spheres), corrole related molecules (orange), and porphyrin related molecules (green), on the silver surface (hatched). Their derived reaction products are shown as combinations of the symbols.

3.3 Metalation of 2HTPP Multilayers with Cobalt and Reaction Depth Profiling

Organic electronic devices are not based on single molecular layers[3] but use thicknesses on the nanometer scale. In order to be able to establish electrical contacts, metals are often vapor deposited on the organic layers. For performance optimization, these contacts often consist of an inert wiring part and a chemically tuned interface layer. The latter often comprises low-work function metals for improved electron injection. However, these metals are typically quite reactive and complex transition regions may be introduced. These buried interfaces might include sharp transition, chemical reactions at interfaces, and interdiffusion layers, *i.e.*, interphases, perpendicular to the interfacial plane.

In the latter cases, the metal-organic interfaces cannot be regarded as simple contacts between a metal and an organic layer anymore, but should be considered as a third layer resulting from reaction and/or diffusion. The processes taking place at those interfaces are essential for properties of organic electronic devices.

Hence, the study of metal-organic interfaces with the focus on "thick" structures, *i.e.*, multilayers, is essential. In this section, the metalation of 2HTPP by cobalt using different sample preparation processes is investigated in detail. Photoemission spectroscopy using a conventional laboratory X-ray source as well as a helium discharge lamp have been used to study the formation of the interface. Incremental deposition of cobalt renders a determination of the reaction products as a function of deposited metal possible – similar to a chemical titration. Since the structure of the interface depends on deposition parameters, the deposition rate and resting phases, *i.e.*, measurement steps, might affect the final interface.

In order to circumvent this influence, a similar interface has been prepared with a single deposition step and investigated by photoemission spectroscopy using monochromatic synchrotron radiation. The chemical composition of formed interface/interphase perpendicular to the surface is reconstructed from spectra acquired with varied photon energy. In an additional experiment, 2HTPP and cobalt have been deposited simultaneously to obtain a homogeneous reference for the reaction layer.

The specimen consist of 2HTPP deposited on cleaned naturally oxidized aluminum foil as an inert substrate and subsequently deposited cobalt.

3 An exception is given for graphene based circuits.

3.3.1 Surface Titration at Constant Photon Energy

In contrast to the discussed well-defined single-layer systems, thicker layers exhibit deviant properties. Diffusion and related processes, such as cluster growth, become more important. This raises the question about the "kinetics" during the formation of the interface.

In this experiment, a 25 nm thick 2HTPP layer has been prepared on a cleaned, naturally oxidized aluminum foil which provides an inert substrate. Cobalt atoms have been incrementally deposited at ambient temperature on the sample with constant flux and varying step sizes until a nominal thickness of 3 nm has been reached. N 1s and Co 2p X-ray photoemission as well as He I_α valence band spectra have been acquired in between the individual deposition steps. Further details are given in Publication [P10].

As shown by the N 1s spectra in Figure 3.22 (a), the spectrum of the metal-free porphyrin molecules shows two distinctive contributions. The signals originate from pyrrolic nitrogen (−NH−) at 400.9 eV as well as iminic nitrogen (−N=) at 398.9 eV, which is in line with previous XPS studies on this molecule.[14] A small shift of the features to higher binding energies is attributed to a reduced photo-hole screening due to the absence of a metallic substrate in close vicinity of the probed molecules.

Upon deposition of the initial small amount of cobalt onto the 2HTPP film at room temperature, a significant change in the N 1s spectrum occurs, *i.e.*, the minimum between the two initial peaks is shallower, which can be explained by a third peak at 399.8 eV. Based on previous studies,[14] this new peak originates from the metalation of 2HTPP molecules by cobalt atoms under the formation of CoTPP.

Further deposition of cobalt causes this new peak to grow on expense of the two original components which is indicating an ongoing metalation reaction. Concurrent to the increasing amount of cobalt, the overall intensity of the N 1s spectrum is reduced. This is attributed to signal damping due to the grown metallic overlayer. The continuation of the metalation reaction upon cobalt deposition is further supported by the Co 2p XP spectra presented in Figure 3.23. The spectrum corresponding to the lowest cobalt coverage is dominated by a complex multiplet structure. The base peaks, *i.e.*, the component with maximal J exhibiting the highest intensity, of the Co 2p doublet appear at 797.1 eV (Co $2p_{1/2}$; $J = 1$) and 781.1 eV (Co $2p_{3/2}$; $J = 2$). Based on the discussions in Section 3.2.5 and in previous studies, this doublet with a spin-orbit split of 16.0 eV is assigned to Co(II) ions.[26,202,203,205,206] This suggests that most cobalt atoms are coordinated and oxidized by the porphyrin. This correlates well with the corresponding N 1s spectra shown in Figure 3.22.

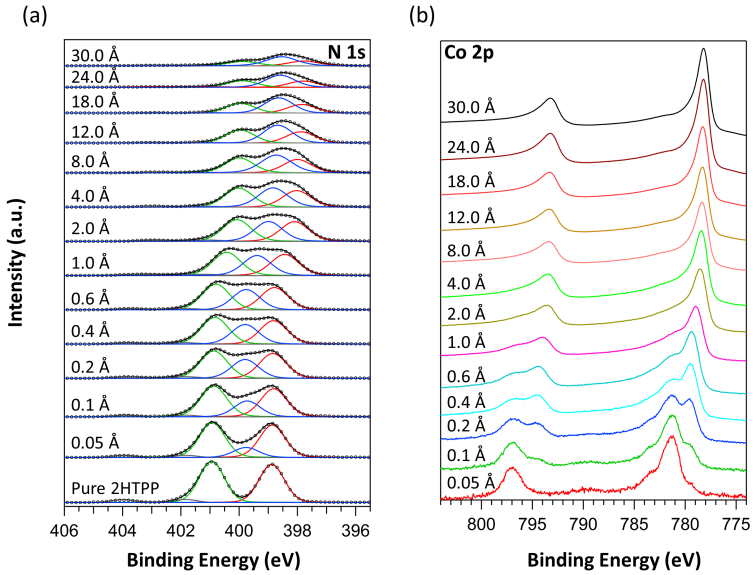

Figure 3.22: *Coverage Dependent N 1s Spectra of 2HTPP Metalated by Cobalt.* 25 nm 2HTPP have been evaporated onto a cleaned Al_2O_3/Al substrate. Subsequently, cobalt has incrementally been dosed onto the sample by e-beam evaporation. The total cobalt amount for each deposition step is displayed above the corresponding spectrum in the graph.

(a) The XP spectra presented original N 1s intensities of this experiment. The two nitrogen species in 2HTPP are damped by deposited cobalt and by a growing layer of CoTPP whose thickness initially increases with metal dosage. All nitrogen species experience dampening by the metallic cover layer at high cobalt coverages. Line Colors: green – pyrrolic nitrogen of 2HTPP; red – iminic nitrogen of 2HTPP; blue – reacted nitrogen in CoTPP; gray – satellites.

(b) The corresponding Co 2p XP spectra are normalized areal intensity for better comparison. Initially mainly reacted cobalt is observed. Upon further dosage a contribution of metallic cobalt appears and soon dominates the spectra.

Additional deposition of cobalt atoms onto this sample causes the minority species to grow. The corresponding pure doublet is located at 794.4 eV (Co $2p_{1/2}$) and 779.5 eV (Co $2p_{3/2}$) and exhibits a smaller spin split of 15.0 eV, which are typical properties for metallic cobalt. Upon further deposition of cobalt atoms for up to 3 nm, this doublet increases in intensity and finally dominates the whole spectrum as shown in Figure 3.22 (b). This indicates that this doublet originates from residual unreacted cobalt atoms. This assumption is further corroborated by the appearance of a Fermi edge at a cobalt coverage of approximately 2 Å. Details on the interpretation of the spectra are presented in Publication [P10].

Figure 3.24 also documents a pronounced binding energy shift of all features in the N 1s, Co 2p, C 1s, as well as a selected feature in the valence band region. The

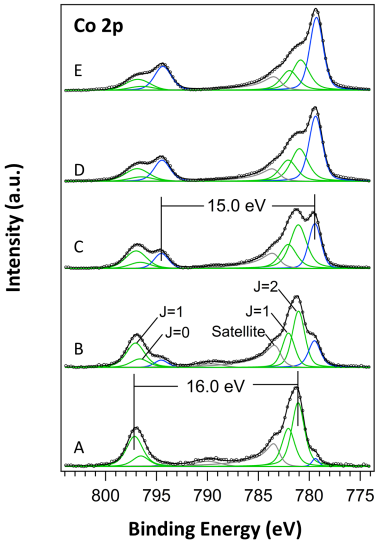

Figure 3.23: *Deconvoluted Coverage Dependent Co 2p Spectra of 2HTPP Metalated by Cobalt.* The shown spectra correspond the first five deposition steps in Figure Figure 3.22 with cobalt coverages of (A) 0.05 Å, (B) 0.1 Å, (C) 0.2 Å, (D) 0.4 Å and (E) 0.6 Å. The total angular momentum J is given for each peak of reacted cobalt. The spin-orbit split energy of the 2p orbitals is stated for the most intense sub-level of each species.

Line colors: green – oxidized cobalt; blue – metallic cobalt; gray – satellites.

relatives shifts as a function of coverage as shown in Figure 3.24 (a). All core levels as well as the examined valence state exhibit a rapid and unanimous energy shift towards lower binding energy. This effect most likely arises from upward band bending associated with long-range electron donation into the organic layers. Details are given in Publication [P10].

Under the assumption of sharp transitions between the involved layers, *i.e.*, 2HTPP, CoTPP, and metallic cobalt, their respective vertical extension of the reaction zone, *i.e.*, the thickness of the CoTPP layer, can be determined from the coverage dependent intensities of the respective N 1s species. A detailed analysis of the spectra is presented in Publication [P10].

During the deposition of the initial small cobalt amounts, the thickness of the reacted layer increases very fast. Almost all cobalt atoms coordinate with 2HTPP molecules and are oxidized. However, with increasing cobalt coverages, the formation of metallic cobalt clusters becomes the dominating effect and the reaction depth increases less. For cobalt coverages above approximately 2.5 nm, the reaction zone exhibits no significant changes and saturates at a thickness of approximately 1.9 nm.

The matching trends for the reaction thickness and the relative peak positions in

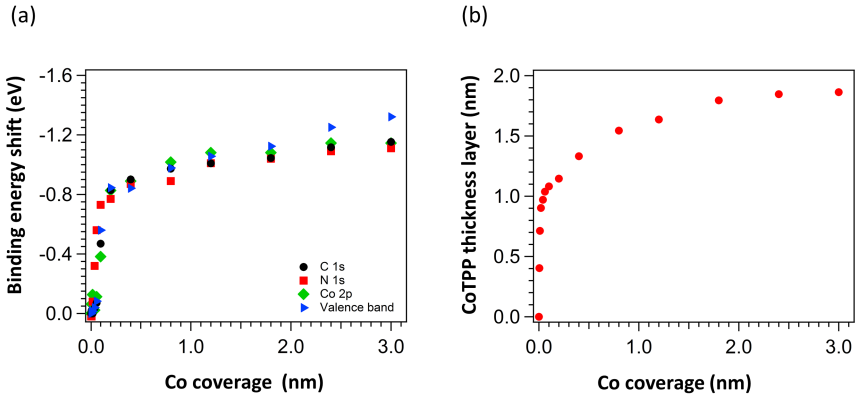

Figure 3.24: *Cobalt Coverage Dependent Quantities.* The evolution of various properties are presented as a function of cobalt coverage on the sample.

(a) The binding energy shifts of the investigated core levels and a selected valence band state are displayed as a function of cobalt coverage. The values are obtained from the individual deconvolution of the corresponding spectra.

(b) The thickness of the CoTPP layer is given as a function of cobalt coverage. The values are calculated from the corresponding N 1s spectra under the assumption of a sharp interface between the reacted CoTPP and unreacted 2HTPP layer.

Figure 3.24 both reveal that the interfacial phase is essentially formed after deposition of 0.1 nm cobalt which corresponds to a half-filled Co(0001) layer[4]. Further deposition of cobalt leads to the growth of the metallic bulk phase on top which completes the interface.

3.3.2 Depth Profiling Using Varied Photon Energy

In this section, HAXPES is used to investigate an organic-metal interphase. *Large* amounts of cobalt deposited onto a *thick* layer of 2HTPP model such a buried interphase. The experiments concerning this topic have mainly been performed at the HIKE end-station, see Section 2.4.3.

As explained in Section 2.1.2, the increased kinetic energy of the photoelectrons due to heightened excitation energy leads to an enlarged information depth. Since HAXPES is also a non-destructive technique, it is predestinated for the investigation of the chemical environments in multilayered systems such as buried interfaces. This study employes hard X-ray synchrotron radiation with energies from 2 keV to 6 keV in steps of 1 keV. In contrast to Section 3.3.1, the organic-metal interface has been established in one deposition step using the same deposition rate as in the previous experiment.

4 This value is derived from the interplanar distance of two (0001) planes in bulk cobalt of 203 pm.

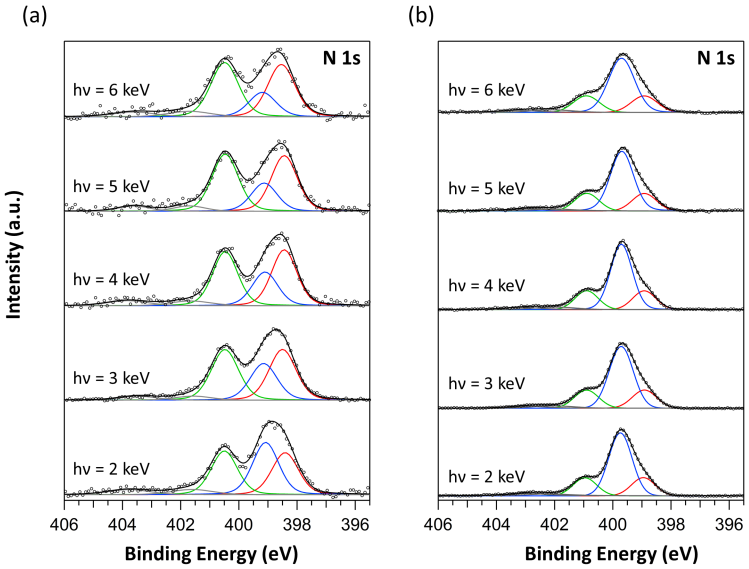

Figure 3.25: *Energy Dependent N 1s Spectra of 2HTPP Metalated by Cobalt.* N 1s spectra of two samples comprising 2HTPP and cobalt with complementary preparation are recorded using different photon energies. For better comparison of the shape, all N 1s spectra are normalized by areal intensity. Both specimen have been prepared on a cleaned, naturally oxidized aluminum substrate.

(a) 1.8 nm cobalt have been deposited onto 12 nm 2HTPP in one step. The fraction corresponding to the reacted nitrogen shows a pronounced dependency on the photon energy.

(b) 40 nm 2HTPP and 1 nm cobalt are simultaneously deposited onto the substrate. The fraction corresponding to the reacted nitrogen shows no dependency on the photon energy.

Line Colors: green – pyrrolic nitrogen of 2HTPP; red – iminic nitrogen of 2HTPP; blue – reacted nitrogen in CoTPP; gray – satellites.

The excitation energy dependent spectra of a sample comprising 12 nm 2HTPP coated with 1.8 nm cobalt are shown in Figure 3.25 (a). Between the two original pyrrolic (−NH−, green) and iminic nitrogen (−N=, red) species, a third peak (−NCo−, blue) raises, which is attributed to the metal-containing complex, *i.e.*, CoTPP. Along an increase in photon energy, the portion of the CoTPP-related peak is decreasing while the relative intensity of the pristine species grows.

This observation can readily be explained under the obvious assumption of a layered system. As explained in Section 2.1.4, a higher excitation energy leads to a larger probing depth. As a result, the detector "sees" more unreacted species in deeper layers. This already proves the intrinsic inhomogeneity of the sample itself.

The vertical chemical composition of the sample can be quantified by examination of the ratio of the intensities corresponding to *reacted* and *unreacted* molecules, which

are proportional to the fitted areas of the related features. Analysis of the spectra yields a reaction depth of approximately 1.4 nm, which agrees well with simulations by SESSA [207–209] (Simulation of Electron Spectra for Surface Analysis) and another straight-forward numerical simulation. However, the incremental deposition of cobalt yields a slightly thicker reaction zone. This discrepancy might be explained by the differences in the deposition methods. Since the initial increments in cobalt coverage are rather small, reaction could have been favored in this case. In addition, the time needed to acquire the XP spectra could provide additional diffusion of metal atoms or deposited molecules. Furthermore, the surface morphology, *i.e.*, roughness, might differ slightly between the samples and influence the reaction depth. The detailed analyses are presented in Publication [P9].

As reference for a possible interphase formed between cobalt and 2HTPP, HAXPES data of a homogeneous sample have been obtained. The pure interphase has been prepared by simultaneous deposition of 40 nm 2HTPP and 1 nm cobalt, resulting in an 1.5-fold stoichiometric amount of cobalt. The corresponding spectra are displayed in Figure 3.25 (b). The spectrum is dominated by peak at 399.7 eV, which is attributed to the metalated nitrogen species (−NCo−, blue), while the other two surrounding peaks are assigned to unreacted pyrrolic (−NH−, 400.9 eV, green) and iminic (−N=, 398.9 eV, red) nitrogen species, respectively.

The peak shapes and the corresponding intensity ratios are constant within the accuracy of the experiment. This confirms the presence of a homogeneous composition and that bulk synthesis of a metalloporphyrin has been achieved. Considering the used amounts of substance and the peak intensities, one can conclude that further *side reactions* occur. On the one hand, the formation of metal clusters in the organic matrix is possible. On the other hand, a reaction of cobalt with the residual gas in the system is possible. The latter possibility is corroborated by the corresponding Co 2p spectra, see Publication [P9] but not analyzed in detail.

Comparison of the results from these two experiments demonstrates that a non-destructive, *i.e.*, *sputtering free*, depth profiling is possible using HAXPES. This renders the investigation of organic-electronic devices comprising metal-organic interface or/and interphase possible. In contrast to the established erosive methods, here a detailed and systematic investigation without sample damage is possible and allows for a rational design of organic electronic devices.

3.4 HAXPES Study of a Coated Cathode for Lithium-Ion Batteries

Apart from the systematic investigations of well-defined layered samples, as shown for metal-organic interfaces and interphases in Section 3.3.2, HAXPES can also provide useful information in more applied systems. One application has been the compositional analysis of an advanced layered electrode which could be used to improve lithium-ion batteries. The investigations have been carried out in cooperation with the group of Prof. Dr. Bernhard Roling at the University of Marburg.

This section gathers the results related to the high kinetic energy photoemission investigations. Their focus lies on determination of the vertical chemical constitution of the surface near region of the specimen. In addition to the elemental composition, an assignment of the individual oxidation states is realized. Publication [P12] provides results from complementary techniques as well as a more detailed description of the sample preparation and the individual analysis procedures.

In this project, a thin-film $LiNi_{0.5}Mn_{1.5}O_4$ (LNMO) cathode coated with $Li_4Ti_5O_{12}$ (LTO) has been electrochemically cycled in a battery electrolyte. The prepared specimen has been investigated by HAXPES with photon energy varied between 2 keV and 6 keV in steps of 1 keV resulting in the spectra shown in Figure 3.26. As discussed in Section 2.1.4, an increased photon energy, and thus raised kinetic energy of emitted photoelectrons, leads to an enhanced inelastic mean free path of these electrons. As a consequence, the information depth becomes a function of excitation energy and non-destructive profiling of the LTO coating becomes possible. The used photon energy in the range of 2 keV to 6 keV allows for a variation of the probing depth between 6 nm and 20 nm.

Quantitative analysis of O 1s, C 1s, and F 1s spectra (not presented here, see Publication [P12]), revealed that the cathode was covered with a 3 nm thick residue originating from the electrolyte. It consists of organic polymers (90 %), metal fluorides, and fluorophosphates which could not be removed by the cleaning procedure after the electrochemical preparation.

A possible mechanism for the origin of this surface layer is presented in Publication [P12] and briefly described here. Ring opening of ethylene carbonate is catalyzed by phosphorous pentafluoride and leads to poly(ethylene carbonate) and poly(ethylene oxide) related decomposition products. The catalyzing strong Lewis-acid originates from the cell's electrolyte, *i.e.*, lithium hexafluorophosphate.

According to the preparation procedure,[39] the LTO layer with a thickness of 400 nm is closed. Since its thickness exceeds the maximal information depth of the used setup

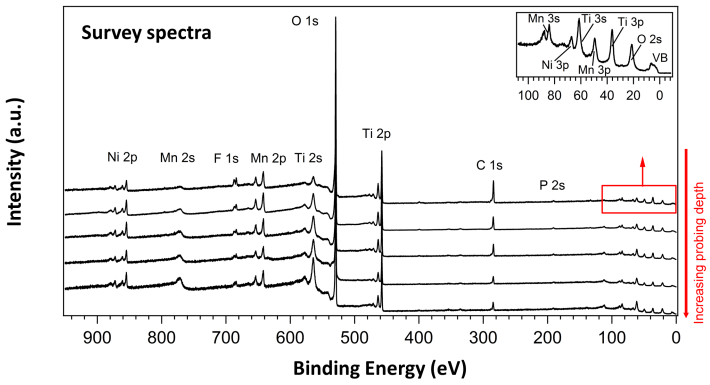

Figure 3.26: *Hard X-Ray Photoemission Survey Spectra of an LTO Coated LNMO Electrode.* Survey spectra of the electrochemically cycled LTO coated LNMO cathode have been acquired using several excitation energies from 2 keV (top) to 6 keV (bottom) in steps of 1 keV. The evolution of the peak intensities of the individual species (assigned in the graph) is correlated to the amount of the observed species. The spectra are normalized by their total areal intensity. Graph is taken from Publication [P12].

by far, the LMNO layer should not contribute to the XP spectra. However, the Ti(IV), Ni(II) and Mn(IV) oxides are found in the the coating layer. Due to the tempering step in the sample preparation and the compatible crystal structures, a uniform mixture of the oxides can be assumed, as shown in Figure 3.27. Applying charge equalization by unobservable lithium ions yields the empirical formula $Li_{1.1}Ni_{0.24}Mn_{0.40}Ti_{1.2}O_4$. The presence of manganese and nickle in the near-surface region indicates that these elements diffuse from the LMNO layer into the LTO coating layer.

The last step assumes that all metal cations have the same oxidation states as in LNMO and LTO. Since the specimen experienced electrochemical charging and discharging, a preservation of the oxidation states is not self-evident. The oxidation state of the involved transition metals, *i.e.*, titanium, nickel, and manganese, have been verified by careful analysis of the related photoemission core level spectra, *i.e.*, Ti 2p, Ni 2p, Mn 2p, and Mn 3s.

Although the primary photoemission lines are sufficient to identify the elements in a sample, their positions are sometimes not characteristic enough to determine the oxidation state. This situation gets even more complicated due to secondary effects, such as shake-up or plasmon loss structures or multiplet splitting. Thus, binding energies corresponding to peak maxima should not be used as a basis to assign chemical states, especially for transition metals.

Comparison of characteristic features, such as satellites and doublet separation energies, with those of defined compounds can provide further insight into the chemical

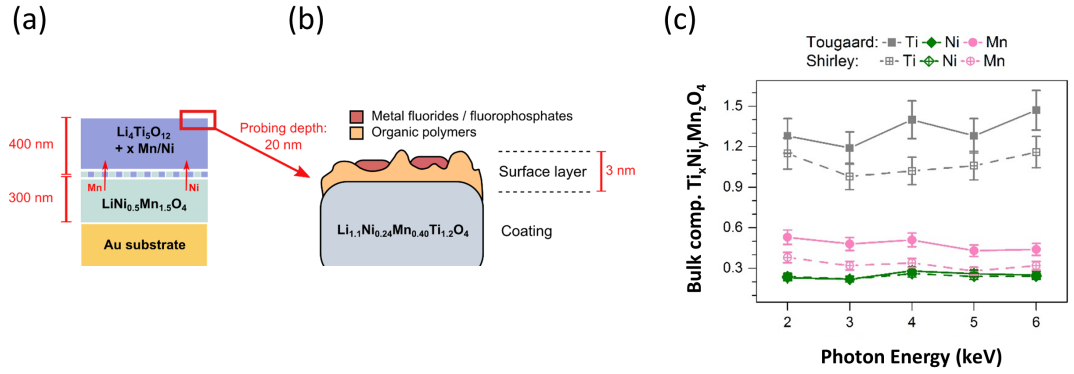

Figure 3.27: *Composition of the LTO Coated LNMO Electrode.* Depth profiles on two scales of the LTO coated LNMO cathode for improved lithium-ion batteries are illustrated and quantified. Figures are taken from Publication [P12].

(a) The idealized large-scale depth profile on the basis of ToF-SIMS data[39] is presented for the sample after the heating step. Nickel and manganese ions diffuse into the LTO top layer.

(b) The detailed near-surface depth profile derived from HAXPES is illustrated. The diffused ions from (a) are distributed homogeneously in the range of probing depth. The cathode is covered by a thin layer consisting of organic polymerized electrolyte decomposition compounds.

(c) The bulk composition $Ti_xNi_yMn_zO_4$ of the coating layer is given as the relation of the relative intensities of the transition metals to the relative intensity of the O 1s oxide signal as a function of photon energy. The relative intensities have been have been corrected by application of a Shirley or a Tougaard background model, respectively. The absence of major composition changes as a function of photon energy, and thus probing depths, indicates a homogeneous vertical composition.

state of the transition metal ions. A full assignment of the species has been achieved in this study by thorough deconvolution of the complex Ti 2p, Ni 2p, and Mn 2p spectra and extensive comparison with reported spectroscopic data.[210–219] Details about the analysis and the specific features are given in Publication [P12].

The diffusion of nickel and manganese ions leads to a doping of the LTO layer. Since both species exhibit an open d-shell – Ni^{2+} (d^8) and Mn^{4+} (d^3) – in this material, they could increase the electronic conductivity of the coating significantly. As a consequence, this effect might explain the very low impedance of the coating material found by previous studies.[39]

The discussion of aspects leaving the photoemission spectroscopy focus can be found in Publication [P12].

3.5 Surface-Assisted Ullmann Coupling Reaction

In Section 3.1, a variety of interactions between organic molecules and a copper substrate have been investigated employing different techniques. It turned out that copper can play a twofold role there. On the one hand, the investigated Cu(111) surface provides a strong interaction to the adsorbed molecules. On the other hand, mobile add-atoms, present on the surface as a two-dimensional gas phase, can serve as reactants and metalate the adsorbate.

Copper atoms also participate in the Ullmann coupling reaction which is known since 1901.[40] Since copper is utilized in its metallic form, it is likely this reaction also occurs on the surface. This part of the presented thesis addresses a surface science based investigation of the Ullmann coupling reaction with complementary techniques. The discovery of self-assembling of the investigated oligophenylene bromides on Cu(111) and Ag(111) motivated a detailed investigation of the produced organic macrocycles. The formation of carbon-carbon bonds yields stable regular structures on the surface inducing quantum effects on the corralled surface area.

3.5.1 Surface Science Investigation of the Ullmann Coupling Reaction

The here presented work has been carried out in cooperation with the group of Prof. Dr. Nian Lin (STM) at the Hong Kong University of Science and Technology as well as the groups of Prof. Dr. Hans-Peter Steinrück (XPS, UPS) and PD Dr. Wolfgang Hieringer (DFT) at the Friedrich-Alexander-Universität Erlangen-Nürnberg. In this project the adsorption and reaction of DB*p*TP (Figure 3.28) and TBB (Figure 3.29) on Cu(111) surface have been studied with XPS, UPS, and STM. DFT calculations provide additional input to the understanding of the observed intermediate structures, see Publication [P2]. Since both substances show similar reactivity towards the copper substrate and exhibit almost identical spectra, the results from photoemission spectroscopy are discussed together.

Figure 3.28: *4,4″-Dibromo*-para-*terphenyl (DB*p*TP).* This building block comprises two reactive bromide groups on the terminal position of the linear terphenyl isomer. Depending of the properties of the node it can form chains or networks.

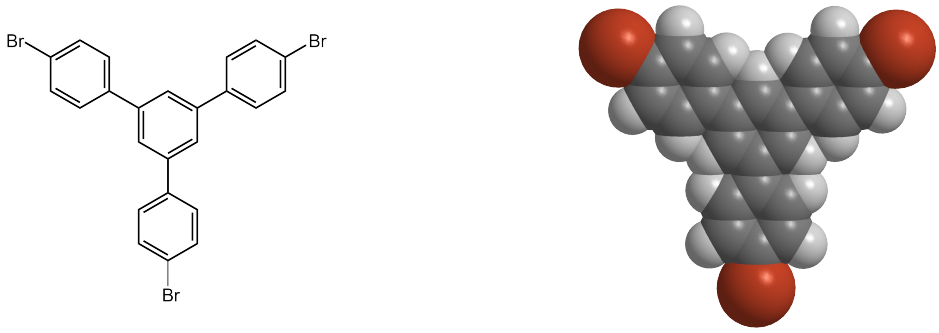

Figure 3.29: *1,3,5-Tris(4-bromophenyl)benzene (TBB).* This compound exhibits three reactive bromide groups and forms two-dimensional coordination networks.

Deposition of submonolayer coverages onto the copper crystal at 170 K leads to formation of a metal-organic networks. The larger linker TBB forms small irregular islands on the surface, see Publication [P2]. In contrast, the linear linker forms a regular network on the surface of slightly deformed hexagons. In this case, three individual molecules are held together by hydrogen bonding.[46] In both cases, the deposited molecules seem intact on the STM pictures.

The corresponding Br 3p spectra at low temperature, exemplarily shown for DB*p*TP, see Figures 3.30 (a) and 3.32 (a), exhibit a pure doublet structure[5] with the $J = {}^{3}/_{2}$ component located at 184.1 eV. This finding is corroborating the assumption that the molecules remain intact.

Heating of monolayer coverages of DB*p*TP and TBB to 240 K leads to a complete conversion of the adsorbed molecules by complete dissociation of the carbon-bromine bond. An activation energy for the bond cleavage can be estimated from these two temperatures and ranges from 47 $^{\mathrm{kJ}}/_{\mathrm{mol}}$ to 67 $^{\mathrm{kJ}}/_{\mathrm{mol}}$. This estimate is considerably lower than the corresponding dissociation energy of bromobenzene in the gas phase of 297 $^{\mathrm{kJ}}/_{\mathrm{mol}}$.[220] However, the obtained activation energy agrees well with the theoretical value of 64 $^{\mathrm{kJ}}/_{\mathrm{mol}}$ reported for dissociation on copper.[221] The chemical nature of this conversion is discussed later in the case of adsorbed multilayers.

Increasing the temperature to 300 K (DB*p*TP) or 393 K (TBB) leads to an insertion of copper atoms between the biradical terphenyl units, as STM investigations[46] reveal, see Figures 1.2 and 3.31 (a). Further annealing to 470 K of these organometallic oligomers results in the formation of carbon-carbon bonds. Depending on the monomers, either polymer chains (DB*p*TB) or covalent two-dimensional networks (TBB) are generated. The formation of the carbon bonds involves an elimination of copper from the intermediate. The resulting structure is shown in the STM topograph

5 Since the analysis focuses on the $3p_{3/2}$ component, the second part of the doublet is only partially recorded and not discussed here.

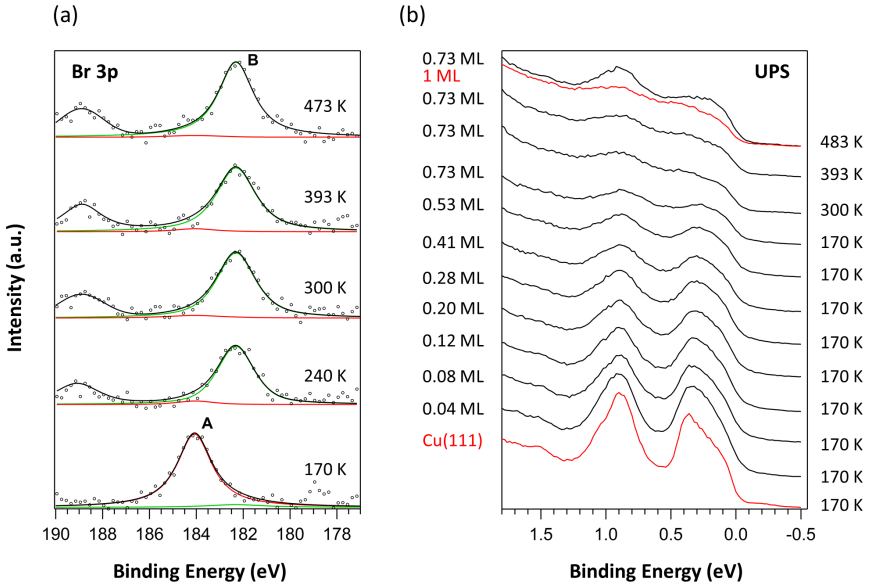

Figure 3.30: *Reaction of DBpTP Submonolayers on Cu(111) Studied by XPS and UPS.* DB*p*TP is deposited on Cu(111) at 170 K and subsequently annealed to the indicated temperatures for two minutes and then cooled down to 300 K for XPS measurement. Graphs are adapted from Publication [P2].

(a) Br 3p spectra of DB*p*TP with an initial coverage of $\theta = 0.041\,\mathrm{ML_S} = 0.9\,\mathrm{ML_M}$ show a full conversion of the bromine containing group between 170 K and 240 K and no desorption at elevated temperatures.

(b) He I_α UP spectra of the stepwise adsorption and annealing of DB*p*TP on Cu(111) are shown. The surface state of the clean surface (bottom, red) is quenched with increasing coverage. At a total coverage of $\theta = 0.032\,\mathrm{ML_S} = 0.73\,\mathrm{ML_M}$ the sample is annealed and the surface state partially recovers. For better comparison, a UP spectrum with a complete DB*p*TP monolayer is added (top, red).

in Figure 3.31 (b). Neither the Br 3p nor the C 1s spectra show pronounced changes for sample temperatures above 240 K. The corresponding spectra are given in Publication [P2].

Several He I_α UP spectra taken during the adsorption of DB*p*TP on Cu(111) are presented in Figure 3.30 (b). The clean copper surface exhibits the surface state and the phantom peak originating from excitation of Cu 3d electrons with He I_β radiation, see Section 3.1.4. The surface state is only partially quenched during adsorption, since the adsorbate forms islands on the substrate.

After incremental deposition of $0.032\,\mathrm{ML_S} = 0.73\,\mathrm{ML_M}$ DB*p*TP, the sample is heated to ambient temperature resulting in a further decrease of intensity which could be attributed to a minor rearrangement of the adsorbate. Upon annealing to 483 K, the surface state recovers due to a reduction of the covered area as a consequence of the

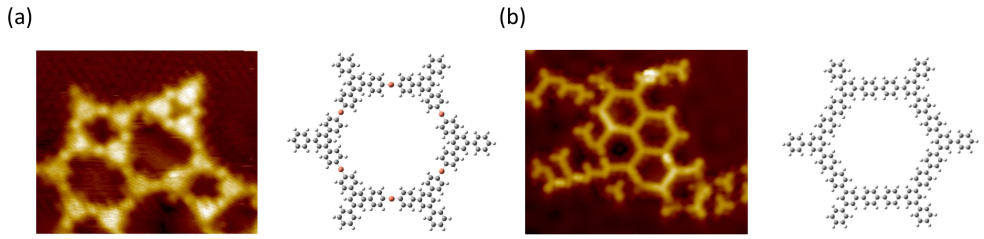

Figure 3.31: *Surface-Assisted Ullmann Coupling Reaction of TBB Molecules on Cu(111).* STM topographs (left) and their corresponding model structures (right) are shown for adsorption of TBB on Cu(111) after annealing to two different temperatures. Graphs are taken from Publication [P2].

(a) The organometallic network with C-Cu-C is formed by annealing to 393 K. The coordination network is flexible and irregular. Copper atoms between the monomers are shown in red.

(b) The organic covalent network is formed by annealing to 473 K exhibiting regular hexagonal structures.

reaction of the adsorbate, as shown in Figure 1.2. This behavior is obvious since the organometallic network with copper bridges certainly needs more space than the corresponding metal free covalent structure. The covalent island formation, which leads to areas on the Cu(111) surface partially free of adsorbates, hence leads to a local recovery of the surface state.[46] This recovery is not observed in case of a fully covered (1 ML_M) sample. Similar to spectra of DB*p*TP on Cu(111) at (sub)monolayer coverages, see Figure 3.30 (a), the Br 3p spectra for a coverage of 4 ML_M exhibit a single doublet at 170 K, see Figure 3.32 (a). The Br $3p_{3/2}$ peak of the pristine molecule located at 184.4 eV (labeled A) is slightly shifted to higher binding energies due to reduced screening of the core hole by the surface.

With increasing temperature, a second peak at 182.2 eV (labeled B) appears and is assigned to bromine detached from the molecule and attached to the surface. In contrast to the monolayer case where the conversion is finished at 240 K, higher temperatures are necessary for a complete reaction of all adsorbed molecules. Between 240 K and 473 K the intensity of the signal related to the detached bromine grows at expense of the intensity of the original bromine species, *i.e.*, no desorption of bromine containing species occurs.

Considering that the first layer of the multilayer can react at 240 K, one must assume that the copper surface plays an important role in scission of the carbon-bromine bond. A rough estimate of the Br $3p_{3/2}$ intensity of the pristine and reacted bromine suggests that the layer in direct contact with the surface has reacted at this temperature. Regarding the results from 2HTPP multilayer metallation (Section 3.3), diffusion of

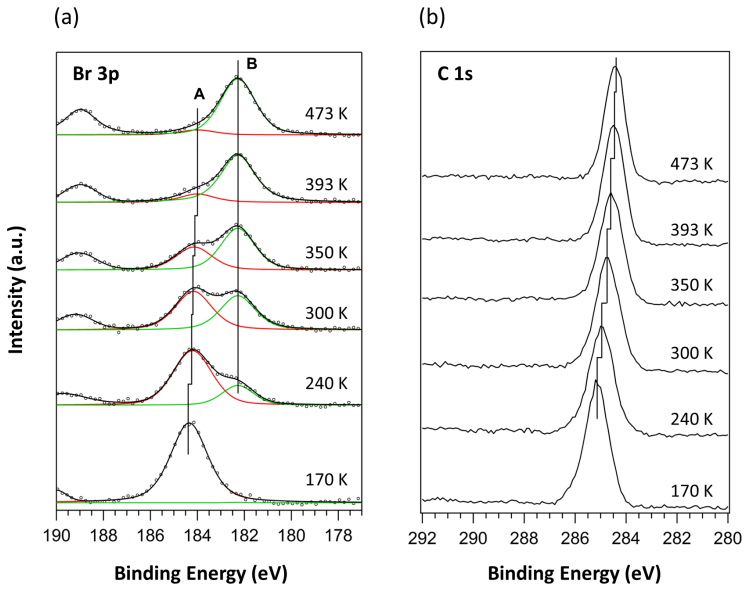

Figure 3.32: *Reaction of DBpTP Multilayers on Cu(111) Studied by XPS.* $\theta = 0.18\,\mathrm{ML_S} = 4\,\mathrm{ML_M}$ DB*p*TP are deposited on Cu(111) at 170 K and subsequently annealed to the indicated temperatures for two minutes and then cooled down to 300 K for XPS measurement. The shift in binding energy for bromine and carbon originates from a work function change caused by bromine atoms on the surface. Neither carbon nor bromine containing fragments desorb. Graphs are adapted from Publication [P2].

(a) The initial Br 3p spectrum only shows species A representing intact molecules. Upon annealing, species B is formed due to detachment of bromine atoms and their adsorption on the surface.

(b) The C 1s spectra of DB*p*TP only show the binding energy shift.

the unreacted molecules to the surface seems plausible.

Figure 3.32 (b) shows that the C 1s peak shifts monotonously towards lower binding energy with increasing temperature. A quantitative analysis reveals that the shift is proportional to the relative intensity of the Br 3p signal for detached bromine atoms (B) for up to 0.8 and saturates at higher ratios.

This can be explained by the fact that bromine atoms on a Cu(111) surface are known to increase its work function. The intact molecules and the central phenylene group of the molecules interact only weakly with the surface, *e.g.*, *via* van der Waals forces. The vacuum level is an appropriate reference level for molecules without direct contact to the metallic substrate or with other weak interaction. Hence, the binding energies of the corresponding core levels, *i.e.*, C 1s and Br $3p_{3/2}$ (A), are pinned to the vacuum level and appear to be shifted to lower binding energies when referenced to the Fermi level. Concurrently, the peak of chemisorbed, *i.e.*, strongly interacting,

bromine on the surface (B) stays at constant position, since it is pinned to the Fermi level.

An analogue discussion addressing the adsorption of TBB is given in Publication [P2].

In addition to the presented core level studies, the valence band region of the mentioned molecules has been investigated by UPS. Figure 3.30 (b) shows the spectra of stepwise adsorption of DB*p*TP on Cu(111). The surface state at 0.3 eV of the clean surface gets almost completely quenched with increasing coverage of the adsorbed molecule. In contrast to the adsorption of 2HTPP, see Section 3.1.2, this state does not vanish completely. This observation is attributed to large areas on the crystal without adsorbed molecules.

At a total coverage of 0.73 ML_M the sample is annealed to 483 K leading to a partial recovery of the surface state. Comparison with the UP spectrum of a complete DB*p*TP monolayer reveals that a recovery of the surface state requires some unoccupied surface area.

The observation of reacting multilayers on the Cu(111) surface raises the question about the corresponding reaction mechanism. Since the reaction take place at low temperature in case of submonolayer coverages, the activation barrier for this reaction step is low. In order to explain a full reaction of thicker, *i.e.*, multimolecular, layers, a diffusion process is necessary to deliver unreacted molecules to the surface. Since molecules become more mobile at elevated temperatures, such a process seems possible. Once a molecule gets into contact with the surface, the carbon-bromine bond is cleaved by the now accessible copper substrate.

3.5.2 Surface-Assisted Organic Synthesis of Honeycombenes

The here presented work has been carried out in cooperation with the group of Prof. Dr. Kai Wu and Dr. Yongfeng Wang (STM, STS) at Peking University as well as the group of PD Dr. Wolfgang Hieringer (DFT) at the Friedrich-Alexander-Universität Erlangen-Nürnberg.

Inspired by the finding that TBB is able to form self-arranged hexagonal structures on a silver surface, more suitable precursors have been employed. The first criterion of such a molecule is certainly the terminal bromophenyl groups used for the surface-assisted Ullmann reaction. Since linear coupling is observed for the linear building block DB*p*TP, the 120° angles for hexagons should be provided by the molecule as a second factor. Furthermore, a variation of target molecule's size is desirable.

Figure 3.33: *4,4″-Dibromo*-meta-*terphenyl (DB*m*TP).* This compound is similar to DB*p*TP, see Figure 3.28, and exhibits two reactive bromide groups as well. The *meta* substitution pattern of the central phenylene group allows the formation of intermolecular nodes in regular patterns which provides access to arrays of zigzag-shaped polymers and small hexagonal nanotroughs (*honeycombenes*) upon annealing.

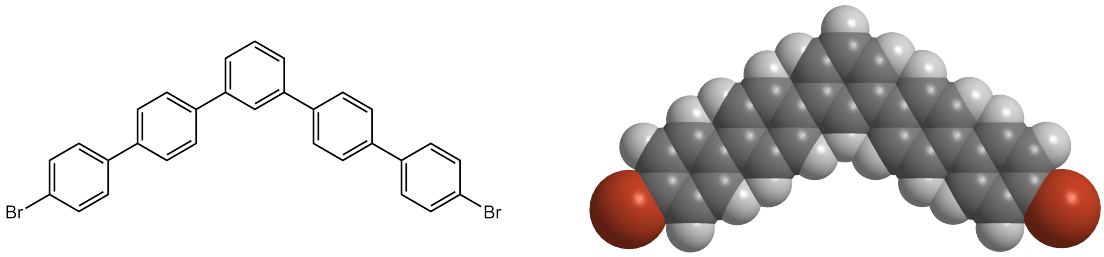

Figure 3.34: *4,4″″-Dibromo*-meta″-*quinquephenyl (DB*m″*QiP).* This compound has an analog structure to DB*m*TP, but contains one additional phenylene unit in each arm. The *meta* substitution pattern of the central phenylene group allows the formation of intermolecular nodes in regular patterns which provides access to arrays of zigzag-shaped polymers and large hexagonal nanotroughs (*honeycombenes*) upon annealing.

Alteration of the *para* substitution pattern of the central phenylene unit in DB*p*TP to *meta* substitution preserves the reactive end groups and provides the necessary

bent in DB*m*TP (Figure 3.33). In order to tune the size of the product, phenylene *extension* groups are inserted in both arms of this molecule generating DB*m*″QiP (Figure 3.34). The experiments involving an asymmetric extension are discussed in Section 3.5.3.

XPS Investigations

Two slightly different submonolayer coverages of the precursor DB*m*TP have been vapor deposited on silver substrates cooled to 80 K. Figure 3.35 opposes the results from two substrate preparation sequences. Part (a) uses sputtering to clean the sample and annealing to heal defects in the Ag(111) surface. In order to tune the surface reactivity, part (b) employs the sputter cleaning process only. This preserves reactive sites, *i.e.*, hole defects and adatoms, on the surface.

The pure Br 3p doublet (Br $3p_{1/2}$ at 190.4 eV and Br $3p_{3/2}$ at 183.8 eV) visible at the lowest temperatures in Figure 3.35 (a) is attributed to intact DB*m*TP molecules. After raising the sample temperature to 300 K, a new doublet appears on the low

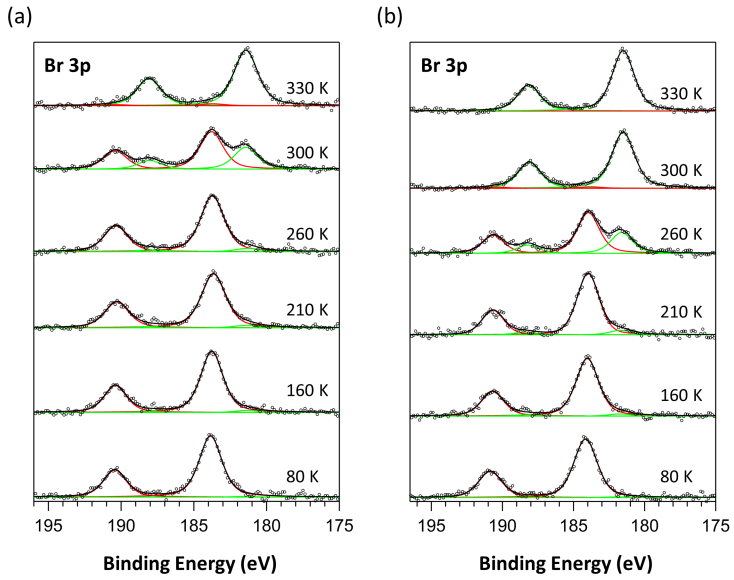

Figure 3.35: *XPS Study of DBmTP on Ag(111).* Normalized Br 3p spectra of DB*m*TP on Ag(111) with different surface preparation methods are opposed. Submonolayer coverages of DB*m*TP are adsorbed at low temperature and heated to the indicated temperatures.

(a) The substrate cleaned by sputtering and subsequent annealing to 760 K shows reaction with $\theta = 0.021\,\mathrm{ML_S} \approx 0.38\,\mathrm{ML_M}$ DB*m*TP at 300 K.

(b) The substrate cleaned by sputtering yet without subsequent annealing shows reaction with $\theta = 0.007\,\mathrm{ML_S} \approx 0.13\,\mathrm{ML_M}$ DB*m*TP at lower temperature, *i.e.*, 260 K.

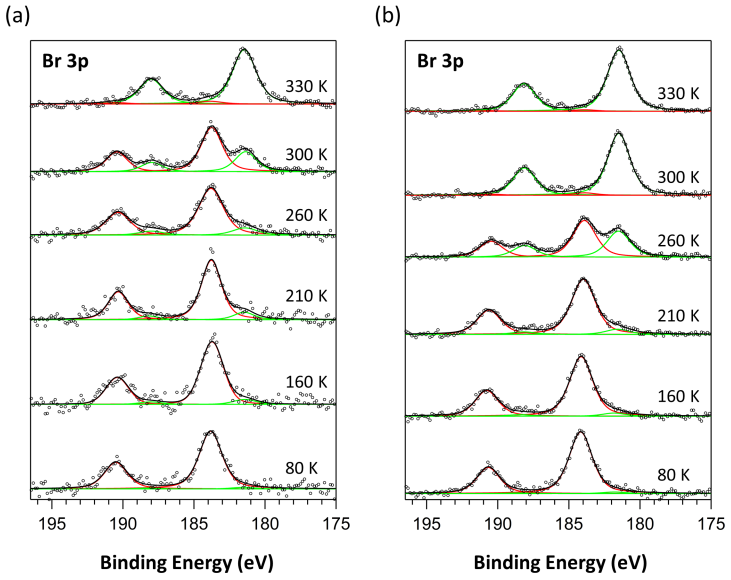

Figure 3.36: *XPS Study of DB*m″*QiP on Ag(111).* Normalized Br 3p spectra of DB*m*″QiP on Ag(111) with different surface preparation methods are opposed. Different coverages of DB*m*″QiP are adsorbed at low temperature and heated to the indicated temperatures.

(a) The substrate cleaned by sputtering and subsequent annealing to 760 K shows significant reaction with $\theta = 0.016\,\mathrm{ML_S} \approx 0.53\,\mathrm{ML_M}$ DB*m*″QiP at 300 K.

(b) The substrate cleaned by sputtering yet without subsequent annealing shows reaction with $\theta = 0.076\,\mathrm{ML_S} \approx 2.53\,\mathrm{ML_M}$ DB*m*″QiP at lower temperature, *i.e.*, 260 K.

binding energy side shifted by 2.3 eV. Based on the previous study presented in Section 3.5.1, this change is attributed to carbon-bromine bond scission and formation of chemisorbed bromine species on the silver surface. An increase in temperature to 330 K causes substantial changes in the observed spectrum again. The initial doublet at higher binding energy almost disappears. This indicates that the cleavage reaction is completed and all bromine is attached to the surface.

For comparison of the surface's influence on the reactivity, DB*m*TP molecules have been deposited onto the simply sputtered Ag(111) sample. The observed results, shown in Figure 3.35 (b), are similar to the previous case in (a). However, all binding energies are shifted by 0.3 eV towards higher values. In addition, the carbon-bromine bond scission starts at lower temperature. Complete conversion of the deposited layer on the sample is achieved already at ambient temperature (300 K). The latter result is not surprising since defects sites are known to exhibit higher reactivity. This leads to the obvious conclusion, that defect sites play a role in the reaction mechanism. The altered peak positions most likely originate from final state effects such as reduced

screening effects presumably due to the rougher surface.

A very similar study has also been performed utilizing DBm''QiP. The substrate has been prepared in the same way as described for DBmTP. Again, approximately 0.5 ML_M educt have been deposited[6] on the annealed surface. The results of the larger adsorbate DBm''QiP, shown in Figure 3.36, reproduce the ones gained from the smaller analogon DBmTP exactly. This verifies that the extension groups only affect the size of the precursor.

Further details are given in Publication [P11].

STM Topography and dI/dV Mapping

The previous part confirmed the expected chemical properties of the precursor molecules as well as the reaction products. In order to characterize the shape of the resulting molecules, STM investigations have been performed. In addition to the pure topography, see Figure 3.37, also dI/dV maps have been acquired, see Figure 3.38, as well as tunneling spectra (not shown here, see Publication [P11]). This part only summarizes the essential results from these investigations to draw a general conclusion. Further results and a more detailed discussion are given in Publication [P11].

The basic scheme of the used Ullmann coupling reaction is drawn in Figure 3.37 (a). The intact precursor molecules are deposited on the surface. As can be seen in Figure 3.37 (b), the DBm''QiP molecules form a long-range ordered supramolecular network at room temperature. The molecules are arranged through quartet nodes formed by a combination of halogen/hydrogen (Br···H) bonds and constructive interaction between the halogen atoms (Br···Br).[47,222]

Annealing of the sample to 640 K results in a detachment of the bromine atoms as shown by XPS in the previous part and formation of carbon-carbon bonds. As has been proven before,[50,51] this procedure can provide a novel class of giant oligophenylene macrocycles with a defined number of monomers. This solvent-free synthesis renders solubility-enhancing alkyl side groups unnecessary and yields an extremely pure product on the surface.

The use of low temperature STM allows for verification of the formed geometry on an atomic scale. A representative STM topography with the corresponding unit cell (overlay) is depicted in Figure 3.37 (c) for cyclotriacontaphenylene ($C_{180}H_{120} = (C_6H_4)_{30}$), called [30]-*honeycombene*. The name arises from the arrangement of hexagonal pods resembling honeycombs and the number of phenylene monomers. Apparently, an

6 Note that the definition of one molecular monolayer implies the size of the regarded molecule and hence the number of molecules in a monolayer is altered.

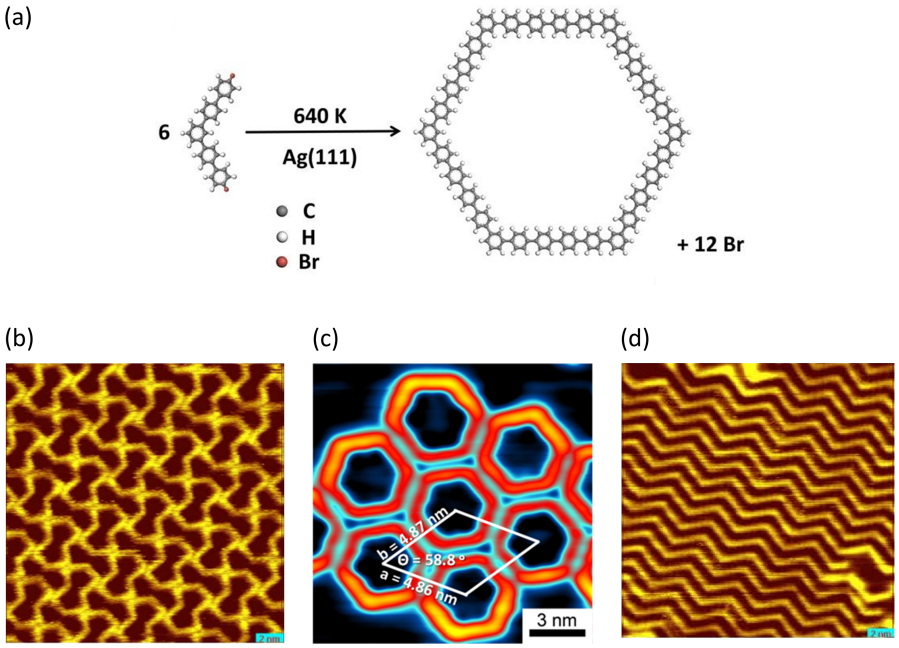

Figure 3.37: *Ullmann Coupling Reaction of DB*m″*QiP on Ag(111).*

(a) Reaction scheme for the synthesis of [30]-honeycombene from 4,4‴″-dibromo-meta-quinquephenyl (DB*m*″QiP) using a Ag(111) substrate in a modified Ullmann reaction.

(b) STM topograph of DB*m*″QiP on Ag(111) adsorbed at 300 K and imaged at 78 K. Tunneling parameters: $U = 0.6$ V, $I = 0.5$ nA. Four molecules are joined with one end each in a node forming a regular pattern on the surface.

(c) STM topograph of an island comprising [30]-honeycombene molecules, imaged at 78 K. The macrocycles have been obtained by annealing of sample (b) to 640 K. Tunneling parameters: $U = 0.2$ V, $I = 0.4$ nA.

(d) STM topograph of another position of sample (c). In addition to ordered arrays of hexagonal rings, zigzag polyphenylene chains are also formed.

intermediate species leading to the [30]-honeycombene macrocycles must self-assemble with hexagonal symmetry on the Ag(111) surface.

Wide area inspection of the surface with the reaction product uncovers the formation of strained macrocycles originating from four to seven precursor molecules, see Figure 3.38 (a-d). However, the preferred cyclic product turns out to include thirty phenylene units and is formed by six DB*m*″QiP precursor molecules in the presence of metallic silver via scission of carbon-bromine bonds. With the diameter of 4.0 nm, it represents the largest shape-persistent, conjugated, and unsubstituted hydrocarbon macrocycle known to date. These findings demonstrate the capabilities of this approach.

Besides macrocycles, annealing of the precursor on Ag(111) also yields zigzag polyphenylene chains as shown in Figure 3.37 (d). Closer inspection reveals that the

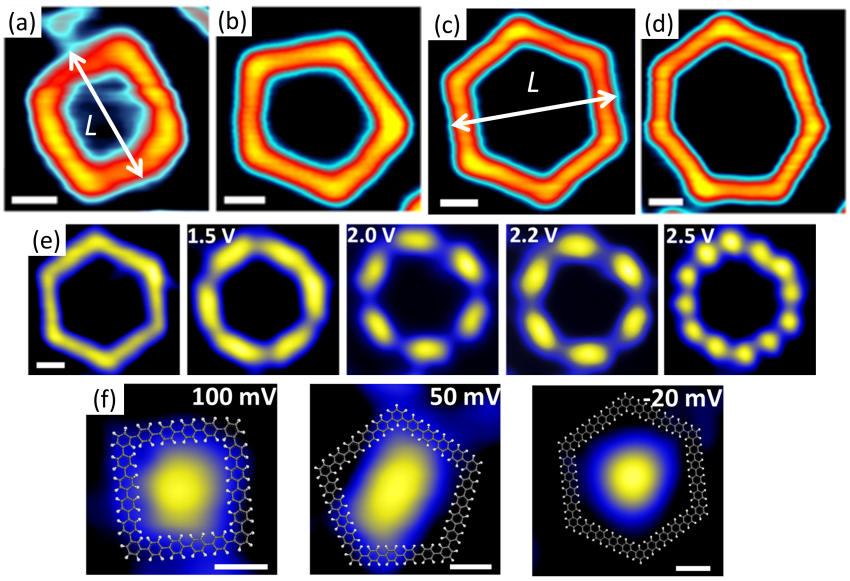

Figure 3.38: *STM and STS Study of Individual Polyphenylene Macrocycles.* Topographs and $\mathrm{d}I/\mathrm{d}V$ maps of polyphenylene macrocycles with varying ring size are shown. The white scale bars correspond to a length of 1 nm.

(a) The topograph of [20]-honeycombene shows a strained square molecule. Tunneling parameters: $U = 0.1\,\mathrm{V}$, $I = 0.02\,\mathrm{nA}$.

(b) The topograph of [25]-honeycombene shows a pentagonal molecule. Tunneling parameters: $U = 0.05\,\mathrm{V}$, $I = 0.02\,\mathrm{nA}$.

(c) The topograph of [30]-honeycombene shows a macrocycle with hexagonal symmetry. Tunneling parameters: $U = 0.1\,\mathrm{V}$, $I = 0.02\,\mathrm{nA}$.

(d) The topograph of [35]-honeycombene shows a slightly deformed heptagon. Tunneling parameters: $U = 0.1\,\mathrm{V}$, $I = 0.02\,\mathrm{nA}$.

(e) Left: This topographic image of [30]-honeycombene is acquired with changed settings. Tunneling parameters: $U = 0.1\,\mathrm{V}$, $I = 0.5\,\mathrm{nA}$. Right: Spatially resolved conductance measurements (experimental $\mathrm{d}I/\mathrm{d}V$ maps) using bias voltages between 1.5 V and 2.5 V (value in the image) and a tunneling current of 0.5 nA image the unoccupied states in the same molecule. Depending on the voltage, a different number of nodes is visible corresponding to different states.

(f) Experimental $\mathrm{d}I/\mathrm{d}V$ maps at the indicated bias voltage showing the confinement of the surface state inside the central cavities of the square [20]-honeycombene, pentagonal [25]-honeycombene, and hexagonal [30]-honeycombene macrocycles (from left to right). The positions of the macrocycles are derived from STM images indicated by the overlaid molecular models.

main axes of these chains prefer orientations related to the high-symmetry directions of the substrate.[51]

In order to gain insight into the electronic structure of these novel macrocycles, dI/dV mapping and tunneling conductance experiments (STS) have been performed on a single [30]-honeycombene molecule. A representative result is shown in Figure 3.38 (e) with experimental dI/dV maps at different bias voltages.

These images provide spatial information about the local density of states (LDOS) for some low energy unoccupied states. As can be seen, at a bias voltage of 1.5 V the maximum LDOS appears at the edges, whereas the corners have lower LDOS. With increasing bias voltage, the images show increasing localization of the density of states at the corners of the macrocycle. At 2.5 V, additional LDOS maxima are visible at the edge centers. *Meta*-linkage is known to interrupt conjugation in the electronic ground state.[223] The edges in the macrocycle experience *para*-conjugation. Since the two phenylene groups corresponding to the adjacent corners of the specific edge are also in *para* position to this paraphenylene fragment, they are also included in the conjugated system of this specific edge. Since one corner phenylene unit shares the conjugated systems of two edges, the resulting overlap of these *para*-conjugated phenylene fragments can lead to a certain amount of second order conjugation, *e.g.*, cross-conjugation[224]. Experimental dI/dV spectra for [30]-honeycombene for several positions in the macrocycle are presented and discussed in Publication [P11].

As shown in Figure 3.38, besides regular hexagonal honeycombenes (c), there are also other minority products including strained macrocycles with square (a), pentagonal (b), and heptagonal (d) shape, exhibiting different ring sizes. All of these macrocycles have been used for a systematic study of ring size effect on electron confinement. Adsorption of these macrocycles on metallic surfaces leads to the confinement of surface state electrons inside the central cavity and result in quantum corrals, as displayed in Figure 3.38 (f).

Confinement of surface state electrons in artificial nanostructures is typically achieved in closed metal quantum corrals[69] and in pores of supramolecular networks.[54,72,73] This work presents the first case using a large single-molecule quantum corral. The dI/dV maps in Figure 3.38 (f) show the standing wave patterns inside the square, pentagonal, and hexagonal macrocycles at the indicated bias voltages for the surface electrons. Related dI/dV spectra measured in the centers of the three macrocycles (not shown here) exhibit a shift of the confined surface state to higher energies with shrinking size of the macrocycles. Tunneling conductance spectra and further details are given in Publication [P11].

The energies of those confined surface states correlate with the size of the macrocycle.

Approximation of the corrals by a simple *particle-in-the-box* model describes the observed pattern well. The measured energy of 100 meV corresponds to a length of $L = 3.3$ nm in case of the square quantum corral in Figure 3.38 (a). The hexagonal quantum corral in Figure 3.38 (c) yields a measured energy of 20 meV which corresponds to a length of $L = 4.8$ nm. These calculated lengths are visualized by white arrows in Figure 3.38 (a,c). Comparison with the STM topographs reveals that they are a small but significant amount larger than the outer dimensions of the macrocycle. This indicates a substantial penetration of the wave function into the confining potential. This is not surprising, since the model used for calculation utilizes a potential with infinitely steep walls in contrast to the finite barrier in the experiment.

3.5.3 Self-Assembling of Molecular Fractals: Sierpiński-Like Triangle

The here presented work has been carried out in cooperation with the group of Prof. Dr. Kai Wu and Dr. Yongfeng Wang (STM) at Peking University.

In this project the adsorption of DB*m*QaP (Figure 3.39) on a Ag(111) surface has been studied by STM. Since this substance comprises the same reactive group as the molecules in Sections 3.5.1 and 3.5.2 a similar reactivity can be assumed. As discussed in Section 2.3, coverages of slightly less than 1 ML_M DB*m*TP form a two-dimensional molecular network on Ag(111). Since DB*m*QaP associates with the identical mechanism, the formation of a corresponding network seems expectable. However, the reduced symmetry of this compound is expected to influence and could eventually even inhibit the formations of the molecular patterns on the surface.

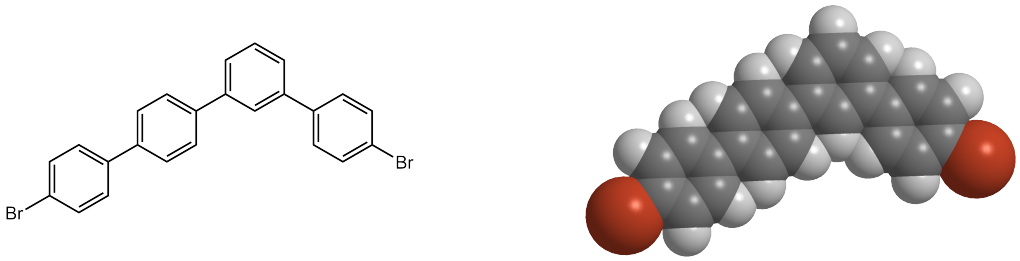

Figure 3.39: *4,4‴-Dibromo*-meta-*Quaterphenyl (DB*m*QaP).* This compound has an analog structure to DB*m*TP, but contains one additional phenylene unit in one of the arms. The asymmetric *meta* substitution pattern of the central phenylene group allows the formation of intermolecular nodes.

Vapor deposition of approximately 0.2 ML_M DB*m*QaP or DB*m*TP and a subsequent slow cooling of the sample down to 4.4 K results in the formation of small islands of the adsorbed molecules without a long range ordering. Surprisingly, these islands

exhibit a porous yet well-defined inner structure, as shown in Figure 3.40 (c,d). Their shape resembles the mathematical construct called Sierpiński triangle (ST).

This set of points can be constructed starting from an equilateral triangle. Subdivision of the initial triangle into four congruent new triangles and removal of the inner one yields a set of three new triangles. Each of these new ones serves as a new initial object for the next iteration of these operations.

Depending on the number of cycles, these sets can exhibit special properties. Application of a few iterations leads to esthetic shapes used in decorative patterns since medieval times, as shown in Figure 3.40 (a,b).[225] Using an infinite number of repetitions, Sierpiński triangles become fractal[7] and exhibit interesting topological and dimensional properties. First of all, it becomes self-similar, *i.e.*, the main triangle is a magnification of one of the sub triangles. Due to this process, the remaining area after an iteration step is reduced to ¾ of the initial one. Hence, with an increasing number of steps, the area approaches zero using the Lebesgue measure. In contrast, the perimeter becomes infinite since every step increases the outline by a factor of 9/6. Furthermore, the *Hausdorff-dimension* of such structures is no longer an integer, hence the name fractal. Since three scaled copies of the initial two-dimensional triangle are created in an iteration step, the Hausdorff-dimension becomes $\log(3)/\log(2) \approx 1.585$.

Although fractals form spontaneously in nature, like snowflakes,[227] it is difficult to generate them in synthetic systems.[226,227] Nevertheless, the STM topographs in Figure 3.40 clearly demonstrate that this goal can be achieved. The usage of self-assembling small molecules on surfaces in order to obtain extended molecular fractals without defects, which will disrupt the repeating pattern, has long been pursued, but – to the best of our knowledge – not been successful before. In this project, a diligent combination of building blocks, surface influence, and preparation routines, the self-assembly of Sierpiński-like triangles could be achieved.

Different generations of fractals have been measured by high-resolution STM. For instance, the molecular fractals DB*m*TP-ST-2 and DB*m*QaP-ST-3 are shown in Figure 3.40 (c,d), respectively. The nomenclature comprises the abbreviation of the precursor molecule and the generation n of the molecular Sierpiński-like triangles. The order n corresponds to the amount of different sizes of larger voids in Figure 3.40. It should be pointed out that the smallest voids formed by three monomers correspond to generation zero in the STM images. Another molecule with adaptive orientation is attached each of the nodes and serves as linker. Altogether, a building block comprises six monomers and three internal nodes. More examples of these molecular fractals with different orders are presented in Publication [P6].

7 A fractal is "exactly the same at every scale or nearly the same at different scales".[226]

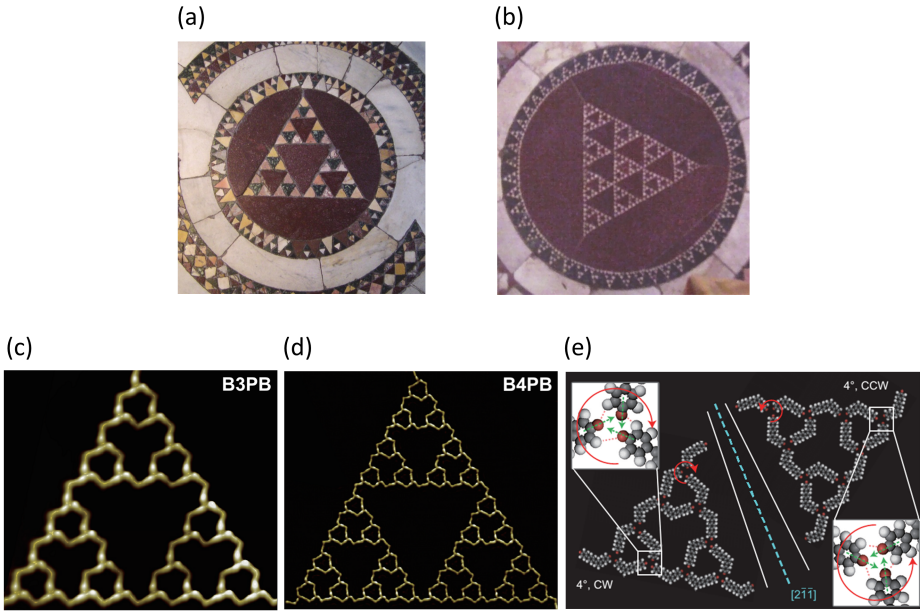

Figure 3.40: *Sierpiński-like Triangles in Art and Surface Science.*

(a) Sierpiński-like triangle pattern as decorative element in a mosaic of the late 11$^{\text{th}}$ century embedded in the floor of Basilica *San Clemente*, Rome. Image taken from Reference [225].

(b) Sierpiński-like triangle pattern as decorative element in a mosaic of the late 13$^{\text{th}}$ century embedded in the floor of the Basilica *Santi Giovanni e Paolo*, Rome. This work depicts a variation in which the largest central triangle has been filled with a self-similar continuation of the pattern. Images taken from Reference [225].

(c) High resolution STM images of a 2$^{\text{nd}}$ generation molecular Sierpiński-like triangle DB*m*TP-ST-2 formed by DB*m*TP (here called B3PB).
Tunneling parameters: Constant height, $U = 0.02\,\text{V}$, $I = 1\,\text{nA}$.

(d) High resolution STM images of a 3$^{\text{rd}}$ generation molecular Sierpiński-like triangle DB*m*QaP-ST-3 formed by DB*m*QaP (here called B4PB).
Tunneling parameters: Constant height, $U = 0.02\,\text{V}$, $I = 1\,\text{nA}$.

(e) Molecular models, here using DB*m*QaP, of the assemblies are presented for both enantiomers and their orientation on the Ag(111) substrate. The red arrows indicate the chirality of the connecting nodes, the green arrows and red dashed lines in the inset graphs indicate intermolecular interactions, see Publication [P6].

Analysis of the Hausdorff dimension by the *box-counting method*, see Publication [P6], results in a value of 1.68 ± 0.01 for DB*m*QaP-ST-3 which slightly but significantly deviates from the theoretical value. This effect can be attributed to the fact that the molecular structure, in contrast to the mathematical model, still exhibits a certain width from the molecules for the perimeter lines. The fact that the found value is greater than the theoretical value supports this assumption.

A closer inspection of the contact points in the molecular triangles reveals that each node is composed of three molecules, as shown in the zoomed insets in Figure 3.40 (e). The interaction of the bromine atoms mainly among each other[228,229] and with the hydrogen in *ortho* position to the bromine substituent on a neighboring molecule leads to an asymmetric arrangement. This induces a small rotation of the individual molecules in the node and thus a symmetry reduction. Since this rotation is possible in two equivalent directions, the node becomes chiral and two enantiomers – either with clockwise (CW) or counterclockwise (CCW) orientation – can be observed on the surface. The CW and CCW domains are both rotated by an absolute value of 4° away from the $[2\bar{1}\bar{1}]$ direction of the Ag(111) surface. This result suggests an influence of the substrate, *i.e.*, a template effect, on the final structure.

The necessarily slow cooling step in the preparation procedure allows for a propagation of the, initially random, dominant chirality through the whole triangle until all nodes feature the same orientation. As a consequence, the observed assemblies become self-similar. The slow cooling seems to play an important role in this process since the yield of fractals on the surface is inverse to the cooling rate of the sample. This indicates a small temperature window in which the structures can be formed.

A careful combination of various aspects rendered the fabrication of a series of defect-free molecular Sierpiński-like triangles under ultrahigh vacuum conditions possible. This includes the design of the asymmetric molecular building block with a 120° backbone, the specific intermolecular interactions, the template effect from the substrate, a suitable molecule-substrate interaction, and a delicate control of experimental parameters such as a suitable coverage as well as an optimized cooling rate for the assembling process.

4 Summary

In this thesis, metal-organic and organic-metal interfaces and/or interphases have been investigated and characterized by photoemission spectroscopy (XPS/HAXPES, and UPS), temperature programmed desorption and reaction (TPD/TPR) as well as scanning tunneling microscopy and spectroscopy (STM/STS). Two different classes of interfaces have been characterized in detail in this thesis with an aim at deeper understanding of the chemical and electronic properties at interfaces.

The first part emphasizes on interfaces comprising porphyrinoid macrocycles. This includes metalation reactions of porphyrins, phthalocyanines, corroles, and their derivatives. In the second topic, adsorbed terminal oligophenylene dibromides undergo Ullmann coupling reactions on Cu(111) and exhibit self-assembly on Ag(111). As a side project, the chemical composition perpendicular to the surface of a cathode for lithium ion batteries has been studied.

Since these individual topics are rather related by the used methods, especially by photoemission spectroscopy, than by their results, their individual results are self-contained and summarized in particular.

4.1 Coordination Chemistry of Porphyrinoid Macrocycles with Coinage Metals

Within the framework of the present study the following systems are investigated, concerning the coordination chemistry of porphyrinoid molecules.

- Coordination of copper atoms by 2HTPP and 2HTPyP on Au(111).
- Metalation of 2HTPP and 2HPc with copper atoms from a on Cu(111) substrate.
- Tuned adsorbate-substrate interaction by adsorbate and substrate variation.
- Coordination of cobalt atoms by a corrole derivative on Ag(111).
- Multilayer metalation of 2HTPP with cobalt atoms.

Investigations using photoemission spectroscopy reveal that the mentioned porphyrinoids are able to react with various metals and form chelate complexes. Introduction of peripheral donor groups renders the formation of networks possible. It is found that the sequential order for the deposition of the metallic and organic components is of lesser importance and that even the substrate might serve as a metal source. This leads to investigations concerning the interaction mechanisms between the two components by means of adsorbate and substrate variation. The electronic properties of the interface between a metalated phthalocyanine and a metallic surface are studied in this context.

Furthermore, the reactions of a substituted corrole with coinage metal substrates and cobalt is explored with great detail. The reactivity towards different substrates is probed as a function of temperature and layer thickness. As a result, the oxidation state of the central metal ion can be assigned. The corresponding valence band structure is compared to the porphyrin analogon.

In addition, the reaction of cobalt with thick layers of 2HTPP is studied by two radiation sources in order to estimate the thickness of the reaction zone. The laboratory based investigation uses incremental reacting amounts of the metal for *titration* of the organic layer. In contrast, the synchrotron based study uses kinetic energy variation on a reacted system.

4.1.1 Coordination of Copper Atoms by 2HTPP and 2HTPyP on Au(111)

Investigations using photoemission spectroscopy prove that 2*H*-tetraphenylporphyrin deposited on a Au(111) surface initially coordinates additionally dispensed copper atoms. Upon annealing, the copper atoms are oxidized under the formation of the Cu(II)TPP complex. Modification of the ligand with pyridyl groups replacing the phenyl substituents yields 2*H*-tetrapyridylporphyrin which exhibits identical reactivity in the molecular center. The four newly introduced nitrogen atoms are each able to coordinate neutral copper atoms. Two of these monodentate groups on different molecules can coordinate to one copper and form a bridging motive.

Additional scanning tunneling microscopy investigations document the formation of two-dimensional networks on the substrate's surface. The generated fabric can be considered as a two-dimensional analogon to metal-organic frameworks (MOF). Hence, it could be used as a template for epitaxially grown metal-organic frameworks.

Mild annealing of the coordination network comprising neutral copper in the initial complex and in the bridges to 450 K leads to oxidation of only the chelated copper atoms. The resulting structure contains copper in two oxidation states coordinated by the same molecule. The chemical state of the network can be changed by temperature.

Further annealing above 520 K causes a degradation of the network under the formation of individual close-packed Cu(II)TPyP molecules. The neutral copper atoms are released from the linking positions and diffuse into the substrate.

4.1.2 Metalation of Tetrapyrroles with Substrate Atoms from Cu(111)

The investigation of *in situ* metalation of porphyrinoid molecules with additional vapor deposited metal atoms is an actively explored field in surface science. However, the metalation reaction of adsorbed porphyrinoid molecules with atoms from the substrate was discovered only recently and many aspects are still to discover. This thesis investigated the metalation of two related tetrapyrroles by atoms from a clean Cu(111) surface.

First, the temperature-dependent chemical and structural transformation from 2HTPP to Cu(II)TPP on Cu(111) has been investigated. Comprehensive studies by STM and XPS show that 2HTPP molecules site-specifically adsorb on Cu(111) with the molecular plane parallel to the substrate at room temperature. After annealing of the sample to 400 K, a small fraction of the adsorbed 2HTPP molecules already show

reaction with copper atoms from the substrate forming CuTPP. STM investigations reveal that CuTPP also show parallel adsorption on Cu(111) at this temperature but at a larger distance to the surface than 2HTPP. Upon annealing to 450 K, all 2HTPP molecules are metalated to CuTPP. However, the molecular plane is tilted in this case. Further sample annealing to 500 K restores the flat-lying orientation, but with a smaller distance to the surface. The latter two changes are attributed to possible successive dehydrogenation of CuTPP.

Moreover, the development of the surface state of Cu(111) in UP spectra is considered. It is largely suppressed by the adsorption of 2HTPP at room temperature. It partially recovers after annealing to 450 K, and is suppressed again after annealing to 500 K. This also supports the above mentioned conclusions drawn from the XPS/STM experimental results.

Second, the redox reaction of 2HPc with copper atoms to CuPc on Cu(111) has been studied. Characteristic changes of the phthalocyanine related N 1s signal prove that 2HPc reacts with the Cu(111) surface and forms CuPc. At submonolayer coverages, partial metalation already occurs at 240 K and is almost completed at ambient temperature. In contrast, for complete metalation of multilayers (four monolayers) of 2HPc an annealing of the sample up to 500 K is necessary.

With the assistance of TPD/TPR, it is demonstrated that molecule exchange between the layers could be a possible pathway for the observed multilayer metalation with atoms from the metallic substrate. This finding is potentially of great importance for organic electronic devices where organic monolayers are used as contact primers in order to adjust energy levels at interfaces between metal electrodes and organic semiconductors.

4.1.3 Tuned Adsorbate-Substrate Interaction with Adsorbate and Substrate

The adsorbate-substrate interaction at submonolayer coverages of 2HTPP molecules has been investigated using Cu(111), Ag(111), and Au(111) as substrates. Analysis of XP spectra shows that, compared to Ag(111) and Au(111), 2HTPP molecules interact stronger with a Cu(111) surface. This interaction mainly happens *via* the iminic nitrogen atoms similar to the local bonding situation in the initial, “sitting-atop” complex during metalation.

Another facet of this investigation focused on the distance between the common substrate Cu(111) and the tetrapyrrole molecule varied by spacer groups. This distance increases from 2HPc over 2HTPP to 2HTTBPP. The different reaction products of

the similar centers of these porphyrins at room temperature show the influence of this distance. A partial reaction of 2HPc with copper atoms from the substrate under formation of the metal complex indicates a strong interaction. The formation of just the initial complexes of 2HTPP molecules with the substrate's copper atoms indicates a reduced reactivity. The substance with the largest distance to the substrate, *i.e.*, 2HTTBPP, shows no obvious interaction with the substrate any more. Hence, the adsorbate-substrate interaction can be tuned by variation of spacer groups influencing the distance between adsorbed molecules and the substrate surface.

In addition, the influence of the nature of the central metal ion in the complex has been studied using Cu(111) as substrate and vapor deposited CoPc as adsorbate. Due to the almost identical geometry of the well-investigated CuPc and CoPc, the distance to the metal surface is fixed and observed effects can be directly attributed to the altered electronic interaction of the central ion and the metallic substrate.

In case of a central cobalt ion, the interaction includes a charge transfer from the substrate's surface to the metal ion. This leads to an additional electronic state located at 0.9 eV below the Fermi edge. In addition, the multiplet splitting, which is observed in unperturbed multilayer spectra of the Co 2p core levels, is quenched if the metal complex is in contact with the surface. The multiplet splitting arises from the non-zero angular momentum of the unpaired electron in the $3d_{z^2}$ orbital. Charge transfer in this semi-occupied molecular orbital leads to a diamagnetic species with no angular momentum.

Furthermore, coverage-dependent UPS measurements examining the secondary electron cut-off and the highest occupied molecular orbital (HOMO) suggest a weak band bending in the multilayer regime.

4.1.4 Metalation of a Substituted Corrole with Cobalt

As seen before, adsorbed porphyrins are able to oxidize the co-adsorbed cobalt atoms into their +II oxidation state under reduction of the pyrrole moieties in the macrocycle. Formal replacement of an iminic by a reactive pyrrolic unit and removal of a methin-bridge of the cycle leads to the substance class of corroles. Here, 2,3,8,12,17,18-hexaethyl-7,13-dimethyl-corrole (3HHEDMC) is used which exhibits a slightly smaller coordination environment and could stabilize trivalent ions.

Utilizing XP and UP spectroscopy to study the reaction of adsorbed corrole with provided cobalt atoms it could be confirmed that the corresponding cobalt(III) corrole complex has been formed. UPS investigations further reveal that the cobalt centers in monolayers of the cobalt(III) corrole complex show a substantial interaction with

the Ag(111) substrate. However, the electronic structure is less affected compared to the case involving Co(II) centers in porphyrin complexes on the same substrate. The electronic properties in the valence band region of the examined cobalt(III) corrole complex are strikingly similar to the isoelectronic Fe(II)TPP complex.

The XPS experiments additionally indicate a possible reaction of 3HHEDMC with silver atoms from the substrate. It is proposed that one of the pyrrolic units in each 3HHEDMC molecule is reduced and a 2HAgHEDMC complex is obtained. A reaction of 3HHEDMC has been observed on a, compared to silver, even less reactive Au(111) surface. Interpretation of the recorded XP spectra lead to the conclusion that Au(III)-corrole complexes are formed in this case.

Since this behavior is rare for these noble metals, further input is required to verify these results and gain deeper insight into the reaction mechanism between 3HHEDMC molecules and metal atoms from the corresponding substrate.

4.1.5 Metalation of 2HTPP Multilayer with Cobalt Atoms

Compared to monolayers, multilayers have much more complex structure which renders their characterization more challenging. In addition, the related interface or interphase between metallic film covering an organic substrate thin film requires even more technical effort. Extending the studies on porphyrinoid molecular monolayers on metal surfaces summarized above, the reaction multilayers of porphyrin molecules with deposited cobalt atoms has also been investigated. Cobalt atoms easily coordinate with 2HTPP molecules at room temperature under the formation of CoTPP. Using a conventional laboratory X-ray source, the metalation a 2HTPP thin film with incremental deposition of cobalt atoms is monitored. The analysis of the obtained spectra show that initially most of the dosed metal atoms react with the organic phase as well as a stagnation of the reaction at higher cobalt coverages yielding approximately 1.9 nm CoTPP. The appearance characteristic features reveal the presence of metallic phases, *i.e.*, clusters merging into a dense film, on the sample.

HAXPES investigations using a varied X-ray excitation energy from 2 keV to 6 keV revealed a depth profile of a sample prepared by subsequent one-step deposition of cobalt atoms onto a prepared 2HTPP thin film. Approximately 1.4 nm CoTPP are produced before a dense metallic cover layer inhibits a further reaction. This experimental result corresponds well with the assumed models using various calculation techniques. As higher kinetic energy leads to increased information depth and HAXPES is non-destructive, it is essential for identifying the unperturbed electronic structures and chemical reactions in bulk phases and buried interfaces.

4.2 Coated Cathode for Lithium-Ion Batteries

As a collaborative side project, the vertical chemical composition of a layered electrode has been studied by HAXPES. The specimen comprising a thin-film $LiNi_{0.5}Mn_{1.5}O_4$ (LNMO) cathode coated with $Li_4Ti_5O_{12}$ (LTO) was probed after electrochemical cycling in a battery electrolyte. A depth profile of the cathode in discharged state was obtained with this non-destructive method employing synchrotron X-rays with photon energy ranging between 2 keV and 6 keV.

It has been found that the entire cathode is covered by a 3.0 nm thin surface layer mainly consisting of organic polymers (90 %) as well as metal fluorides and fluorophosphates. Manganese and nickel of the $LiNi_{0.5}Mn_{1.5}O_4$ layer are found to diffuse into the $Li_4Ti_5O_{12}$ coating under preservation of their respective oxidation states. Most likely, this process occurs during the heating steps involved in the preparation of the cathode.

The coating layer itself consists of a uniform mixture of Li(I), Ti(IV), Ni(II), and Mn(IV) oxides with the overall composition of $Li_{1.1}Ni_{0.24}Mn_{0.40}Ti_{1.2}O_4$. The found doping of the $Li_4Ti_5O_{12}$ layer with the open d-shell ions Ni^{2+} (d^8) and Mn^{4+} (d^3) explains the in electrochemical investigations observed decreases of the impedance of the LTO coating which corresponds to an increased performance of the battery.

4.3 Bromoarenes on (111) Surfaces

As another major topic in this thesis covers the reaction and behavior of terminal oligophenylene dibromides with target-oriented geometries on (111) surfaces of coinage metal single crystals.

- Ullmann coupling reaction of DB*p*TP and TBB on Cu(111).
- Surface-assisted synthesis of honeycombenes on Ag(111).
- Self-assembly of molecular Sierpiński triangle fractals on Ag(111).

The Ullmann coupling reaction of arylbromides using solid copper as catalyst and yielding biphenyls is studied on a single crystal surface by photoemission spectroscopy as well as scanning tunneling microscopy and spectroscopy. Pilot tests with small precursor molecules on copper provide information on the spectroscopic features and topographic information about the observed self-assembling during the individual reaction steps. Larger precursors with specific geometry on silver render the formation of gigantic macrocycles and their examination possible. The usage of an asymmetric precursor results in fractal patterns on the surface.

4.3.1 Ullmann Coupling of DB*p*TP and TBB on Cu(111)

The adsorption and reaction of 4,4″-dibromo-*para*-terphenyl (DB*p*TP) and 1,3,5-tris(4-bromophenyl)benzene (TBB) on a Cu(111) surface has been studied with comprehensive surface science based characterization techniques, *i.e.*, XPS, UPS, and STM, as well as DFT calculations for theoretical support. The detachment of bromine from the precursor occurs between 170 K and 240 K at submonolayer coverages. The estimated activation energy between 47 $^{kJ}/_{mol}$ and 67 $^{kJ}/_{mol}$ for this process is considerably lower than the corresponding bond energy. This clearly indicates that the Cu(111) surface is involved in this process. A complete conversion of the bromine substituents requires heating to 473 K in case several molecular layers have been deposited. This observation is in line with the previous findings that the copper surface plays a crucial role in this reaction.

Dehalogenation leads to chemisorbed bromine on the surface, which effectively suppresses the surface state of the Cu(111) crystal. The remaining bodies of the molecules undergo linkage under formation of organometallic oligomers. Annealing of these intermediates leads to elimination of bridging copper atoms and to the formation of carbon bonded covalent two-dimensional networks.

STM images of the resulting covalent two-dimensional mesh formed by TBB molecules with varying pore sizes show a preference for hexagonal shapes.

4.3.2 Surface-Assisted Synthesis of Honeycombenes on Ag(111)

Utilizing a modification of the Ullmann coupling reaction, a class of giant hexagonal oligophenylene macrocycles has been synthesized in a solvent-free approach on silver under ultrahigh vacuum conditions. Coupling of six 4,4‴-dibromo-*meta*″-quinquephenyl (DB*m*″QiP) molecules on Ag(111) yields [30]-honeycombene, a hexagonal cyclotriaconta-phenylene – $(C_6H_4)_{30} = C_{180}H_{120}$, assembled in hexagonal islands on the surface. With a molecular diameter of 4.0 nm, the well-ordered arrays of hexagonal rings represent the largest shape-persistent, conjugated, and unsubstituted hydrocarbon macrocycle known to date. Minority species, including strained macrocycles like the square [20]-honeycombene (cycloicosaphenylene $C_{120}H_{80}$), the pentagonal [25]-honeycombene (cyclopentacosaphenylene $C_{150}H_{100}$), and the heptagonal [35]-honeycombene (cyclopentatriacontaphenylene $C_{210}H_{140}$), have also been observed on the same sample.

Furthermore, these macrocycles serve as organic quantum corrals leading to confinement of surface state electrons inside the central cavity. Calculation using *particle-in-a-box* models suggest a partial penetration of the wave functions – corresponding to the electronic surface state – into the confining potential generated by the macrocycles.

The here presented honeycombene film with well-defined pore sizes and spatial distribution could potentially serve as a templates for the growth of nanoparticles on the substrate surface. Additionally, catalytic, electronic, or mechanic applications are imaginable.

4.3.3 Self-Assembly of Molecular Sierpiński Triangle Fractals on Ag(111)

By a combination of specific precursor design of DB*p*TP and 4,4‴-dibromo-*meta*-quaterphenyl (DB*m*QaP) as well as prudential sample preparation, defect-free Sierpiński triangle fractals have been obtained *via* self-assembly on a Ag(111) at temperatures below 80 K. The intermolecular halogen/α-hydrogen interaction is the driving force for the well-defined cohesion of the individual molecules.

Sierpiński triangles of different generations, *i.e.*, levels of self-similarity respectively size, have been observed by STM. The obtained supramolecular triangles of up to four

generations are chiral. The relative orientation of the bromo-substituents of all nodes within a triangular network is constant but can differ from island to island.

The presented method to realize fractal patterns on a surface gives an esthetic contribution to the class of surface self-assembled structures.

List of Figures

List of Tables

Bibliography

[1] Milgrom, L. R. *The colors of life: an introduction to the chemistry of porphyrins and related compunds.* Oxford University Press, New York, **1997**.

[2] Agostinis, P.; Berg, K.; Cengel, K. A.; Foster, T. H.; Girotti, A. W.; Gollnick, S. O.; Hahn, S. M.; Hamblin, M. R.; Juzeniene, A.; Kessel, D.; Korbelik, M.; Moan, J.; Mroz, P.; Nowis, D.; Piette, J.; Wilson, B. C.; and Golab, J. Photodynamic Therapy of Cancer: An Update. *Ca-a Cancer Journal for Clinicians*, **2011**, *61*(4), 250. doi:10.3322/caac.20114.

[3] Vogel, E. Porphyrinoid macrocycles: A cornucopia of novel chromophores. *Pure Appl. Chem.*, **1996**, *68*(7), 1355. doi:10.1351/pac199668071355.

[4] Gottfried, J. M. Surface chemistry of porphyrins and phthalocyanines. *Surf. Sci. Rep.*, **2015**, *70*(3), 259. doi:10.1016/j.surfrep.2015.04.001.

[5] Lukasczyk, T.; Flechtner, K.; Merte, L. R.; Jux, N.; Maier, F.; Gottfried, J. M.; and Steinrück, H.-P. Interaction of cobalt(II) tetraarylporphyrins with a Ag(111) surface studied with photoelectron spectroscopy. *J. Phys. Chem. C*, **2007**, *111*(7), 3090. doi:10.1021/jp0652345.

[6] Mochida, I.; Suetsugu, K.; Fujitsu, H.; and Takeshita, K. Enhanced catalytic activity of cobalt tetraphenylporphyrin on titanium dioxide by evacuation at elevated temperatures for intensifying the complex-support interaction. *J. Phys. Chem.*, **1983**, *87*(9), 1524. doi:10.1021/j100232a015.

[7] Rakow, N. A. and Suslick, K. S. A colorimetric sensor array for odour visualization. *Nature*, **2000**, *406*(6797), 710. doi:10.1038/35021028.

[8] Guillaud, G.; Simon, J.; and Germain, J. P. Metallophthalocyanines: Gas sensors, resistors and field effect transistors. *Coord. Chem. Rev.*, **1998**, *178-180, Part 2*, 1433. doi:10.1016/S0010-8545(98)00177-5.

[9] Kadish, K.; Smith, K.; and Guilard, R., editors. *The Porphyrin Handbook*, volume 1-20. Academic Press, San Diego, **2000-2003**.

[10] Kadish, K.; Smith, K.; and Guilard, R., editors. *Handbook of Porphyrin Science*, volume 1-35. World Scientific Publishing Co., Singapore, **2010-2014**.

[11] Yoshimoto, S. and Itaya, K. Advances in supramolecularly assembled nanostructures of fullerenes and porphyrins at surfaces. *Journal of Porphyrins and Phthalocyanines*, **2007**, *11*(05), 313. doi:10.1142/S1088424607000369.

[12] Otsuki, J. STM studies on porphyrins. *Coord. Chem. Rev.*, **2010**, *254*(19-20), 2311. doi:10.1016/j.ccr.2009.12.038.

[13] Buchner, F.; Flechtner, K.; Bai, Y.; Zillner, E.; Kellner, I.; Steinrück, H. P.; Marbach, H.; and Gottfried, J. M. Coordination of iron atoms by tetraphenylporphyrin monolayers and multilayers on Ag(111) and formation of iron-tetraphenylporphyrin. *J. Phys. Chem. C*, **2008**, *112*(39), 15458. doi:10.1021/jp8052955.

[14] Gottfried, J. M.; Flechtner, K.; Kretschmann, A.; Lukasczyk, T.; and Steinrück, H. P. Direct synthesis of a metalloporphyrin complex on a surface. *J. Am. Chem. Soc.*, **2006**, *128*(17), 5644. doi:10.1021/ja0610333.

[15] Chen, M.; Feng, X.; Zhang, L.; Ju, H.; Xu, Q.; Zhu, J.; Gottfried, J. M.; Ibrahim, K.; Qian, H.; and Wang, J. Direct Synthesis of Nickel(II) Tetraphenylporphyrin and Its Interaction with a Au(111) Surface: A Comprehensive Study. *J. Phys. Chem. C*, **2010**, *114*(21), 9908. doi:10.1021/jp102031m.

[16] Li, Y.; Xiao, J.; Shubina, T. E.; Chen, M.; Shi, Z.; Schmid, M.; Steinrück, H.-P.; Gottfried, J. M.; and Lin, N. Coordination and Metalation Bifunctionality of Cu with 5,10,15,20-Tetra(4-pyridyl)porphyrin: Toward a Mixed-Valence Two-Dimensional Coordination Network. *J. Am. Chem. Soc.*, **2012**, *134*(14), 6401. doi:10.1021/ja300593w.

[17] Kretschmann, A.; Walz, M.-M.; Flechtner, K.; Steinrück, H.-P.; and Gottfried, J. M. Tetraphenylporphyrin picks up zinc atoms from a silver surface. *Chem. Commun.*, **2007**, (6), 568. doi:10.1039/b614427f.

[18] Flechtner, K.; Kretschmann, A.; Bradshaw, L. R.; Walz, M.-M.; Steinrueck, H.-P.; and Gottfried, J. M. Surface-confined two-step synthesis of the complex (ammine)(meso-tetraphenylporphyrinato)-zinc(II) on Ag(111). *J. Phys. Chem. C*, **2007**, *111*(16), 5821. doi:10.1021/jp071531d.

[19] Shubina, T. E.; Marbach, H.; Flechtner, K.; Kretschmann, A.; Jux, N.; Buchner, F.; Steinrück, H.-P.; Clark, T.; and Gottfried, J. M. Principle and mechanism of direct porphyrin metalation: Joint experimental and theoretical investigation. *J. Am. Chem. Soc.*, **2007**, *129*(30), 9476. doi:10.1021/ja072360t.

[20] Auwärter, W.; Ecija, D.; Klappenberger, F.; and Barth, J. V. Porphyrins at interfaces. *Nat. Chem.*, **2015**, *7*(2), 105. doi:10.1038/nchem.2159.

[21] Klappenberger, F. Two-dimensional functional molecular nanoarchitectures - Complementary investigations with scanning tunneling microscopy and X-ray spectroscopy. *Prog. Surf. Sci.*, **2014**, *89*(1), 1. doi:10.1016/j.progsurf.2013.10.002.

[22] Grill, L.; Dyer, M.; Lafferentz, L.; Persson, M.; Peters, M. V.; and Hecht, S. Nanoarchitectures by covalent assembly of molecular building blocks. *Nat. Nanotechnol.*, **2007**, *2*(11), 687. doi:10.1038/nnano.2007.346.

[23] Shi, Z. L. and Lin, N. Porphyrin-Based Two-Dimensional Coordination Kagome Lattice Self-Assembled on a Au(111) Surface. *J. Am. Chem. Soc.*, **2009**, *131*(15), 5376. doi:10.1021/ja900499b.

[24] Hieringer, W.; Flechtner, K.; Kretschmann, A.; Seufert, K.; Auwarter, W.; Barth, J. V.; Gorling, A.; Steinrück, H. P.; and Gottfried, J. M. The Surface Trans Effect: Influence of Axial Ligands on the Surface Chemical Bonds of Adsorbed Metalloporphyrins. *J. Am. Chem. Soc.*, **2011**, *133*(16), 6206. doi:10.1021/ja1093502.

[25] Peisert, H.; Uihlein, J.; Petraki, F.; and Chasse, T. Charge transfer between transition metal phthalocyanines and metal substrates: The role of the transition metal. *J. Electron Spectrosc. Relat. Phenom.*, **2015**, *204, Part A*, 49. doi:10.1016/j.elspec.2015.01.005.

[26] Schmid, M.; Kaftan, A.; Steinrueck, H.-P.; and Gottfried, J. M. The electronic structure of cobalt(II) phthalocyanine adsorbed on Ag(111). *Surf. Sci.*, **2012**, *606*(11-12), 945. doi:10.1016/j.susc.2012.02.012.

[27] Ishii, H.; Sugiyama, K.; Ito, E.; and Seki, K. Energy level alignment and interfacial electronic structures at organic metal and organic organic interfaces. *Adv. Mater.*, **1999**, *11*(8), 605. doi:10.1002/(sici)1521-4095(199906)11:8<605::aid-adma605>3.3.co;2-h.

[28] Watkins, N. J.; Yan, L.; and Gao, Y. Electronic structure symmetry of interfaces between pentacene and metals. *Appl. Phys. Lett.*, **2002**, *80*(23), 4384. doi:10.1063/1.1485129.

[29] Choong, V. E.; Mason, M. G.; Tang, C. W.; and Gao, Y. G. Investigation of the interface formation between calcium and tris-(8-hydroxy quinoline) aluminum. *Appl. Phys. Lett.*, **1998**, *72*(21), 2689. doi:10.1063/1.121100.

[30] Kahn, A.; Koch, N.; and Gao, W. Y. Electronic structure and electrical properties of interfaces between metals and pi-conjugated molecular films. *J. Polym. Sci. Part B Polym. Phys*, **2003**, *41*(21), 2529. doi:10.1002/polb.10642.

[31] Gavrila, G.; Zahn, D. R. T.; and Braun, W. High resolution photoemission spectroscopy: Evidence for strong chemical interaction between Mg and 3,4,9,10-perylene-tetracarboxylic dianhydride. *Appl. Phys. Lett.*, **2006**, *89*(16), 162102. doi:10.1063/1.2356305.

[32] Shen, C. F.; Kahn, A.; and Schwartz, J. Role of metal-molecule chemistry and interdiffusion on the electrical properties of an organic interface: The Al-F16CuPc case. *J. Appl. Phys.*, **2001**, *90*(12), 6236. doi:10.1063/1.1419263.

[33] Seah, M. P. and Dench, W. A. Quantitative electron spectroscopy of surfaces: A standard data base for electron inelastic mean free paths in solids. *Surf. Interface Anal.*, **1979**, *1*(1), 2. doi:10.1002/sia.740010103.

[34] Goodenough, J. B. and Kim, Y. Challenges for Rechargeable Li Batteries. *Chem. Mater.*, **2010**, *22*(3), 587. doi:10.1021/cm901452z.

[35] Scrosati, B. Recent advances in lithium ion battery materials. *Electrochim. Acta*, **2000**, *45*(15-16), 2461 . doi:10.1016/S0013-4686(00)00333-9.

[36] Cabana, J.; Casas-Cabanas, M.; Omenya, F. O.; Chernova, N. A.; Zeng, D.; Whittingham, M. S.; and Grey, C. P. Composition-Structure Relationships in the Li-Ion Battery Electrode Material $LiNi_{0.5}Mn_{1.5}O_4$. *Chem. Mater.*, **2012**, *24*(15), 2952. doi:10.1021/cm301148d.

[37] Gellert, M.; Gries, K. I.; Zakel, J.; Ott, A.; Spannenberger, S.; Yada, C.; Rosciano, F.; Volz, K.; and Roling, B. $LiNi_0.5Mn_1.5O_4$ Thin-Film Cathodes on Gold-Coated Stainless Steel Substrates: Formation of Interlayers and Electrochemical Properties. *Electrochim. Acta*, **2014**, *133*, 146. doi:10.1016/j.electacta.2014.03.184.

[38] Pieczonka, N. P. W.; Liu, Z.; Lu, P.; Olson, K. L.; Moote, J.; Powell, B. R.; and Kim, J.-H. Understanding Transition-Metal Dissolution Behavior in $LiNi_0.5Mn_1.5O_4$ High-Voltage Spinel for Lithium Ion Batteries. *J. Phys. Chem. C*, **2013**, *117*(31), 15947. doi:10.1021/jp405158m.

[39] Gellert, M.; Gries, K. I.; Zakel, J.; Kranz, S.; Bradler, S.; Hornberger, E.; Mueller, S.; Yada, C.; Rosciano, F.; Volz, K.; and Boling, B. Charge Transfer across the Interface between $LiNi_{0.5}Mn_{1.5}O_4$ High-Voltage Cathode Films and Solid Electrolyte Films. *J. Electrochem. Soc.*, **2015**, *162*(4), A754. doi:10.1149/2.0891504jes.

[40] Ullmann, F. and Bielecki, J. Synthesis in the Biphenyl series. (I. Announcement). *Ber. Dtsch. Chem. Ges.*, **1901**, *34*, 2174. doi:10.1002/cber.190103402141.

[41] Aarts, J. F. M. and Phelan, K. G. Dehalogenation of fluoro- and chlorobenzene on Pd(111) studied by electron energy loss spectroscopy. *Surf. Sci.*, **1989**, *222*(2-3), L853. doi:10.1016/0039-6028(89)90355-5.

[42] Blake, M. M.; Nanayakkara, S. U.; Claridge, S. A.; Fernandez-Torres, L. C.; Sykes, E. C. H.; and Weiss, P. S. Identifying Reactive Intermediates in the Ullmann Coupling Reaction by Scanning Tunneling Microscopy and Spectroscopy. *J. Phys. Chem. A*, **2009**, *113*(47), 13167. doi:10.1021/jp903590c.

[43] Xi, M. and Bent, B. E. Mechanisms of the Ullmann coupling reaction in adsorbed monolayers. *J. Am. Chem. Soc.*, **1993**, *115*(16), 7426. doi:10.1021/ja00069a048.

[44] Syomin, D. and Koel, B. E. Adsorption of iodobenzene (C_6H_5I) on Au(111) surfaces and production of biphenyl (C_6H_5-C_6H_5). *Surf. Sci.*, **2001**, *490*(3), 265. doi:10.1016/s0039-6028(01)01319-x.

[45] Di Giovannantonio, M.; El Garah, M.; Lipton-Duffin, J.; Meunier, V.; Cardenas, L.; Fagot Revurat, Y.; Cossaro, A.; Verdini, A.; Perepichka, D. F.; Rosei, F.; and Contini, G. Insight into Organometallic Intermediate and Its Evolution to Covalent Bonding in Surface-Confined Ullmann Polymerization. *ACS Nano*, **2013**, *7*(9), 8190. doi:10.1021/nn4035684.

[46] Wang, W.; Shi, X.; Wang, S.; Van Hove, M. A.; and Lin, N. Single-Molecule Resolution of an Organometallic Intermediate in a Surface-Supported Ullmann Coupling Reaction. *J. Am. Chem. Soc.*, **2011**, *133*(34), 13264. doi:10.1021/ja204956b.

[47] Chung, K.-H.; Koo, B.-G.; Kim, H.; Yoon, J. K.; Kim, J.-H.; Kwon, Y.-K.; and Kahng, S.-J. Electronic structures of one-dimensional metal-molecule hybrid chains studied using scanning tunneling microscopy and density functional theory. *Phys. Chem. Chem. Phys.*, **2012**, *14*(20), 7304. doi:10.1039/c2cp23295b.

[48] Walch, H.; Gutzler, R.; Sirtl, T.; Eder, G.; and Lackinger, M. Material- and Orientation-Dependent Reactivity for Heterogeneously Catalyzed Carbon-Bromine Bond Homolysis. *J. Phys. Chem. C*, **2010**, *114*(29), 12604. doi:10.1021/jp102704q.

[49] Blunt, M. O.; Russell, J. C.; Champness, N. R.; and Beton, P. H. Templating molecular adsorption using a covalent organic framework. *Chem. Commun.*, **2010**, *46*(38), 7157. doi:10.1039/c0cc01810d.

[50] Fan, Q.; Wang, C.; Han, Y.; Zhu, J.; Kuttner, J.; Hilt, G.; and Gottfried, J. M. Surface-Assisted Formation, Assembly, and Dynamics of Planar Organometallic Macrocycles and Zigzag Shaped Polymer Chains with C-Cu-C Bonds. *ACS Nano*, **2013**, *8*(1), 709. doi:10.1021/nn405370s.

[51] Fan, Q.; Wang, C.; Han, Y.; Zhu, J.; Hieringer, W.; Kuttner, J.; Hilt, G.; and Gottfried, J. M. Surface-Assisted Organic Synthesis of Hyperbenzene Nanotroughs. *Angew. Chem. Int. Ed.*, **2013**, *52*(17), 4668. doi:10.1002/anie.201300610.

[52] Park, J.; Kim, K. Y.; Chung, K.-H.; Yoon, J. K.; Kim, H.; Han, S.; and Kahng, S.-J. Interchain Interactions Mediated by Br Adsorbates in Arrays of Metal-Organic Hybrid Chains on Ag(111). *J. Phys. Chem. C*, **2011**, *115*(30), 14834. doi:10.1021/jp203129f.

[53] Faul, C. F. J. and Antonietti, M. Ionic self-assembly: Facile synthesis of supramolecular materials. *Adv. Mater.*, **2003**, *15*(9), 673. doi:10.1002/adma.200300379.

[54] Klappenberger, F.; Kühne, D.; Krenner, W.; Silanes, I.; Arnau, A.; García de Abajo, F. J.; Klyatskaya, S.; Ruben, M.; and Barth, J. V. Tunable Quantum Dot Arrays Formed from Self-Assembled Metal-Organic Networks. *Phys. Rev. Lett.*, **2011**, *106*(2), 026802. doi:10.1103/PhysRevLett.106.026802.

[55] Schlickum, U.; Decker, R.; Klappenberger, F.; Zoppellaro, G.; Klyatskaya, S.; Ruben, M.; Silanes, I.; Arnau, A.; Kern, K.; Brune, H.; and Barth, J. V. Metal-Organicrganic Honeycomb Nanomeshes with Tunable Cavity Size. *Nano Lett.*, **2007**, *7*(12), 3813. doi:10.1021/nl072466m.

[56] Kuehnle, A. Self-assembly of organic molecules at metal surfaces. *Curr. Opin. Colloid Interface Sci.*, **2009**, *14*(2), 157. doi:10.1016/j.cocis.2008.01.001.

[57] Barth, J. V. Molecular architectonic on metal surfaces. *Annu. Rev. Phys. Chem.*, **2007**, *58*, 375. doi:10.1146/annurev.physchem.56.092503.141259.

[58] Desiraju, G. R. Supramolecular Synthons in Crystal Engineering-A New Organic Synthesis. *Angew. Chem. Int. Ed.*, **1995**, *34*(21), 2311. doi:10.1002/anie.199523111.

[59] Prins, L. J.; Reinhoudt, D. N.; and Timmerman, P. Noncovalent synthesis using hydrogen bonding. *Angew. Chem. Int. Ed.*, **2001**, *40*(13), 2382. doi:10.1002/1521-3773(20010702)40:13<2382::aid-anie2382>3.0.co;2-g.

[60] Larson, J. W. and McMahon, T. B. Gas-phase bihalide and pseudobihalide ions. An ion cyclotron resonance determination of hydrogen bond energies in XHY- species (X, Y = F, Cl, Br, CN). *Inorg. Chem.*, **1984**, *23*(14), 2029. doi:10.1021/ic00182a010.

[61] James, S. L. Metal-organic frameworks. *Chem. Soc. Rev.*, **2003**, *32*(5), 276. doi:10.1039/b200393g.

[62] Pawin, G.; Wong, K. L.; Kwon, K.-Y.; and Bartels, L. A Homomolecular Porous Network at a Cu(111) Surface. *Science*, **2006**, *313*(5789), 961. doi:10.1126/science.1129309.

[63] Wyrick, J.; Kim, D.-H.; Sun, D.; Cheng, Z.; Lu, W.; Zhu, Y.; Berland, K.; Kim, Y. S.; Rotenberg, E.; Luo, M.; Hyldgaard, P.; Einstein, T. L.; and Bartels, L. Do Two-Dimensional "Noble Gas Atoms" Produce Molecular Honeycombs at a Metal Surface? *Nano Lett.*, **2011**, *11*(7), 2944. doi:10.1021/nl201441b.

[64] Stöhr, M.; Wahl, M.; Galka, C. H.; Riehm, T.; Jung, T. A.; and Gade, L. H. Controlling molecular assembly in two dimensions: The concentration dependence of thermally induced 2D aggregation of molecules on a metal surface. *Angew. Chem. Int. Ed.*, **2005**, *44*(45), 7394. doi:10.1002/anie.200502316.

[65] Crommie, M. F.; Lutz, C. P.; and Eigler, D. M. Imaging standing waves in a two-dimensional electron gas. *Nature*, **1993**, *363*(6429), 524. doi:10.1038/363524a0.

[66] Hasegawa, Y. and Avouris, P. Direct Observation of Standing Wave Formation at Surface Steps Using Scanning Tunneling Spectroscopy. *Phys. Rev. Lett.*, **1993**, *71*(7), 1071. doi:10.1103/PhysRevLett.71.1071.

[67] Li, J. T.; Schneider, W. D.; and Berndt, R. Local density of states from spectroscopic scanning-tunneling-microscope images: Ag(111). *Phys. Rev. B*, **1997**, *56*(12), 7656. doi:10.1103/PhysRevB.56.7656.

[68] Li, J. T.; Schneider, W. D.; Berndt, R.; and Crampin, S. Electron confinement to nanoscale Ag islands on Ag(111): A quantitative study. *Phys. Rev. Lett.*, **1998**, *80*(15), 3332. doi:10.1103/PhysRevLett.80.3332.

[69] Crommie, M. F.; Lutz, C. P.; and Eigler, D. M. Confinement of Electrons to Quantum Corrals on a Metal Surface. *Science*, **1993**, *262*(5131), 218. doi:10.1126/science.262.5131.218.

[70] Manoharan, H. C.; Lutz, C. P.; and Eigler, D. M. Quantum mirages formed by coherent projection of electronic structure. *Nature*, **2000**, *403*(6769), 512. doi:10.1038/35000508.

[71] Heller, E. J.; Crommie, M. F.; Lutz, C. P.; and Eigler, D. M. Scattering and absorption of surface electron waves in quantum corrals. *Nature*, **1994**, *369*(6480), 464. doi:10.1038/369464a0.

[72] Kepcija, N.; Huang, T. J.; Klappenberger, F.; and Barth, J. V. Quantum confinement in self-assembled two-dimensional nanoporous honeycomb networks at close-packed metal surfaces. *J. Chem. Phys.*, **2015**, *142*(10). doi:101931 10.1063/1.4913244.

[73] Klappenberger, F.; Kuehne, D.; Krenner, W.; Silanes, I.; Arnau, A.; Javier Garcia de Abajo, F.; Klyatskaya, S.; Ruben, M.; and Barth, J. V. Dichotomous Array of Chiral Quantum Corrals by a Self-Assembled Nanoporous Kagome Network. *Nano Lett.*, **2009**, *9*(10), 3509. doi:10.1021/nl901700b.

[74] Wilder, J. W. G.; Venema, L. C.; Rinzler, A. G.; Smalley, R. E.; and Dekker, C. Electronic structure of atomically resolved carbon nanotubes. *Nature*, **1998**, *391*(6662), 59. doi:10.1038/34139.

[75] Venema, L. C.; Wildöer, J. W. G.; Janssen, J. W.; Tans, S. J.; Tuinstra, H. L. J. T.; Kouwenhoven, L. P.; and Dekker, C. Imaging Electron Wave Functions of Quantized Energy Levels in Carbon Nanotubes. *Science*, **1999**, *283*(5398), 52. doi:10.1126/science.283.5398.52.

[76] Diebold, U. The surface science of titanium dioxide. *Surf. Sci. Rep.*, **2003**, *48*(5-8), 53. doi:10.1016/S0167-5729(02)00100-0.

[77] Echenique, P. M.; Berndt, R.; Chulkov, E. V.; Fauster, T.; Goldmann, A.; and Höfer, U. Decay of electronic excitations at metal surfaces. *Surf. Sci. Rep.*, **2004**, *52*(7-8), 219. doi:10.1016/j.surfrep.2004.02.002.

[78] Krenner, W.; Kuehne, D.; Klappenberger, F.; and Barth, J. V. Assessment of Scanning Tunneling Spectroscopy Modes Inspecting Electron Confinement in Surface-Confined Supramolecular Networks. *Sci. Rep.*, **2013**, *3*. doi:1454 10.1038/srep01454.

[79] Lobo-Checa, J.; Matena, M.; Mueller, K.; Dil, J. H.; Meier, F.; Gade, L. H.; Jung, T. A.; and Stoehr, M. Band Formation from Coupled Quantum Dots Formed by a Nanoporous Network on a Copper Surface. *Science*, **2009**, *325*(5938), 300. doi:10.1126/science.1175141.

[80] Kuhn, H. and Huber, W. Kastentestfunktion als Näherung für die Wellenfunktion des Elektrons im Wasserstoffatom und im Wasserstoffmolekelion. *Helv. Chim. Acta*, **1952**, *35*(4), 1155. doi:10.1002/hlca.19520350409.

[81] Ishii, H. and Seki, K. Energy level alignment at organic/metal interfaces studied by UV photoemission: Breakdown of traditional assumption of a common vacuum level at the interface. *IEEE Trans. Electron Devices*, **1997**, *44*(8), 1295. doi:10.1109/16.605471.

[82] Harima, Y.; Kodaka, T.; Okazaki, H.; Kunugi, Y.; Yamashita, K.; Ishii, H.; and Seki, K. A relationship between a metal work function and a diffusion potential at Schottky barriers in photovoltaic cells based on a molecular semiconductor. *Chem. Phys. Lett.*, **1995**, *240*(4), 345. doi:10.1016/0009-2614(95)00540-K.

[83] Seki, K.; Tani, T.; and Ishii, H. Electronic structures of organic-inorganic interfaces studied by UV photoemission. *Thin Solid Films*, **1996**, *273*(1-2), 20. doi:10.1016/0040-6090(95)06765-5.

[84] Ishii, H.; Yoshimura, D.; Sugiyama, K.; Narioka, S.; Hamatani, Y.; Kawamoto, I.; Miyazaki, T.; Ouchi, Y.; and Seki, K. Electronic structure of 8-hydroxyquinoline aluminum (alq3)/metal interfaces studied by UV photoemission. *Synth. Met.*, **1997**, *85*(1-3), 1389. doi:10.1016/S0379-6779(97)80286-X.

[85] Seki, K.; Ito, E.; and Ishii, H. Energy level alignment at organic/metal interfaces studied by UV photoemission. *Synth. Met.*, **1997**, *91*(1-3), 137. doi:10.1016/S0379-6779(98)80075-1.

[86] Sugiyama, K.; Yoshimura, D.; Ito, E.; Miyazaki, T.; Hamatani, Y.; Kawamoto, I.; Ishii, H.; Ouchi, Y.; and Seki, K. Electronic structure of organic carrier transporting material / metal interfaces as a model interface of electroluminescent device studied by UV photoemission. *Synth. Met.*, **1997**, *86*(1-3), 2425. doi:10.1016/S0379-6779(97)81185-X.

[87] Yoshimura, D.; Ishii, H.; Narioka, S.; Sei, M.; Miyazaki, T.; Ouchi, Y.; Hasegawa, S.; Harima, Y.; Yamashita, K.; and Seki, K. The electronic structure of porphyrin/metal interfaces studied by UV photoemission spectroscopy. *Synth. Met.*, **1997**, *86*(1-3), 2399. doi:10.1016/S0379-6779(97)81177-0.

[88] Kroemer, H. Band offsets and chemical bonding: The basis for heterostructure applications. *Phys. Scr.*, **1996**, *T68*, 10. doi:10.1088/0031-8949/1996/t68/001.

[89] Xiao, J. The Study of Molecular Band Offsets at the Heteromolecular Interface. Ph.D. thesis, University of Nebraska, **2009**.

[90] Strayer, R. W.; Mackie, W.; and Swanson, L. W. Work function measurements by the field emission retarding potential method. *Surf. Sci.*, **1973**, *34*(2), 225. doi:10.1016/0039-6028(73)90117-9.

[91] Hill, I. G.; Rajagopal, A.; Kahn, A.; and Hu, Y. Molecular level alignment at organic semiconductor-metal interfaces. *Appl. Phys. Lett.*, **1998**, *73*(5), 662. doi:10.1063/1.121940.

[92] Wandelt, K. and Hulse, J. E. Xenon adsorption on palladium. I. The homogeneous (110), (100), and (111) surfaces. *J. Chem. Phys*, **1984**, *80*(3), 1340. doi:10.1063/1.446815.

[93] Ito, E.; Oji, H.; Ishii, H.; Oichi, K.; Ouchi, Y.; and Seki, K. Interfacial electronic structure of long-chain alkane/metal systems studied by UV-photoelectron and metastable atom electron spectroscopies. *Chem. Phys. Lett.*, **1998**, *287*(1-2), 137. doi:10.1016/S0009-2614(98)00153-5.

[94] Witte, G.; Lukas, S.; Bagus, P. S.; and Woll, C. Vacuum level alignment at organic/metal junctions: "Cushion" effect and the interface dipole. *Appl. Phys. Lett.*, **2005**, *87*(26), 3. doi:263502 10.1063/1.2151253.

[95] Kuhlenbeck, H.; Saalfeld, H. B.; Buskotte, U.; Neumann, M.; Freund, H. J.; and Plummer, E. W. π-d backbonding band dispersion and final-state effects for the (2×1) *p2mg* phase of CO on Ni(110). *Phys. Rev. B*, **1989**, *39*(6), 3475. doi:10.1103/PhysRevB.39.3475.

[96] Mitsui, T.; Rose, M. K.; Fomin, E.; Ogletree, D. F.; and Salmeron, M. Dissociative hydrogen adsorption on palladium requires aggregates of three or more vacancies. *Nature*, **2003**, *422*(6933), 705. doi:10.1038/nature01557.

[97] Seki, K.; Yanagi, H.; Kobayashi, Y.; Ohta, T.; and Tani, T. UV photoemission study of dye/AgBr interfaces in relation to spectral sensitization. *Phys. Rev. B*, **1994**, *49*(4), 2760. doi:10.1103/PhysRevB.49.2760.

[98] Brillson, L. J. The structure and properties of metal-semiconductor interfaces. *Surf. Sci. Rep.*, **1982**, *2*(2), 123. doi:10.1016/0167-5729(82)90001-2.

[99] Hill, I. G. and Kahn, A. Combined photoemission/in vacuo transport study of the indium tin oxide/copper phthalocyanine/*N,N′*-diphenyl-*N,N′*-bis(l-naphthyl)-1,1′biphenyl-4,4″diamine molecular organic semiconductor system. *J. Appl. Phys.*, **1999**, *86*(4), 2116. doi:10.1063/1.371018.

[100] Ishii, H.; Hasegawa, S.; Yoshimura, D.; Sugiyama, K.; Narioka, S.; Sei, M.; Ouchi, Y.; Seki, K.; Harima, Y.; and Yamashita, K. Electronic structures of porphyrins and their interfaces with metals studied by UV photoemission. *Mol. Cryst. Liq. Cryst. Sci. Technol. Sect. A-Mol. Cryst. Liq. Cryst.*, **1997**, *296*, 427. doi:10.1080/10587259708032338.

[101] Gao, Y. Surface analytical studies of interfaces in organic semiconductor devices. *Mater. Sci. Eng. R-Rep.*, **2010**, *68*(3), 39. doi:10.1016/j.mser.2010.01.001.

[102] Nordling, C.; Sokolowski, E.; and Siegbahn, K. Precision Method for Obtaining Absolute Values of Atomic Binding Energies. *Phys. Rev.*, **1957**, *105*(5), 1676. doi:10.1103/PhysRev.105.1676.

[103] Moulder, J. and Chastain, J. *Handbook of X-ray Photoelectron Spectroscopy: A Reference Book of Standard Spectra for Identification and Interpretation of XPS Data.* Physical Electronics Division, Perkin-Elmer Corporation, **1992**.

[104] Siegbahn, K. Electron spectroscopy for chemical analysis (e.s.c.a.). *Philosophical Transactions of the Royal Society of London Series a-Mathematical and Physical Sciences*, **1970**, *268*(1184), 33. doi:10.1098/rsta.1970.0060.

[105] Hagstrom, S.; Nordling, C.; and Siegbahn, K. Electron spectroscopy for chemical analysis. *Phys. Lett.*, **1964**, *9*(3), 235. doi:10.1016/0031-9163(64)90062-9.

[106] Siegbahn, K. and Edvarson, K. ß-Ray spectroscopy in the precision range of $1 : 10^5$. *Nucl. Phys.*, **1956**, *1*(8), 137. doi:10.1016/S0029-5582(56)80022-9.

[107] Robinson, H. and Rawlinson, W. The magnetic spectrum of the beta rays excited in metals by soft X rays. *Phil. Mag.*, **1914**, *28*, 277. doi:10.1080/14786440808635209.

[108] Broglie, M. D. Sur les spectres corpusculaires des éléments. *Compt. Rend. Acad. Sci.*, **1921**, *172*, 274. doi:10.1051/jphys-rad:0192100209026500.

[109] Schmid, M.; Steinrück, H.-P.; and Gottfried, J. M. A new asymmetric Pseudo-Voigt function for more efficient fitting of XPS lines. *Surf. Interface Anal.*, **2014**, *46*(8), 505. doi:10.1002/sia.5521.

[110] Duke, C. B. The birth and evolution of surface science: Child of the union of science and technology. *Proc. Natl. Acad. Sci. U.S.A.*, **2003**, *100*(7), 3858. doi:10.1073/pnas.0730358100.

[111] Jablonski, A. and Powell, C. J. The electron attenuation length revisited. *Surf. Sci. Rep.*, **2002**, *47*(2-3), 35. doi:Pii s0167-5729(02)00031-6.

[112] Ertl, G. and Küppers, J. *Low Energy Electrons and Surface Chemistry.* 2nd edition, VCH Verlagsgesellschaft, Weinheim, Germany, **1985**.

[113] SPECS. *User Manual for UV-Source UVS 10/35.*, version 2.4 edition, **2009**.

[114] Chelvayohan, M. and Mee, C. H. B. Work function measurements on (110), (100) and (111) surfaces of silver. *J. Phys. C: Solid State Phys.*, **1982**, *15*(10), 2305. doi:10.1088/0022-3719/15/10/029.

[115] Dweydari, A. W. and Mee, C. H. B. Work Function Measurements on (100) and (110) Surfaces of Silver. *Phys. Status Solidi A*, **1975**, *27*(1), 223. doi:10.1002/pssa.2210270126.

[116] Carlson, T. A. and McGuire, G. E. Study of the x-ray photoelectron spectrum of tungsten-tungsten oxide as a function of thickness of the surface oxide layer. *J. Electron Spectrosc. Relat. Phenom.*, **1972**, *1*(2), 161. doi:10.1016/0368-2048(72)80029-X.

[117] Powell, C. J. and Jablonski, A. Progress in quantitative surface analysis by X-ray photoelectron spectroscopy: Current status and perspectives. *J. Electron Spectrosc. Relat. Phenom.*, **2010**, *178-179*, 331. doi:10.1016/j.elspec.2009.05.004.

[118] Seah, M. P.; Gilmore, I. S.; and Spencer, S. J. Quantitative XPS: I. Analysis of X-ray photoelectron intensities from elemental data in a digital photoelectron database. *J. Electron Spectrosc. Relat. Phenom.*, **2001**, *120*(1-3), 93. doi:10.1016/S0368-2048(01)00311-5.

[119] Wagner, C. D. Sensitivity factors for XPS analysis of surface atoms. *J. Electron Spectrosc. Relat. Phenom.*, **1983**, *32*(2), 99. doi:10.1016/0368-2048(83)85087-7.

[120] Atomic Calculation of Photoionization Cross-Sections and Asymmetry Parameters. `https://vuo.elettra.eu/services/elements/WebElements.html`.

[121] Berger, M.; Hubbell, J.; Seltzer, S.; Chang, J.; Coursey, J.; Sukumar, R.; Zucker, D.; and Olsen, K. XCOM: Photon Cross Sections Database. `http://www.nist.gov/pml/data/xcom/`, **2010**.

[122] Cumpson, P. J. and Seah, M. P. Elastic scattering corrections in AES and XPS .2. Estimating attenuation lengths and conditions required for their valid use in overlayer/-substrate experiments. *Surf. Interface Anal.*, **1997**, *25*(6), 430. doi:10.1002/(SICI)1096-9918(199706)25:6<430::AID-SIA254>3.0.CO;2-7.

[123] Lesiak, B.; Kosinski, A.; Jablonski, A.; Kover, L.; Toth, J.; Varga, D.; Cserny, I.; Zagorska, M.; Kulszewicz-Bajer, I.; and Gergely, G. Determination of the inelastic mean free path of electrons in polythiophenes using elastic peak electron spectroscopy method. *Appl. Surf. Sci.*, **2001**, *174*(1), 70. doi:10.1016/s0169-4332(01)00025-3.

[124] Tanuma, S.; Powell, C. J.; and Penn, D. R. Calculations of Electron Inelastic Mean Free Paths for 31 Materials. *Surf. Interface Anal.*, **1988**, *11*(11), 577. doi:10.1002/sia.740111107.

[125] Tanuma, S.; Powell, C. J.; and Penn, D. R. Calculations of Electron Inelastic Mean Free Paths II. Data for 27 Elements over the 50-2000 eV Range. *Surf. Interface Anal.*, **1991**, *17*(13), 911. doi:10.1002/sia.740171304.

[126] Tanuma, S.; Powell, C. J.; and Penn, D. R. Calculations of Electron Inelastic Mean Free Paths III. Data for 15 Inorganic Compunds over the 50-2000 eV Range. *Surf. Interface Anal.*, **1991**, *17*(13), 927. doi:10.1002/sia.740171305.

[127] Tanuma, S.; Powell, C. J.; and Penn, D. R. Inelastic Mean Free Paths of Low-Energy Electrons in Solids. *Acta Phys. Pol. A*, **1992**, *81*(2), 169.

[128] Tanuma, S.; Powell, C. J.; and Penn, D. R. Calculations of Electron Inelastic Mean Free Paths (IMFPs) IV. Evaluation of Calculated IMFPs and of the Predictive IMFP Formula TPP-2 for Electron Energies between 50 and 2000 eV. *Surf. Interface Anal.*, **1993**, *20*(1), 77. doi:10.1002/sia.740200112.

[129] Tanuma, S.; Powell, C. J.; and Penn, D. R. Calculations of Electron Inelastic Mean Free Paths. V. Data for 14 Organic Compounds over the 50-2000 eV Range. *Surf. Interface Anal.*, **1994**, *21*(3), 165. doi:10.1002/sia.740210302.

[130] Tanuma, S.; Powell, C. J.; and Penn, D. R. Calculations of electron inelastic mean free paths (IMFPs) .6. Analysis of the Gries inelastic scattering model and predictive IMFP equation. *Surf. Interface Anal.*, **1997**, *25*(1), 25. doi:10.1002/(sici)1096-9918(199701)25:1<25::aid-sia207>3.0.co;2-2.

[131] Tanuma, S.; Powell, C. J.; and Penn, D. R. Calculation of electron inelastic mean free paths (IMFPs) VII. Reliability of the TPP-2M IMFP predictive equation. *Surf. Interface Anal.*, **2003**, *35*(3), 268. doi:10.1002/sia.1526.

[132] Tanuma, S.; Powell, C. J.; and Penn, D. R. Calculations of electron inelastic mean free paths. VIII. Data for 15 elemental solids over the 50-2000 eV range. *Surf. Interface Anal.*, **2005**, *37*(1), 1. doi:10.1002/sia.1997.

[133] Tanuma, S.; Powell, C. J.; and Penn, D. R. Calculations of electron inelastic mean free paths. IX. Data for 41 elemental solids over the 50 eV to 30 keV range. *Surf. Interface Anal.*, **2011**, *43*(3), 689. doi:10.1002/sia.3522.

[134] Ashley, J. C.; Tung, C. J.; and Ritchie, R. H. Inelastic interactions of electrons with polystyrene-calculations of mean free paths, stopping powers, and CSDA ranges. *IEEE Trans. Nucl. Sci.*, **1978**, *25*(6), 1566. doi:10.1109/tns.1978.4329573.

[135] Hamor, M. J.; Hamor, T. A.; and Hoard, J. L. The Structure of Crystalline Tetraphenylporphine. The Stereochemical Nature of the Porphine Skeleton. *J. Am. Chem. Soc.*, **1964**, *86*(10), 1938. doi:10.1021/ja01064a008.

[136] Madura, P. and Scheidt, W. R. Stereochemistry of Low-Spin Cobalt Porphyrins. 8. α, β, γ, δ-Tetraphenylporphinatocobalt (II). *Inorg. Chem.*, **1976**, *15*(12), 3182. doi:10.1021/ic50166a056.

[137] Zhu, J.; Bebensee, F.; Hieringer, W.; Zhao, W.; Baricuatro, J. H.; Farmer, J. A.; Bai, Y.; Steinrück, H.-P.; Gottfried, J. M.; and Campbell, C. T. Formation of the Calcium/Poly(3-Hexylthiophene) Interface: Structure and Energetics. *J. Am. Chem. Soc.*, **2009**, *131*(37), 13498. doi:10.1021/ja904844c.

[138] McCafferty, E. and Wightman, J. P. Determination of the concentration of surface hydroxyl groups on metal oxide films by a quantitative XPS method. *Surf. Interface Anal.*, **1998**, *26*(8), 549. doi:10.1002/(sici)1096-9918(199807)26:8<549::aid-sia396>3.3.co;2-h.

[139] Hickmott, T. W. and Ehrlich, G. Structure-sensitive chemisorption: The mechanism of desorption from tungsten. *J. Phys. Chem. Solids*, **1958**, *5*(1), 47. doi:10.1016/0022-3697(58)90131-8.

[140] Bebensee, F. Metal-Polymer Interfaces Studied with Adsorption Microcalorimetry and Photoelectron Spectroscopy. Ph.D. thesis, Friedrich-Alexander-Universität Erlangen-Nürnberg, **2010**.

[141] Redhead, P. A. Thermal desorption of gases. *Vacuum*, **1962**, *12*(4), 203. doi:10.1016/0042-207X(62)90978-8.

[142] Tamm, P. W. and Schmidt, L. D. Binding States of Hydrogen on Tungsten. *J. Chem. Phys*, **1971**, *54*(11), 4775. doi:10.1063/1.1674753.

[143] Binnig, G. and Rohrer, H. Scanning tunneling microscopy. *Surf. Sci.*, **1983**, *126*(1), 236. doi:10.1016/0039-6028(83)90716-1.

[144] Besenbacher, F. Scanning tunnelling microscopy studies of metal surfaces. *Rep. Prog. Phys.*, **1996**, *59*(12), 1737. doi:10.1088/0034-4885/59/12/004.

[145] Binnig, G. and Rohrer, H. Scanning tunneling microscopy-from birth to adolescence. *Rev. Mod. Phys.*, **1987**, *59*(3), 615. doi:10.1103/RevModPhys.59.615.

[146] Hansma, P. K. and Tersoff, J. Scanning tunneling microscopy. *J. Appl. Phys.*, **1987**, *61*(2), R1. doi:10.1063/1.338189.

[147] Chen, C. J. *Introduciton to Scanning Tunneling Microscopy.* 1st Edition, Oxford University Press, New York, **1993**.

[148] Tersoff, J. and Hamann, D. R. Theory and Application for the Scanning Tunneling Microscope. *Phys. Rev. Lett.*, **1983**, *50*(25), 1998. doi:10.1103/PhysRevLett.50.1998.

[149] Tersoff, J. and Hamann, D. R. Theory of the scanning tunneling microscope. *Phys. Rev. B*, **1985**, *31*(2), 805. doi:10.1103/PhysRevB.31.805.

[150] Bardeen, J. Tunnelling from a Many-Particle Point of View. *Phys. Rev. Lett.*, **1961**, *6*(2), 57. doi:10.1103/PhysRevLett.6.57.

[151] Franc, G. and Gourdon, A. Covalent networks through on-surface chemistry in ultra-high vacuum: state-of-the-art and recent developments. *Phys. Chem. Chem. Phys.*, **2011**, *13*(32), 14283. doi:10.1039/c1cp20700h.

[152] Fanta, P. E. The Ullmann Synthesis of Biaryls. *Synthesis-Stuttgart*, **1974**, (1), 9. doi:10.1055/s-1974-23219.

[153] Villagomez, C. J.; Zambelli, T.; Gauthier, S.; Gourdon, A.; Stojkovic, S.; and Joachim, C. STM images of a large organic molecule adsorbed on a bare metal substrate or on a thin insulating layer: Visualization of HOMO and LUMO. *Surf. Sci.*, **2009**, *603*(10-12), 1526. doi:10.1016/j.susc.2008.10.057.

[154] Binnig, G.; Rohrer, H.; Gerber, C.; and Weibel, E. Tunneling through a controllable vacuum gap. *Appl. Phys. Lett.*, **1982**, *40*(2), 178. doi:10.1063/1.92999.

[155] Binnig, G.; Rohrer, H.; Gerber, C.; and Weibel, E. Surface Studies by Scanning Tunneling Microscopy. *Phys. Rev. Lett.*, **1982**, *49*, 57. doi:10.1103/PhysRevLett.49.57.

[156] Binnig, G.; Frank, K. H.; Fuchs, H.; Garcia, N.; Reihl, B.; Rohrer, H.; Salvan, F.; and Williams, A. R. Tunneling Spectroscopy and Inverse Photoemission: Image and Field States. *Phys. Rev. Lett.*, **1985**, *55*(9), 991. doi:10.1103/PhysRevLett.55.991.

[157] Becker, R. S.; Golovchenko, J. A.; Hamann, D. R.; and Swartzentruber, B. S. Real-Space Observation of Surface States on Si(111) 7x7 with the Tunneling Microscope. *Phys. Rev. Lett.*, **1985**, *55*(19), 2032. doi:10.1103/PhysRevLett.55.2032.

[158] Hamers, R. J.; Tromp, R. M.; and Demuth, J. E. Surface Electronic Structure of Si (111)-(7x7) Resolved in Real Space. *Phys. Rev. Lett.*, **1986**, *56*(18), 1972. doi:10.1103/PhysRevLett.56.1972.

[159] Hamers, R. J.; Tromp, R. M.; and Demuth, J. E. Electronic and geometric structure of Si(111)-(7x7) and Si(001) surfaces. *Surf. Sci.*, **1987**, *181*(1), 346. doi:10.1016/0039-6028(87)90176-2.

[160] Hamers, R. J. Atomic-resolution surface spectroscopy with the scanning tunneling microscope. *Annu. Rev. Phys. Chem.*, **1989**, *40*, 531. doi:10.1146/annurev.pc.40.100189.002531.

[161] Gottfried, J. M. Surface Chemistry of Porphyrins and other Complex Adsorbate Systems. Habilitation, Friedrich-Alexander-Universität Erlangen-Nürnberg, **2009**.

[162] Gorgoi, M.; Svensson, S.; Schäfers, F.; Öhrwall, G.; Mertin, M.; Bressler, P.; Karis, O.; Siegbahn, H.; Sandell, A.; Rensmo, H.; Doherty, W.; Jung, C.; Braun, W.; and Eberhardt, W. The high kinetic energy photoelectron spectroscopy facility at BESSY progress and first results. *Nucl. Instrum. Methods Phys. Res., Sect. A*, **2009**, *601*(1-2), 48. doi:10.1016/j.nima.2008.12.244.

[163] Schaefers, F.; Mertin, M.; and Gorgoi, M. KMC-1: A high resolution and high flux soft x-ray beamline at BESSY. *Rev. Sci. Instrum.*, **2007**, *78*(12). doi:123102 10.1063/1.2808334.

[164] Horcas, I.; Fernandez, R.; Gomez-Rodriguez, J. M.; Colchero, J.; Gomez-Herrero, J.; and Baro, A. M. WSXM: A software for scanning probe microscopy and a tool for nanotechnology. *Rev. Sci. Instrum.*, **2007**, *78*(1). doi:013705 10.1063/1.2432410.

[165] Gottfried, J. M. and Marbach, H. Surface-Confined Coordination Chemistry with Porphyrins and Phthalocyanines: Aspects of Formation, Electronic Structure, and Reactivity. *Z. Phys. Chem.*, **2009**, *223*(1-2), 53. doi:10.1524/zpch.2009.6024.

[166] Auwärter, W.; Weber-Bargioni, A.; Brink, S.; Riemann, A.; Schiffrin, A.; Ruben, M.; and Barth, J. V. Controlled metalation of self-assembled porphyrin nanoarrays in two dimensions. *ChemPhysChem*, **2007**, *8*(2), 250. doi:10.1002/cphc.200600675.

[167] Bai, Y.; Buchner, F.; Wendahl, M. T.; Kellner, I.; Bayer, A.; Steinrück, H.-P.; Marbach, H.; and Gottfried, J. M. Direct metalation of a phthalocyanine monolayer on Ag(111) with coadsorbed iron atoms. *J. Phys. Chem. C*, **2008**, *112*(15), 6087. doi:10.1021/jp711122w.

[168] Buchner, F.; Schwald, V.; Comanici, K.; Steinrück, H.-P.; and Marbach, H. Microscopic evidence of the metalation of a free-base porphyrin monolayer with iron. *ChemPhysChem*, **2007**, *8*(2), 241. doi:10.1002/cphc.200600698.

[169] Écija, D.; Auwärter, W.; Vijayaraghavan, S.; Seufert, K.; Bischoff, F.; Tashiro, K.; and Barth, J. V. Assembly and Manipulation of Rotatable Cerium Porphyrinato Sandwich Complexes on a Surface. *Angew. Chem. Int. Ed.*, **2011**, *50*(17), 3872. doi:10.1002/anie.201007370.

[170] Weber-Bargioni, A.; Reichert, J.; Seitsonen, A. P.; Auwärter, W.; Schiffrin, A.; and Barth, J. V. Interaction of cerium atoms with surface-anchored porphyrin molecules. *J. Phys. Chem. C*, **2008**, *112*(10), 3453. doi:10.1021/jp076961i.

[171] Buchner, F.; Xiao, J.; Zillner, E.; Chen, M.; Roeckert, M.; Ditze, S.; Stark, M.; Steinrück, H.-P.; Gottfried, J. M.; and Marbach, H. Diffusion, Rotation, and Surface Chemical Bond of Individual 2H-Tetraphenylporphyrin Molecules on Cu(111). *J. Phys. Chem. C*, **2011**, *115*(49), 24172. doi:10.1021/jp206675u.

[172] Shi, Z.; Lin, T.; Liu, J.; Liu, P. N.; and Lin, N. Regulating a two-dimensional metallo-supramolecular self-assembly of multiple outputs. *CrystEngComm*, **2011**, *13*(18), 5532. doi:10.1039/c1ce05340j.

[173] Li, Y. and Lin, N. Combined scanning tunneling microscopy and kinetic Monte Carlo study on kinetics of Cu-coordinated pyridyl-porphyrin supramolecular self-assembly on a Au(111) surface. *Phys. Rev. B*, **2011**, *84*(12). doi:125418 10.1103/PhysRevB.84.125418.

[174] Fain, S. C. and McDavid, J. M. Work-function variation with alloy composition: Cu-Au. *Phys. Rev. B*, **1976**, *13*(4), 1853. doi:10.1103/PhysRevB.13.1853.

[175] Grillo, F.; Früchtl, H.; Francis, S. M.; and Richardson, N. V. Site selectivity in the growth of copper islands on Au (111). *New J. Phys.*, **2011**, *13*(1), 013044. doi:10.1088/1367-2630/13/1/013044.

[176] Buchner, F.; Zillner, E.; Rockert, M.; Glassel, S.; Steinrück, H. P.; and Marbach, H. Substrate-Mediated Phase Separation of Two Porphyrin Derivatives on Cu(111). *Chem. Eur. J.*, **2011**, *17*(37), 10226. doi:10.1002/chem.201100462.

[177] Rojas, G.; Chen, X.; Bravo, C.; Kim, J. H.; Kim, J. S.; Xiao, J.; Dowben, P. A.; Gao, Y.; Zeng, X. C.; Choe, W.; and Enders, A. Self-Assembly and Properties of Nonmetalated Tetraphenyl-Porphyrin on Metal Substrates. *J. Phys. Chem. C*, **2010**, *114*(20), 9408. doi:10.1021/jp1012957.

[178] Diller, K.; Klappenberger, F.; Marschall, M.; Hermann, K.; Nefedov, A.; Woll, C.; and Barth, J. V. Self-metalation of 2H-tetraphenylporphyrin on Cu(111): An x-ray spectroscopy study. *J. Chem. Phys.*, **2012**, *136*(1), 14705. doi:10.1063/1.3674165.

[179] Haq, S.; Hanke, F.; Dyer, M. S.; Persson, M.; Iavicoli, P.; Amabilino, D. B.; and Raval, R. Clean Coupling of Unfunctionalized Porphyrins at Surfaces To Give Highly Oriented Organometallic Oligomers. *J. Am. Chem. Soc.*, **2011**, *133*(31), 12031. doi:10.1021/ja201389u.

[180] Gonzalez-Moreno, R.; Sanchez-Sanchez, C.; Trelka, M.; Otero, R.; Cossaro, A.; Verdini, A.; Floreano, L.; Ruiz-Bermejo, M.; Garcia-Lekue, A.; Martin-Gago, J. A.; and Rogero, C. Following the Metalation Process of Protoporphyrin IX with Metal Substrate Atoms at Room Temperature. *J. Phys. Chem. C*, **2011**, *115*(14), 6849. doi:10.1021/jp200533a.

[181] Xiao, J.; Ditze, S.; Chen, M.; Buchner, F.; Stark, M.; Drost, M.; Steinrück, H.-P.; Gottfried, J. M.; and Marbach, H. Temperature-Dependent Chemical and Structural Transformations from 2H-tetraphenylporphyrin to Copper(II)-Tetraphenylporphyrin on Cu(111). *J. Phys. Chem. C*, **2012**, *116*(22), 12275. doi:10.1021/jp301757h.

[182] Goldoni, A.; Pignedoli, C. A.; Di Santo, G.; Castellarin-Cudia, C.; Magnano, E.; Bondino, F.; Verdini, A.; and Passerone, D. Room Temperature Metalation of 2H-TPP Monolayer on Iron and Nickel Surfaces by Picking up Substrate Metal Atoms. *ACS Nano*, **2012**, *6*(12), 10800. doi:10.1021/nn304134q.

[183] Krause, B.; Durr, A. C.; Schreiber, F.; Dosch, H.; and Seeck, O. H. Thermal stability and partial dewetting of crystalline organic thin films: 3,4,9,10-perylenetetracarboxylic dianhydride on Ag(111). *J. Chem. Phys.*, **2003**, *119*(6), 3429. doi:10.1063/1.1589471.

[184] Stöhr, M.; Gabriel, M.; and Moller, R. Analysis of the three-dimensional structure of a small crystallite by scanning tunneling microscopy: Multilayer films of 3,4,9,10-perylenetetracarboxylic-dianhydride (PTCDA) on Cu(110). *Europhys. Lett.*, **2002**, *59*(3), 423. doi:10.1209/epl/i2002-00212-8.

[185] Käfer, D.; Wöll, C.; and Witte, G. Thermally activated dewetting of organic thin films: the case of pentacene on SiO2 and gold. *Appl. Phys. A*, **2009**, *95*(1), 273. doi:10.1007/s00339-008-5011-3.

[186] Kowarik, S.; Gerlach, A.; Leitenberger, W.; Hu, J.; Witte, G.; Wöll, C.; Pietsch, U.; and Schreiber, F. Energy-dispersive X-ray reflectivity and GID for real-time growth studies of pentacene thin films. *Thin Solid Films*, **2007**, *515*(14), 5606. doi:10.1016/j.tsf.2006.12.020.

[187] Chen, M.; Roeckert, M.; Xiao, J.; Drescher, H.-J.; Steinrueck, H.-P.; Lytken, O.; and Gottfried, J. M. Coordination Reactions and Layer Exchange Processes at a Buried Metal-Organic Interface. *J. Phys. Chem. C*, **2014**, *118*(16), 8501. doi:10.1021/jp5019235.

[188] Buchner, F.; Kellner, I.; Hieringer, W.; Gorling, A.; Steinrück, H. P.; and Marbach, H. Ordering aspects and intramolecular conformation of tetraphenylporphyrins on Ag(111). *Phys. Chem. Chem. Phys.*, **2010**, *12*(40), 13082. doi:10.1039/c004551a.

[189] Brede, J.; Linares, M.; Kuck, S.; Schwoebel, J.; Scarfato, A.; Chang, S.-H.; Hoffmann, G.; Wiesendanger, R.; Lensen, R.; Kouwer, P. H. J.; Hoogboom, J.; Rowan, A. E.; Broering, M.; Funk, M.; Stafstrom, S.; Zerbetto, F.; and Lazzaroni, R. Dynamics of molecular self-ordering in tetraphenyl porphyrin monolayers on metallic substrates. *Nanotechnology*, **2009**, *20*(27). doi:275602 10.1088/0957-4484/20/27/275602.

[190] Auwärter, W.; Klappenberger, F.; Weber-Bargioni, A.; Schiffrin, A.; Strunskus, T.; Woll, C.; Pennec, Y.; Riemann, A.; and Barth, J. V. Conformational adaptation and selective adatom capturing of tetrapyridyl-porphyrin molecules on a copper (111) surface. *J. Am. Chem. Soc.*, **2007**, *129*(36), 11279. doi:10.1021/ja071572n.

[191] Alfredsson, Y.; Åhlund, K., J.and Nilson; Kjeldgaard, L.; O'Shea, J. N.; Theobald, J.; Bao, Z.; Mråtensson, N.; Sandell, A.; Puglia, C.; and Siegbahn, H. Phase and molecular orientation in metal-free phthalocyanine films on conducting glass: Characterization of two deposition methods. *Thin Solid Films*, **2005**, *493*(1-2), 13. doi:10.1016/j.tsf.2005.05.012.

[192] Alfredsson, Y.; Brena, B.; Nilson, K.; Åhlund, J.; Kjeldgaard, L.; Nyberg, M.; Luo, Y.; Mårtensson, N.; Sandell, A.; Puglia, C.; and Siegbahn, H. Electronic structure of a vapor-deposited metal-free phthalocyanine thin film. *J. Chem. Phys.*, **2005**, *122*(21), 214723. doi:10.1063/1.1924539.

[193] Stepanow, S.; Miedema, P. S.; Mugarza, A.; Ceballos, G.; Moras, P.; Cezar, J. C.; Carbone, C.; de Groot, F. M. F.; and Gambardella, P. Mixed-valence behavior and

strong correlation effects of metal phthalocyanines adsorbed on metals. *Phys. Rev. B*, **2011**, *83*(22), 220401. doi:10.1103/PhysRevB.83.220401.

[194] Gargiani, P.; Angelucci, M.; Mariani, C.; and Betti, M. G. Metal-phthalocyanine chains on the Au(110) surface: Interaction states versus *d*-metal states occupancy. *Phys. Rev. B*, **2010**, *81*, 085412. doi:10.1103/PhysRevB.81.085412.

[195] Salomon, E.; Amsalem, P.; Marom, N.; Vondracek, M.; Kronik, L.; Koch, N.; and Angot, T. Electronic structure of CoPc adsorbed on Ag(100): Evidence for molecule-substrate interaction mediated by Co 3*d* orbitals. *Phys. Rev. B*, **2013**, *87*, 075407. doi:10.1103/PhysRevB.87.075407.

[196] Mugarza, A.; Robles, R.; Krull, C.; Korytár, R.; Lorente, N.; and Gambardella, P. Electronic and magnetic properties of molecule-metal interfaces: Transition-metal phthalocyanines adsorbed on Ag(100). *Phys. Rev. B*, **2012**, *85*(15), 155437. doi:10.1103/PhysRevB.85.155437.

[197] Glaser, M.; Peisert, H.; Adler, H.; Aygül, U.; Ivanovic, M.; Nagel, P.; Merz, M.; Schuppler, S.; and Chassé, T. Electronic structure at transition metal phthalocyanine-transition metal oxide interfaces: Cobalt phthalocyanine on epitaxial MnO films. *J. Chem. Phys*, **2015**, *142*(10), 101918. doi:http://dx.doi.org/10.1063/1.4907899.

[198] Buchner, F.; Warnick, K.-G.; Woelfle, T.; Goerling, A.; Steinrueck, H.-P.; Hieringer, W.; and Marbach, H. Chemical Fingerprints of Large Organic Molecules in Scanning Tunneling Microscopy: Imaging Adsorbate-Substrate Coupling of Metalloporphyrins. *J. Phys. Chem. C*, **2009**, *113*(37), 16450. doi:10.1021/jp904680c.

[199] Bai, Y.; Buchner, F.; Kellner, I.; Schmid, M.; Vollnhals, F.; Steinrück, H.-P.; Marbach, H.; and Gottfried, J. M. Adsorption of cobalt (II) octaethylporphyrin and 2H-octaethylporphyrin on Ag(111): new insight into the surface coordinative bond. *New J. Phys.*, **2009**, *11*. doi:125004 10.1088/1367-2630/11/12/125004.

[200] Schroeder, P. G.; France, C. B.; Park, J. B.; and Parkinson, B. A. Orbital Alignment and Morphology of Pentacene Deposited on Au(111) and SnS2 Studied Using Photoemission Spectroscopy. *J. Phys. Chem. B*, **2003**, *107*(10), 2253. doi:10.1021/jp025807n.

[201] Koch, N. Energy levels at interfaces between metals and conjugated organic molecules. *J. Phys. Condens. Matter*, **2008**, *20*(18). doi:184008 10.1088/0953-8984/20/18/184008.

[202] Briggs, D. and Gibson, V. A. Direct observation of multiplet splitting in 2p photoelectron peaks of cobalt complexes. *Chem. Phys. Lett.*, **1974**, *25*(4), 493. doi:10.1016/0009-2614(74)85350-9.

[203] Ivanova, T.; Naumkin, A.; Sidorov, A.; Eremenko, I.; and Kiskin, M. X-ray photoelectron spectra and electron structure of polynuclear cobalt complexes. *J. Electron Spectrosc. Relat. Phenom.*, **2007**, *156-158*(0), 200. doi:10.1016/j.elspec.2006.12.005.

[204] Di Santo, G.; Castellarin-Cudia, C.; Fanetti, M.; Taleatu, B.; Borghetti, P.; Sangaletti, L.; Floreano, L.; Magnano, E.; Bondino, F.; and Goldoni, A. Conformational Adaptation and Electronic Structure of 2H-Tetraphenylporphyrin on Ag(111) during Fe Metalation. *J. Phys. Chem. C*, **2011**, *115*(10), 4155. doi:10.1021/jp111151n.

[205] Frost, D. C.; McDowell, C. A.; and Woolsey, I. S. Evidence for multiplet splitting of 2p photoelectron lines of transition metal complexes. *Chem. Phys. Lett.*, **1972**, *17*(3), 320. doi:10.1016/0009-2614(72)87086-6.

[206] Frost, D. C.; McDowell, C. A.; and Woolsey, I. S. X-ray photoelectron spectra of cobalt compounds. *Mol. Phys.*, **1974**, *27*(6), 1473. doi:10.1080/00268977400101251.

[207] Werner, W. S. M.; Smekal, W.; Hisch, T.; Himmelsbach, J.; and Powell, C. J. Simulation of Electron Spectra for Surface Analysis (SESSA)for quantitative interpretation of (hard) X-ray photoelectron spectra(HAXPES). *J. Electron Spectrosc. Relat. Phenom.*, **2013**, *190*, 137. doi:10.1016/j.elspec.2013.06.007.

[208] Werner, W. S. M. Electron transport in solids for quantitative surface analysis. *Surf. Interface Anal.*, **2001**, *31*(3), 141. doi:10.1002/sia.973.

[209] Smekal, W.; Werner, W. S. M.; and Powell, C. J. Simulation of electron spectra for surface analysis (SESSA): a novel software tool for quantitative Auger-electron spectroscopy and X-ray photoelectron spectroscopy. *Surf. Interface Anal.*, **2005**, *37*(11), 1059. doi:10.1002/sia.2097.

[210] Mousty-Desbuquoit, C.; Riga, J.; and Verbist, J. J. Electronic structure of titanium(III) and titanium(IV) halides studied by solid-phase x-ray photoelectron spectroscopy. *Inorg. Chem.*, **1987**, *26*(8), 1212. doi:10.1021/ic00255a008.

[211] Mayer, J. T.; Diebold, U.; Madey, T. E.; and Garfunkel, E. Titanium and Reduced Titania Overlayers on Titanium Dioxide(110). *J. Electron Spectrosc. Relat. Phenom.*, **1995**, *73*(1), 1. doi:10.1016/0368-2048(94)02258-5.

[212] Oku, M.; Wagatsuma, K.; and Kohiki, S. Ti 2p and Ti 3p X-ray photoelectron spectra for TiO_2, $SrTiO_3$ and $BaTiO_3$. *Phys. Chem. Chem. Phys.*, **1999**, *1*(23), 5327. doi:10.1039/a907161j.

[213] Grosvenor, A. P.; Biesinger, M. C.; Smart, R. S. C.; and McIntyre, N. S. New interpretations of XPS spectra of nickel metal and oxides. *Surf. Sci.*, **2006**, *600*(9), 1771. doi:10.1016/j.susc.2006.01.041.

[214] Atanasov, M. and Reinen, D. Non-local electronic effects in core-level photoemission, UV and optical electronic absorption spectra of nickel oxides1. *J. Electron Spectrosc. Relat. Phenom.*, **1997**, *86*(1-3), 185. doi:10.1016/S0368-2048(97)00065-0.

[215] Biesinger, M. C.; Lau, L. W. M.; Gerson, A. R.; and Smart, R. S. C. The role of the Auger parameter in XPS studies of nickel metal, halides and oxides. *Phys. Chem. Chem. Phys.*, **2012**, *14*(7), 2434. doi:10.1039/c2cp22419d.

[216] Biesinger, M. C.; Payne, B. P.; Grosvenor, A. P.; Lau, L. W. M.; Gerson, A. R.; and Smart, R. S. C. Resolving surface chemical states in XPS analysis of first row transition metals, oxides and hydroxides: Cr, Mn, Fe, Co and Ni. *Appl. Surf. Sci.*, **2011**, *257*(7), 2717. doi:10.1016/j.apsusc.2010.10.051.

[217] Nesbitt, H. W. and Banerjee, D. Interpretation of XPS Mn(2p) spectra of Mn oxyhydroxides and constraints on the mechanism of MnO_2 precipitation. *Am. Mineral.*, **1998**, *83*(3-4), 305. doi:10.2138/am-1998-3-414.

[218] Gupta, R. P. and Sen, S. K. Calculation of multiplet structure of core p-vacancy levels. *Phys. Rev. B*, **1974**, *10*(1), 71. doi:10.1103/PhysRevB.10.71.

[219] Gupta, R. P. and Sen, S. K. Calculation of multiplet structure of core p-vacancy levels. II. *Phys. Rev. B*, **1975**, *12*(1), 15. doi:10.1103/PhysRevB.12.15.

[220] Ladacki, M. and Szwarc, M. Studies of the variations in bond dissociation energies of aromatic compounds. 1. Mono-bromo-aryles. *Proceedings of the Royal Society of London Series a-Mathematical and Physical Sciences*, **1953**, *219*(1138), 341. doi:10.1098/rspa.1953.0151.

[221] Björk, J.; Hanke, F.; and Stafström, S. Mechanisms of Halogen-Based Covalent Self-Assembly on Metal Surfaces. *J. Am. Chem. Soc.*, **2013**, *135*(15), 5768. doi:10.1021/ja400304b.

[222] Yoon, J. K.; Son, W.-j.; Chung, K.-H.; Kim, H.; Han, S.; and Kahng, S.-J. Visualizing Halogen Bonds in Planar Supramolecular Systems. *J. Phys. Chem. C*, **2011**, *115*(5), 2297. doi:10.1021/jp110891y.

[223] Gaab, K. M.; Thompson, A. L.; Xu, J. J.; Martinez, T. J.; and Bardeen, C. J. Meta-conjugation and excited-state coupling in phenylacetylene dendrimers. *J. Am. Chem. Soc.*, **2003**, *125*(31), 9288. doi:10.1021/ja029489h.

[224] Phelan, N. F. and Orchin, M. Cross conjugation. *J. Chem. Educ.*, **1968**, *45*(10), 633. doi:10.1021/ed045p633.

[225] Conversano, E. and Tedeschini-Lalli, L. Sierpinsky Triangles in Stone, on Medieval Floors in Rome. *Aplimat J. Appl. Math.*, **2011**, *4*, 113.

[226] Mandelbrot, B. B. *The Fractal Geometry of Nature.* W. H. Freemann and Company, New York, **1982**.

[227] Libbrecht, K. G. The physics of snow crystals. *Rep. Prog. Phys.*, **2005**, *68*(4), 855. doi:10.1088/0034-4885/68/4/r03.

[228] Politzer, P.; Murray, J. S.; and Clark, T. Halogen bonding: an electrostatically-driven highly directional noncovalent interaction. *Phys. Chem. Chem. Phys.*, **2010**, *12*, 7748. doi:10.1039/C004189K.

[229] Clark, T. σ-Holes. *Wiley Interdisciplinary Reviews: Computational Molecular Science*, **2013**, *3*(1), 13. doi:10.1002/wcms.1113.

[230] Chen, M.; Xiao, J.; Steinrueck, H.-P.; Wang, S.; Wang, W.; Lin, N.; Hieringer, W.; and Gottfried, J. M. Combined Photoemission and Scanning Tunneling Microscopy Study of the Surface-Assisted Ullmann Coupling Reaction. *J. Phys. Chem. C*, **2014**, *118*(13), 6820. doi:10.1021/jp4121468.

[231] Shang, J.; Wang, Y.; Chen, M.; Dai, J.; Zhou, X.; Kuttner, J.; Hilt, G.; Shao, X.; Gottfried, J. M.; and Wu, K. Assembling molecular Sierpinski triangle fractals. *Nat. Chem.*, **2015**, *7*(5), 389. doi:10.1038/nchem.2211.

[232] Sachs, M.; Gellert, M.; Chen, M.; Drescher, H.-J.; Kachel, S. R.; Zhou, H.; Zugermeier, M.; Gorgoi, M.; Roling, B.; and Gottfried, J. M. $LiNi_0.5Mn_1.5O_4$ high-voltage cathode coated with $Li_4Ti_5O_12$: a hard X-ray photoelectron spectroscopy (HAXPES) study. *Phys. Chem. Chem. Phys.*, **2015**, *17*(47), 31790. doi:10.1039/c5cp03837e.

Acknowledgment

First and foremost, I would like to thank Prof. Dr. Michael Gottfried for providing me the opportunity to conduct my doctorate in Germany – initially in Erlangen and later in his own group in Marburg – as well as for his continuous support, guidance, and advice during my study. I am grateful to Prof. Dr. Hans-Peter Steinrück for his warm admission in Germany and his inspirational mentorship during my time in Erlangen.

I would like to express my gratitude to Dr. Martin Schmid for introducing me to the laboratories in Germany and his wise instructions. I would also like to thank Dr. Jie Xiao for pleasant cooperations and fruitful discussions during my study in Erlangen.

Cooperation – regarding scanning tunneling techniques – with Prof. Dr. Kai Wu and Dr. Yongfeng Wang at Peking University as well as Prof. Dr. Nian Lin at Hong Kong University of Science and Technology is gratefully acknowledged. Support from PD Dr. Wolfgang Hieringer providing density functional theory calculations is also highly appreciated.

Furthermore, I would like to express my great gratitude to my closest coworkers Hans-Jörg Drescher, Han Zhou, and Malte Zugermeier in Erlangen and Marburg. I highly acknowledge the teamwork during beamtimes at BESSY II also with Benedikt Klein, Claudio Krug, Malte Sachs, and Stefan Renato Kachel. Support by the beam line scientists Dr. Mihaela Gorgoi and Dr. Ruslan Ovsyannikov at BESSY II is also gratefully acknowledged here.

Support from the workshops – electricians, glassblowers, precision mechanics, and technicians – in Erlangen and in Marburg is greatly appreciated. Furthermore, my thanks go to all staff members of both workgroups, in Erlangen and in Marburg, as well as to the members of external collaboration partners for the warm and friendly atmosphere and fruitful cooperation.

From the bottom of my heart, I would like to thank my parents, brothers, and sister for the enduring encouragement and endless support during my studies.

Curriculum Vitae

In the online version of this thesis the personal data is removed for privacy protection.

A Technical Drawings

This appendix contains the technical drawings related to the evaporator presented in Section 2.4.6. Images are scaled by 71 % to fit a page, chamfers are 1X45°, threads are cut to maximum depth, and one piece each is to be manufactured. Dimensions are given in millimeters and decimal degrees. Tubes are designated by $\varnothing_{\text{outer}} \times d_{\text{wall}}$ and parts are made from 1.4301 if not stated otherwise.

The used coaxial heating wire with a diameter of 1 mm and a length of 450 mm from Thermocoax comprises a stainless steel sheath, no cold ends, and ceramic connectors.

A.1 Evaporator for Delicate Organic Substances

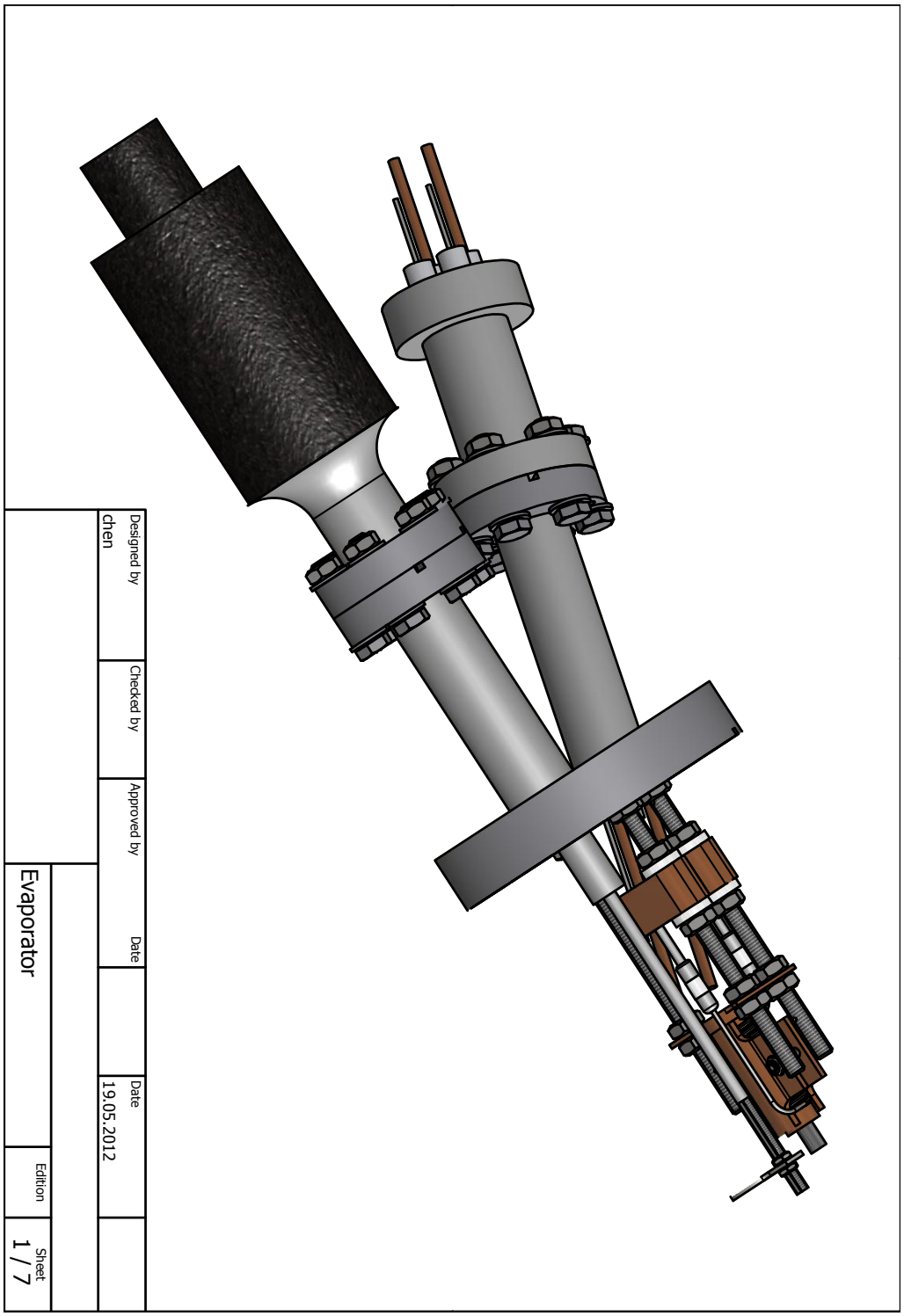

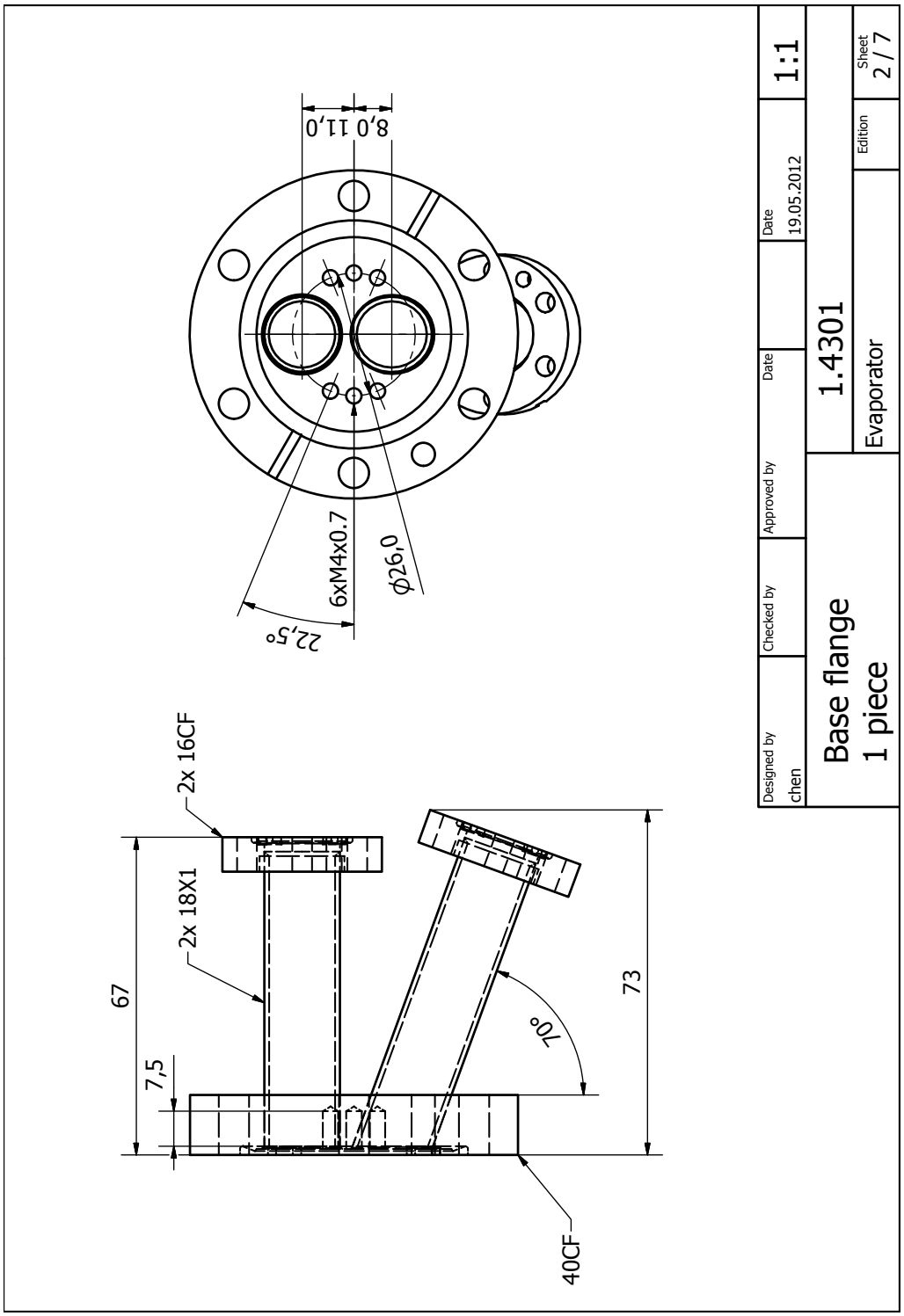
8,0 11,0
6xM4x0.7
ϕ26,0
22,5°
2x 16CF
2x 18X1
67
7,5
73
10°
40CF
Designed by
chen
Checked by
Approved by
Date
Base flange
1 piece
1.4301
Evaporator
Date
19.05.2012
Edition
1:1
Sheet
2 / 7

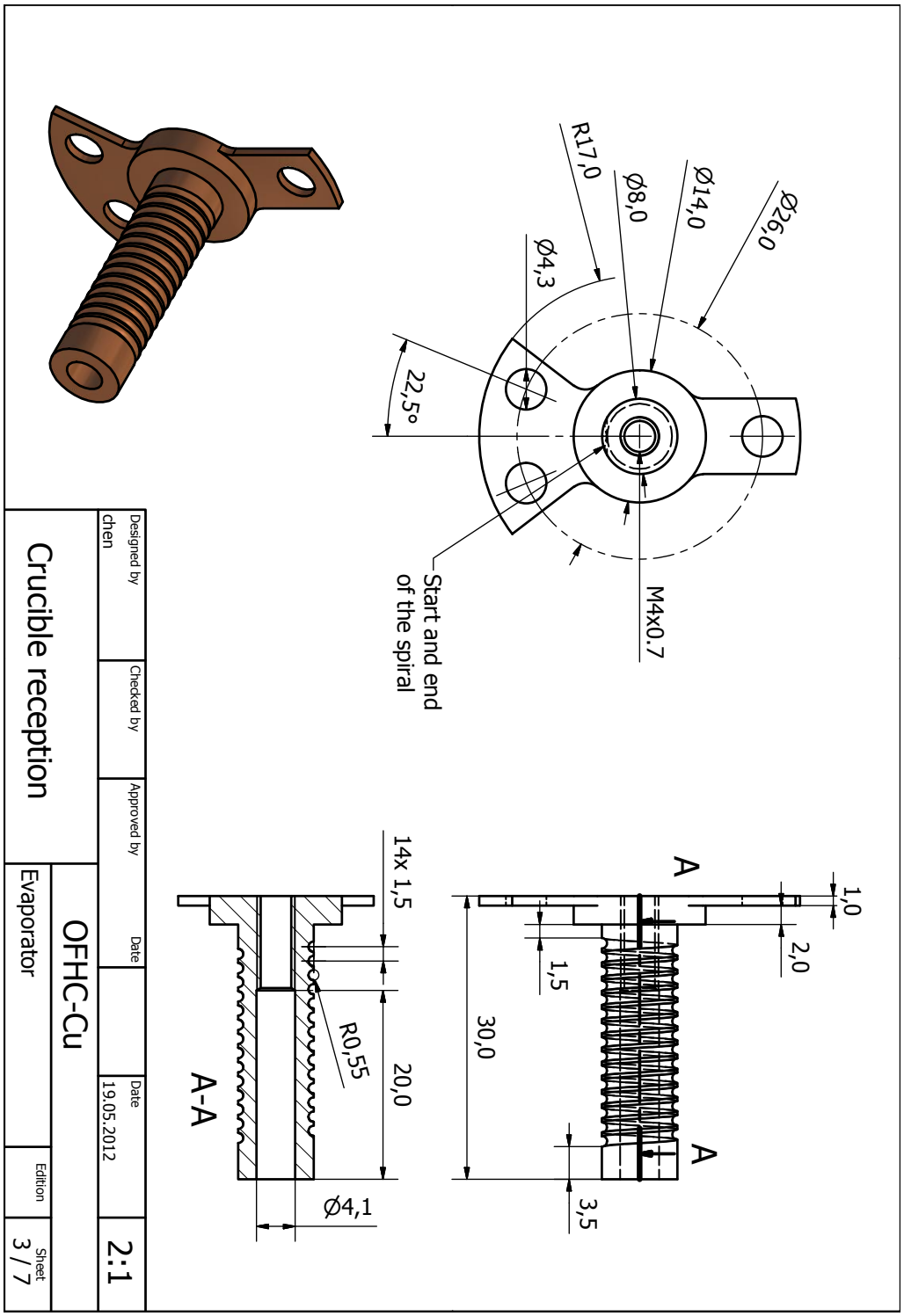
Ø26,0
Ø14,0
Ø8,0
R17,0
Ø4,3
22,5°
Start and end of the spiral
M4x0.7
A
A
1,0
2,0
1,5
30,0
3,5
14x 1,5
R0,55
20,0
A-A
Ø4,1
Designed by
chen
Checked by
Approved by
Date
Date
19.05.2012
Crucible reception
OFHC-Cu
Evaporator
Edition
Sheet
3 / 7
2:1

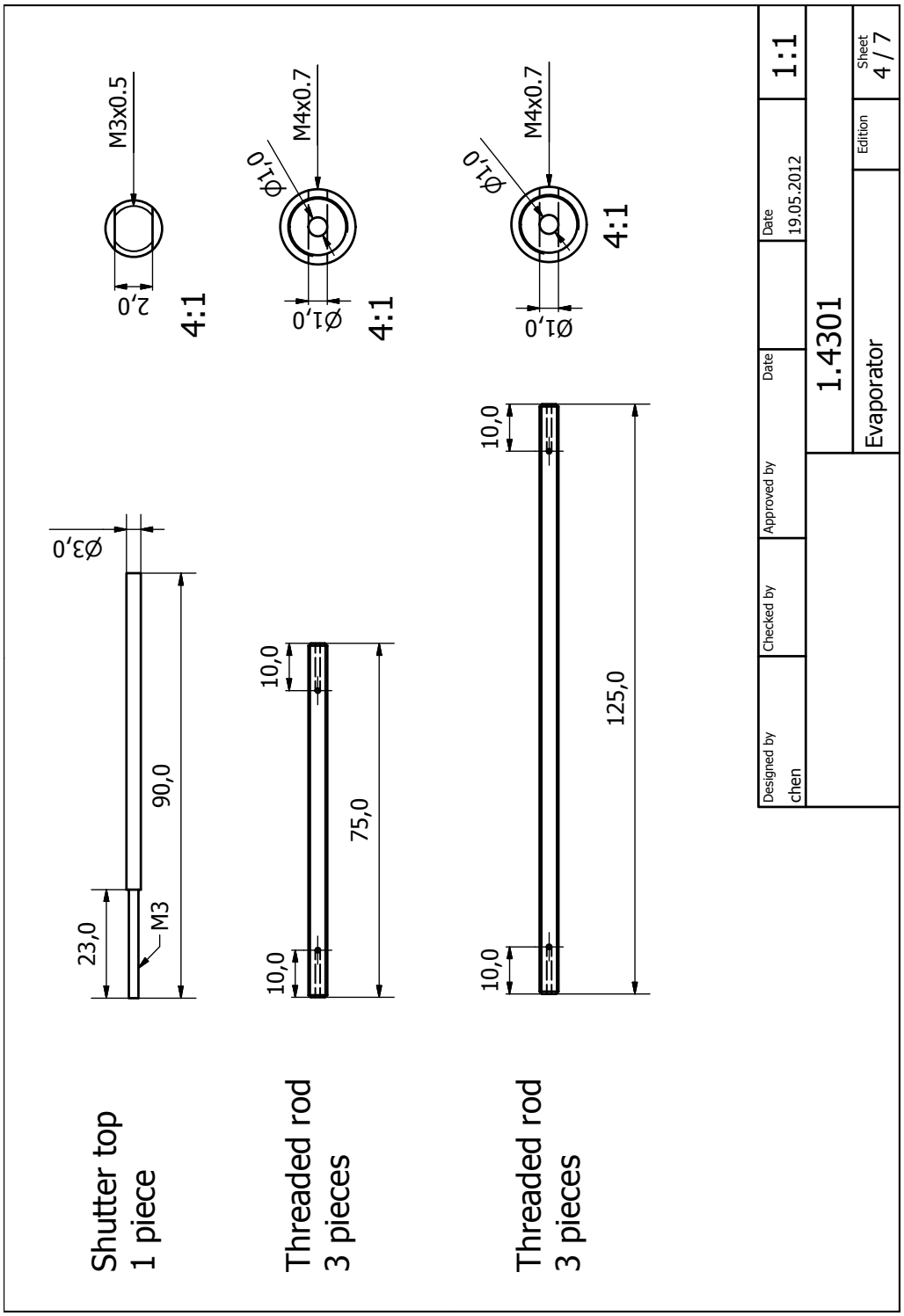
M3x0.5
2,0
4:1
M4x0.7
Ø1,0
4:1
M4x0.7
Ø1,0
4:1
Ø3,0
23,0
M3
90,0
Shutter top
1 piece
10,0
10,0
75,0
Threaded rod
3 pieces
10,0
10,0
125,0
Threaded rod
3 pieces
Designed by
chen
Checked by
Approved by
Date
Date
19.05.2012
1:1
1.4301
Evaporator
Edition
Sheet
4 / 7

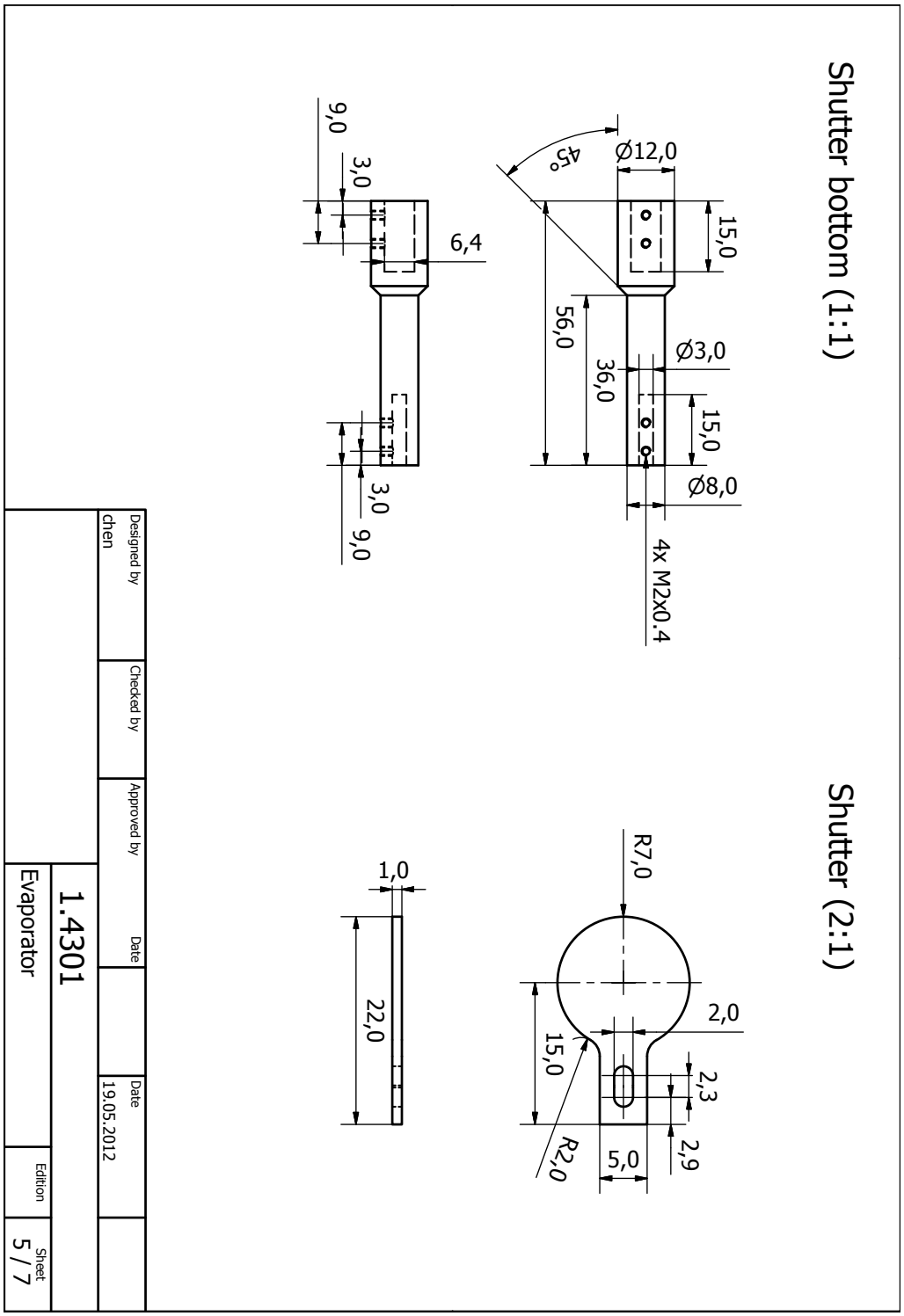
Shutter bottom (1:1)
Shutter (2:1)
Ø12,0
45°
15,0
56,0
36,0
Ø3,0
15,0
Ø8,0
4x M2x0.4
9,0
3,0
6,4
3,0
9,0
1,0
22,0
R7,0
2,0
15,0
2,3
2,9
R2,0
5,0
Designed by
chen
Checked by
Approved by
Date
Date
19.05.2012
1.4301
Evaporator
Edition
Sheet
5 / 7

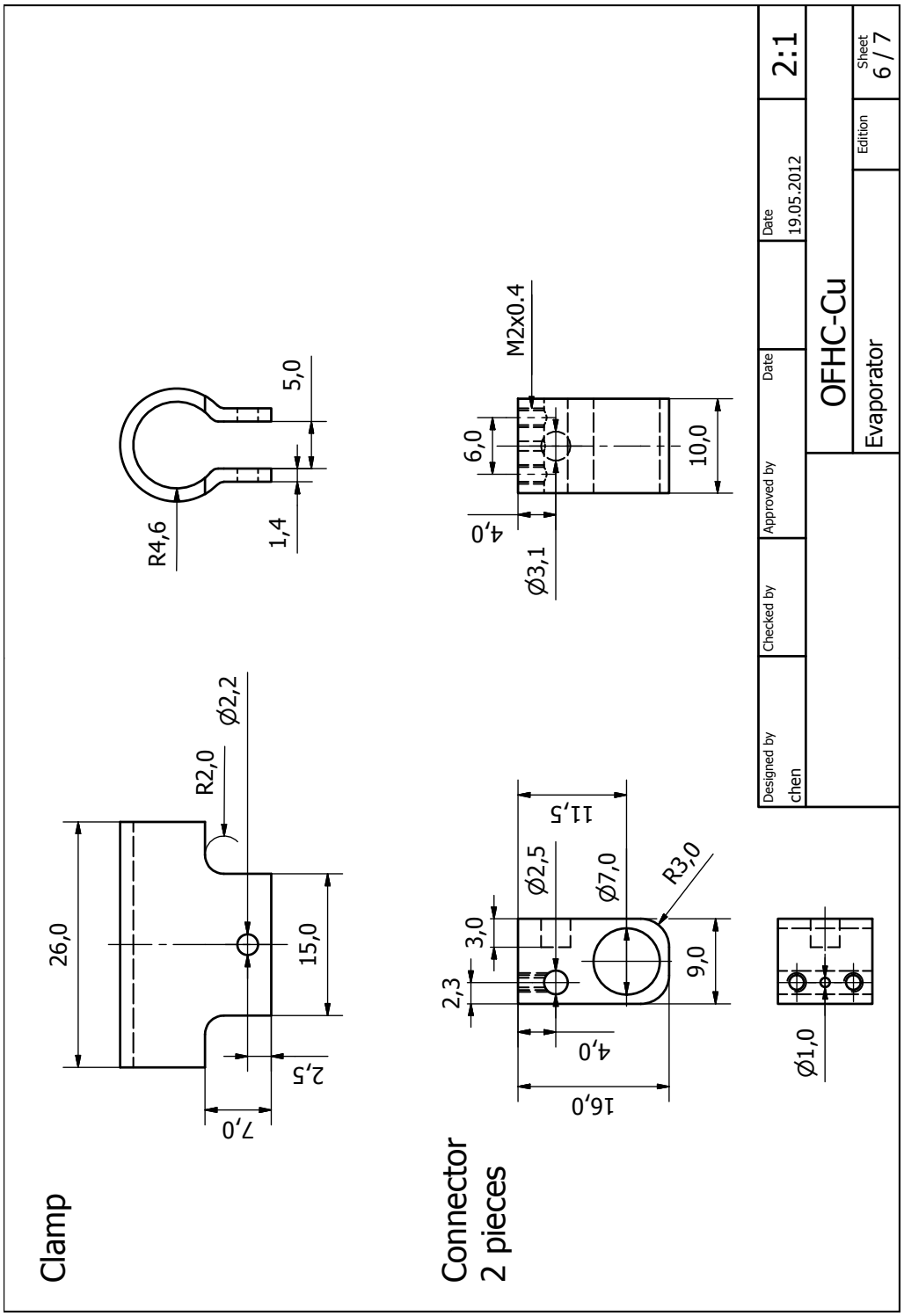
Clamp
26,0
R2,0
Ø2,2
15,0
2,5
7,0
R4,6
1,4
5,0
Connector
2 pieces
M2x0.4
6,0
10,0
4,0
Ø3,1
11,5
Ø2,5
Ø7,0
R3,0
3,0
2,3
9,0
4,0
16,0
Ø1,0
Designed by
chen
Checked by
Approved by
Date
Date
19.05.2012
2:1
OFHC-Cu
Evaporator
Edition
Sheet
6 / 7

PARTS LIST			
ITEM	QTY	PART NUMBER	DESCRIPTION
1	1	Base flange	
2	1	Crucible reception	
3	1	Shutter	
4	1	Shutter rod bottom	
5	3	ISO 4032 - M2	Hexagon nuts, style 1 - Product grades A and B
6	1	DIN 913 - M4 x 20	Hexagon Socket Set Screw
7	2	DIN 913 - M2 x 4	Hexagon Socket Set Screw
8	1	BRM-133	Rotational Feedthrough
9	1	A0443-1-CF	Power/thermocouple Combination Feedthrough
10	24	DIN 125 - A 4.3	Washer
11	25	ISO 4032 - M4	Hex Nut
12	12	ISO 4017 - M4 x 20	Hex-Head Bolt
13	1	GAZ M45	Glassy Carbon Crucible
14	1	1NcAc10/45cm/2xCP10	Thermocoax
15	1	Clamp	
16	2	Power connector A	
17	1	Power connector B	
18	4	Split bushes inner M4	
19	1	ISO 4762 - M2 x 10	Hexagon Socket Head Cap Screw
20	6	DIN 913 - M2 x 3	Hexagon Socket Set Screw
21	3	Threaded rod -75	
23	1	Shutter rod top-75	

Designed by: chen
Checked by:
Approved by:
Date:
Date: 19.05.2012
Evaporator
Edition
Sheet 7 / 7

B Scientific Publications

This chapter gathers the published, accepted and submitted publications referred to in this work:

Publication [P1] Coordination Reactions and Layer Exchange Processes at a Buried Metal-Organic Interface
M. Chen, M. Roeckert, J. Xiao, H.-J. Drescher, H.-P. Steinrück, O. Lytken, J.M. Gottfried
J. Phys. Chem. C, **2014**, *118*, 8501-8507.
doi:10.1021/jp5019235. Identical to Reference [187].

Publication [P2] Combined Photoemission and Scanning Tunneling Microscopy Study of the Surface-Assisted Ullmann Coupling Reaction
M. Chen, J. Xiao, H.-P. Steinrück, S. Wang, W. Wang, N. Lin, W. Hieringer, J.M. Gottfried
J. Phys. Chem. C, **2014**, *118*, 6820-6830.
doi:10.1021/jp4121468. Identical to Reference [230].

Publication [P3] Diffusion, Rotation, and Surface Chemical Bond of Individual 2*H*-Tetraphenylporphyrin Molecules on Cu(111)
F. Buchner, J. Xiao, E. Zillner, M. Chen, M. Roeckert, S. Ditze, M. Stark, H.-P. Steinrück, J.M. Gottfried, H. Marbach
J. Phys. Chem. C, **2011**, *115*, 24172-24177.
doi:10.1021/jp206675u. Identical to Reference [171].

Publication [P4] Temperature-Dependent Chemical and Structural Transformations from 2*H*-Tetraphenylporphyrin to Copper(II)-Tetraphenylporphyrin on Cu(111)
J. Xiao, S. Ditze, M. Chen, F. Buchner, M. Stark, M. Drost, H.-P. Steinrück, J.M. Gottfried, H. Marbach
J. Phys. Chem. C, **2012**, *116*, 12275-12282.
doi:10.1021/jp301757h. Identical to Reference [181].

Publication [P5] Coordination and Metalation Bifunctionality of Cu with 5,10,15,20-Tetra(4-pyridyl)porphyrin: Toward a Mixed-Valence Two-Dimensional Coordination Network
Y. Li, J. Xiao, T.E. Shubina, M. Chen, Z. Shi, M. Schmid, H.-P. Steinrück, J.M. Gottfried, N. Lin
J. Am. Chem. Soc., **2012**, *134*, 6401-6408.
doi:10.1021/ja300593w. Identical to Reference [16].

Publication [P6] Assembling molecular Sierpiński triangle fractals
J. Shang, Y. Wang, M. Chen, J. Dai, X. Zhou, J. Kuttner, G. Hilt, X. Shao, J.M. Gottfried, K. Wu
Nature Chemistry, **2015**, *7*, 389-393.
doi:10.1021/ja300593w. Identical to Reference [231].

Publication [P7] Interfacial chemical bond, charge transfer and weak band bending of cobalt phthalocyanine on Cu(111)
Min Chen, Jie Xiao, Hans-Peter Steinrück, M. Schmid, and J. Michael Gottfried
Unpublished

Publication [P8] Oxidation State Tuning in Ligand-Metal Surface Reaction: Formation of Co(III)-Corrole on Ag(111)
Min Chen, M. Schmid, M. Bröring, J. M. Gottfried
Unpublished

Publication [P9] Formation of a Metal/Organic Interphase Monitored Using a Well-Defined Porphyrin Metalation Reaction: A Hard X-Ray Photoelectron Spectroscopy (HAXPES) Study
M. Chen, Han Zhou, Malte Zugermeier, Benedikt Klein, Claudio Krug, Hans-Jörg Drescher, Mihaela Gorgoi and J. Michael Gottfried
Unpublished

Publication [P10] Investigation of the Multilayer Metalation and Interface Formation between Co and 2HTPP
M. Chen, Falk Niefind, Stefan Spannenberger, Han Zhou, Malte Zugermeier, J. Michael Gottfried
Unpublished

Publication [P11] Honeycombenes: Particle in a Box and Particle on a Ring
M. Chen, J. Shang, Y. Wang, K. Wu, J. Kuttner, G. Hilt, W. Hieringer, J. Michael Gottfried
Unpublished

Publication [P12] $LiNi_{0.5}Mn_{1.5}O_4$ High-Voltage Cathode Coated with $Li_4Ti_5O_{12}$: A Hard X-ray Photoelectron Spectroscopy (HAXPES) Study
M. Sachs, M. Gellert, M. Chen, H.-J. Drescher, S.R. Kachel, H. Zhou, M. Zugermeier, M. Gorgoi, B. Roling, J.M. Gottfried
Phys. Chem. Chem. Phys., **2015**, *17*, 31790-31800.
doi:10.1039/c5cp03837e. Identical to Reference [232].

In the online version of this thesis the individual publications are removed due to copyright issues.